The Thesis Committee for Nancy Anne Larson
Certifies that this is the approved version of the following thesis:

Structural Performance of ASR/DEF Damaged Prestressed Concrete Trapezoidal Box Beams with Dapped Ends

APPROVED BY
SUPERVISING COMMITTEE:

Supervisor:

Oguzhan Bayrak

James Jirsa

Structural Performance of ASR/DEF Damaged Prestressed Concrete Trapezoidal Box Beams with Dapped Ends

by

Nancy Anne Larson, BSCE

Thesis

Presented to the Faculty of the Graduate School of

The University of Texas at Austin

in Partial Fulfillment

of the Requirements

for the Degree of

Master of Science in Engineering

The University of Texas at Austin

August 2010

Dedication

To my parents,

Mom, for your childhood determination to provide your own children with LEGOs

Dad, due to your interest and support we are one step closer to your prestressing springs

I love you

Acknowledgements

I greatly appreciate the financial support from the Texas Department of Transportation that made this project possible.

I would like to thank my advisors, Dr. Oguzhan Bayrak and Dr. James O. Jirsa. Your guidance and confidence helped me to overcome any difficulties and ensured that I got the most out of this learning experience. You have encouraged me to grow and have helped to prepare me for the next step in my education.

Furthermore I would like to thank the people who make up Ferguson Structural Engineering Laboratory. All my peers without whose cooperation concrete would never be cast and tests would not run smoothly. I would like to thank the team of Catherine Hovell, Dave Dunkman, and Andrew Moore for all of your help and sharing your test setup. Alejandro Avendaño, thank you for your advice and checking up on us from time to time. Dean Deschenes thank you for sharing your ASR/DEF expertise and your superior photography talents.

I am deeply grateful for all the help and guidance that I received from the Ferguson Structural Engineering Lab staff. Andrew Valentine, Blake Stasney, and Dennis Fillip were always willing and able to provide us with a helping hand. Eric Schell and Mike Wason, thank you for your guidance in instrumentation. Barbara Howard and Jessica Hanten, thank you for ensuring the lab is run smoothly and helping us with project supplies.

Finally, I could not have completed this thesis without my project team. The determination and organization of Bryan Bindrich got the experimental portion up and running and enabled Tz-Wei Wang and I to complete the project. Eulalio Fernández, thank you for all of your help with the NDT analysis and epoxying the autopsy beam.

August 13, 2010

Abstract

Structural Performance of ASR/DEF Damaged Prestressed Concrete Trapezoidal Box Beams with Dapped Ends

Nancy Anne Larson, BSCE

The University of Texas at Austin, 2010

Supervisor: Oguzhan Bayrak

Across the State of Texas and many other areas of the world, relatively young concrete structures have developed signs of premature concrete deterioration. Large cracks form on the surface of the concrete due to expansive forces from alkali-silica reaction (ASR) and delayed-ettringite formation (DEF). The goal of this project is to assess the effect of ASR/DEF on the trapezoidal box beam bridges in the US 59 corridor and Katy Central Business District (CBD) HOV lanes in Houston, TX. Five dapped-end beams were rejected during the casting process and have been in storage at a local precast yard for nearly fifteen years. These beams have been subject to accelerated deterioration and represent the potential severity of the ongoing ASR/DEF distress within the dapped-end regions of the in-service trapezoidal box beams. The results from five load tests, corresponding strut-and-tie models, and forensic investigation are used to provide insights into the relationship between the severity of the deterioration and the capacity margin.

Table of Contents

List of Tables

List of Figures

CHAPTER 1
Introduction

1.1 OVERVIEW

Across the State of Texas and many other areas of the world, relatively young concrete structures have developed signs of premature concrete deterioration. In a number of cases, severe surface cracking and occasional spalling have been identified as symptoms of both alkali-silica reaction (ASR) and delayed-ettringite formation (DEF). Uncertainty with regards to the structural effects of the deterioration have led engineers to commonly err on the side of caution; costly repair or replacement schemes have been frequently implemented to eliminate long-term concerns. Such an approach could have a significant effect on future financial outlays in the State of Texas. It is estimated that the Texas Department of Transportation (TxDOT) has more than one billion dollars worth of prematurely damaged infrastructure in the Houston District alone (Vogel, 2008).

Most of the bridges on the US 59 corridor (between IH 610 and BW 8) and the Katy Central Business District (CBD) HOV lanes were constructed with prestressed trapezoidal concrete box beams. After a little more than a decade in service, many of the exterior box beams are showing signs of premature concrete deterioration. TxDOT's current strategy for mitigation of the deterioration is a waterproofing treatment priced at 10 dollars per square foot of beam surface. The Katy-CBD HOV lanes contain 26,644 linear feet of trapezoidal box beams and more than 300,000 square feet of treatable surface area. At the market rate, the total cost for waterproofing would exceed the original purchase price (2.6 million dollars) of the box beams (Vogel, 2008).

Previous laboratory testing of ASR/DEF-affected reinforced and prestressed concrete beams has not revealed any drastic implications for the flexure or shear strength of simple, well-detailed elements. While the results are generally promising, it is difficult to extrapolate the results to larger, more complex field structures. TxDOT Houston District engineers face such a challenge in evaluating the effects of severe ASR/DEF

deterioration within the dapped ends of the trapezoidal box beams described above. Load testing has never been performed to investigate the effects of premature concrete deterioration on the structural performance of dapped ends. The majority of research with ASR/DEF affected members focused on much smaller, rectangular sections. The unique load transfer mechanisms and reinforcement details within a dapped end render the test results found in the literature unsuitable for evaluation purposes.

1.2 PROJECT OBJECTIVES AND SCOPE

Five trapezoidal box beams were cast but not erected within the US 59 corridor. The beams were rejected during the casting process due to void rotation and concrete consolidation issues. Over the past fifteen years, the box beams have been exposed to the elements in the Traylor Brothers' precast yard in Houston, TX. Four of the beams were cast in July of 1995 and showed signs of premature concrete deterioration (ASR and/or DEF) varying from mild to severe. The fifth beam was cast in November of 1995 and showed little to no sign of premature concrete deterioration; more or less representative of an "undamaged" beam.

The cracked surfaces of these beams are assumed to represent the condition of the bridge beams currently in service in 10 to 30 years, depending on environmental exposure conditions and coatings that may be applied on these structural elements. It is important to appreciate that the deleterious chemical mechanisms ASR and DEF occur at a slower rate in the actual bridge beams due to the weather protection provided by the reinforced concrete bridge deck.

Through an interagency testing contract, the Houston District of Texas Department of Transportation provided funding for The University of Texas at Austin (UT Austin) to conduct structural tests on the dapped ends of the prestressed concrete trapezoidal box beams. The results from load testing of the four beams with moderate to severe levels of ASR/DEF damage were to be compared with the results from the "undamaged" segment. In addition, UT was to conduct a structural autopsy on one of the heavily cracked beams. Load testing was performed at the Phil M. Ferguson Structural

Engineering Laboratory (FSEL) of the University of Texas. The results of the tests provide immediate insight to the severity of the problem that exists in most of the bridges with the US 59 corridor and the Katy Central Business District HOV lanes. Careful review of the project's findings will enable TxDOT engineers to make better repair/replacement recommendations for the trapezoidal box beam bridges as well as other structures affected by premature concrete deterioration within the State of Texas.

The scope of this study included: (1) preparation and shipment of the beams to FSEL, (2) preparation of a load testing frame and instrumentation, (3) load testing of dapped ends with varying degrees of ASR/DEF-related damage, (4) epoxy injection and sectioning of one severely damaged beam, and (5) recommendations regarding application of the load testing results to the structural evaluation of the prestressed concrete trapezoidal beams affected by ASR and/or DEF.

1.3 ORGANIZATION

The work conducted over the course of the two-year study is described in the flowing six chapters: Chapter 2 – Background, Chapter 3 – Experimental Program, Chapter 4 – Experimental Results and Analysis, Chapter 5 – Forensic Investigation, and Chapter 6 – Summary and Conclusions. A brief outline of each chapter is provided below.

Background information pertinent to the current study is presented in Chapter 2. First, the history of the design of reinforced and prestressed concrete beams with dapped-ends is summarized and the aspects of the structural behavior that will likely control the load carrying capacity of the beams are identified. Second, the premature concrete deterioration mechanisms, alkali-silica reaction (ASR) and delayed ettringite formation (DEF), are described to provide a background on their chemical compositions and physical implications. Finally, relevant research on ASR/DEF affected beams is discussed to provide a basis for the structural assessment of the dapped-ends of the trapezoidal prestressed concrete beams examined in this study.

The experimental program, including the tasks related to the acquisition, preparation, and testing of the five segments, is outlined in Chapter 3. The structural details of the trapezoidal box girders, including the dap geometry, mild reinforcement layout, and strand debonding patterns, are examined first. The full range of deterioration, including both ASR/DEF related damage and structural properties and defects, encompassed by the five box beams is then revealed. Finally, the test setup, instrumentation and loading procedure of the dapped-end segments are described.

Measurements and observations made during the course of the load tests performed on the dapped-ends of the five trapezoidal prestressed concrete beams are presented in Chapter 4. The damage critical to the structural performance of the dapped-end detail is examined and the load-deformation response and ultimate strength of each segment are then reported with respect to the level of cracking (i.e. light, moderate, or heavy). Finally, application of strut-and-tie modeling provisions from ACI 318-08, AASHTO LRFD 2009, and TxDOT Project 0-5253 allow the capacity margin of the ASR/DEF-damaged dapped ends to be assessed.

Three forensic techniques applied to the trapezoidal box beam segments are discussed in Chapter 5. First, the findings of a petrographic analysis are used to establish the nature of the deterioration found within three of the beam segments. Second, the results of the structural autopsy of an epoxy injected beam are examined to reveal notable interior cracking which contributed to the behavior and load-carrying capacity of the damaged segments. Finally, estimates of the ASR/DEF-related expansion, obtained from elastic rebound testing of the strained transverse reinforcement, are summarized and compared to the qualitative damage assessments.

The experimental investigation performed during this study is summarized in Chapter 6. Conclusions and recommendations regarding the structural performance of the ASR/DEF-affected trapezoidal prestressed concrete beams with dapped-end are presented. Finally, suggestions are made for future work within the State of Texas including focusing on the issue of further deterioration and the potential loss of confinement through ASR/DEF-induced reinforcement fracture.

CHAPTER 2
Background

2.1 OVERVIEW

Evaluation of the ASR/DEF-affected trapezoidal box beams required a broad knowledge base due to the complexity of the problem at hand. It was recognized that proper evaluation and application of the structural test results would require knowledge of: (1) the design and detailing of dapped ends, (2) the latest strut-and-tie modeling methods, (3) the physical effects of ASR/DEF deterioration, and (4) historically significant test results from ASR/DEF-affected structures. This chapter will provide the information necessary to draw measured conclusions and observations from the results presented in the remainder of this document.

First, the history of the design of reinforced and prestressed concrete beams with dapped ends is summarized. In this context, the layout of the beams with dapped ends used in the US-59 corridor in Houston and tested under this project is discussed. The aspects of the structural behavior that will likely control the load carrying capacity of the beams are identified. Second, the premature concrete deterioration mechanisms, alkali-silica reaction and delayed ettringite formation, are described to provide a background on their chemical compositions and physical implications. Characteristics common to both mechanisms are compared to the current state of the prestressed concrete trapezoidal girders under investigation. Finally, relevant research on alkali-silica reaction (ASR) and delayed ettringite formation (DEF) is reviewed. Previous laboratory research is discussed to form the basis for the structural assessment of the dapped-end ASR/DEF damaged prestressed trapezoidal box girders.

2.2 DESIGN OF DAPPED ENDS OF REINFORCED AND PRESTRESSED CONCRETE BEAMS

Beams with dapped ends are commonly used in the transportation industry. They help to reduce the superstructure depths resulting in an efficient utilization of space and

resources. Dapped ends are also used in bridges with drop-in girders which allow for increased span lengths. Their use in bridges results in aesthetically pleasing structures by maintaining a constant depth between the beam and bent cap. A simplified diagram of a dapped-end beam and inverted tee bent cap is illustrated in Figure 2-1.

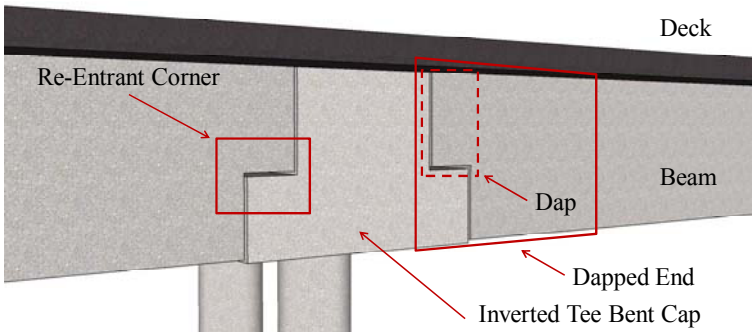

Figure 2-1: Bridge Beams with Dapped Ends

Several design challenges are created when a concrete beam is dapped as the ends of simply supported beams are subjected to the highest shear forces. A large amount of the shear-resisting concrete is removed with the reduction of the beam's height and a severe stress concentration is developed at the re-entrant corner (shown in Figure 2-1). Despite the wide use of dapped-end beams, studies on their behavior are limited. The first analyses evaluating the elastic stress distribution of forces were completed in the early 1970s at the University of Washington. Additional research in the late 1970's by Mattock & Chan was conducted to determine the design of dapped-end beams and became the basis of the PCI Design Handbook's recommendations. Further research has been conducted to improve original design equations and develop new methods, including strut-and-tie modeling in TxDOT Project 1127 performed by the University of Texas, as well as shear friction and diagonal bending. The design method given in the PCI Design Handbook and strut-and-tie modeling (STM) are the main design methods examined in this study.

2.2.1 PCI Design Handbook (2004)

Section 4.6.3 of the PCI Design Handbook examines beams with recessed or dapped bearing areas. The behavior of these regions can be studied based on several

potential failure modes as described in Figure 2-2. The PCI Design Handbook's method is based on corbel provisions and a reinforcement layout for resisting the different cracking patterns and beam failure.

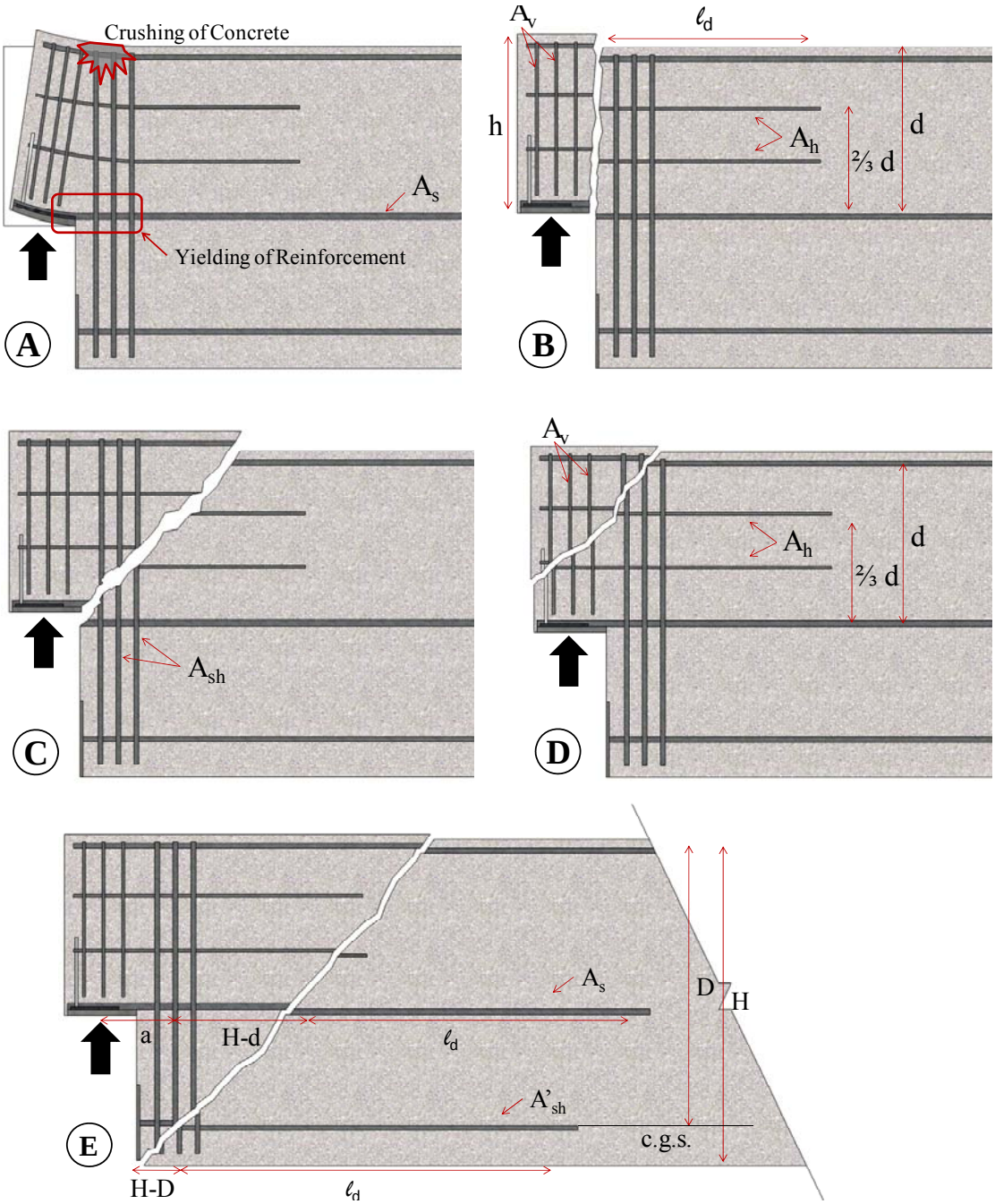

Figure 2-2: Potential Failure Modes and Required Reinforcement (Adapted from PCI Design Handbook 2004).

Failure by flexure (cantilever bending) and axial tension in the beam extension can be prevented by providing flexural or axial tension reinforcement similar to that for column corbels as shown in Figure 2-2A. Figure 2-2B illustrates a direct shear failure at the junction of the dap and the main body of the member. A combination of vertical and horizontal reinforcement is incorporated to preclude that mode of failure. The failure mechanism shown in Figure 2-2C results from diagonal tension emanating from the re-entrant corner. This failure mode is controlled by providing shear and hanger reinforcement, A_{sh}, which should be placed as close to the re-entrant corner as possible. The failure mode depicted in Figure 2-2D represents diagonal tension in the beam extension and is controlled with the horizontal and vertical shear reinforcement, A_h and A_v. Diagonal tension failure in the main body of the beam is shown in Figure 2-2E and is primarily controlled by providing a full development length for A_s beyond the potential diagonal crack. Anchorage of all reinforcement is critical in this end region (PCI 2004). Additional stirrups are provided throughout the section where required.

2.2.2 Strut-and-Tie Modeling

Strut-and-tie modeling has been incorporated into recent codes to offer an effective method for lower bound strength estimates and designs of disturbed areas (D-regions) in reinforced and prestressed concrete structures. Based on applications of the theory of plasticity, a strut-and-tie model (STM) can be used to represent and simplify the flow of forces through a structure. An efficient STM can be constructed using the elastic stress field diagram. Because STMs were developed to design the shear critical and disturbed regions of structures, the design technique is viewed as an excellent tool for modeling the dapped ends of prestressed concrete beams.

Strut-and-tie models are composed of three elements: struts, ties, and nodes. Struts represent compression elements and are typically displayed with dashed lines on a model such as the one shown in Figure 2-3. Ties are tension elements and are shown as solid lines. Reinforcing steel carries the load in ties while struts are typically made up of concrete or a combination of concrete and steel. Nodes represent the intersection of two

or more elements of a strut and tie model. All ties should be properly anchored so that the force can develop at the inner face of the nodal zone

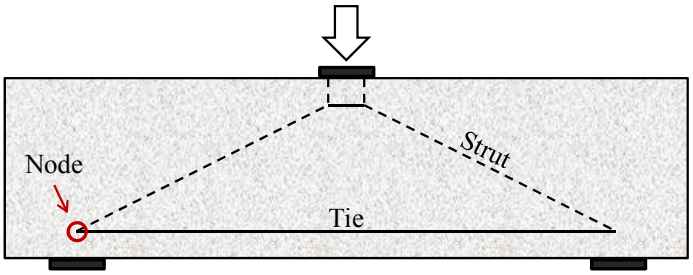

Figure 2-3: A Strut and Tie Model

2.2.2.1 Design Provisions

The following sections outline the three design provisions, AASHTO LRFD Bridge Design Specifications (2009 interim), ACI 318-08, and the STM design guidelines developed under TxDOT research project 0-5253, used to calculate the capacity of the beams. The same strut-and-tie model is utilized in conjunction with the aforementioned three methods.

2.2.2.1.1 AASHTO LRFD Design Method (2009 interim)

Section 5.6.3 of *AASHTO LRFD Bridge Design Specifications*, referred to as AASHTO LRFD in the subsequent discussion, includes a discussion on the strut-and-tie method for modeling deep beams. AASHTO LRFD considers the strength of struts, ties, and nodes in the design of a structure.

In order to proportion the strut, the nominal resistance of an unreinforced strut is defined by AASHTO LRFD as:

$$P_{ns} = f_{cu} * A_{cs} \qquad \textbf{Equation 2-1} \text{ (5.6.3.3.1-1)}$$

Where:

P_{ns} = nominal resistance of a compressive strut (kip)

f_{cu} = limiting compressive stress (ksi)

A_{cs} = effective cross sectional area (ksi)

The value of A_{cs} is determined by considering the available concrete area and the anchorage conditions at the end of the strut. When a strut is anchored by reinforcement, the effective concrete area extends a distance up to six bar diameters from the anchored bar.

The limiting compressive stress f_{cu} considers the compressive strength of the concrete and strains imposed on the concrete.

$$f_{cu} = \frac{f'_c}{0.8 + 170\varepsilon_1} \leq 0.85 f'_c$$ ***Equation 2-2*** (5.6.3.3.3-1)

In which:

$$\varepsilon_1 = \varepsilon_s + (\varepsilon_s + 0.002)\cot^2 \alpha_s$$ ***Equation 2-3*** (5.6.3.3.3-2)

Where:

α_s = smallest angle between the compressive strut and adjoining tension ties (°)

ε_s = tension strain in the concrete in the direction of the tension tie (in./in.)

f'_c = specified compressive strength (ksi)

If the concrete is not crossed by or joined to ties, it can resist a compressive stress of $0.85f'_c$. As the angle between the strut and tie decreases, ε_1 increases and the limiting compressive stress decreases. Because the strain in the tie is required to calculate the capacity of the strut, the AASHTO LRFD design procedure is an iterative method.

The tie reinforcement should be properly anchored so that the force can develop at the inner face of the nodal zone (i.e as the tie exits the extended nodal zone). AASHTO LRFD defines the nominal resistance of a tie as:

$$P_{nt} = f_y * A_{st} + A_{ps}[f_{pe} + f_y]$$ ***Equation 2-4*** (5.6.3.4.1-1)

Where:

A_{st} = total area of longitudinal mild steel reinforcement in the it (in.^{2})

A_{ps} = area of prestressing steel (in.^{2})

f_y = yield strength of mild steel longitudinal reinforcement (ksi)

f_{pe} = stress in prestressing steel due to prestress after losses (ksi)

P_{nt} = nominal resistance of a tensile tie (kip)

The second term in the equation ensures that the prestressing steel does not reach its yield point and provides a measure of control over unlimited cracking. The increase in the stress in the prestressing strands is limited to the same increase that the mild steel will undergo, hence the term f_y is used in the brackets of Equation 2-4.

Special consideration has to be given for the development of the prestressing strand. The full effective prestress force, f_{pe}, is developed at a distance, l_d, from the end of a member as calculated with Equation 2-5.

$$l_d \geq \kappa(f_{ps} - \frac{2}{3} f_{pe}) d_b \qquad \textbf{\textit{Equation 2-5}} \text{ (5.11.4.2-1)}$$

Where:

d_b = nominal strand diameter (in)

f_{ps} = average stress in prestressing steel at nominal resistance of the member (ksi)

f_{pe} = effective stress in prestressing strand after all losses (ksi)

κ = 1.6 for pretensioned members with a depth greater than 24.0 inches

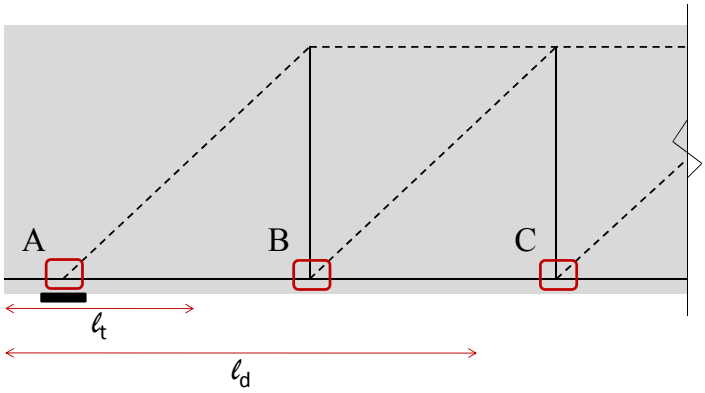

Figure 2-4: Consideration of Prestressing Strands

In the case where a node is located within the transfer length of the prestressing strand, shown as Node "A" in Figure 2-4, only a portion of the full stress in the prestressing strand can be considered. The design stress within the transfer length is calculated using Equation 2-6 from AASHTO LRFD Section 5.11.4.2 on the development of prestressing strand. The stress at a point between the transfer and development length of the strand, Node "B" shown in Figure 2-4, can be calculated using Equation 2-7 (AASHTO LRFD Equation 5.11.4.2-3). The stress in a tie past the

development length of the strand, such as the one to the right of Node "C" in Figure 2-4, is taken as $f_{pe} + f_y$. Once the stress in the prestressing strand is determined, the strength of the tie can be calculated using Equation 2-4.

$$f_{px} = \frac{f_{pe} * l_{px}}{60 d_b} \qquad \textbf{Equation 2-6} \text{ (5.11.4.2-2)}$$

$$f_{px} = f_{pe} + \frac{l_{px} - 60 d_b}{l_d - 60 d_b} * (f_{ps} - f_{pe}) \qquad \textbf{Equation 2-7} \text{ (5.11.4.2-3)}$$

Where:

l_{px} = distance from free end of prestress strands to section under consideration (in)

f_{px} = design stress in prestensioned strand at nominal flexural strength (ksi)

Nodes are proportioned based on the elements framing into them. A summary of the types of nodes and their corresponding concrete stress limits is provided in Table 2-1. These stresses and the corresponding effective concrete area are used to determine the capacity of the node. The reductions in allowable stress of CCT and CTT nodes are based on the adverse effect of the tensile straining caused by the ties.

Table 2-1: AASHTO LRFD Stress Limits for Nodes

Concrete Compressive Stress Limits in Node Regions (f'$_c$)	
"CCC" node – bounded by compressive struts and bearing areas	0.85
"CCT" node – anchored by a one-direction tension tie	0.75
"CTT" node – anchoring tension ties in more than one direction	0.65

2.2.2.1.2 TxDOT 5253 STM Design Guidelines

The STM design guidelines and provisions developed in TxDOT Project 5253 recommend the use of strut-and-tie models for designing D-regions near supports and concentrated loads. These provisions are based on the STM recommendations in *fib* (1999) and are significantly simpler and more accurate than the current method included in AASHTO LRFD Design Specifications. Implementation of the TxDOT Project 5253

improvements is expected to resolve many long-standing barriers to widespread use of strut-and-tie modeling within engineering practice.

TxDOT 5253 provisions recognize that stresses in a strut-and-tie model concentrate at the nodal zones and that the capacity of the model is directly related to the geometry of these nodal regions. Without distinguishing between the two, the design of the node-to-strut interface indirectly accounts for the design of a strut. References to the stress checks at CTT nodes have been removed because they are typically smeared nodes and are therefore not critical. Emphasis of deep beam design is placed on the critical stresses in the singular CCC and CCT nodal regions. Anchorage of reinforcement at all nodes is required.

The available capacity in the bearing face is calculated using an efficiency factor for a CCT node and can be increased using a triaxial confinement factor based on the bearing plate the size of the plane and the geometry of the member. An illustration using the prestressed trapezoidal box girders with dapped ends is shown in Figure 2-5.

$$P_{n_b} = m * \nu * f'_c * A_1 \qquad \textbf{\textit{Equation 2-8}} \text{ (5.6.3.3.3-1)}$$

Where:

P_{nb} = nominal bearing resistance

m = bearing capacity modification factor, $\sqrt{\frac{A_2}{A_1}} \leq 2$, as shown in Figure 2-5

ν = concrete efficiency factor (Table 2.2)

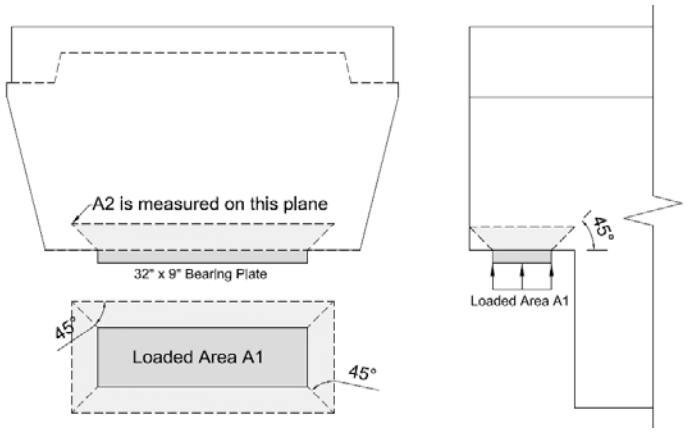

Figure 2-5 Definition of A1 and A2 for the Triaxial Confinement Factor

Like AASHTO LRFD, the TxDOT 5253 provisions reduce the allowable stress in a node. The varying concrete efficiency factors, *v*, are summarized in Table 2-2. Along with the type of node, TxDOT 5253 provisions also consider the face of the node in the calculations.

Table 2-2: TxDOT 5253 Node Limits

Concrete Efficiency Factors for Node Faces	
Bearing and back face of a CCC node	0.85
Bearing and back face of a CCT node	0.70
Strut-to-node interfaces with proper crack control reinforcement	$0.85–f'_c/20\text{ksi} \leq 0.65$
Strut-to-node interfaces of CCC and CCT nodes without proper crack control reinforcement	0.45

The stress that must be resisted by the back face of a CCT node can be attributed to the anchorage of the tie. If the tie is adequately developed, bond stresses are not critical and need not be applied as a direct force to the back face of a CCT node. Checks of smeared nodes are not required because their geometry is not well defined and they do not control the capacity of D-regions.

The strength of a tie is determined by multiplying the available area of steel by its yield strength as in Equation 2-4. Equation 2-6 and Equation 2-7 from AASHTO LRFD Section 5.11.4.2 are used where special considerations need to be taken for the development of the prestressing strand.

2.2.2.1.3 ACI 318-08 Strut and Tie Design Method

Like AASHTO LRFD, ACI318-08 differs from the TxDOT 5253 STM provisions in that struts, ties, and nodes are all considered in the design. The nominal strut capacity depends on the concrete strength and the cross sectional area of the strut and is modified by a strut efficiency factor as shown in Equation 2-9. This factor depends on the type of strut and whether is it properly reinforced as shown in Table 2-3.

$$P_{strut} = 0.85\beta_s * f'_c * A_{cs} \qquad \textbf{Equation 2-9} \text{ (A-2 \& A-3)}$$

Where:

P_{strut} = nominal strut capacity

β_s = strut efficiency factor from Table 2-4.

A_{cs} = cross sectional area of strut

Table 2-3: ACI 318-08 Strut Limits (A.3.2)

Strut Efficiency Factor, β_s	
Uniform strut	1.0
Bottle shaped struts with proper reinforcement	0.80
Struts in tension members	0.80
All other cases	0.60

Ties are defined in the same manner as the previous two methods in that their nominal strength is determined by their yield strength and steel area as shown in Equation 2-4. Like in the AASHTO LRFD Design Specifications, special considerations are taken for the development of the prestressing strand. Using the bilinear relationship between steel stress and distance from the free end of a strand (ACI318-08 *Figure R12.9*), the available stress in the strand is calculated. Equation 2-10 was used for sections less than the transfer length of the strand, while Equation 2-11 considers the stress in sections between the transfer and development length.

$$f_{se} = \frac{3 * l_{avail}}{d_b} \qquad \textbf{Equation 2-10}$$

$$f_{ps} - f_{se} = \frac{l_{avail}}{d_b} - \frac{f_{se}}{3} \qquad \textbf{Equation 2-11}$$

Where:

l_{avail} = length from free end of the strand to the edge of the extended nodal region

d_b = diameter of prestressing strand

f_{ps} = available stress in prestressing strand

f_{se} = stress in prestressing strand after all losses

Separate efficiency factors, based on the type of node, are used for the nodal zone strength checks and are shown in Table 2-4. These factors modify the product of the concrete stresses, $0.85f'_c$, and the corresponding effective concrete area, A_{nz}, to determine the capacity of the node. Again, the reductions in allowable nodal stress are based on the adverse effect of the tensile straining caused by the presence of ties.

Table 2-4: ACI 318-08 Node Limits (A.5.2)

Node Efficiency Factor, β_n	
Bounded by struts and bearing areas	1.0
Anchoring one tie	0.75
Anchoring one or more tie	0.60

2.3 DESIGN METHODS FOR BEAMS WITH DAPPED ENDS

Previous research on the application of strut-and-tie models for the design of dapped ends of reinforced and prestressed concrete beams as compared to previously accepted procedures (e.g. PCI Design Handbook Method) is discussed in this section.

2.3.1 Mader (1990)

Mader (1990) investigated the methods for detailing the discontinuity in the ends of dapped pretensioned beams. Unlike most studies, emphasis was placed on incorporating prestressing forces into the design. Three design methods were compared: PCI design method, Menon/Furlong design method, and the strut-and-tie method. The Menon/Furlong design was developed especially for pretensioned beams but will not be discussed herein because it incorporates a steel strap across the dap and re-entrant corner; a detail not commonly utilized in modern prestressed concrete beams.

Mader's first specimen was designed and detailed using the Prestressed Concrete Institute method (PCI 1994). The reinforcement layout was identical to the one shown in Figure 2-2 with #5 hoops as hanger reinforcement (A_{sh}), 3-#5 bars as the dap flexural reinforcement (A_s), #3 hoops as dap stirrups (A_v), and a #3 hoop and a #4 hoop as the horizontal bars (A_h). The flexural reinforcement, A'_{sh}, was the same for all designs and

included two #5 bars, six #6 bars and, eighteen 3/8” strands in order to provide a 25% increase in flexural strength to ensure a shear failure.

In addition to the specimen discussed above, Mader (1990) designed two dapped ends based on different strut-and-tie models. The orthogonal design most resembles the reinforcement layout in the dapped ends of the prestressed concrete beams under investigation and is shown in Figure 2-6. The corresponding strut-and-tie model is shown in Figure 2-7. The inclined strut-and-tie model (not shown in this document) incorporated hooked bars across the dap and re-entrant corner similar to the steel strap found in the Menon/Furlong design. Both of these details were found to be difficult to construct due to congestion of reinforcement. Coincidentally, such complicated details were not used in the design of the prestressed concrete trapezoidal box beams that are being investigated in this project.

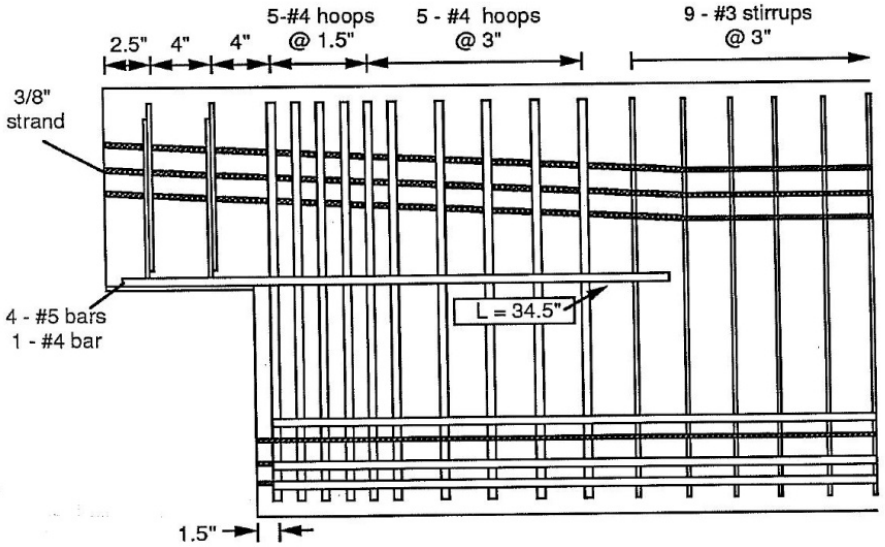

Figure 2-6: Reinforcement Layout for STM (Mader 1990)

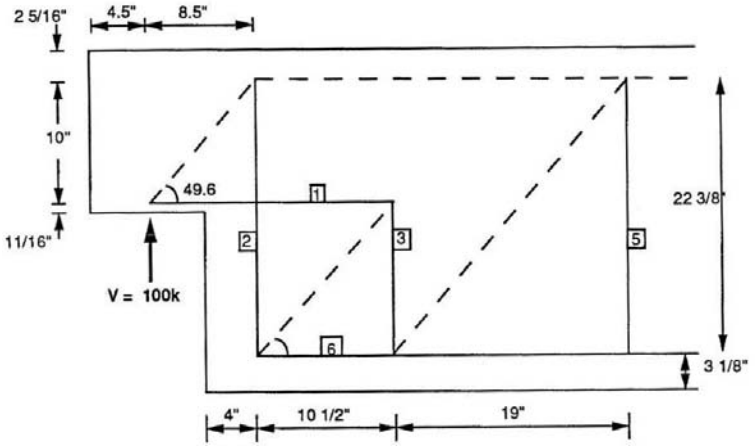

Figure 2-7: Strut-and-Tie Model (Mader 1990)

All specimens were tested in shear and showed visible cracks at very low loads with the first crack appearing at the re-entrant corner. Cracks were more evenly distributed across the depth of the beam in the strut-and-tie specimens which failed at loads that were 15-20% higher than predicted.

The specimen that was designed using the PCI Design Handbook approach failed at a lower load due to poor detailing of the end vertical reinforcement. The vertical #5 reinforcing bars which were bent to confine the prestressing reinforcement straightened out, causing the concrete cover to spall as seen in Figure 2-8. This created an immediate loss in anchorage capacity and led to a premature failure in this specimen.

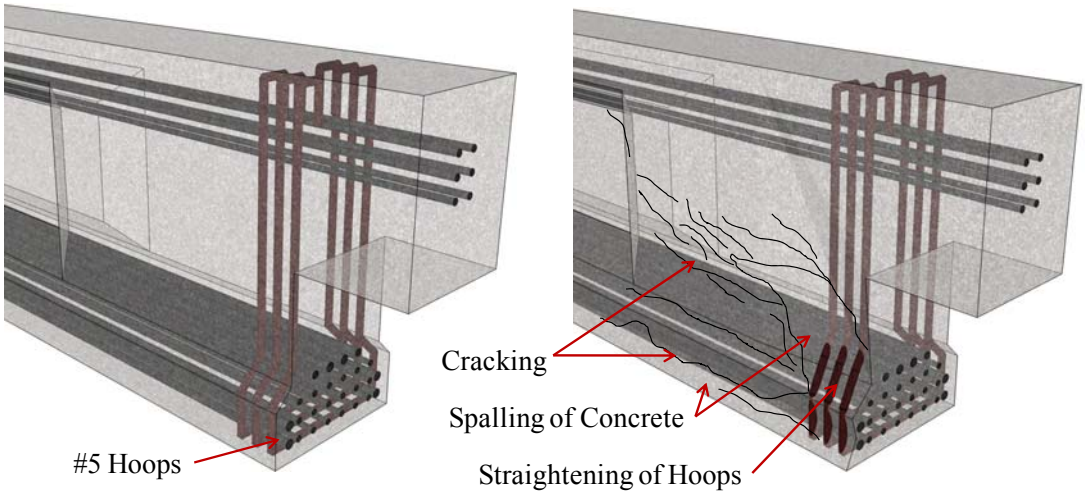

Figure 2-8: Poor End Detailing

The main vertical (hanger) reinforcement immediately adjacent to the dap yielded in all test specimens. Increases in strand strain were very small during the tests, as the tendons were not able to pick up any additional load in the transfer region. The strains decreased significantly when longitudinal cracks formed, weakening the anchorage of the strands.

The strut-and-tie model used to design the beam was not modified to distinguish between mild and prestressed reinforcement except that the prestress force was used as an externally applied load. The remaining load-carrying capacity of the tendon was limited to the residual capacity, or the tendon capacity minus the applied effective prestress force. After the tests, new models were developed in which prestress forces were applied at nodes along the transfer length in order to represent prestress transfer to the concrete in a somewhat more realistic manner.

2.3.2 Barton, Anderson, Bouadi, Jirsa, & Breen (1991)

The study by Barton et al. (1991) compared strut-and-tie models against the accepted methods of the PCI Design Handbook and the Menon/Furlong design. The objective was to develop experimental data for verifying various elements in strut-and-tie models.

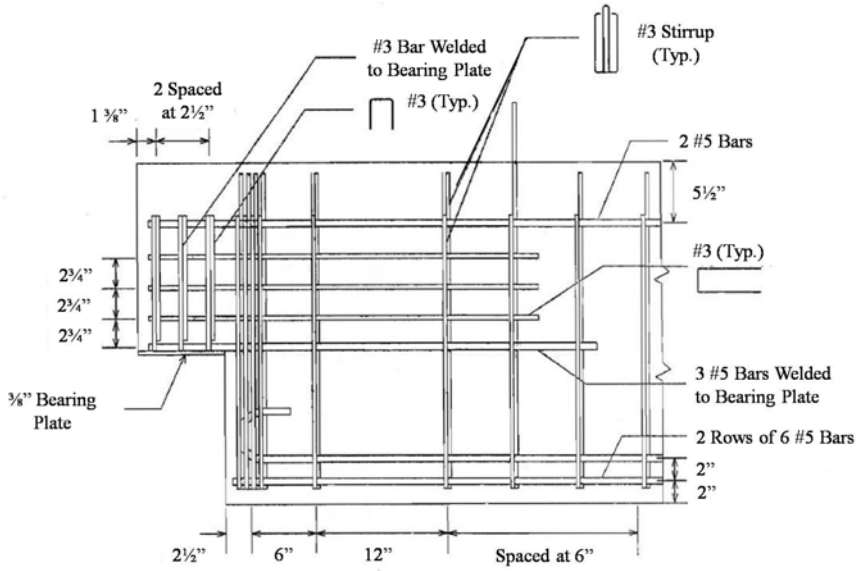

Figure 2-9: Reinforcement Layout for PCI Specimen (Barton et al., 1991)

Based on the performance of the specimen detailed using the PCI design handbook, Figure 2-9, it was determined that the most efficient location for the vertical hanger reinforcement was as close to the interface between the dap and the full depth section as possible. The researchers concluded that the tie bars should also be placed in a closely spaced group. Proper anchorage, especially in the horizontal flexural reinforcement, was found to be critical in developing the strength of the specimen and an increase in concrete cover was found to improve anchorage capacity.

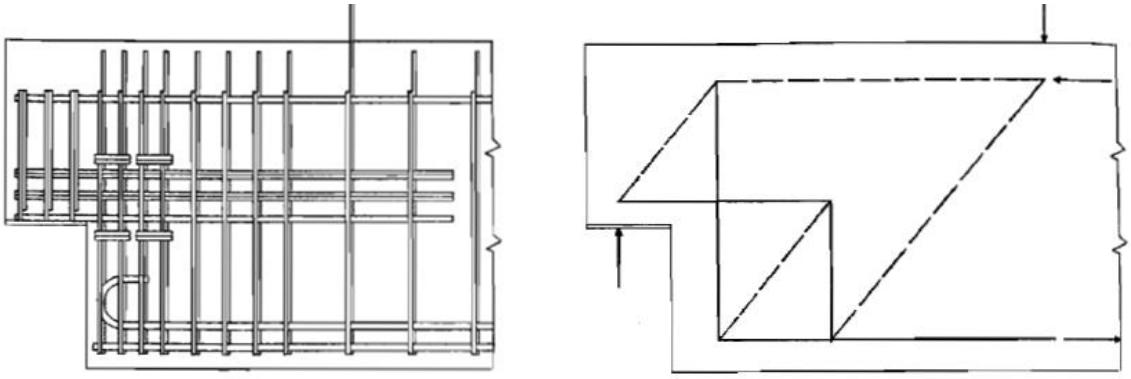

Figure 2-10: Typical Orthogonal Strut-and-Tie Model (Barton et al., 1991)

The orthogonal strut-and-tie model shown in Figure 2-10 closely represented the elastic stresses in the member and provided efficient placement of reinforcement for construction. Testing proved that the model was an efficient representation of the flow of forces through the end block. Results from Barton et al. indicated that the dapped-end beam detail can be efficiently and effectively designed using strut-and-tie models.

2.3.3 Bergmeister, Breen, Jirsa, & Kreger (1993)

Bergmeister et al. (1993) expanded on the findings of Batron et al. to examine the application of strut-and-tie modeling to typical details in structural concrete bridges. The project presented specific recommendations for choosing the critical dimensions and carrying out detailed computations using strut-and-tie models.

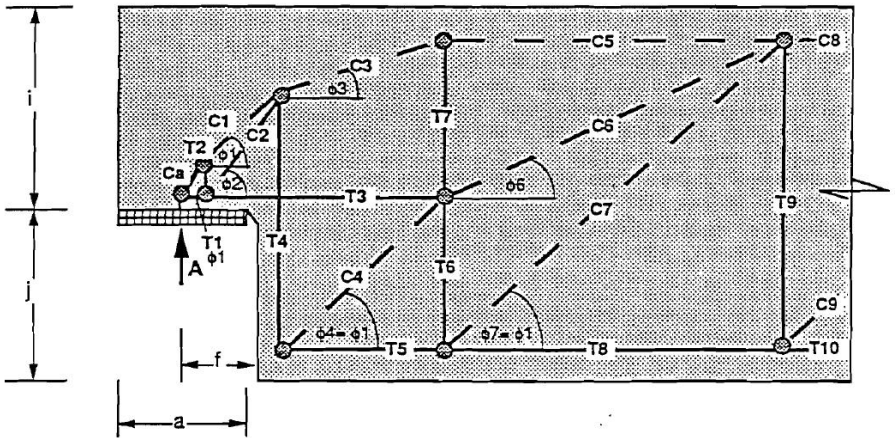

Figure 2-11: Proposed STM for Dapped End (Bergmeister 1993)

Different strut-and-tie models were compared with test results from Barton et al. to evaluate a design approach and create the recommended model that is shown in Figure 2-11. The strut angles in the test specimens examined ranged between 45° and 55° and tended to increase as the beam was loaded. Hence, an angle of 55° was used in the recommended model. The addition of strut C6 in Figure 2-11 represented the fanning (or spread) of the compressive stresses as the struts utilized a larger amount of the available area with the increase in applied load.

Bergmeister et al. concluded that the use of the strut-and-tie model given in Figure 2-11 was an efficient way of detailing reinforcement in concrete discontinuity regions. The calculations for ties were simple and straightforward but the checks of struts and nodes were found to be laborious and subjective to the designer's assumptions. In most cases it was found that ties controlled the design and it was reported that advances in strut-and-tie design would lead to easier calculations. Despite the difficulty in implementing them, STMs were found to be a rational approach that could be used for detailing circumstances that were not covered by other procedures.

According to Bergmeister et al., a strut-and-tie model for a prestressed concrete member is similar to a reinforced concrete member if appropriate assumptions and calculations are made to determine the stress levels in the tendons at failure. The stress level depends principally on whether the tendons have been effectively bonded to the

concrete. Mild steel is required to resist anchorage force concentrations and distribute support reactions and can be designed using strut-and-tie models. Prestressing forces are applied like other external loads on the strut-and-tie models, and changes in the forces in the tendons due to other load effects are treated as internal forces or tie forces. As mentioned by Mader (1990), the prestressing force is applied to nodes along the transfer length of the strands. With proper bond, the prestressing steel can also serve as mild reinforcement with the remaining capacity in the tie taken as the reserve capacity in the strand and the capacity of any additional non-prestressed regular reinforcement.

2.4 PRESTRESSED CONCRETE TRAPEZOIDAL BEAMS WITH DAPPED ENDS

The typical reinforcement used in the dapped-end regions of the prestressed concrete box beams under investigation is shown in Figure 2-12. The reinforcement layout is similar to the beams designed using the the PCI Design Handbook, and those tested by Mader et al. (1990), Barton et al. (1991), and Bergmeister et al. (1993). The large amount of hanger reinforcement, 10-#6 bars, is concentrated adjacent to the dap-to-full section boundary. The bars at the bottom of the dap, the 3-#5 U bars and 12 bent #7's strengthen the region and help to transfer shear into the full depth section. 58 to 64 prestressing strands, with 34 to 40 fully bonded strands, make up the primary flexural reinforcement. 3-#6 U bars provide additional tensile capacity in the beams' end-blocks within the prestress transfer region.

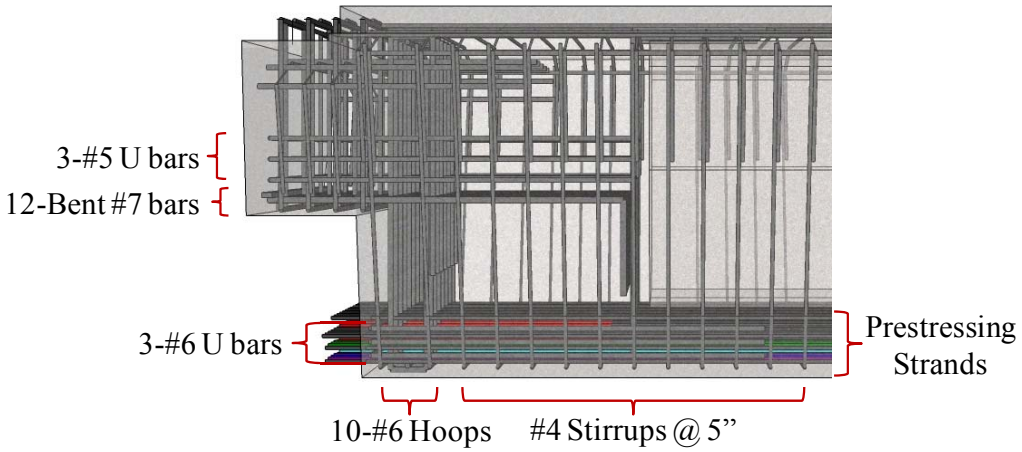

Figure 2-12: Typical Reinforcement Layout for Dapped Ends of Trapezoidal Beams

One of the major concerns with the prestressed concrete trapezoidal beams is the capacity of the extended portion (dap). This smaller section has less concrete to resist the heavy shears in the ends of beams. Tests by Mader (1990) found cracks forming at the re-entrant corner under very low applied loads. As seen in Figure 2-12, the dap in the beams is much more heavily reinforced and was the focus of the first test conducted under this project. The strength of this section did not control the failure of the first test specimen and it was concluded that the "dap failure" was not critical for the test specimens of this study due to the presence of heavy reinforcement in this region.

The critical component of the dapped-end beams (Figure 2-12) is actually the anchorage of the prestressing strands. Each strut-and-tie model in the previous research has a node in the bottom corner of the beam at the end of the hanger reinforcement. This node is very close to the edge of the beam and does not typically allow for complete development of the prestressing strands (as shown in Figure 2-13). Tie 2 represents the heavy hanger reinforcement while Tie 3 consists of the prestressing strands and #6 bars at the bottom of the beam. Coupled with the high amount of debonded strands (shown colored in Figure 2-12), the small amount of concrete available for strand bonding severely weakens this tie at the node and can become (and in fact is) the critical component in these beams (as shown in Chapter 4).

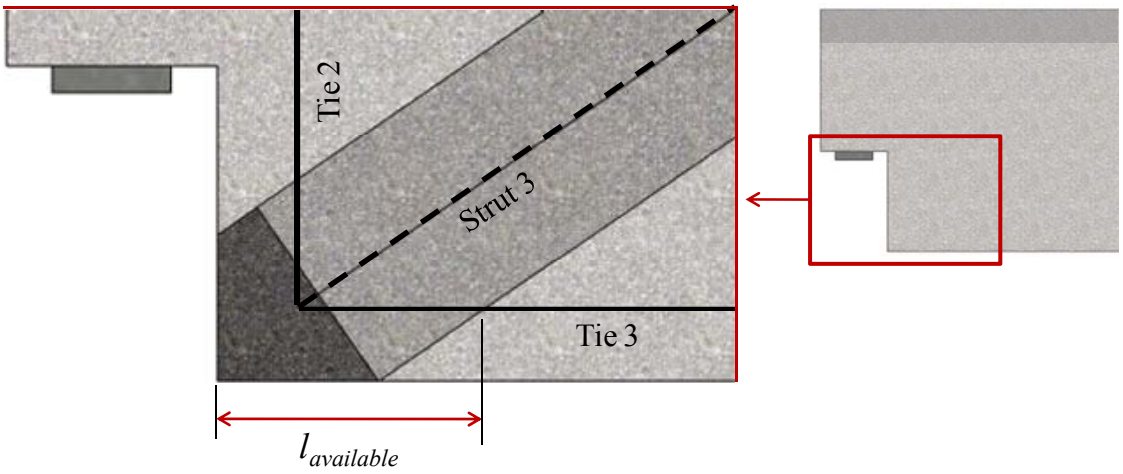

Figure 2-13: Extended Nodal Zone and Reinforcement Anchorage

2.5 PREMATURE CONCRETE DETERIORATION MECHANISMS

The trapezoidal box beams with dapped ends tested in this study were affected by two premature concrete deterioration mechanisms. Alkali-silica reaction (ASR) and delayed ettringite formation (DEF) subject the concrete to expansive forces, leading to cracking on the surface of structural elements. Alkali-silica reactivity was first identified as a concrete durability problem in the late 1930's, and significant research has been conducted on it since that time. Delayed ettringite formation was first identified as a potential problem in concrete exposed to high curing temperatures during the early 1980's.

The surface cracking patterns and visible interior damages caused by either mechanism are virtually indistinguishable from a structural engineer's perspective. A brief discussion of the chemical and physical properties of the mechanisms will be provided, but no distinction will be made towards their deleterious effects in the rest of this report. For a detailed description on ASR and DEF, refer to Bauer et al. (2006).

2.5.1 (ASR) Alkali-Silica Reaction

ASR results from a combination of high-alkali cement and siliceous aggregates in the concrete mixture. The reactive silica within the course and/or fine aggregates dissolves in the highly basic concrete pore solution and reacts with the alkalis to form a viscous gel. This gel expands as it absorbs water, generating pressure within the aggregates and hardened cement paste. In the presence of sufficient moisture the pressure can easily exceed the tensile strength of the concrete, producing map cracking and/or surface pop-outs.

The expansive capability of the gel is influenced by a number of factors including the reactive aggregate, concentration of alkalis within the pore solution and the availability of sufficient moisture. The reaction is highly responsive to materials, mixture characteristics, and exposure conditions as described in the following table. This sensitivity results in significant variation of deterioration not only between two identical members, but even within a single member.

Table 2-5: Necessities of ASR and Sources of Variability (Deschenes et al., 2009)

Reactive Aggregate	Sufficient Alkali	Sufficient Moisture
Amount of Reactive Silica in Aggregate	Amount of Cement	Volume-to-Surface Area Ratio
Reactivity Level of Silica	Cement Alkali Content	Water-to-Cement Ratio
Aggregate Particle Size	Alkalis from Aggregates, Admixtures, Etc.	Permeability
Distribution in Mixture	Migration and Leaching of Alkalis	Climate and Exposure

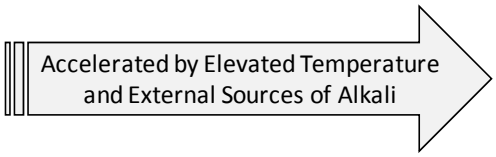

2.5.2 (DEF) Delayed-Ettringite Formation

Ettringite is the product of a reaction between sulfates, calcium aluminates, and water. The natural formation of ettringite occurs during the early hydration process prior to the hardening of the cement and does not pose a risk to concrete durability. Damage is caused by delayed ettringite forming in the hardened concrete (Boenig et al., 2002).

DEF is a form of sulfate attack that occurs when the concrete is subjected to temperatures in excess of 158°F (70°C) early in the curing process. When fresh concrete is exposed to high temperatures the ettringite decomposes and the sulfates and aluminates become trapped within the early cement hydration products (Bauer et al., 2006). Over a period of time, the sulfates and aluminates diffuse out of the hydration products to react and form ettringite. The reformation of ettringite produces expansive forces and micro-cracking of the hardened concrete paste.

The growth of ettringite leads to bulk expansion of the cement paste and the development of cracks and gaps around the aggregates. The ettringite then proceeds to fill the recently formed cracks and create rims surrounding the aggregates, furthering the

overall expansion and crack development. The formation of large amounts of ettringite within the hardened cement paste can cause expansions of magnitudes well in excess of those found due to ASR (Bauer et al., 2006).

The potential for delayed ettringite formation is depended on three conditions: (1) concrete curing temperatures in excess of 158°F (70° C), (2) sufficient moisture to allow for the formation of ettringite, and (3) decomposed ettringite or high amounts of sulfur. Wide variations in cement composition (sulfate content), mixture characteristics (porosity), and exposure conditions will lead to an equivalent variation of deterioration as seen with ASR.

2.5.3 Diagnosing ASR and DEF

As discussed earlier, the external symptoms of the deterioration mechanism are virtually indistinguishable. To the naked eye, *"the resulting damage [of DEF] is very similar to that caused by ASR, as would be expected for any internal expansive type reactions within a non-ductile material"* (Lawrence et al., 1999). Forensic testing of a specimen is required to determine if ASR and/or DEF is the cause of the cracking.

In 2004, researchers from the Concrete Durability Center (CDC) at the University of Texas at Austin removed cores from a beam in this study for forensic evaluation. Residual expansion measurements were performed on the cores to determine the presence of ASR and DEF in the concrete beam. The scanning electron microscope (SEM) images in Figure 2-14 showed large gapping around aggregate with ettringite filling the gaps. There were also signs of distress within the aggregates, suggesting that ASR did occur. The amount of ettringite and gapping implied that DEF was the main cause of the deterioration, but it is likely that ASR took place throughout the beam, triggering DEF in some sections (Folliard & Drimalas, 2008).

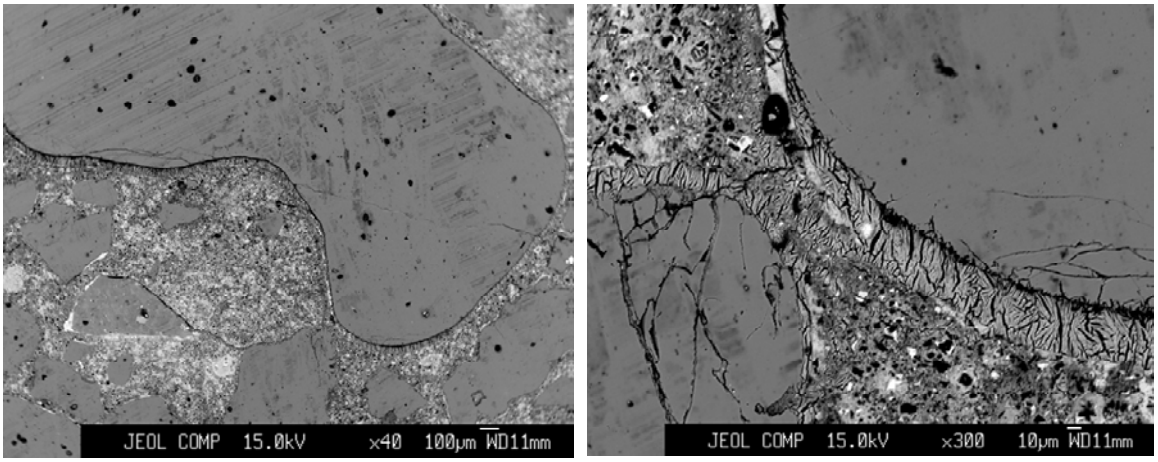

Figure 2-14: SEM Image of End Region (Folliard & Drimalas, 2008)

Because the difference between ASR and DEF can only be determined with forensic testing, and since they are virtually indistinguishable from a structural engineer's perspective, no further distinction will be made between ASR and DEF in reference to their deleterious capabilities.

2.5.4 Effects of ASR and DEF

Premature concrete deterioration mechanisms result in concrete expansion and map cracking and often other symptoms including efflorescence, pop-outs, and surface discoloration. In stressed regions, the cracking is aligned with the compressive stress trajectories. This can be seen in ASR/DEF-damaged box beams: cracks emanated from the bottom corner of the beam, propagated to mid-depth, and continued on as horizontal cracks along the length of the beam (Figure 2-15). The cracks start at roughly a 30-degree angle where the stress is minimal then bend over as large compressive stresses develop within the concrete surrounding the prestressing strands.

Figure 2-15: Premature Concrete Deterioration

Visual observations showed a concentration of cracking in the end regions of the beams. Three and a half feet of the full section of the beam past the extended portion, or dap, was solid concrete while the remaining portion is hollow as shown in Figure 2-16.

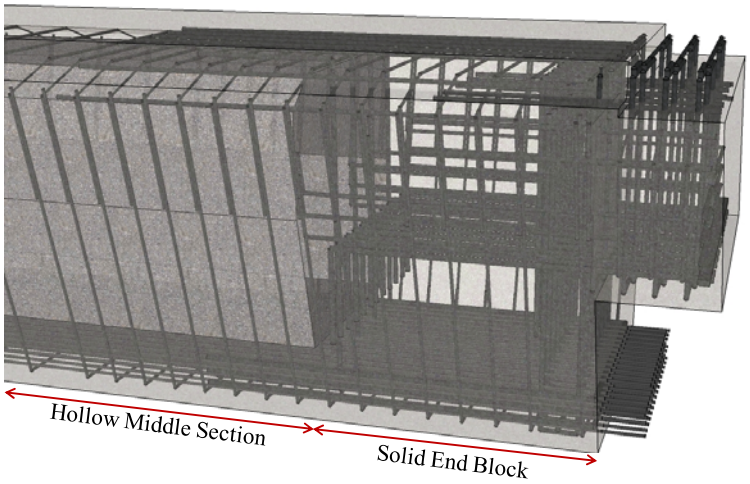

Figure 2-16: Beam Concrete and Rebar Layout

The larger volume of concrete found in the end block likely resulted in higher curing temperatures in that region and hence created a higher potential for delayed ettringite formation. End regions of the beams were shear-critical and contained larger amounts of transverse reinforcement than the middle region. The combination of smaller stirrup spacing and the solid concrete core forces the ASR/DEF related expansions outward, creating cracking on the surface of the concrete as illustrated in Figure 2-17.

Expansions along the transverse reinforcement were restrained effectively while expansions perpendicular to the stirrups resulted in bulging of the cross section.

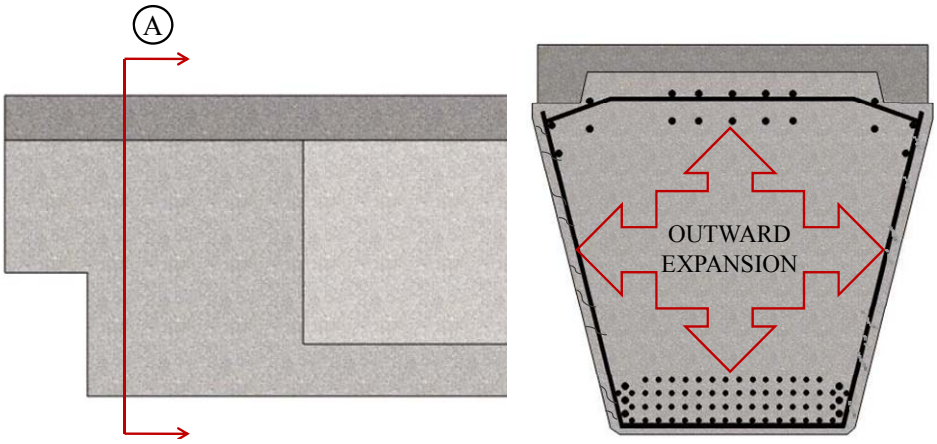

Figure 2-17: Section A: Concrete Expansion in the Solid End Block

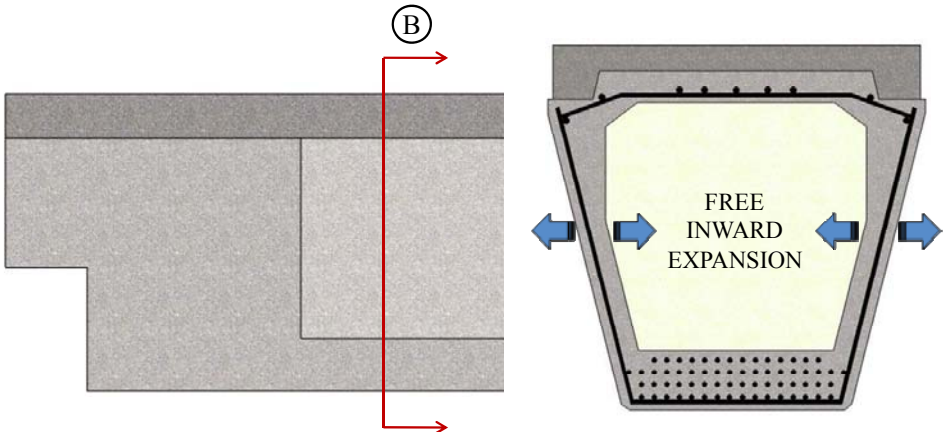

Figure 2-18: Section B: Concrete Expansion in the Hollow Middle Section

The same degree of heavy cracking on the concrete surface was not found in the void region. There are a number of plausible explanations for this phenomenon:

- The webs of the trapezoidal box beam were free to expand inward as the styrofoam did not provide much restraint. Such behavior would alleviate expansion and cracking in the plane of the webs. The expansion behavior of the hollow cross-section is described in Figure 2-18.
- Curing temperatures not only have a marked effect on the initiation of DEF, but on the rate and magnitude of ASR development (Deschenes et

al. 2009). The lack of mass concrete within the void region most likely resulted in lower curing temperatures and reduced risks of deleterious ASR/DEF.

- The thin concrete webs of the box beam may not have retained sufficient moisture to sustain deleterious ASR/DEF over time. Rapid drying of the hollow region would mitigate the development of severe ASR/DEF.

2.6 PREVIOUS RESEARCH ON STRUCTURES AFFECTED BY ASR/DEF

It has been frequently assumed that ASR/DEF-induced expansion may be closely related to a loss of structural capacity. The majority of studies on the strength of a concrete structure indicated minimal adverse influence of ASR/DEF on the strength of members subjected to flexure. Researchers disagree, however, over whether the ASR/DEF-induced cracking increases or decreases a structure's shear capacity.

Deschenes et al. (2009) studied extensively the research projects over the last three decades in which verifying the structural implication of ASR/DEF damage was an objective. The details of the test specimens used in previous research studies are given in Table 2-6. Each reinforced concrete beam in Table 2-6 was fabricated in a laboratory and generally included tests with reactive and nonreactive aggregate for strength and stiffness comparisons. Various techniques including outdoor exposure and heated water baths were used to accelerate the deterioration and the expansion of the concrete and crack widths were monitored over time. Once the desired level of distress was achieved, the beams were typically tested under symmetric two-point loading with identical shear spans on either side of a constant moment region. Flexural failures were induced by providing a sufficient number of stirrups along each shear span while shear failures were achieved by the manipulation of longitudinal reinforcement and shear span-to-depth ratios. Clark (1989) conducted and reviewed a great number of shear tests on beams without stirrups. These specimens are not included in Table 2-6 due to the discouraged use of such details (Deschenes et al., 2009).

With the exception of the tests by Deschenes at al. (2009), all of the previous tests on ASR-affected reinforced concrete members were relatively small. None of the beams included in Table 2-6 were over 24 inches in depth or 21 inches in width. It is known that shear does not scale well and that results from small tests cannot be reliably extrapolated to evaluate the performance of large structural members.

Table 2-6: Studies of Reinforced Concrete Beams Affected by ASR

(Adapted from Deschenes et al., 2009)

Reference		Number of Tests	Specimen Details					Failure Mode
			h	b	ρ	ρ_v	a/d	
Clark 1989	Kyoto University, Japan	11	8 in	8 in	0.8-1.8 %	0.2-0.3 %	2.5	Flexure
	Ritsumeikan University, Japan	16	8	8	1.2	0.2	2.5	Flexure
	Giffu Univerisity, Japan	18	7	4	1.7	*	2.8	Flexure
	Kobe Univeristy, Japan	20	8	8	0.8-1.2	0.0-0.3	1.5-2.5	Flexure/Shear
	Konoike Construction Co., Japan	8	20	20	0.5	*	2.5	Flexure
	Takenaka Research Laboratory, Japan	3	20	10	0.9	*	3.3	Flexure
	Public Works Research Institute, Japan	27	20	20	0.2-1.4	0.0-0.4	-	Flexure
	Swamy and Al-Asali	3	4	3	1.8	1.3	3.1	Flexure
Chana and Korobokis, 1991		24	8	4	2.3	0.2	5.6	Shear
Ahmed, Burley and Rigden, 1998		8	5	3	2.7	0.4	3.6	Shear
Fan and Hanson, 1998		6	10	6	0.4-1.0	0.3	2.2	Flexure
Deschenes, Bayrak and Folliard, 2009		6	42	21	3.1	0.15-0.31	1.85-3	Shear
Total/Range		150	4-42	3-21	0.2-3.1	0.0-1.3	1.5-5.6	

* *shear reinforcement provided throughout the length* - unspecified

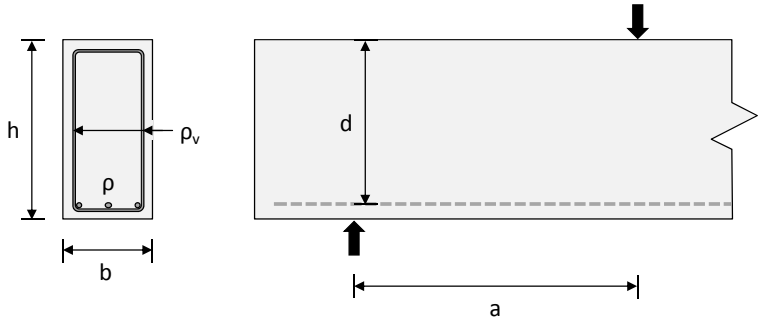

Brown et al. (2006) compiled the results of thousands of shear critical beam tests for TxDOT Project 4371, *Design for Shear in Reinforced Concrete Using Strut-and-Tie Models*. These results were assembled in Figure 2-19 by Deschenes at al. (2009) for a comparison of effective concrete shear area that is used for the beams tested in this project. For the purpose of this study, a majority of the ASR/DEF specimens included in Table 2-6 are below the fortieth percentile of effective shear area in the database. This figure is revisited to put the scale of testing in context with the typical specimens employed in the history of shear research.

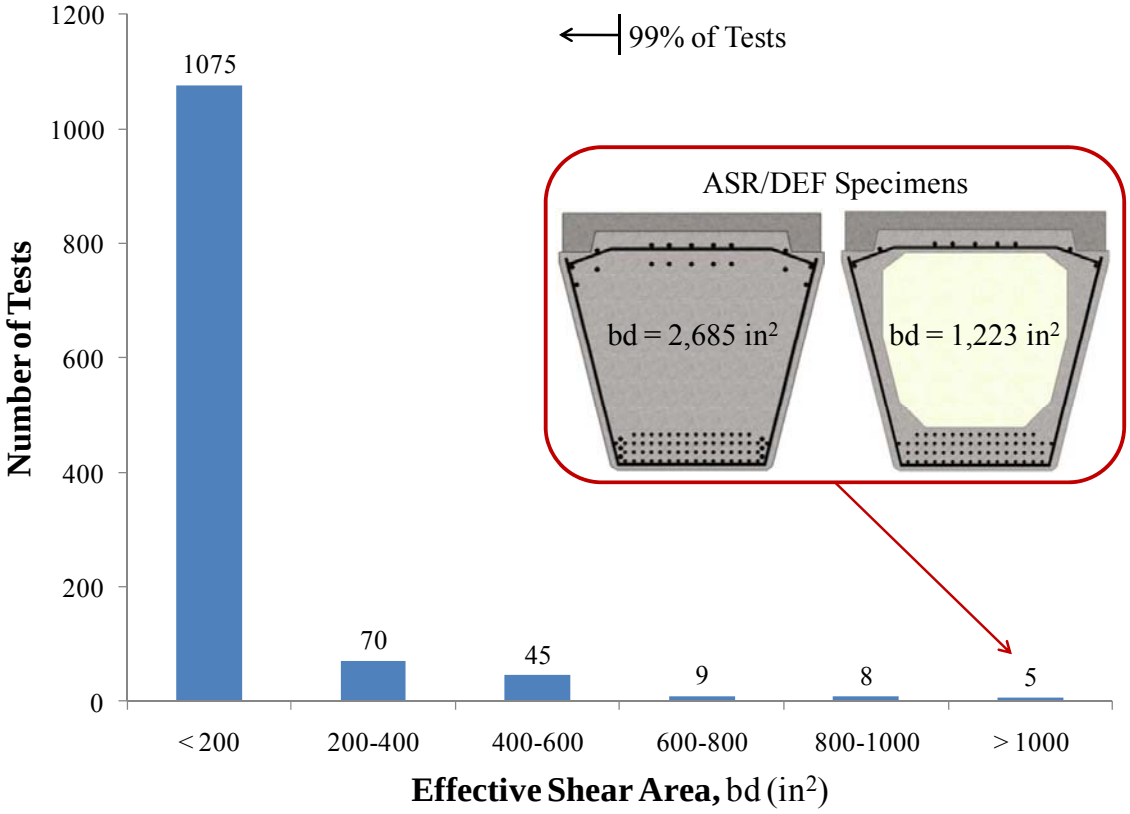

Figure 2-19: TxDOT Project 0-4371 Shear Database – Effective Shear Area (Adapted from Deschenes et al., 2009)

All of the tests included in Table 2-6 were performed on specimens built in laboratories where ASR and/or DEF reactive concrete was batched. Reactive aggregate was carefully chosen and proportioned to reproduce the effects of in-situ premature

concrete deterioration. The test specimens then underwent special curing techniques to accelerate the deterioration process. As realistic as the accelerated ASR/DEF damage seen in specimens included in Table 2-6 may be, they were aimed at mimicking field conditions that occur over a much longer period of time. The trapezoidal box beams in this study developed ASR/DEF damage in the field and under "more realistic" conditions. The concrete was designed for structural purposes and is the same concrete mixture that was used for the beams in the US 59 corridor in Houston, TX. The beams under investigation have not been introduced to any acceleration processes other than exposure to the elements in a precaster's yard. Full exposure to the elements allowed ASR/DEF deterioration to develop at a much faster rate than found in the deck-protected trapezoidal box beams in the field. With that being the case, the beams selected for this study represent the future condition of the beams within the US-59 corridor in Houston, TX. In short, they can be viewed as the worst-case representations of the damage found in the field.

2.6.1 Large Scale Shear Tests on ASR/DEF-Affected Concrete

Because there is no known research performed on any beams similar to the full scale ASR/DEF-affected prestressed trapezoidal box beams with dapped ends, the review of relevant research is limited. Three experimental programs in which large-scale tests were conducted on ASR/DEF-affected beams are introduced here. Specimens tested in these research studies experienced little if any change in shear strength due to ASR/DEF but failed in a manner differing from the beams under investigation.

2.6.1.1 Clayton et al. (1990)

Clayton et al. (1990) tested 400 mm high and 200 mm wide (15.75 by 7.87 inches) prestressed I-beams subject to ASR deterioration. Four beams were evaluated at a pre-reaction stage, at the first sign of cracking (at an expansion of 1mm/m), and at full expansion after a five-month conditioning regime in 38°C water. A non-reactive concrete mixture provided the baseline for comparisons. Shear tests were performed on the 2.5

meter (8 feet, 2.5 inch) beams by applying a single point load at a shear span-to-depth ratio of 2.0. The results showed comparable shear strengths between the control specimen and a reactive specimen at the pre-reaction stage. A 23% decrease in strength between the reactive and control specimen at first noticeable ASR cracking was reported. Subsequently a strength gain back to the shear capacity of the non-reactive specimen was noted after extensive cracking. Clayton et al. suggested that the apparent increase in shear capacity was due to the continuing ASR-induced expansion engaging the shear reinforcement, providing additional concrete restraint. No substantial loss of bond between the concrete and the prestressing strand was found in this study.

2.6.1.2 Boenig et al. (2001)

Boenig et al. (2001) investigated the effect of ASR/DEF damage on the shear and flexural strength of prestressed box sections at Ferguson Structural Engineering Laboratory (FSEL) at the University of Texas at Austin (UT Austin). Fifty-six prestressed concrete box girders were fabricated by a precaster in the summer of 1991 but were never installed in TxDOT bridges because they displayed premature concrete deterioration while still in the storage yard. Four of those girders, representing a typical range of damage, were brought to FSEL for testing. The beams were 48-inches wide and 27-inches tall, with the majority of the ASR/DEF deterioration located in the 26-inch long solid end blocks. Each of the four beams was tested at a shear span-to-depth ratio of 1.9 and the results revealed a 14% decrease in shear capacity for the heavily deteriorated beam. Strand slip in the anchorage zone was also noticeably increased in heavily cracked beams. Although this indicated that the bond between the strand and concrete had been affected, anchorage failure was not the controlling factor as all beams failed in web crushing.

2.6.1.3 Deschenes et al. (2009)

Deschenes at al. (2009) sought to establish a relationship between ASR/DEF deterioration and the shear capacities of affected bridge bent caps. Six large-scale

specimens with cross sections measuring 21 inches by 42 inches were fabricated at FSEL. After a prolonged exposure period, three beams, representing undamaged, mild, and moderate levels of deterioration, were tested in shear. The necessity of large-scale testing was emphasized in this project due to the complexity of ASR/DEF deterioration and poor scaling effects of shear behavior. No significant loss of shear capacity was found at low to moderate levels of ASR-induced deterioration (0.09% to 0.63% transverse concrete expansions) and it was strongly recommended to continue with testing of higher levels of premature concrete deterioration.

2.6.2 Effects of ASR/DEF Damage on Reinforcement Anchorage

As discussed in Section 2.4 and Chapter 4, the governing failure mode for the dapped-end beams under investigation was shear-induced anchorage failure of the prestressing tendons at the bottom corner of the beam. In order to support this observation, previous research of the ASR/DEF effects on the bond strength between steel and concrete is presented.

2.6.2.1 Chana and Thompson (1992)

Chana and Thompson (1992) examined the shear strength of reinforced concrete beams with poorly anchored reinforcing bars. The beams were relatively small with a cross section of 100 mm by 200 mm (3.9 by 7.9 inches) and a development length of 5 times the bar diameter past the center line of the support. Four different stages of ASR expansion were examined including a nonreactive specimen. All reactive specimens had an ASR crack along the potential shear failure plane prior to testing. The maximum reduction in shear strength was approximately 23% between the nonreactive and highly reactive specimen. Chana and Thompson concluded that their test results were encouraging given that the decrease in shear strength was relatively modest with respect to the poor anchorage of the primary tension tie.

2.6.2.2 Bach et al. (1993)

Bach et al. (1993) examined the effects of ASR on the anchorage of four beams with a rectangular cross section of 180 mm by 360 mm (7.1 by 14.2 inches) and a length of 4300 mm (14 feet). After curing, the reactive beams were exposed outdoors for four weeks and then stored in saturated NaCl at 50°C. The control beam was stored in water for 3 to 4 weeks before testing. The beams were then tested under symmetric two-point loading with identical shear spans on either side of a constant moment area. The results found a 20 to 30% reduction in the anchorage strength due to ASR deterioration.

2.6.2.3 Ahmed et al. (1999)

Ahmed et al. (1999) completed a similar study on 120 mm by 100 mm (4.7 by 3.9 inch) beams with a total length of 1300 mm (4 feet 3 inches). Two concrete mixtures were used to compare the behavior of six non-reactive beams to another six beams subject to ASR deterioration under static loading. The beams were tested in four-point loading and different lap lengths were used at the center of each uniform bending zone. Beams B1-A, B2-A, B3-A, B4-A, and B-5-A, having lap lengths of 5, 8, 12, 20, and 32 times bar diameter, showed a reduction in strength of 6.3, 5.1, 4.4, 3.3, and 2.8 percent compared to their respective control specimens. Ahmed et al. concluded that the concrete expansion did have a noticeable effect on the concrete-to-steel bond within the lap length of the tensile reinforcement.

2.6.3 Concrete Expansion and Steel Strain

As the concrete expands due to ASR/DEF, it is restrained by the reinforcing steel. When subject to high levels of expansion, the steel could develop high levels of strain with a potential for yielding or even fracturing. Studies conducted on steel strain due to premature concrete deterioration are examined in this section.

2.6.3.1 Mohammed et al. (2003)

Mohammed et al. (2003) investigated ASR-induced strains over the concrete surface and embedded steel bars in the concrete. Specimens measuring 250 mm by 250 mm by 600 mm (9.8 x 9.8 x 23.6 inches) were developed with reactive and non-reactive coarse aggregates and varying levels of internal restraint. Strain gages were attached to the embedded steel and demec studs were used to measure concrete strain. Their test results strongly suggested that ASR-induced strains depend on the restraint provided by the steel in the concrete. The location of the reinforcement was also significant: smaller surface strains were observed if the steel bars were located near the concrete surface. The strain in the bar closest to the surface was higher than a bar far from the surface. Mohammed et al. recommended further research to understand the expansion process in large structural components with heavy confinement by stirrups.

2.6.3.2 Kubo et al. (2003)

If the amount of reinforcing steel is relatively small compared to the volume of concrete, the steel could develop large strains to the point of fracture. A study by Kubo et al., published in 2003, examined the fracture of steel bars in the footings of concrete piers. Fractures were found in the bends of the reinforcing steel at the base of the footing under investigation. Large diagonal cracks were also found to extend beyond the embedded steel due to the loss of restraint. Model specimens measuring 300 mm by 300 mm by 900 mm (11.8 by 11.8 by 35.4 inches) were constructed with reactive aggregate in order to determine the mechanism of fracture of the steel bar. The tensile strains at the bends of the steel bars were found to increase along with the expansion of the concrete. The experimental results revealed that the stress at the reinforcement bends was at or beyond the yield strength of the steel regardless of the reinforcement ratio. Kubo et al. (2003) concluded that the fracture of the steel bar was caused by a combination of bending-related defects at the bends and large tensile strains imposed by ASR expansion.

2.6.3.3 Miyagawa et al. (2006)

According to Miyagawa (2006), Japan has at least 30 ASR-damaged structures, including highway and railroad bridges, with confirmed rebar fractures. The researchers found fractures in the bends of reinforcing bars in an ASR-affected, T-shaped pier that was constructed in 1979. The pier had been repaired in 1989 and again in 1992 with a surface coating and crack injection in an effort to prevent further ASR expansion. Fractures in the bent section of the stirrups were discovered during an investigation in 1999 as shown in Figure 2-15B. The researchers noticed that at the location of the fractured stirrups there were extensive cracks perpendicular to the direction of the reinforcing steel (Figure 2-20A). The fractures also corresponded to areas where the amount of steel bars was too small to confine the concrete expansion.

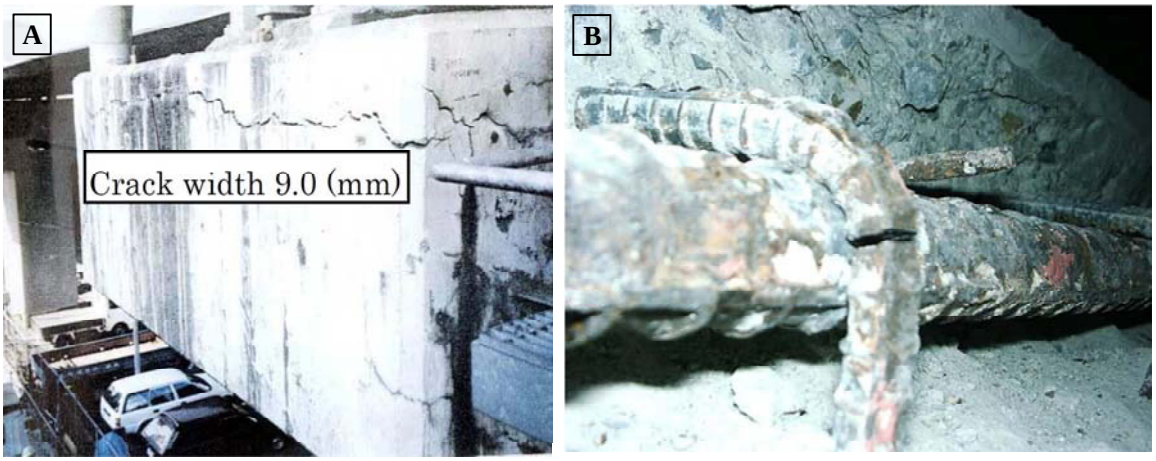

Figure 2-20: (A) Example of Pier Damage (B) Fracture of Reinforcing Bar (Miyagawa 2006)

In order to determine the severity of the ASR expansion, it was important to determine the mechanism behind the fracture of the reinforcing bars. Miyagawa et al. performed a series of tensile tests on steel bars with different bend radii and found that the rib shape on the bars and the bending radius had a significant influence on the bar fractures. The fracture of the reinforcing bars was presumed to be due to the bending operation leading to localized strain and cracking with strain aging of the steel that increased its sensitivity to fracture. Cracking of the concrete led to moisture penetration

and corrosion while ASR expansion generated large stresses on the inner surface of the bend.

Miyagawa et al. concluded that as long as the stirrups had not fractured due to the ASR expansion, the structural integrity was not seriously compromised. The loss of confinement of the concrete through the fracture of the reinforcement would lead to the rapid weakening of the core and an unquestionable loss of structural safety. This observation will become critical when examining the shear strength of ASR/DEF-affected structures.

2.6.3.4 Reinforcement Standards

Before the possibility of bend fractures can be dismissed, it is important to note the differences in the Japanese and American reinforcing standards as summarized in Table 2-7. Japanese researchers including Kubo et al. (2003) and Miyahawa et al. (2007) have conducted a series of studies in response to the discovery of more than thirty structural elements with stirrups fractured due to ASR/DEF-induced concrete expansions. The proposed mechanism involved the combination of bending operation decreasing the bars' mechanical properties and ASR/DEF expansions generating large stresses on the inner surface of the bend. Miyagawa et al. also found that the rib shape on the bars and the bending radius had a significant influence on the bar fractures.

Most ASR/DEF-affected elements are substructures and the Japanese typically use grade 40 reinforcement in their foundation elements. A comparison between the American GR40 reinforcement and the equivalent Japanese SD295 reveal that the Japanese standards require a stronger (42.6-56.9 vs. 40 ksi) and more ductile (18% vs. 12% elongation) steel. This strength advantage is offset by the smaller allowable bend radius. For grade 40 reinforcement, the ACI minimum bend radius is greater than the JSCE guidelines for standard hooks and #3 stirrups or ties. The two standards require the same minimum bend radius for larger stirrups and ties. Japanese reinforcement may be stronger and more ductile than its American counterpart, but the minimum bend radius, a key component in the ASR/DEF-induced bar fracture mechanism, is smaller. Therefore it

is difficult to directly compare results from studies on the effects of ASR/DEF expansion on the fracture of Japanese reinforcement to structural elements in the United States.

Similarly, for grade 60 reinforcement bars, the Japanese standard requires a stronger (56.9-74.0 vs. 60 ksi) and more ductile (16% vs. 9% elongation) steel. The minimum bend radii for standard hooks is the same for both guidelines and JSCE requires a larger radius for all bars with the exception of #3 bars for stirrups and ties. In the US, the use of grade 60 reinforcement in prestressed and reinforced concrete structures is fairly typical. The combination of weaker, more brittle steel with smaller bend radii would suggest that the US GR60 reinforcement would be more prone to fracture than the Japanese SD390. In short, further studies of ASR/DEF-induced expansions and the resulting steel strain should be conducted to determine the probability of reinforcement fracture.

Table 2-7: Comparison between Japanese and American Reinforcement Standards (Deschenes, 2009)

Grade 40 Reinforcement or Equivalent

Standard	Type	$f_{y,\,min}$	$f_{u,\,min}$	Elongation
		[ksi]	[ksi]	[%]
JIS G 3112 - 1987	SD295	42.6 -56.9	64.0	18
ASTM A615 - 2008	GR40	40.0	60.0	12

Bar Size	Diameter	Minimum Bend Radius			
		Standard Hooks		Stirrups and Ties	
		JSCE	ACI	JSCE	ACI
	[in]	[in]	[in]	[in]	[in]
3	0.375	0.94	1.13	0.56	0.75
4	0.500	1.25	1.50	1.00	1.00
5	0.625	1.56	1.88	1.25	1.25
6	0.750	1.88	2.25	1.50	1.50

A number of points to keep in mind:

- Japanese standards were revised in 1990
- Pre-1990 standards are most representative of ASR-affected structures
- It is unlikely that bend radius requirements have changed since the 1970's
- Most affected elements are substructures (foundations)
- Japanese typically use GR 40 reinforcement in foundation elements
- Poor deformation (knot) details on reinforcement are believed to have initiated fractures

Grade 60 Reinforcement or Equivalent

Standard	Type	$f_{y,\,min}$	$f_{u,\,min}$	Elongation
		[ksi]	[ksi]	[%]
JIS G 3112 - 1987	SD390	56.9 -74.0	81.1	16
ASTM A615 - 2008	GR60	60.0	90.0	9

Bar Size	Diameter	Minimum Bend Radius			
		Standard Hooks		Stirrups and Ties	
		JSCE	ACI	JSCE	ACI
	[in]	[in]	[in]	[in]	[in]
3	0.375	1.13	1.13	0.56	0.75
4	0.500	1.50	1.50	1.25	1.00
5	0.625	1.88	1.88	1.56	1.25
6	0.750	2.25	2.25	1.88	1.50
7	0.875	2.63	2.63	2.19	1.75
8	1.000	3.00	3.00	2.50	2.00
9	1.128	3.38	3.38	2.82	2.26
10	1.270	3.81	3.81	3.18	2.54
11	1.410	4.23	4.23	3.53	2.82

Sources

(2010) Eisuke Nakamura
(1987) JIS G 3112
(2002) JSCE Guidelines
(2008) ASTM A615
(2008) ACI 318

2.7 SUMMARY

Premature concrete deterioration mechanisms are a growing concern around the world. Alkali-silica reaction and delayed ettringite formation subject the concrete to expansive forces, resulting in large cracks on the surface of the concrete. In previous experimental research conducted on large-scale concrete beams, there were no significant decreases in shear or flexural capacity, but none of the studies have involved full-scale prestressed trapezoidal box beams with dapped ends.

Through review of common dapped-end details and test results, the ultimate strength of the dapped-end trapezoidal box beams was found to be uniquely governed (in the context of ASR/DEF-related structural research) by shear-induced anchorage failure. The short development length of the primary flexural reinforcement at the dap-to-full section interface generally precludes dapped ends from failing in diagonal strut crushing (seen by Boenig et al. 2001 in standard end box beam tests). Furthermore, researchers have found that ASR/DEF weakens the bond between the reinforcement and concrete to varying degrees. It was suggested that breakdown of the reinforcement bond could have a further detrimental effect on the anchorage of the prestressing strands in the beams considered in this study.

Other concerns regarding the long-term integrity of the trapezoidal box beams centered on the vulnerability of the reinforcement to fracture. It has been commonly suggested that the loss of material strength in the concrete is balanced by the compressive stress generated as ASR/DEF expansions are restrained by the steel reinforcement. Moderate to high levels of premature concrete deterioration have been found to yield the shear reinforcement, and in some cases, ASR/DEF expansion caused fractures at bends in the bar. High strains in the steel have not resulted in loss of capacity as concluded in laboratory tests, but fracture of the stirrups could potentially lead to a loss of structural safety that engineers need to be aware of.

In short, examination of the research results reported in the literature provided valuable insight into the structural behavior of trapezoidal box beams used to construct

the US-59 corridor in Houston, TX. However, it became clear that the conclusive answers needed to achieve the objectives of this investigation could not be found in the literature. A large-scale experimental program was needed to study the behavior of the trapezoidal prestressed concrete beams with dapped ends.

CHAPTER 3
Experimental Program

3.1 OVERVIEW

While the Texas Department of Transportation recognizes that ASR/DEF-affected segments of the US 59 corridor will require durability-related repairs (i.e. application of crack sealants, waterproofing agents, etc.), it is unclear whether structural retrofits will be required. Fortunately, long-term storage of five rejected trapezoidal box beams provided an opportunity to assess the structural effects of the deterioration within the laboratory. Tasks related to the acquisition, preparation, and testing of the five segments are described herein.

The structural details of the five trapezoidal box girders are examined first. Many aspects of the original design are reviewed, including the dap geometry, mild reinforcement layout, and strand debonding patterns. The full range of deterioration encompassed by the five box beams is then revealed. More specifically, the pre-test condition of each segment is assessed from both durability (i.e. ASR/DEF-related cracking and spalling) and structural (i.e. construction defects and material properties) standpoints. Finally, the test setup, instrumentation and loading procedure of the dapped-end segments are described.

3.2 ASR/DEF-DAMAGED TRAPEZOIDAL BOX BEAMS (1995)

Over 25,000 linear feet of trapezoidal box beams were fabricated by Traylor Bros., Inc for the US 59 corridor expansion (begun in 1991 and completed in 1999). From July to November of 1995, five beams were rejected by TxDOT (less than two percent of the total footage) and remained in the yard. The basis for rejection of each beam is summarized in Table 3-1. It should be noted that the defects were judged to have no impact on the viability of the research program; as substantiated later in this chapter.

Table 3-1: Rejection of Trapezoidal Box Beams

Erection Mark	Cast Date	Reason for Rejection
RF-3R-9	7/6/1995	Void floated during concrete placement
RF-3R-12	7/9/1995	Lack of concrete consolidation
RF-1R-1	7/26/1995	Concrete did not set in a limited area of web and soffit
RF-2R-6	7/28/1995	Void floated during concrete placement
MLL-9-34	11/9/1995	Incorrect end skew

Due to the size of the box beams and costs related to disposal, Traylor Bros. elected to store the rejected elements at the Mesa Precast Yard. The storage conditions were typical of any other production beam; each end of the beam was supported by concrete blocks placed upon firm ground (Figure 3-1).

Figure 3-1: Trapezoidal Box Beam Storage at Mesa Precast Yard

All five of the trapezoidal box beams were continuously exposed to the hot, humid climate of Houston, Texas for nearly fifteen years. During a site visit in 2008, UT Austin researchers noted a wide range of ASR/DEF-related damage; the most severe of which greatly exceeded the damage found within the US 59 corridor bridge structures. The beams were, in effect, a complete representation of the past, present, and future damage found within the US 59 corridor structures. Knowledge to be gathered through structural testing of the box beams was potentially invaluable to those planning future US

59 corridor maintenance. Recognizing the technical value of such an endeavor, the Houston District of the Texas Department of Transportation commissioned the current study.

3.2.1 Acquisition of the Trapezoidal Box Beams

As fabricated, the trapezoidal box beams ranged from 102 to 113 feet in length and weighed between 65 and 71 tons. To facilitate transportation to (and within) Ferguson Structural Engineering Laboratory, each of the box beams were cut into three sections of equal weight. The resulting fifteen segments ranged from 32 to 40 feet in length and weighed between 21.8 and 23.5 tons; within the hauling length and laboratory crane limitations (Figure 3-2).

Figure 3-2: Arrival of Beam Segments from Mesa Precast Yard
(A) Transport via Tractor-Trailer, (B) Offloading with Spreader Beam and Nylon Straps, (C) Temporary Storage in FSEL

Three of the beam segments were taken directly into Ferguson Structural Engineering Laboratory and temporarily stored in anticipation of testing. The remaining twelve beam segments were offloaded via mobile crane and placed on a stable paved surface near the laboratory. After the first round of testing was complete, additional segments were moved into the laboratory via a similar set of operations (Figure 3-3).

Figure 3-3: Handling of Beam Segments with a Mobile Crane

Six of the fifteen beam segments were not suited to the purpose of the current study; i.e. to evaluate the structural performance of *dapped ends* with ASR/DEF deterioration. These six segments featured a combination of either cut ends or standard block ends and were therefore set aside for alternate courses of research. The dapped-end segments and the one standard end segment used in this project are listed in Table 3-2. The erection mark from the full beam length and the new segment labels are included for

referencing purposes. Shop drawings corresponding to each erection mark are included in Appendix A.

Table 3-2: Selected Beam Segments

Segment ID	Erection Mark	Damage	Purpose
N-II	MLL-9-34	Little to None	Load Test
L-II	RF-3R-12	Light	Load Test
M-I	RF-3R-9	Moderate	Load Test
M-II	RF-3R-9	Moderate	Load Test
H-II	RF-1R-1	Heavy	Load Test
H-A	RF-1R-1	Heavy	Autopsy
N-P	MLL-9-34	Little to None	Petrography
M-P	RF-2R-6	Moderate	Petrography
H-P	RF-1R-1	Heavy	Petrography

The new labeling scheme shown in Table 3-2 was developed to better describe the test segments and facilitate comparisons of the test results. The first term indicates the level of distress in the beam: undamaged (N) to light (L), moderate (M), or heavy (H) cracking. Qualitative determination of the damage level is described in Section 3.3.2. The second term indicates the type of test: dapped-end test at a shear span-to-depth ratio of 1.2 (I), dapped-end test at a shear span-to-depth ratio of 1.85 (II), petrographic analysis (P), or autopsy (A). For clarity, all future discussions concerning the various beam segments will reference this labeling convention.

3.2.2 Structural Details of Trapezoidal Box Beams

In order to establish a basis for the evaluation of ASR/DEF- and construction-related damages described in Section 3.3, the original trapezoidal box beam design is described here. To begin, the geometry of the dapped end, solid end block, and hollow void region are illustrated in Figure 3-4. While the implementation of trapezoidal box

beams with dapped ends was intended to provide aesthetically-pleasing superstructures, fabrication of the unique cross-section could prove to be challenging; as evidenced by the rejected box beams included within this study.

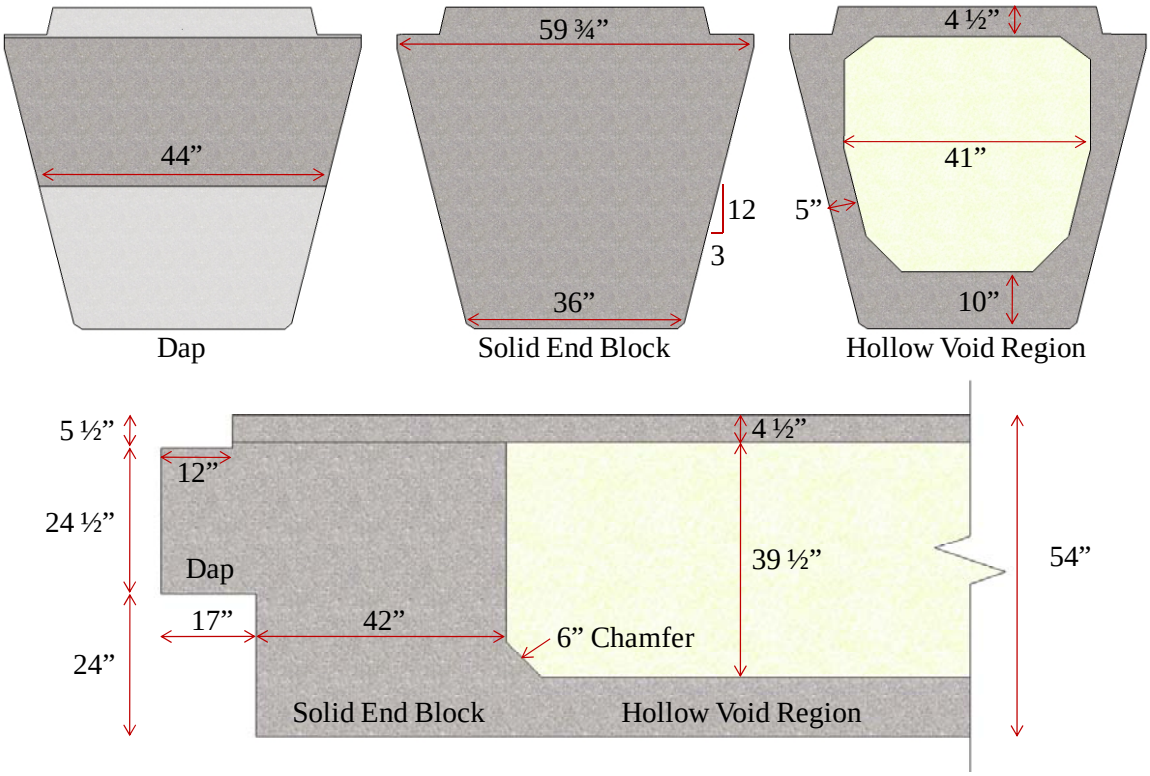

Figure 3-4: Dimensions of a Standard Trapezoidal Box Beam

The eight dapped-end segments were virtually identical with the exception of two minor details. First, the dapped ends of segments N-II and N-P were skewed at 33 degrees; all other segments featured square ends. Secondly, the amount and configuration of the flexural reinforcement varied from segment to segment. Non-skewed segments, including L-II, M-I, M-II, and H-II, typically contained 62 one-half inch prestressing strands with 24 of those debonded according to the schedule shown in Figure 3-5A. Skewed segments N-II/N-P contained 58 prestressing strands with 34 fully bonded as shown in Figure 3-5B. In both cases, the longer debonded lengths were concentrated at the edges of the beam (i.e. under each of the box beam webs). This detail, in combination

with the high level of debonding (about 40%), was expected to have adverse effects on the flexural and shear capacity of the member in the end block region.

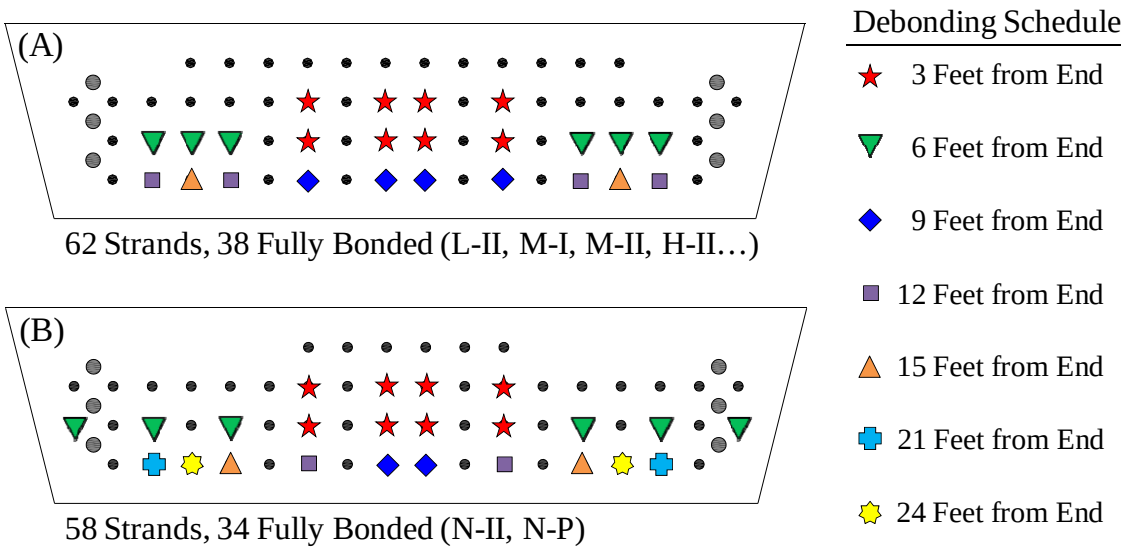

Figure 3-5: Debonding Schedules for the Dapped-End Segments

The reinforcement layout (shown in Figure 3-6) was standard for all of the segments. In order to prevent failure of the dap, the end block of each beam was heavily reinforced. The horizontal dap reinforcement was welded to a plate at the end face and anchored with a 90° hook two inches from the inner face of the end block (1). Additional horizontal hooked bars were provided up to two thirds of the dap height to help prevent cracking at the reentrant corner (2). The large amount of vertical reinforcement located near the reentrant corner (3) was a feature of both strut-and-tie modeling and PCI Design Handbook design methods (refer to Chapter 2). This hanger reinforcement extended down past the prestressing strands and, along with three bent bars at the bottom of the beam (4), helped to provide confinement. Reinforcement sizes and spacing are provided within the detailed shop drawings included in Appendix A.

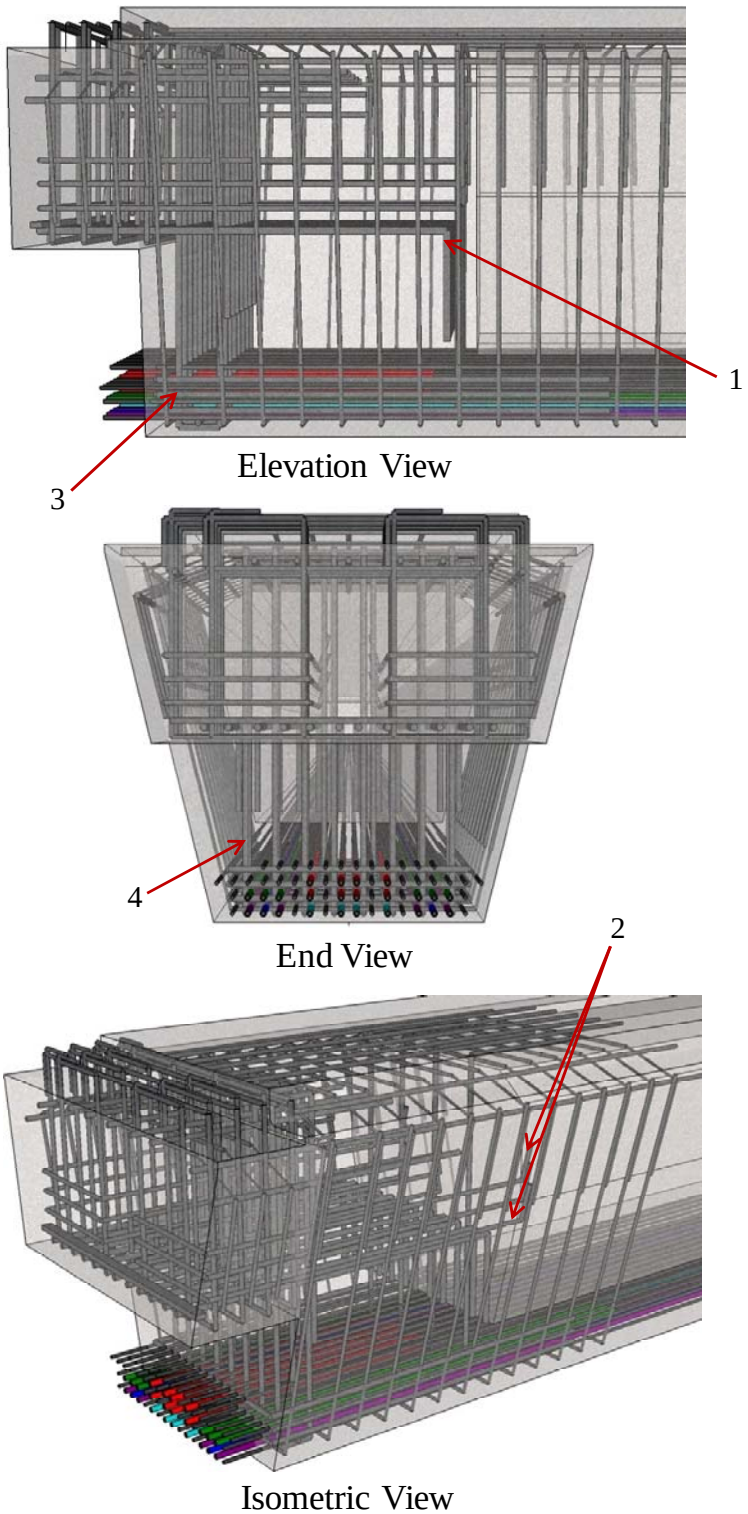

Figure 3-6: Dapped-End Reinforcement Configuration

3.3 PRE-TEST CONDITION OF BOX BEAM SEGMENTS (2008)

Upon arrival each of the beam segments were examined for construction defects and ASR/DEF-related damage. The condition survey served two purposes: (1) to determine each segment's suitability for dapped-end testing and (2) to qualitatively establish the level of ASR/DEF-induced cracking and damage within each segment. The results of the survey are summarized in Table 3-3 and detailed within the subsections below.

Table 3-3: Pre-Test Condition of Box Beam Segments

Segment ID	Construction Defects	ASR/DEF-Related Damage
N-II	Wrong End Skew	Little to No Cracking
L-II	Poor Consolidation	Light Cracking
M-I	Slight Void Rotation	Moderate Cracking
M-II	Slight Void Rotation	Moderate Cracking
H-II	Honeycombing, Previous Coring	Heavy Cracking
H-A	Consolidation	Heavy Cracking
N-P	Wrong End Skew	Little to No Cracking
M-P	23 Feet of Top Flange Missing	Moderate Cracking, Leaching
H-P	Honeycombing, Previous Coring	Heavy Cracking

It is essential to recognize that the dapped-end tests were only conducted on segments deemed fit for the purposes of the structural investigation. The segments that had defects rendering their structural performance questionable were not tested.

3.3.1 Construction Defects

Placement of the styrofoam void during the multi-stage cast was challenging and could lead to void floatation and consolidation issues (shown respectively in Figure 3-7 and Figure 3-8). In order to exclude segments with significant defects from the dapped-end testing program, all surfaces of each segment were thoroughly examined.

Figure 3-7: Examples of Vertical and Horizontal Void Misalignment

Figure 3-8: Example of Poor Consolidation

Measurements of the web and flange thickness were taken at the cut ends of each segment, and in one unique circumstance, along the length of one segment (M-I) using a non-destructive technique. Obervations of void floatation at the cut end generally did not reveal noticeable deviation from the required 5-inch webs and 4.5-inch top flange and the

non-destructive measurements concluded that the combination of both web widths summed to ten inches. However, inspection of the cut ends provided no information on of void floatation along the length of the segments. After testing segment L-II, which showed no void movement in the initial assessment, a cut was made through the test region. It was discovered that translation of the void decreased the web to 2.5-inches on one side. In spite of the thin web, the load-carrying capacity of L-II was governed by shear-induced anchorage failure (similar to that of the remaining segments, see Chapter 4) within the solid end block region.

It should be noted that the failure of each segment was unrelated to any of the defects referred to here (see Chapter 4). Rather, this discussion is meant to highlight the difficult nature of box beam construction and potential field implications. Based on the inspection of the alternate beam segments (rejected for reasons other than void floatation), it is likely that many in-service trapezoidal box beams are subject to void misalignment along their lengths. In the context of the current study, void misalignment did not appear to influence dap performance. However, such misalignment may be detrimental to other limit states such as shear strength of the box webs.

A few cores were sampled from the end block of segment H-II by Folliard in 2008 for materials research purposes. Although several of these cores were located in the critical dapped-end region, no stirrups were damaged and the removal of cores did not appear to have a significant effect on the behavior of the beam.

3.3.2 ASR/DEF-Related Damage

Each of the five segments subjected to structural testing (i.e. N-II, L-II, M-I, M-II and H-II) was fabricated with the same type of cement, coarse and fine aggregates (refer to Table 3-4). With the exception of the admixture dosage and water-to-cement ratio, the concrete mixture design was consistent for the five segments. It is therefore safe to assume that the alkali loading (derived from the cementitious materials) was relatively consistent as well (whether subjected to ASR/DEF deterioration or not). The concrete

mixture designs for the dapped-end segments are summarized in Table 3-8 and detailed in Appendix A.

Table 3-4: Concrete Materials

Aggregate		Water	Cement	Admixture		
Fine	**Course**			**Type A**	**Type D**	**Type F**
Hallet-Porter	Vulcan Materials	Well	Capitol Type III	WRDA/HYCOL	Daratard 17	WRDA-19

Table 3-5: Concrete Mixture Designs

Batch Design (One Cubic Yard)	N-II	L-II to H-II
Fine Aggregate	1492 lbs	1301 lbs
Course Aggregate	1686 lbs	1686 lbs
Water	190 lbs	263 lbs
Cement	658 lbs	658 lbs
Admixture A	121 oz	-
Admixture D	-	78 oz
Admixture F	684 oz	625 oz

Barring any major differences in the storage conditions, the wide range of ASR/DEF deterioration encompassed within this study can only be attributed to variations in the curing temperature. Investigation of the air temperatures corresponding to each of the casting days further substantiates this inference (refer to Table 3-6). The temperature in the northeast Houston area was as high as 100°F during the placement of the heavily damaged segment (H-II) and only as high as 77°F during the placement of the least damaged segment (N-II). The qualitative damage levels assigned within this section

generally correlate well to the maximum temperature measured on the corresponding casting dates.

Table 3-6: Maximum and Mean Air Temperatures at Casting

Segment ID	Cast Date	Max Temperature	Mean Temperature
N-II	11/9/1995	77	64
L-I	7/9/1995	93	82
M-I	7/6/1995	93	82
M-II	7/6/1995	93	82
H-II	7/26/1995	100	90
Data Source: www.wunderground.com (2010)			

Assessment of the ASR/DEF-related cracking and damage was conducted almost exclusively on a visual basis; arbitrary crack width and spacing measurements only served to guide the assessment process. Noted features of the deterioration and the rationale behind each of the qualitative damage levels are described below.

3.3.2.1 N-II

Examination of segment N-II, shown in Figure 3-9 with cracks outlined in black, revealed little more than minor cracking. The largest crack was located at the vertical interface of the solid end block and hollow void section. It was 0.05 inches wide. Hairline map cracking in the middle of the end block and a few small cracks radiating from the bottom corner were the only other indications of ASR/DEF deterioration. The pre-existing damage was deemed inconsequential and segment N-II was selected to represent the performance of an “undamaged” dapped-end beam.

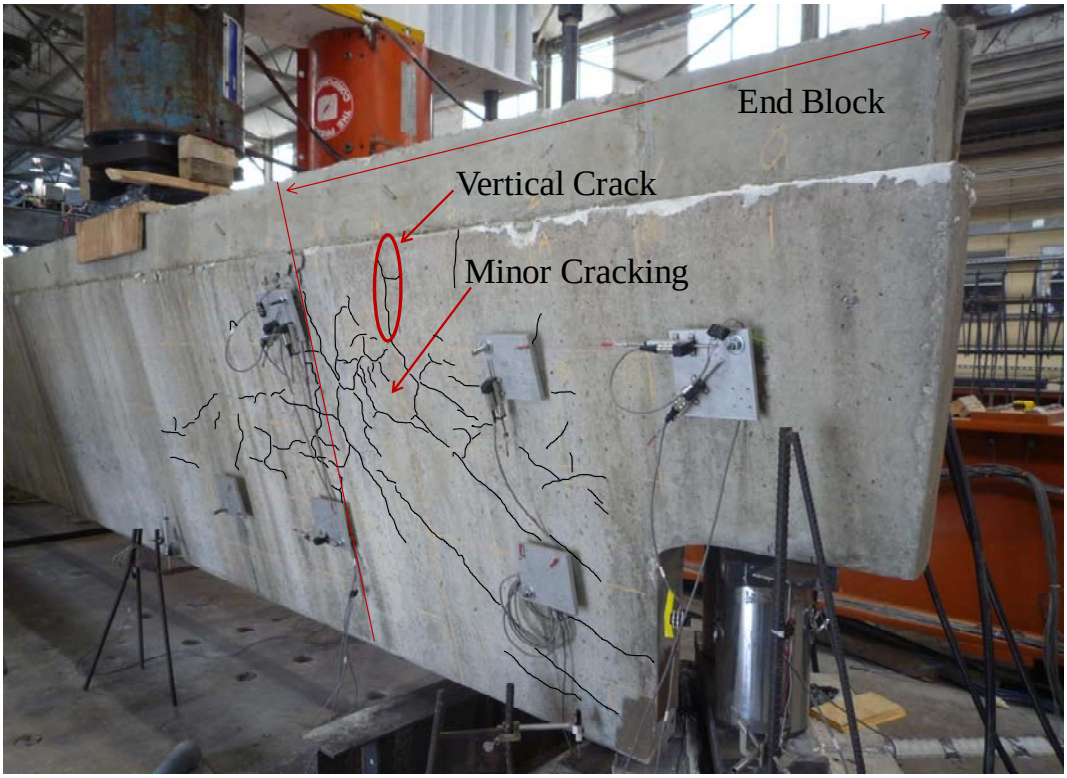

Figure 3-9: Minor Damage in End Block of N-II

3.3.2.2 L-II

The largest crack (measuring 0.05 inches in width) in segment L-II was also located at the vertical interface of the solid end block and hollow void section. This was, in fact, the case for all three segments classified as lightly or moderately damaged. The commonalities with segment N-II typically ended there. Map cracking within the end block and discrete cracks in the transfer length region of segment L-II (i.e. radiating diagonally from the bottom corner of the beam) were more prominent (up to 0.016 inches in width). There was also a slight lack of consolidation below the load point due to improper vibration after the second casting stage (shown in Figure 3-10). A mid-depth horizontal crack ran through this area, suggesting that the ASR/DEF-induced cracking might have been influenced by a cold joint. Due to the limited widths of the most significant cracks (in relation to the remaining segments), L-II was selected to represent the performance of a “lightly damaged” dapped-end beam.

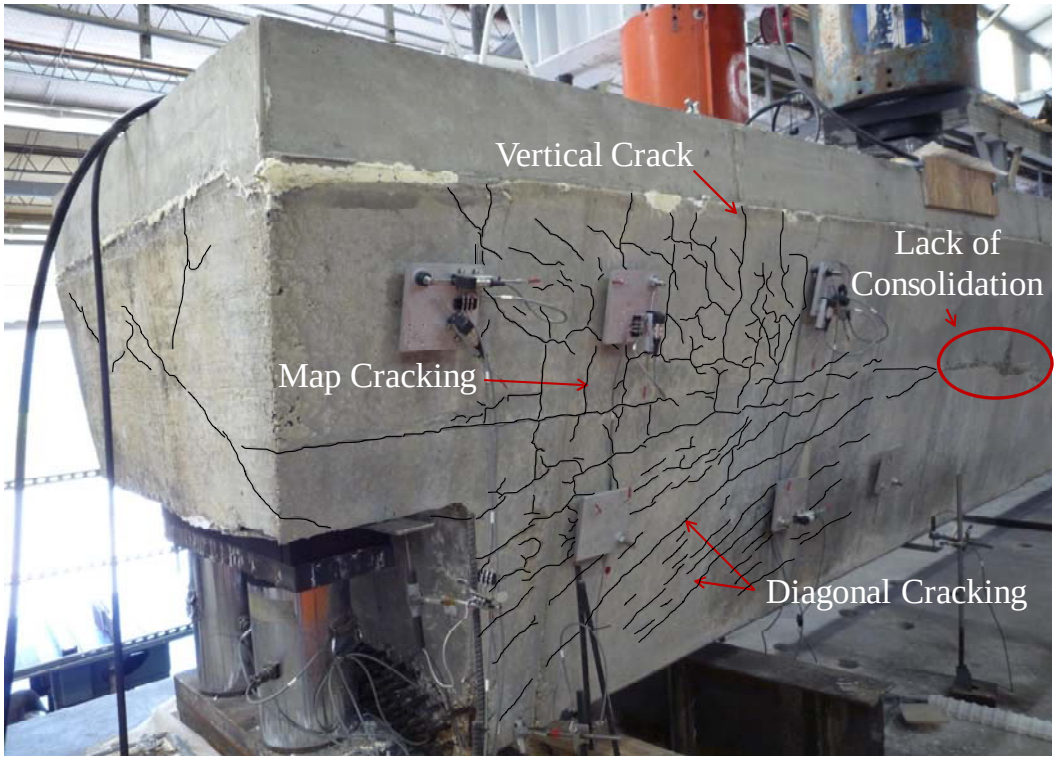

Figure 3-10: Mildly Damaged End Region of L-II

3.3.2.3 M-I/M-II

Segments M-I and M-II were obtained from opposite ends of the same trapezoidal box beam (RF-3R-9 as listed in Table 3-1) and consequently featured similar signs of deterioration. Map cracking was extensive in the solid end block regions; crack widths ranged from hairline to 0.06 inches. Diagonal cracks again radiated from the bottom corner of each dapped end towards mid-depth. The mid-depth crack then extended the full length of the beam as shown in Figure 3-11. The width of the diagonal cracks in the anchorage region was nearly double that found in segment L-II (0.03 inches versus 0.016 inches). Based on this observation, the ASR/DEF-related damage in segments M-I and M-II was classified as “moderate.”

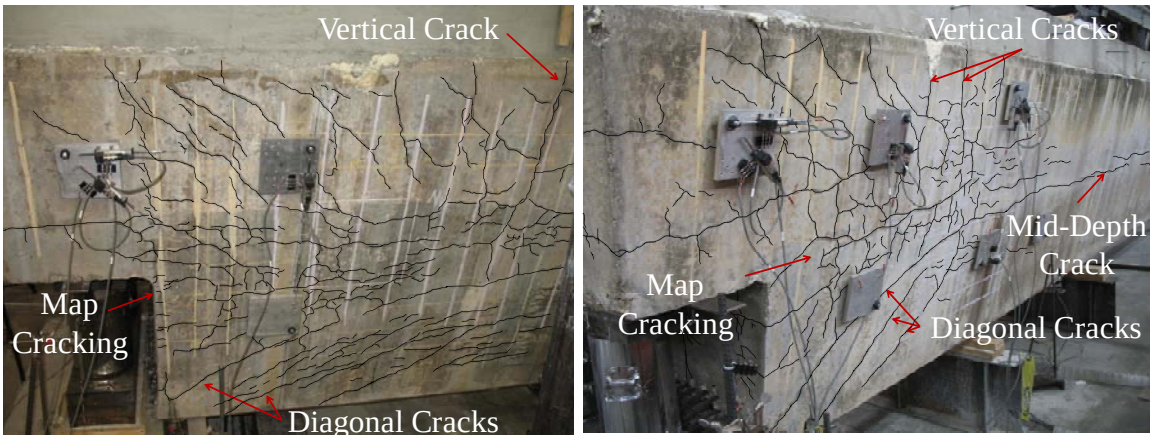

M-I M-II

Figure 3-11: Moderately Damaged End Regions of Segments M-I and M-II

3.3.2.4 H-II

The ASR/DEF-related damage to segment H-II was unparalleled in the current testing program. The largest cracks on the west face of the segment (referred to as "Large ASR/DEF Cracks" in Figure 3-12) were 0.06 and 0.164 inches wide. Previous coring on the dapped end was extensive, but had no impact on the mode of failure; failure ultimately occurred in bottom corner of the full-depth section (discussed in Chapter 4). Cracking on the east face was even more severe; maximum crack widths exceeded one quarter of an inch (see Figure 3-13). Due to the extent and exceptional severity of the map cracking, H-II was selected to represent the "heavily damaged" dapped-end beam.

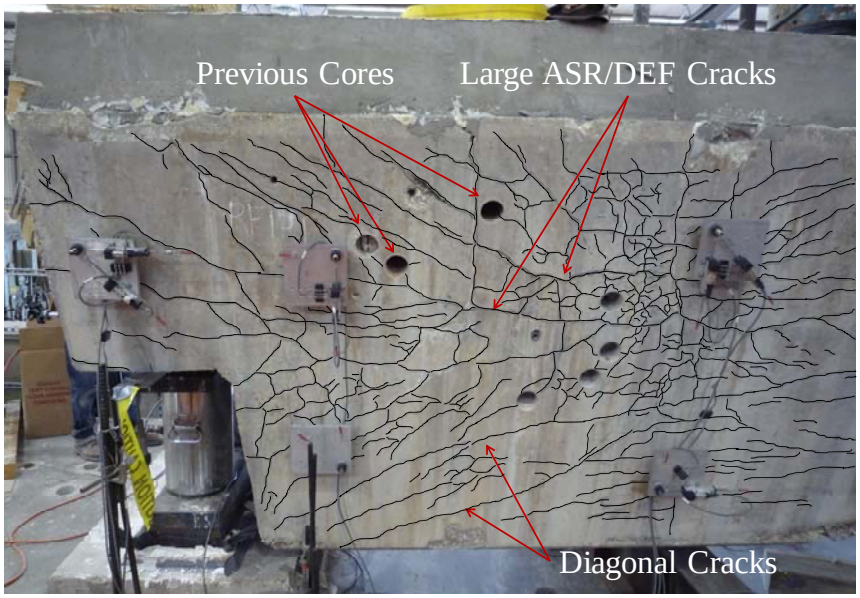

Figure 3-12: Heavily Damaged End Region of H-II (West Face)

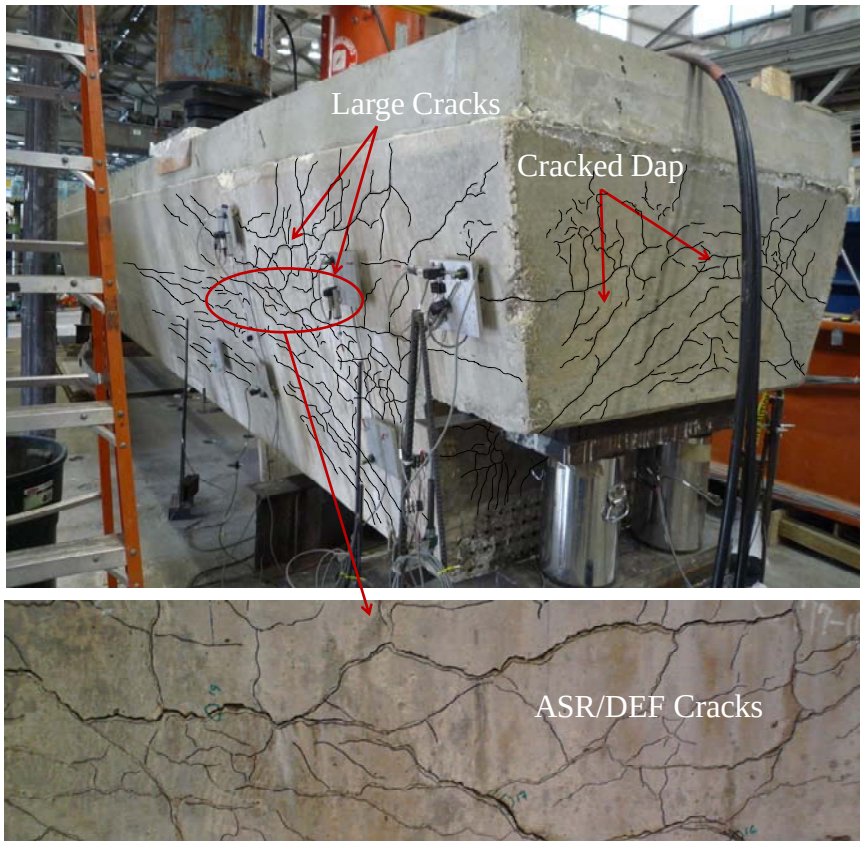

Figure 3-13: Heavily Damaged End Region of H-II (Northeast Corner)

3.3.3 Material Properties

Determination of the concrete and reinforcement strengths was critical to the analysis of the test results via strut-and-tie modeling (please refer to Chapter 4). A number of concrete cores and several lengths of reinforcement were sampled from the beam segments subjected to dapped-end testing.

Segments N-II, L-II, M-I, M-II, and H-II were cored after the dapped-end test was completed. The cores were extracted from the face of the dap as shown for L-II and H-II in Figure 3-14. The face of the dap was the only suitable area in the test region as it was free of extensive shear cracks and closely spaced reinforcement. The cores measured 3¾ inches in diameter and were cut to lengths of 7½ inches to provide the required aspect ratio. The core extraction procedures of ASTM C42 and compression testing procedures of ASTM C39 were followed. It should be noted that the preparation tasks and mechanical tests were conducted soon after the original core extraction date to minimize moisture loss and potential relaxation of the damaged samples.

L-II H-II

Figure 3-14: Core Extraction Locations for L-II and H-II

As mentioned in Chapter 2, extraction of a core removes the peripheral restraint and augments existing microstructural damage. Coring-related damage may cause a reduction in strength and stiffness not representative of the structure and thereby lead to inappropriate conclusions. It was nevertheless important to obtain an estimate, even if it

was a lower bound, for the compressive strength of the concrete in the ASR/DEF distressed beams. The compression test results were corrected for the effects of coring as recommended by ASTM C42 ($f'_c = (f'_{c,\ core})/0.85$). The average core strengths (three samples per segment) are summarized in Table 3-7. The compressive strengths required and measured at seven days are included for comparison purposes.

Table 3-7: Compressive Strength of the Dapped-End Segments

	N-II	**L-II**	**M-I**	**M-II**	**H-II**
at 7 Days	8.6 ksi	7.6 ksi	-	-	8.3 ksi
at 14+ Years	9.3 ksi	9.6 ksi	11.8 ksi	8.6 ksi	6.4 ksi
Required	5.4 ksi	5.8 ksi	-	-	6.0 ksi

The compressive strengths of the undamaged and lightly cracked segments (N-II and L-II, respectively) have increased about 15 percent (on average) over the fourteen years of storage. While the strength gain is meager in comparison to traditional precast concrete mixtures, the final compressive strength was well in excess of the seven day requirements stipulated by TxDOT. Compressive strength information was not available for segments M-I and M-II as records were not kept for the beam (RF-3R-9 as listed in Table 3-1). If the assumption is made that similar requirements were applied then no significant strength deficiencies have resulted as a consequence of the ASR/DEF deterioration.

In contrast, the concrete compressive strength of the heavily cracked segment (H-II) was significantly less than the reported seven-day strength and only marginally higher than the seven-day requirement. The notable reduction in compressive strength over the last fourteen years substantiates the conclusions drawn during the visual inspection; segment H-II was subjected to severe ASR/DEF deterioration. It is important to keep in mind that the compression testing results are not necessarily indicative of the structural performance. Due to the potential for coring-related damage and loss of in-situ restraint, only load tests can provide an accurate assessment of the structural performance.

In an alternate effort to verify the yield strength of the mild reinforcement used in the beams, two no. 4 bars (transverse reinforcement) and one no. 6 bar (longitudinal reinforcement) were removed from segment H-II. The bars were loaded to failure in a universal testing machine. An extensometer was used to measure the elongation of the bar as tension was applied. The stress-strain response of all three bars was typical of standard grade 60 reinforcement. The stresses at yield and fracture for each bar are summarized in Table 3-8.

Table 3-8: Reinforcement Tensile Strength

Bar Size	Purpose	f_y	f_u
No. 4	Transverse Reinforcement	70 ksi	96 ksi
No. 6	Longitudinal Reinforcement	63 ksi	104 ksi

The reinforcement properties were coupled with the concrete compression testing results (described above) to provide estimates of the dapped-end strength. Results of the dapped-end tests and strut-and-tie models can be found in Chapter 4.

3.4 DAPPED-END TESTING PROGRAM

The objective of the testing program was to establish the effects of ASR/DEF deterioration on the structural performance of dapped-end trapezoidal box beams. The undamaged (N-II), lightly cracked (L-II), moderately cracked (M-I and M-II), and heavily cracked (H-II) box beam segments (described above) provided a sufficiently large range of deterioration to accomplish that objective. Dapped-end testing commenced in January of 2009. All five segments were tested by the beginning of October in that same year. A schedule of the testing is provided in Table 3-9 for reference purposes. It is important to note that the results of the first test (M-I) led to a shift in the test procedure. As discussed in detail within Chapter 4, the shear span-to-depth ratio was increased to focus the study on the performance of the flexural reinforcement anchorage.

Table 3-9: Schedule of Dapped-End Testing

Segment ID	Shear Span-to-Depth Ratio	Test Date
M-I	1.20	1/29/2009
M-II	1.85	3/2/2009
L-II	1.85	5/21/2009
H-II	1.85	7/21/2009
N-II	1.85	10/5/2009

The critical aspects of the dapped-end testing program at Ferguson Structural Engineering Laboratory, including the test setup, instrumentation and testing procedures are detailed in the following sections.

3.4.1 Test Setup

A high capacity test setup designed for shear testing of U-beams (TxDOT Project 0-5831) was well suited to the dapped-end testing program. Modifications to the existing setup were minimal; greatly facilitating the experimental work. End and isometric views of the set-up are shown in Figure 3-15 and Figure 3-16, respectively.

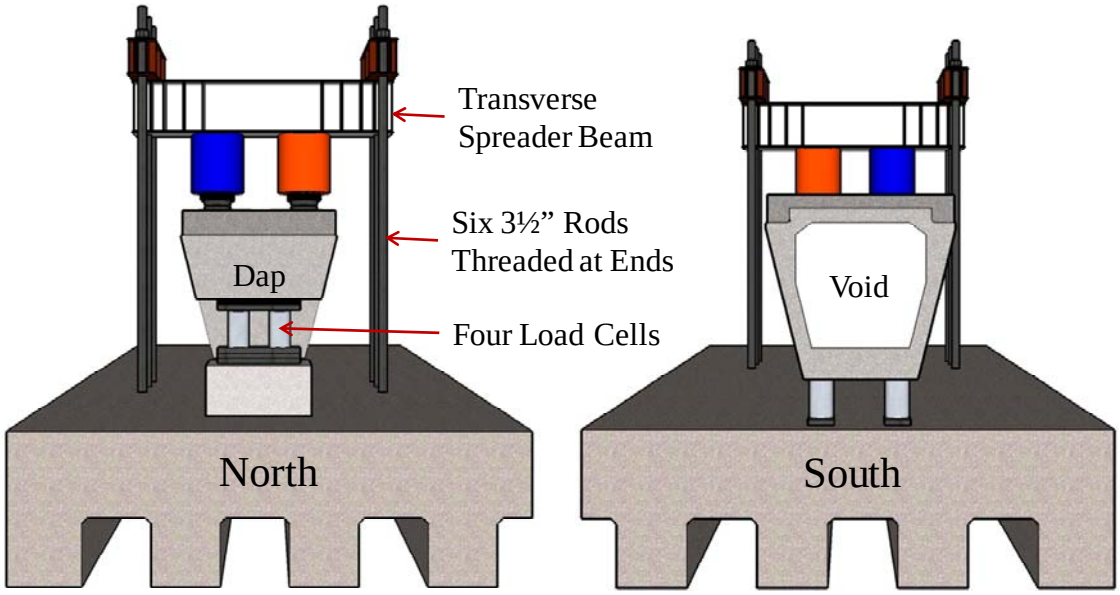

Figure 3-15: North and South End of Test Setup

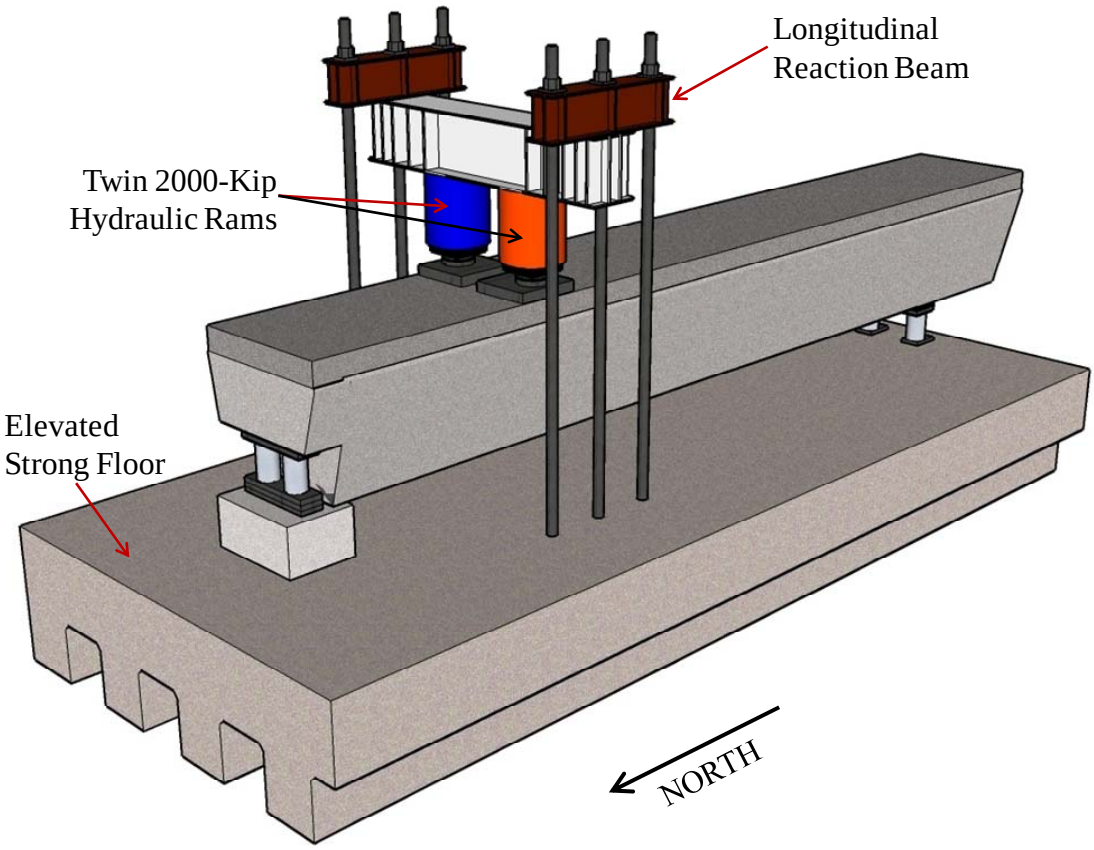

Figure 3-16: View of Test Setup Looking South East

Load was applied to the beam with two 2,000 kip hydraulic rams (as shown in Figure 3-17). A 12-inch spherical head attached to the piston of each ram accommodated slight misalignments between the loading apparatus and the top of the box beam segment. Two 4-inch thick steel plates with dimensions of 26 inches by 24 inches were set in hydrostone to evenly distribute the load to both box beam webs. When hydraulic pressure was applied, the rams reacted against the white transverse spreader beam that transferred the load to the two brown longitudinal reaction beams. The load was then transferred to the elevated strong floor by six 3½-inch steel rods. A nut secured the threaded portion of each steel rod to the top of the longitudinal reaction beam and the bottom of the elevated strong floor. Access to the bottom-side nuts was provided by tunnels at regular intervals in the strong floor as shown in Figure 3-15 and Figure 3-16.

Figure 3-17: Four-Million Pound Loading Apparatus

The ends of each box beam were supported by a total of three bearing plates: one at the dapped end and one under each web at the cut end of the beam (Figure 3-18). The dapped-end bearing plate measured 32 inches by 9 inches and was placed with its long side perpendicular to the longitudinal axis of the beam. The other bearing plates measured 16 inches by 9 inches and were placed under each web parallel to the longitudinal axis of the beam.

3.4.2 Instrumentation and Data Acquisition

The structural performance of each dapped end was characterized by load and deformation measurements. Techniques and instruments unique to this testing program are described herein.

3.4.2.1 Load Measurements

Four 1,000-kip load cells were used to measure the self weight of the beam and the load applied by the hydraulic rams. The typical arrangement of all four load cells is

shown in Figure 3-18. The following description of the support hardware is intended to demonstrate the care taken to ensure clear boundary conditions and accurate load measurements.

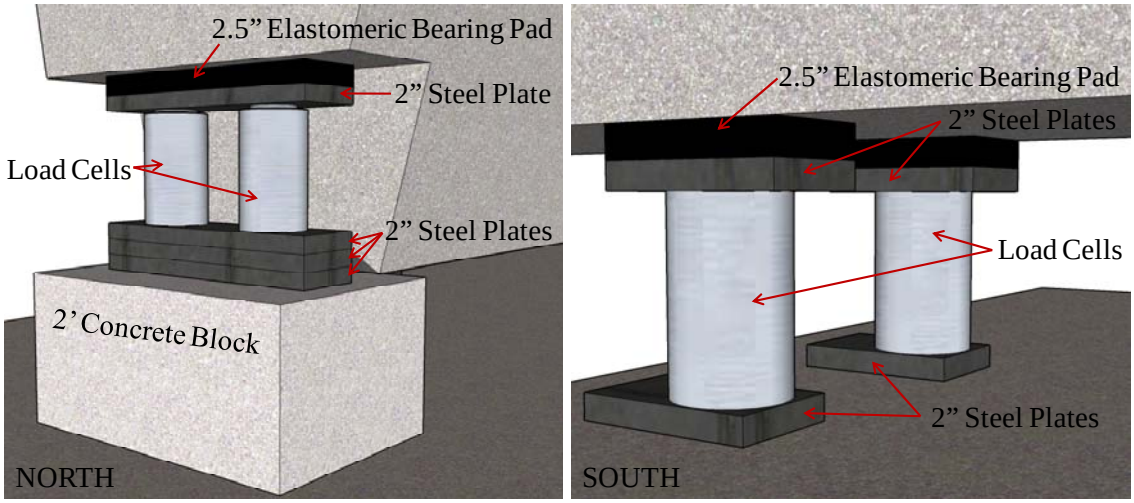

Figure 3-18: North and South Supports of Test Setup

To evenly distribute each reaction, a 2½-inch thick, 5-laminate elastomeric bearing pad was placed between the bottom-side of the box beam and each bearing plate. The 2-inch thick bearing plates were typically counter-bored on the bottom face to accept each of the load cells; preventing slippage between the surface of the plate and the slightly convex top of the load cell. The bottom of the load cells were then secured to another 2-inch plate with a ½-inch diameter threaded rod, forming a stable reaction system. At the cut end, the 2-inch thick steel plate rested directly on the elevated strong floor. At the dapped end, a 2-foot high support block was necessary to account for the height difference between the bottom of the beam and the bottom of the dap.

N-II, the only skewed beam tested in the current study, presented unique challenges at the time of setup. The load cells and bearing plates were kept in their original position at the south (cut) end of the beam but rotated to account for the skew at the dapped end. Careful measurements were taken to ensure that the center of the two load cells corresponded to the center of the beam along its longitudinal axis as shown in Figure 3-19.

Figure 3-19: Skewed Support for Segment N-II

3.4.2.2 Deformation Measurements

Deflections and crack openings were measured with linear potentiometers. The deflections were generally recorded at four different locations along the length of the beam: at the two supports, at the bottom of the dapped end of the beam, and at the load point. Arrangement of the linear potentiometers for a typical load test is shown in Figure 3-20. The load point deflections reported in Chapter 4 have been corrected for movement at the two supports.

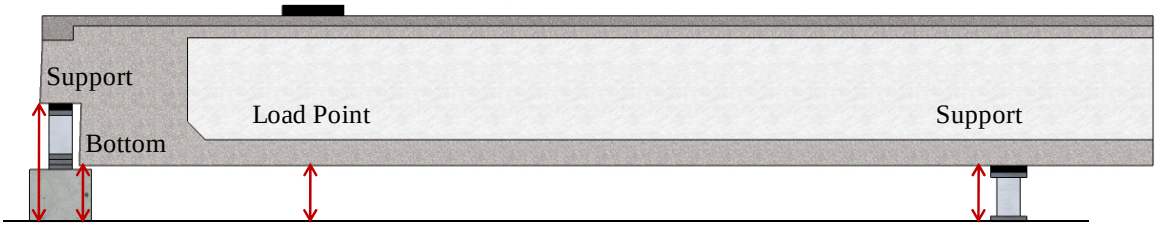

Figure 3-20: Measurement of Segment Deflections

Linear potentiometers were also used to measure average concrete strains at the void and dap sections during each test. Each setup, commonly referred to as a shear-deformation gage, included three linear potentiometers arranged to form a 45-degree right triangle (shown in Figure 3-21). The linear potentiometers were secured to aluminum plates that were free to rotate about three ½-inch threaded rods (epoxied into the concrete). Piano wire was used to connect the plunger end of each linear potentiometer to eye hooks on the plates. All of the potentiometers were set at half stroke to accommodate movement in either direction. The completed assembly (shown in Figure 3-21) monitored the relative movement of each rod with respect to the other rods. This effectively measured the opening of cracks which crossed the horizontal, vertical, and diagonal wires. Four shear deformation gages were used to monitor the concrete deformation at the dap and void sections of both beam faces. The position of each shear deformation gage corresponded to components which were subjected to significant load/deformation demands: (1) the concrete strut between the load and flexural reinforcement anchorage and (2) the reentrant corner at the dap. The location of each shear deformation gage length in relation to the primary load paths is shown in Figure 3-22.

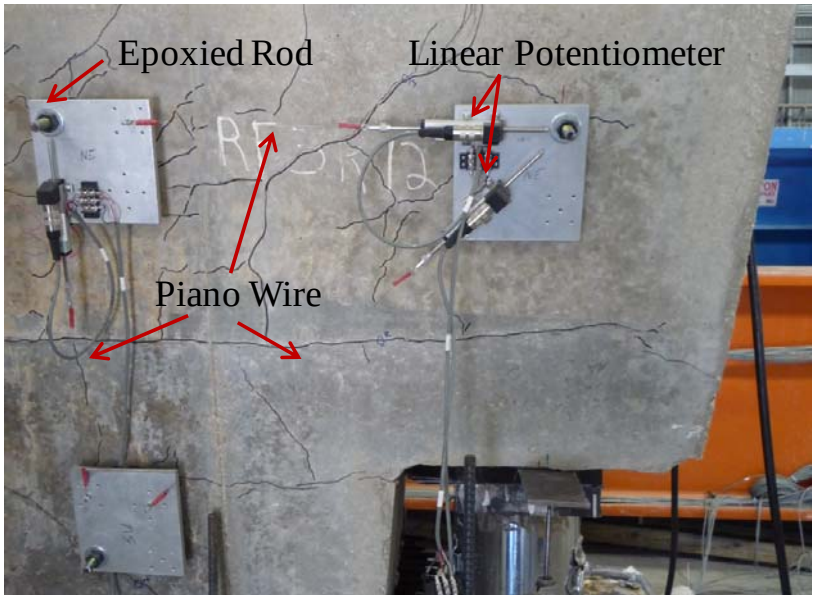

Figure 3-21: Measurement of Concrete Deformation

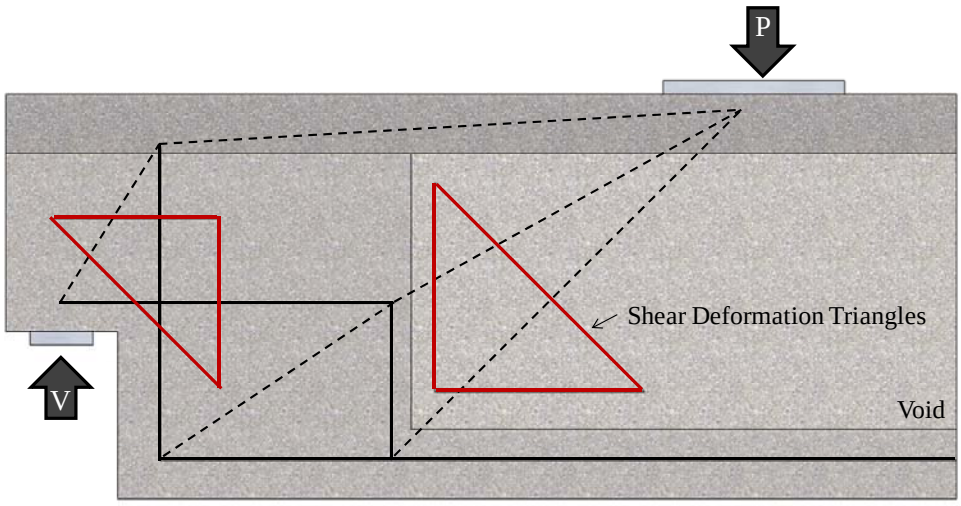

Figure 3-22: Position of Shear Deformation Gages at the Void and Dap

3.4.2.3 Data Acquisition

Segment L-II is shown in Figure 3-23 completely instrumented. Each of the transducers (load cells and linear potentiometers) were wired to bridge completion modules and then interrogated via a 120-channel scanner. The voltage output was converted into engineering data using predetermined calibration factors. Data acquisition software was used for real-time monitoring and storage of the transducer output.

Figure 3-23: L-II Fully Instrumented for Dapped-End Testing

3.4.3 Test Procedure

The preparation and testing of each dapped-end segment was identical: (1) box beam placement, (2) deck placement, and (3) load application. Each of the steps is described in detail within the following sections.

3.4.3.1 Box Beam Placement

The heaviest box beam segments weighed over twenty-three tons; just shy of the laboratory crane capacity of twenty-five tons. Following the addition of a concrete topping slab (described in the following section) the weight of the segment would undoubtedly exceed the crane capacity. For this reason, accurate placement of the segment prior to the addition of the topping slab was essential. The topped segment would have to be tested in its final position (illustrated in Figure 3-23); large adjustments would not be possible.

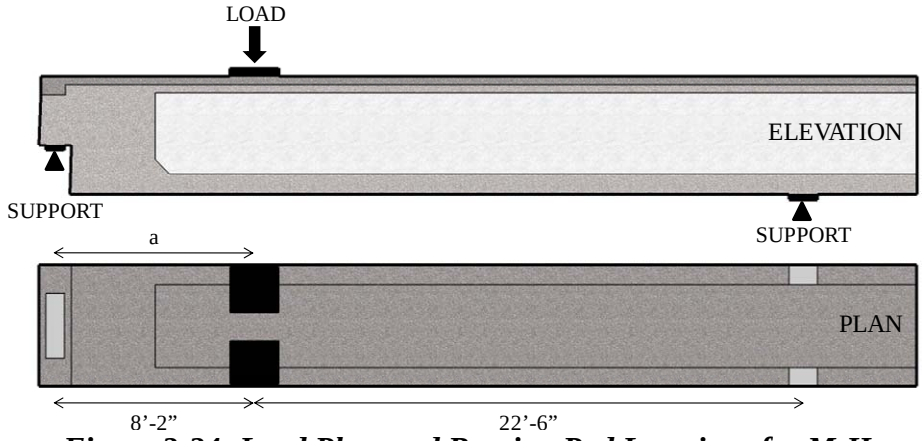

Figure 3-24: Load Plate and Bearing Pad Locations for M-II

Careful attention was paid to the placement of the box beam segments to ensure the correct shear span was established. This was critical to achieving the desired behavior and ensuring compatibility between the test results. In the context of the current project, the shear span was defined as the distance between the centerlines of the support and load bearing plates. Two shear span configurations were tested. Segment M-I was positioned to establish a shear span of 64 inches, while the remaining segments were positioned to establish shear spans of 98 inches. At an effective depth (defined as the distance from the

top of the slab to the centroid of the prestressing strands) of 53 inches, the resulting shear span-to-depth ratios were 1.20 (for M-I) and 1.85 (for segments N-II through H-II).

3.4.3.2 Deck Placement

Once the segment was in its final testing position, the 4-inch topping slab was placed. The concrete deck served one purpose: to raise the moment capacity of the beam and ensure a dapped-end failure. After each successful test, the beams were cut in half with a concrete wire saw to facilitate removal from the laboratory.

While the thickness of the precast flange was required to be 4½ inches, it typically varied from beam to beam and within the segment itself (depending on void floatation). Wood forms were therefore fabricated and adjusted as necessary to achieve a total top flange thickness of 8½ inches. TxDOT requirements for top mat deck reinforcement guided the detailing of the cast-in-place slab. No. 4 bars, spaced at 9 inches longitudinally, were crossed by no. 5 bars spaced at 6 inches transversely. The constructed formwork and assembled reinforcing mat are shown prior to concrete placement in Figure 3-25.

Figure 3-25: Formwork and Rebar for the Topping Slab

The top of the segment was wetted before casting to prevent it from absorbing moisture from the fresh concrete. The concrete was placed via a gated bucket attached to

the overhead crane. Internal vibrators were used to consolidate the concrete around the reinforcement and within the coped section at the dapped end. A screed was used to achieve the proper slab depth and create a smooth, level surface appropriate for loading. Students at Ferguson Laboratory are shown placing the deck concrete in Figure 3-26.

Figure 3-26: Casting the Deck of Segment H-II

Four-inch diameter cylinders were cast with the deck to obtain the compressive strength at the time of dapped-end testing. They were stored alongside each segment until testing. The topping concrete was designed to achieve 10 ksi in twenty-eight days. The rapid strength gain of the high strength mixture minimized the curing period. The same mix was used for all five test segments and the corresponding compressive strengths can be found in Table 3-10.

Table 3-10: Deck Cylinder Strength

	M-I	**N-II**	**L-II**	**M-II**	**H-II**
Cylinder A	5.7 ksi	7.7 ksi	9.3 ksi	9.1 ksi	8.3 ksi
Cylinder B	5.7 ksi	7.7 ksi	8.7 ksi	9.5 ksi	7.2 ksi
Cylinder C	5.9 ksi	7.8 ksi	9.1 ksi	8.7 ksi	8.7 ksi
Average	5.8 ksi	7.7 ksi	9.1 ksi	9.1 ksi	8.0 ksi

3.4.3.3 Load Application

The topped segment was typically ready for testing after a short curing period of seven days. Prior to testing, the segments were carefully lifted one end at a time (due to crane limitations) and placed onto the load cells. The self weight of each test segment (summarized in Table 3-11) was recorded to provide an accurate measurement of the total dapped-end capacity. To that end, the load measurements referenced in Chapter 4 represent all of the forces resisted by the dapped end, including the weight of the beam and associated testing hardware.

Table 3-11: Pre-Test Segment Measurements

	M-I	**N-II**	**L-II**	**M-II**	**H-II**
Short Shear Span	64 in	98 in	98 in	98 in	98 in
Long Shear Span	267 in	251 in	271 in	270 in	273 in
Total Length	35.9 ft	32.2 ft	35.8 ft	35.9 ft	36.6 ft
North Self-Weight	26.9 kips	24.8 kips	29.7 kips	30.1 kips	30.2 kips
South Self-Weight	34.8 kips	21.6 kips	30.9 kips	31.6 kips	31.7 kips
Total Self-Weight	61.7 kips	46.4 kips	60.6 kips	61.7 kips	61.9 kips

Pre-existing cracks were marked, pre-test pictures were taken and multiple cameras were setup to provide a record of the test. Following a brief check of the instrumentation, load was applied through the twin hydraulic rams. Pressure was supplied by a hydraulic pump. Loading increments of 100 kips (total load) were applied until the first new crack was observed. Following that observation, the load increments were decreased to 50 and 25 kips in order to carefully observe the crack progression and accurately record critical loads. Once the newly formed cracks exceeded 0.06 inches in width, the beam was loaded until failure. The results of the five dapped-end tests are presented in Chapter 4.

3.5 SUMMARY

The objective of the testing program was to determine the effects of ASR/DEF deterioration on the structural performance of dapped-end trapezoidal box beams. The five beams rejected by TxDOT for the US 59 corridor project provided a complete representation of the past, present, and future damage within the bridges. The beams were cut into thirds and shipped to Ferguson Structural Engineering Laboratory where five dapped-end segments were chosen for load testing.

The five segments had a variety of construction-related defects that did not appear to discredit the validity of the test program. All defects were located outside of the flexural reinforcement anchorage zone critical to the dapped-end capacity. Further examination of the five segments revealed a wide range of deterioration. The "undamaged" segment exhibited little more than fine map cracking. The "heavily" damaged segment had extensive map cracking with individual cracks measuring in excess of one-quarter inch in width. The results of compression tests conducted on extracted core samples confirmed the visual assessment of the deterioration. Long-term strength gain was negatively impacted by the most severe deterioration. Despite this observation, it was clear that only load testing could provide an accurate assessment of the structural effects of the ASR/DEF deterioration.

Finally, the test setup, instrumentation and loading procedure were described. The segments were carefully placed in the testing frame to obtain the appropriate shear span-to-depth ratio (1.2 for segment M-I and 1.85 for segments N-II through H-II). Following deck placement, the beam was loaded to failure with two 2,000 kip hydraulic rams. Load cells at each bearing point recorded the weight of the beam and the superimposed loads. Linear potentiometers were used to measure the deflection of the beam and concrete strain across the dap and hollow void regions. The test results are presented in Chapter 4 and compared to the strut-and-tie capacities calculated using the material properties in Chapter 5.

CHAPTER 4
Experimental Results and Analysis

4.1 OVERVIEW

In order to ascertain the structural effects of ongoing ASR/DEF deterioration in the US 59 corridor bridge structures (please refer to Chapter 1), five dapped ends representative of both current and expected states of deterioration were load tested. Tasks related to the acquisition, preparation, and testing of the five segments were described in Chapter 3. Measurements and observations made during the course of the testing program are summarized here and examined with respect to contemporary design codes.

To begin, the pre-test condition of each box beam segment is re-examined to identify damage critical to the structural performance of the dapped-end detail. The load-deformation response and ultimate strength of each dapped end are then reported with respect to the level of cracking. Examination and comparison of the test results provides insights into the relationship between the severity of the ASR/DEF-related damage and the structural performance of each dapped end. Finally, application of strut-and-tie modeling provisions from ACI 318-08, AASHTO LRFD 2009, and TxDOT Project 0-5253 allow the capacity margin of the ASR/DEF-damaged dapped ends to be assessed.

4.2 ASR/DEF-RELATED DAMAGE TO DAPPED-END SEGMENTS

Prior to each load test, ASR/DEF-related surface cracking was marked and thoroughly documented through photographs and crack width measurements (as described within Chapter 3). The crack mapping efforts served two purposes: (1) to facilitate the identification of load-induced cracking and (2) to provide insight into the magnitude and directionality of the ASR/DEF-induced damage. While the severity of the damage was qualitatively assessed in Chapter 3, a brief comparison of the cracking patterns, as shown in Figure 4-1, will assist efforts to interpret the test results presented within Section 4.3.

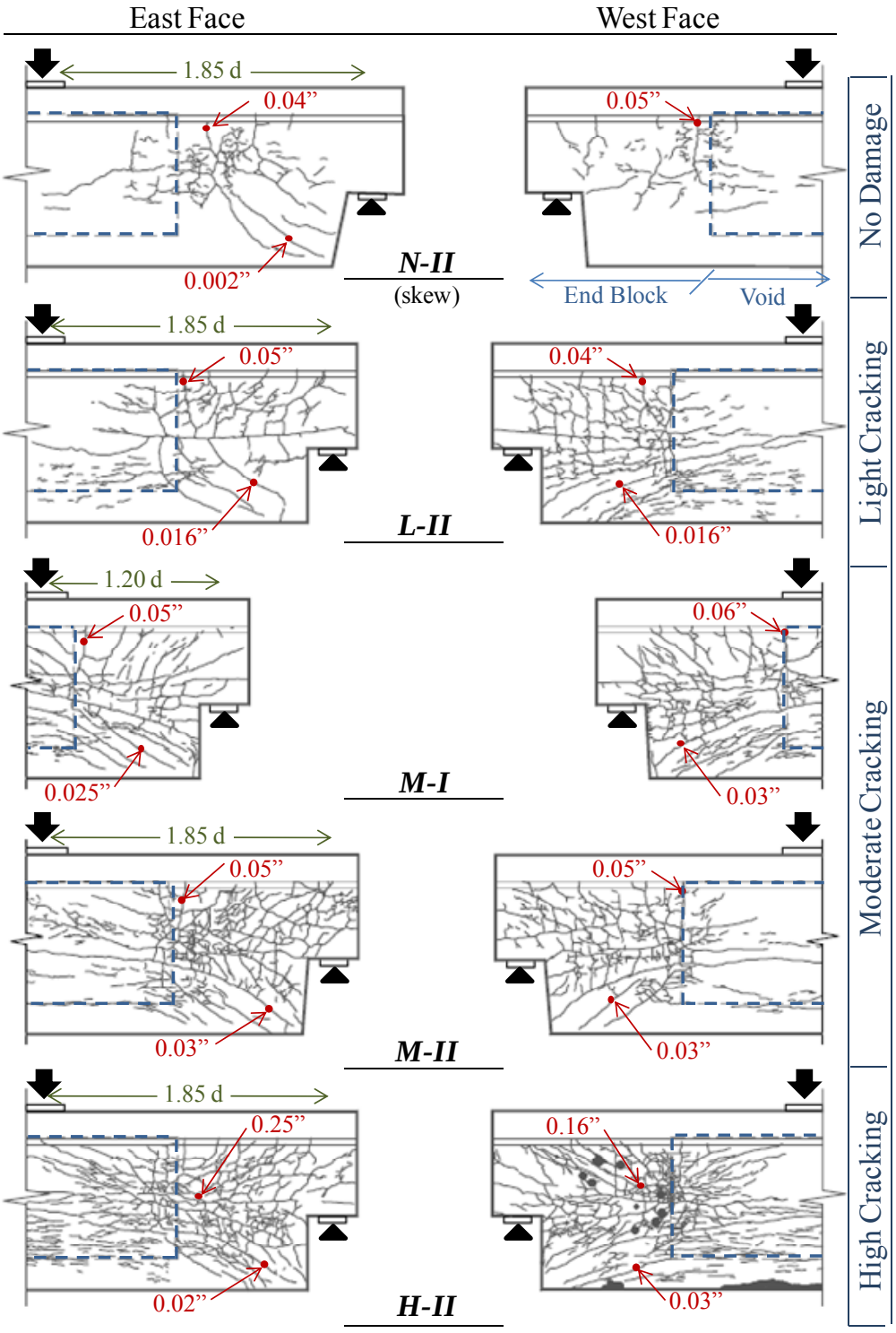

Figure 4-1: ASR/DEF-Related Damage to Dapped Ends

The five dapped ends were either undamaged (segment N-II) or subject to light (L-II), moderate (M-I, M-II) or heavy (H-II) cracking. Variation of the crack widths within a given segment was generally large and ranged from hairline (less than 0.002 inches) to one-quarter of an inch in the most damaged segment (H-II). The most notable cracks within each dapped end were of similar shape and location as those found within the other segments. All of the dapped ends (including "undamaged" N-II) were subject to a large vertical crack (around 0.05 inches in width) at the transition between the end block and hollow beam section. Diagonal cracks (from 0.02 to 0.03 inches in width) radiating from the bottom corner of each dapped end were also a common feature among all the segments (however, N-II had a much smaller crack of 0.002 inches). The length and width of the diagonal cracks along with the overall appearance of the beam were used to gage the overall severity of the ASR/DEF-related damage (refer to Figure 4-1).

The position of the vertical cracks did not coincide with the load path and were not considered relevant to the structural performance. The diagonal cracks, on the other hand, were likely to significantly affect the integrity of the dapped end. These cracks were located in a critical area in which forces from both hanger reinforcement and strand anchorage forces were transferred (as identified in Chapter 2). Close attention was therefore paid to the growth of the diagonal cracks within each of the dapped-end tests.

4.3 STRUCTURAL PERFORMANCE OF DAPPED-END SEGMENTS

The structural performance of each dapped-end segment was characterized through deflection, crack width, strain and load measurements. Results and observations for all five dapped-end tests are presented in this section. The discussion is organized to highlight the structural consequences of ongoing ASR/DEF deterioration. The behavior of "undamaged" segment N-II is presented first and serves as a basis for the evaluation of the results from the deteriorated segments (arranged from light to heavy damage). Critical observations and conclusions with regards to the structural performance of ASR/DEF-affected dapped ends are presented in Section 4.4.

4.3.1 No Significant ASR/DEF-Related Damage (Segment N-II)

Due to the small amount of scattered cracking on the concrete surface, segment N-II was selected to represent the performance of an undamaged dapped-end beam. The segment geometry, reinforcement, and deterioration were thoroughly documented in Chapter 3. Pertinent structural details are repeated here for convenience. Thirty-four of the fifty-eight strands were fully bonded at the end of the test segment which was skewed at approximately 32 degrees. At the time of testing, the concrete strength of the dapped end (obtained through compression testing of cores) was estimated to be 9.3 ksi.

Segment N-II was tested at a shear span of 1.85 times the effective depth. The initial application of load yielded a linear response and little additional cracking. The load-deflection response of the "undamaged" dapped end is shown in Figure 4-2. The shear stress, plotted on the vertical axis, represents all forces resisted by the dapped end, including the weight of the beam and associated testing hardware. The measured deflection at the load point, plotted on the horizontal axis, was adjusted to account for movement at the supports and overall rigid body motion of the segment. For the purposes of comparing the stiffness to the results of the other four dapped-end tests, the shear stress was normalized by the concrete strength and web area. The deflection was also normalized by the full span length, which varied due to the length of the beam and the condition of the cut end. It should be noted that the results from all five dapped-end tests were corrected and normalized as necessary to illustrate key points and observations.

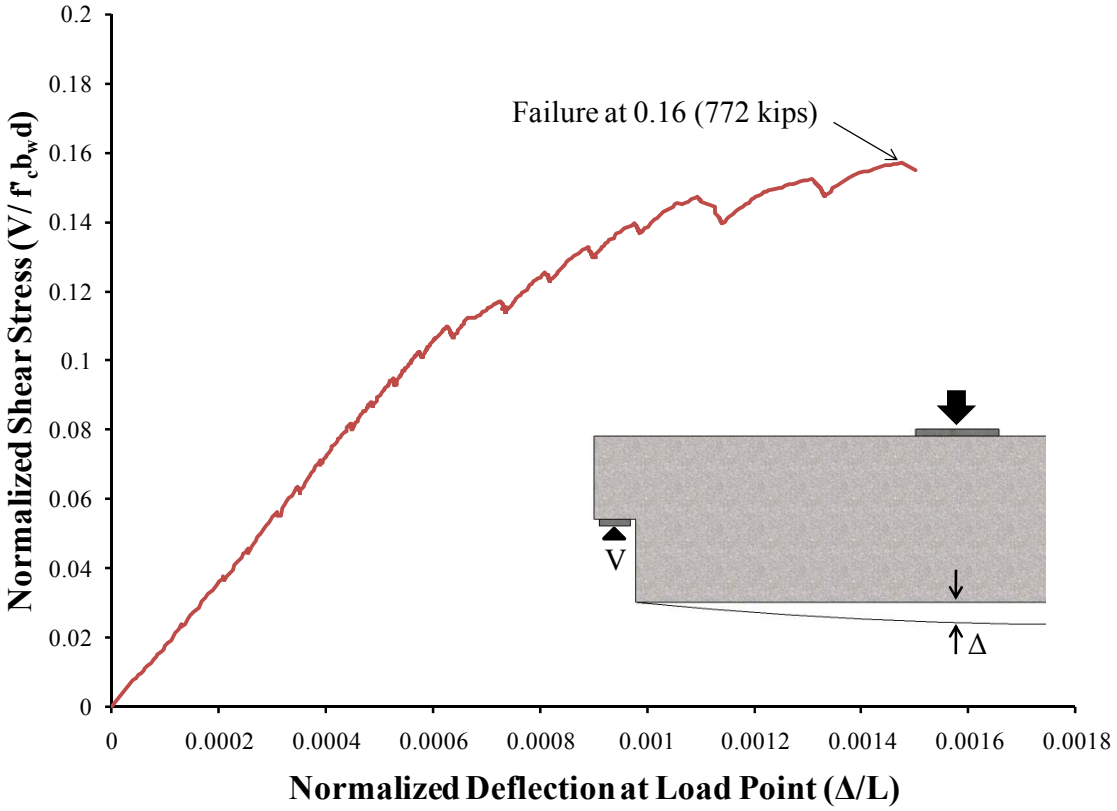

Figure 4-2: Load-Deflection Response of Segment N-II

While slight widening and lengthening of pre-existing ASR/DEF-related cracks was noted early on, it did not appear to degrade the stiffness of the beam in any meaningful way. The first load-induced cracks were visually noted at 57 percent of the maximum applied shear, with the first noticeable change in stiffness occurring shortly thereafter (70 percent). More significant cracking between the load and support did not develop until nearly 90 percent of the maximum applied shear was achieved; progression of the load-induced cracking is illustrated in Figure 4-3. At that point, the diagonal cracking was accompanied by cracks on the end face of the dap. Further application of load extended the crack network and caused sliding of existing crack faces relative to one another. The extensive cracking and translation, in addition to the occurrence of minor spalling in the dap region, were indicative of imminent failure. The maximum shear force experienced by segment N-II was 772 kips.

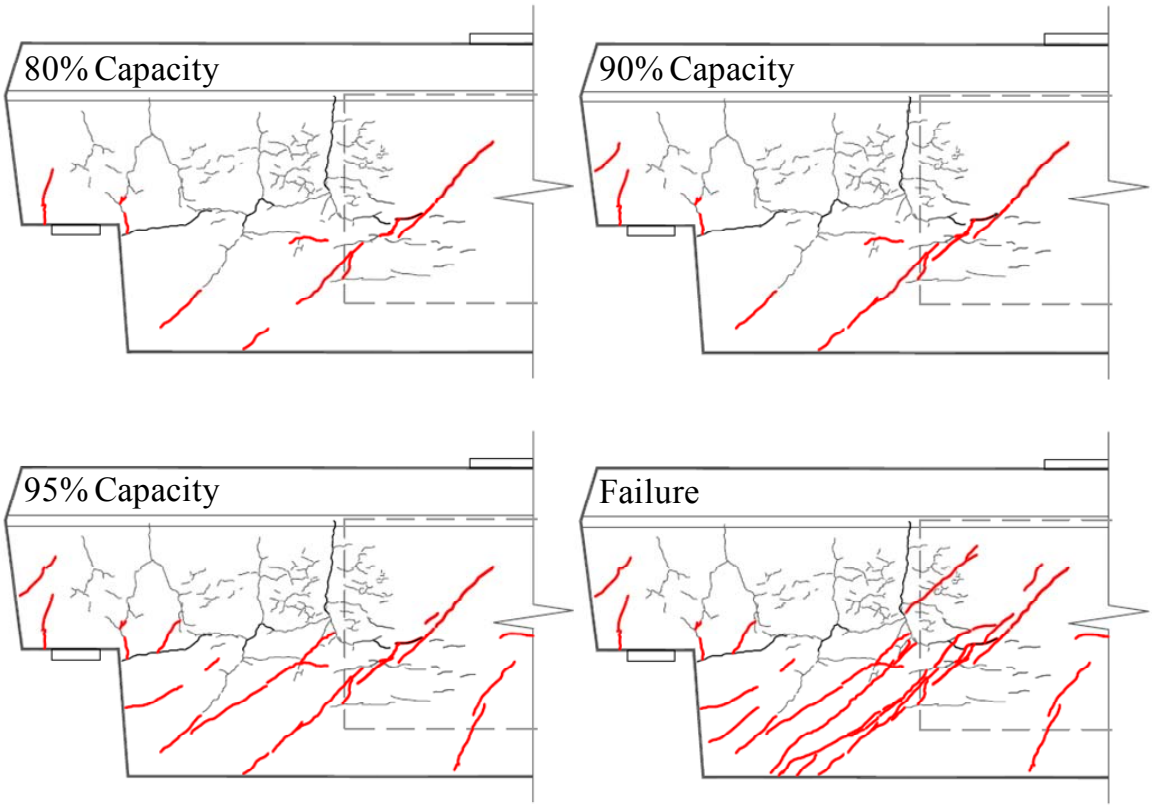

Figure 4-3: Diagonal Cracking on the West Face of Segment N-II

The growth of several cracks was monitored over the course of the test to assist in the identification of the failure mode. A comparison of the initial and final crack widths is presented in Figure 4-4. Significant increases in the crack widths were generally limited to those cracks located in the bottom corner of the dapped end (crack numbers 5, 6, and 7 in Figure 4-4). Growth of the existing cracks was nearly continuous from the start of the test. The diagonal crack (number 5), which emanated from the corner and stopped short of the beam mid-depth, grew to nearly ten times its original size right before failure. Such behavior was uncharacteristic of a shear failure, which generally produces a significantly wide crack along the full length of the primary diagonal strut (here, located between the load and bottom corner).

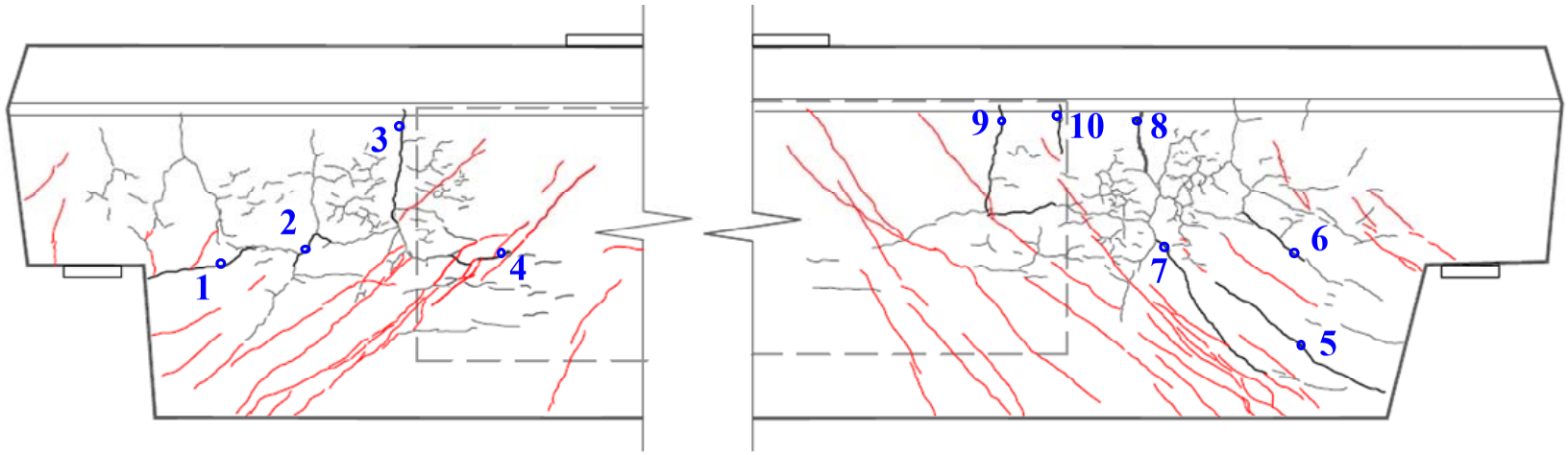

N-II (West Face) N-II (East Face)

Crack	West				East					
	1	2	3	4	5	6	7	8	9	10
Initial	0.002	0.010	0.050	0.002	0.002	0.005	0.020	0.040	0.016	0.020
Final	0.005	0.016	0.050	0.010	0.020	0.010	0.035	0.040	0.020	0.030
Growth	150 %	60%	0%	400%	900%	100%	75%	0%	25%	50%

Figure 4-4: Measured Growth of Primary Cracks in Segment N-II

The magnitudes of the average concrete strains recorded by the surface-mounted linear potentiometers suggest that the deformation was concentrated at the bottom corner of the end block. The average concrete strain measurements for segment N-II are summarized in Figure 4-5. They are plotted against the percentage of the maximum applied shear to simplify future comparisons. The maximum average concrete strain measured at either the dap or the web section was on the order of 1.5 millistrain; insufficient to initiate the yielding of the transverse reinforcement necessary to precipitate a shear failure. Tension testing of transverse reinforcement samples indicated that yielding would correspond to a deformation of 2.4 millistrain (on average, discussed in Chapter 3). Furthermore, the lack of post-failure strain growth implies that the cracking found within the reentrant corner and void regions was not associated with the loss of load-carrying capacity.

With regards to the overall nature of the concrete strains, the diagonal measurements at the dap and void region generally proved to be the most sensitive to the application of load. This is consistent with formation of cracks at the reentrant corner and along the primary strut; both nearly perpendicular to the diagonal gage lengths.

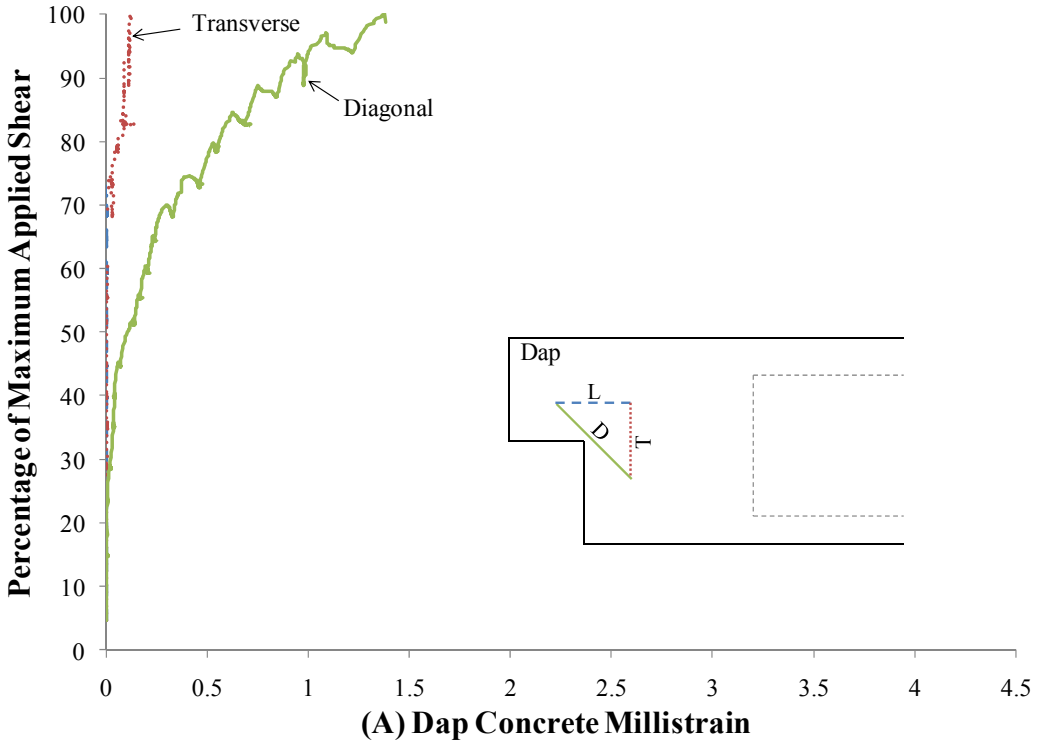

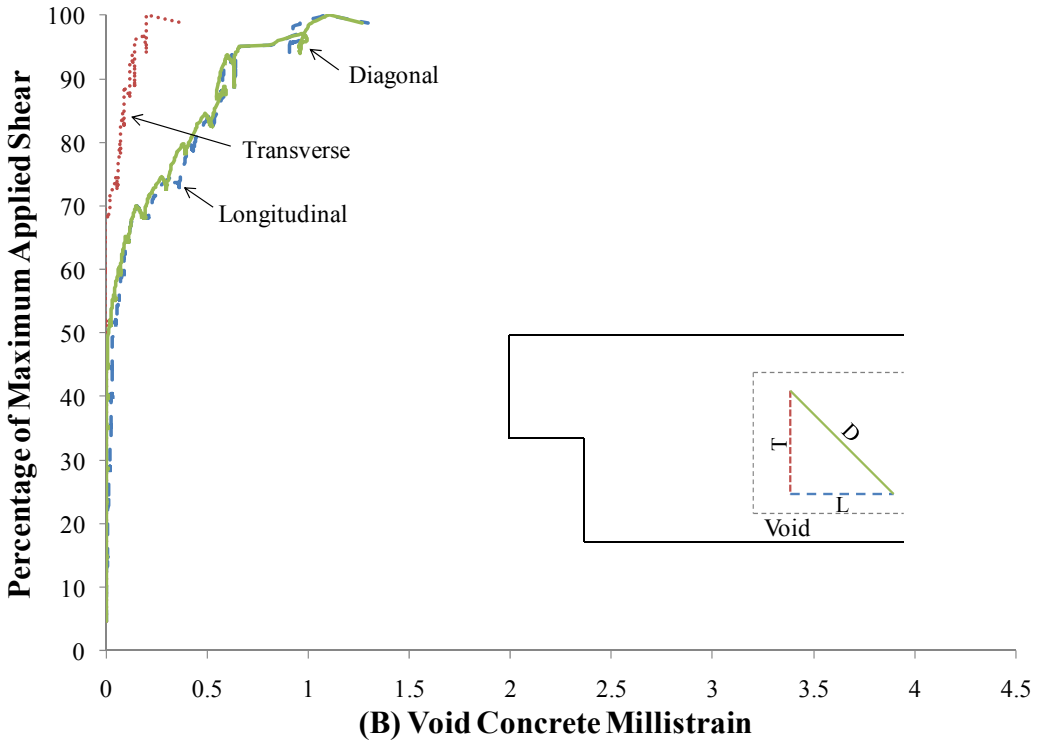

Figure 4-5: Average Concrete Strain History for Segment N-II

Closer examination of the load-induced cracking revealed wide cracks which ran along the bottom side of the beam (see Figure 4-6). The nature of the cracking suggested that the tie anchoring the lower end of the diagonal strut was no longer capable of maintaining equilibrium. Due to the limited length available for anchorage of the flexural reinforcement, this explanation was most logical. The failure mechanism was therefore classified as a shear-induced anchorage failure.

Figure 4-6: Post-Failure Cracking in Segment N-II

The structural performance of N-II did not appear to be significantly compromised by the limited deterioration noted in Figure 4-1. The development of a diagonal crack was independent of any existing cracking and provided sufficient warning of failure. The shear-induced anchorage failure was clearly defined by sound of strands slipping and a drop in the applied load, resulting in an ultimate shear capacity of 772 kips.

4.3.2 Light to Heavy ASR/DEF-Related Damage (L-II, M-I, M-II, and H-II)

The four damaged segments tested within this study were selected to demonstrate the time-dependent effects of ASR/DEF deterioration on the structural performance and strength of trapezoidal box beams with dapped ends. The first three segments (L-II, M-I, and M-II) represented the early to intermediate stages of deterioration. They were subject to extensive, random cracking as well as a few discrete diagonal cracks which emanated from the bottom corner of the dap (within the prestress transfer length). The fourth segment (H-II) represented the severe stage of deterioration among the beams. While it generally shared the abovementioned damage characteristics, the largest cracks were several orders of magnitude wider than those found in the other segments. The overall maximum crack width ranged from 0.016 inches in segment L-II to 0.25 inches in segment H-II. The width of the discrete diagonal cracks, previously identified as the most deleterious aspect of the deterioration in Section 4.2, varied from 0.016 to 0.030 inches.

All four of the segments featured sixty-two prestressing strands; thirty-eight of which were bonded over the full length. With the exception of segment H-II, no substantial ASR/DEF-related loss of concrete strength was evident from core tests. The concrete strength, of segments L-II, M-I, and M-II ranged from 8.6 to 11.8 ksi and exceeded the required design strength. Cores extracted from segment H-II yielded a compressive strength of 6.4 ksi at the time of testing; well below the seven-day strength of 8.3 ksi. While the loss of compressive strength does not necessarily indicate a loss of structural capacity, the low values obtained from the cores were further evidence of the severe deterioration found within that segment and the difficulty in extracting cores that were not near visible cracks.

M-I was the first ASR/DEF-damaged dapped end to be tested. The initial objective of the study was to evaluate the capacity of the dap (i.e. the shallow beam extension) as controlled by direct or diagonal shear through the reentrant corner. The original intent was to study the performance of the dap only. M-I was therefore tested at a relatively short shear span-to-depth ratio of 1.2 to maximize demand on the extended

portion of the beam end. The load-deflection response of segment M-I is plotted along with the results of the other damaged segments in Figure 4-7. The linear-elastic response of the segment is markedly stiffer than the other damaged segments due to the shorter shear span-to-depth ratio. Degradation of the beam stiffness due to the growth and development of cracking was not apparent until the load exceeded 80 percent of the maximum applied shear. Audible strand slip and rapid crack growth at the bottom corner of the dapped end signaled the unexpected: shear-induced anchorage failure at a maximum applied shear of 912 kips.

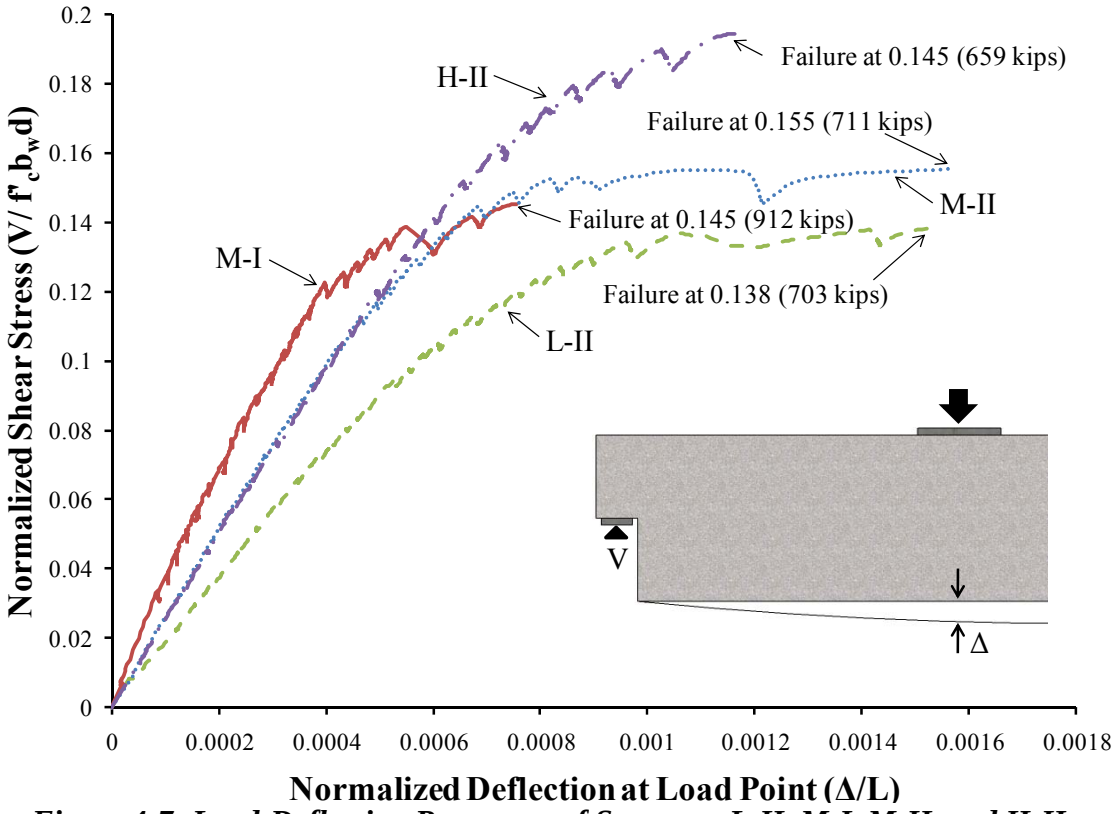

Figure 4-7: Load-Deflection Responses of Segments L-II, M-I, M-II, and H-II

The results of the load test on segment M-I clearly indicated that the flexural reinforcement anchorage at the bottom corner was the controlling aspect of the dapped-end design. To properly assess the effects of ASR/DEF deterioration on the anchorage detail, the remaining three segments (L-II, M-II, and H-II) were tested at a shear span-to-depth ration of 1.85. Examined independently, the load-deflection behavior of each

damaged segment was not markedly different than the others. The linear-elastic response generally softened between 70 and 80 percent of the maximum applied shear as a result of preexisting crack growth and new crack development. Examined collectively, however, a trend between the dapped-end stiffness and level of cracking emerges. As depicted in Figure 4-7, the stiffness of the distressed dapped ends appears to increase as a function of the damage severity. It is likely that restraint of the ASR/DEF-related expansions by the dapped-end reinforcement led to the development of compression within the structural core concrete; eliciting a stiffer material response. ASR/DEF-induced compression has been shown to be capable of offsetting (and superseding) the loss of mechanical strength or stiffness due to the microstructural cracking (Deschenes et al., 2009).

The presence of ASR/DEF-induced compression also provides a logical explanation for the observed delay of first cracking in the damaged segments. The development of load-induced cracking for the segments subjected to light (L-II) and heavy (H-II) cracking are shown in Figure 4-8. The illustrations effectively cover the full range of behavior noted during the damaged segment tests. The behavior of segment L-II was similar to the undamaged segment N-II. First cracking was noted to occur at a slightly higher percentage of the capacity (67 percent), but an extensive crack network was nonetheless present prior to failure. The behavior of H-II (subject to 0.25-inch wide cracks) was drastically different. Substantial cracking did not develop at any point in the dapped-end test; including failure (refer to Figure 4-8). The only notable crack on either face of segment H-II (shown in Figure 4-13) corresponded to a preexisting ASR/DEF crack; impending failure was not apparent. Segments M-I and M-II were intermediate cases of the abovementioned behavior. Overall, the results suggest that either greater ASR/DEF-related damage led to the development of higher internal compressive stresses which further delayed the formation of load-induced cracking or that there was no need for more cracks to form is extensive cracking already existed.

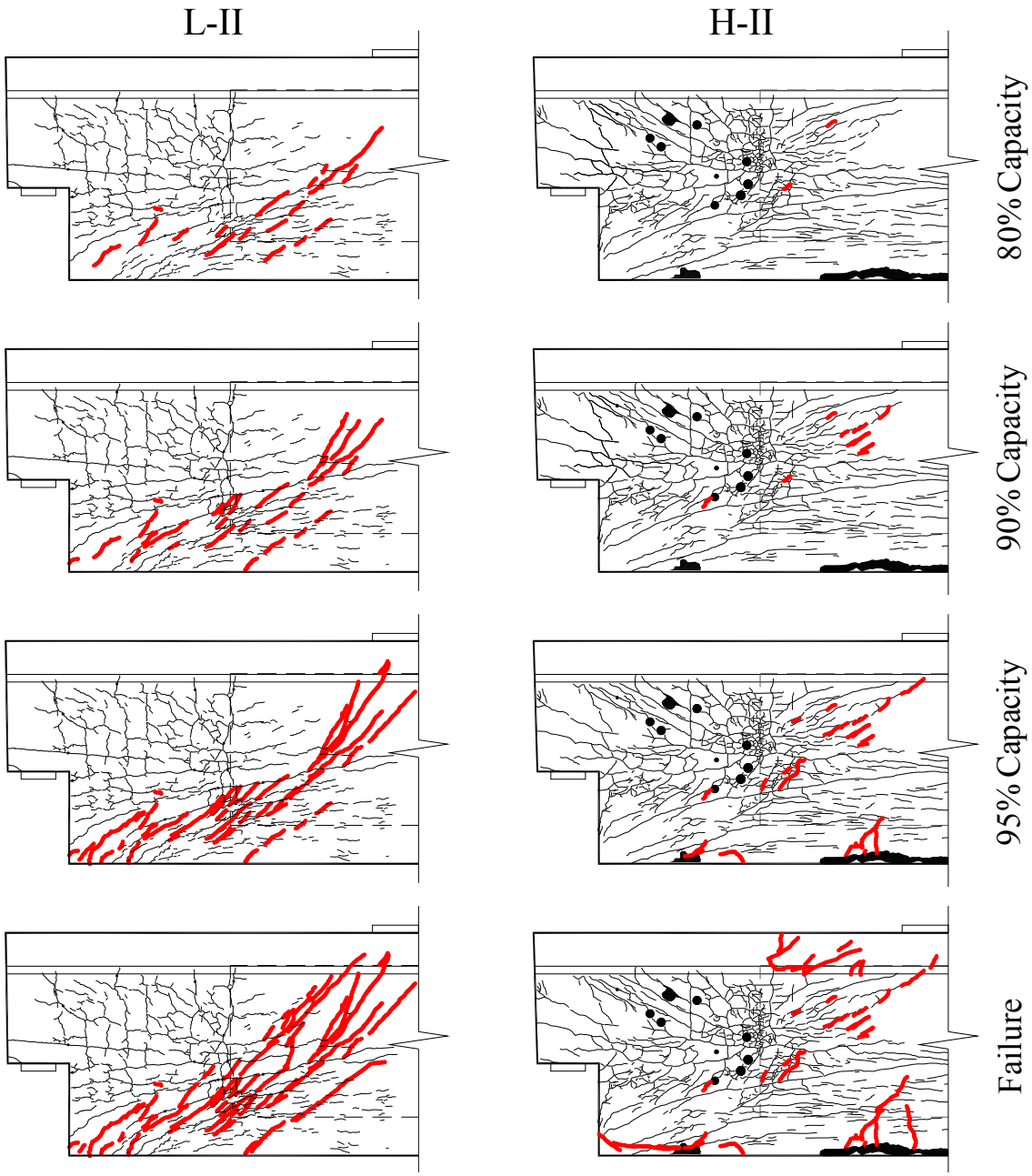

Figure 4-8: Diagonal Cracking on the West Faces of Segments L-II and H-II

Measurements of the concrete deformation (e.g. strains and crack widths) provided further insight into the mechanics of the ASR/DEF-affected dapped ends. As in N-II, the diagonal measurements at the dap and web section for L-II through H-II were the most sensitive to the application of load. Therefore, the less sensitive longitudinal and

transverse strain measurements were not presented. This consideration simplified examination of the results and facilitates the identification of meaningful trends.

The concrete strain response at the dap and void of each damaged beam are plotted in Figure 4-9. The most notable feature of these plots is the especially stiff response of the damaged daps. The maximum deformation measured at the diagonal of the undamaged dap was nearly 1.5 millistrain. In contrast, the deformation of each damaged dap was surprisingly stiff and yielded no more than 0.5 millistrain by the onset of failure. The results suggest that the demands placed on the dap were insufficient to overcome the ASR/DEF-induced compression. Decompression does not seem to occur as few if any new cracks were noted at the dap of the damaged segments (refer to Figure 4-10 through Figure 4-13). Furthermore, the relatively stiff response of each damaged dap most likely contributed to the overall increase in the segment stiffness.

The concrete strain response of each damaged web was not significantly different than that measured during the undamaged segment test. Among the damaged segments, there were no meaningful differences or trends noted with regards to the initiation, stiffness or magnitude of the responses. Due to the average nature of the measurement and the variability of ASR/DEF-related expansions, it is unreasonable to expect clear indications of the loads corresponding to web decompression and subsequent cracking. Crack width measurements did provide further substantiation of the assumed internal mechanics of the damaged segments. Load testing of the undamaged dapped end (N-II) yielded near continuous growth of select preexisting cracks. Most significantly, the diagonal crack emanating from the bottom corner of the dap (number 5) showed notable growth with only forty percent of the maximum shear applied. In contrast, growth of the largest preexisting crack within segment H-II (¼-inch to begin) only occurred within the last two load increments (i.e. at loads exceeding 80 percent of the maximum applied shear). Furthermore, the relative growth of the ASR/DEF-related cracking within the damaged dapped-ends was generally less than that found in the undamaged segment. The results of the crack width measurements are summarized per segment in Figure 4-10 through Figure 4-13.

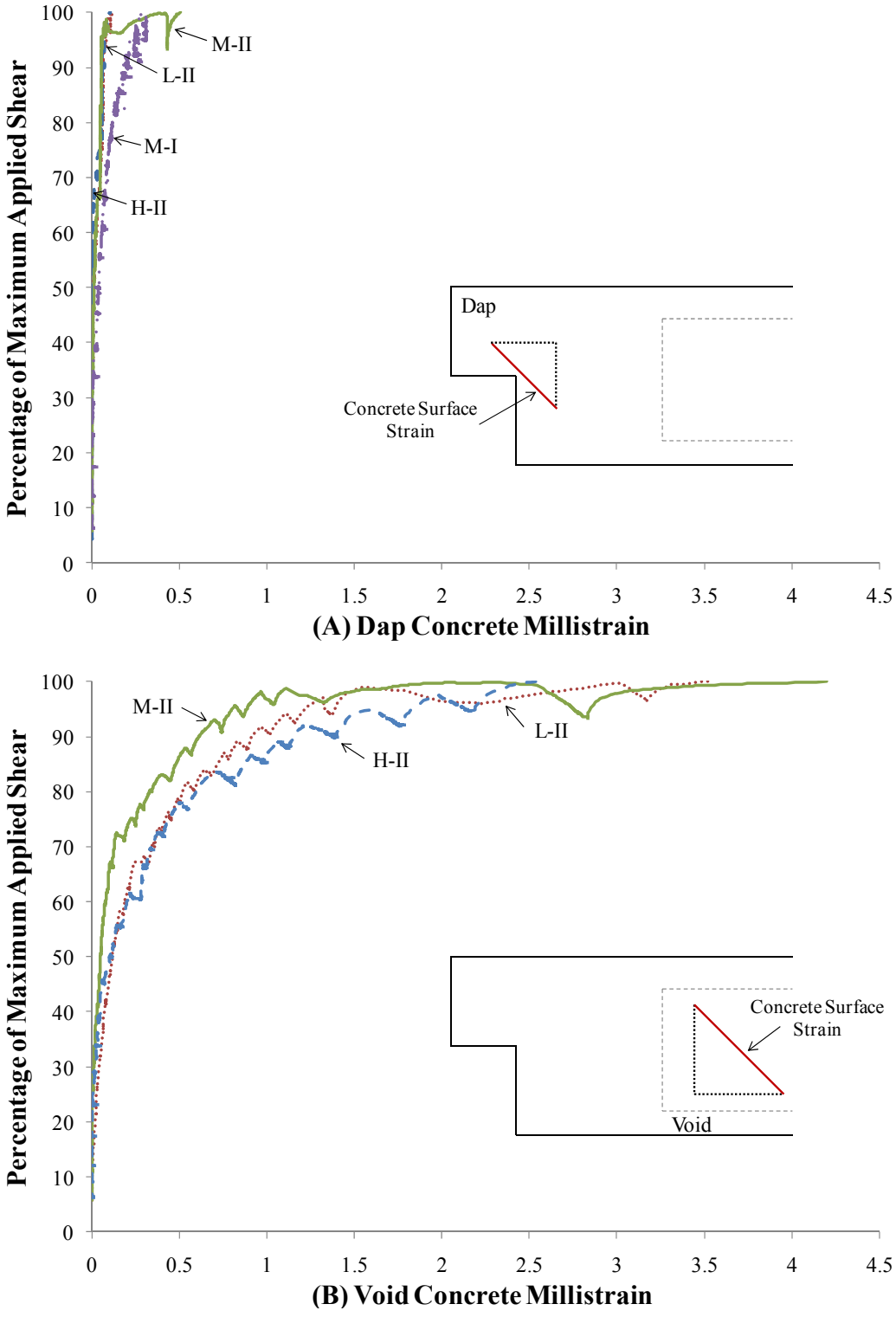

Figure 4-9: Concrete Strain Histories for the ASR/DEF-Damaged Segments

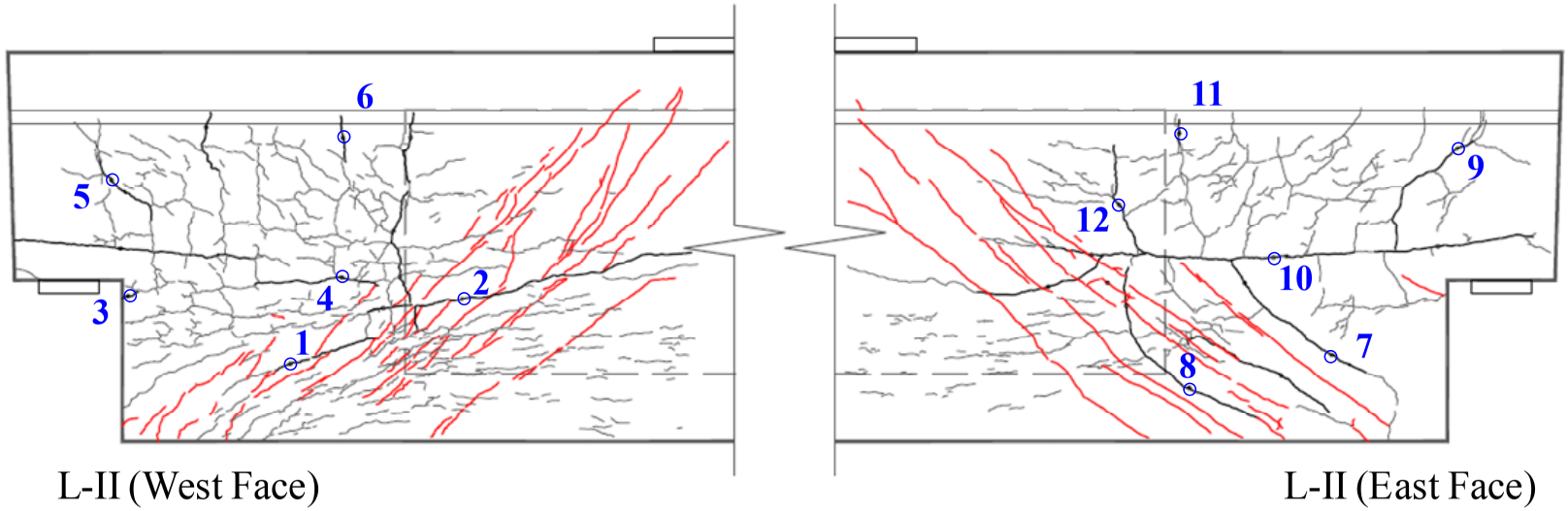

Crack	West						East					
	1	2	3	4	5	6	7	8	9	10	11	12
Initial	0.016	0.013	0.005	0.030	0.025	0.040	0.016	0.013	0.050	0.040	0.050	0.035
Final	0.030	0.020	0.016	0.035	0.025	0.040	0.016	0.013	0.050	0.060	0.050	0.035
Growth	88%	54%	220%	17%	0%	0%	0%	0%	0%	50%	0%	0%

Figure 4-10: Measured Growth of Primary Cracks in Segment L-II

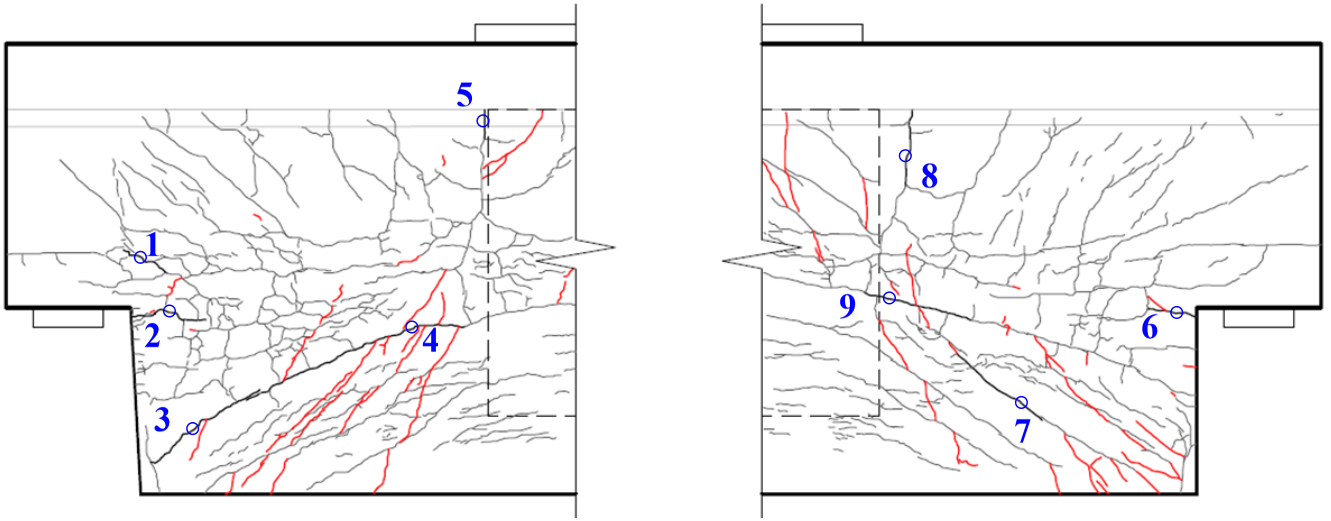

Crack	West					East			
	1	2	3	4	5	6	7	8	9
Initial	0.030	0.013	0.030	0.013	0.060	0.005	0.025	0.050	0.040
Final	0.025	0.016	0.040	0.013	0.060	0.016	0.125	0.050	0.040
Growth	-17%	23%	33%	0%	0%	220%	400%	0%	0%

Figure 4-11: Measured Growth of Primary Cracks in Segment M-I

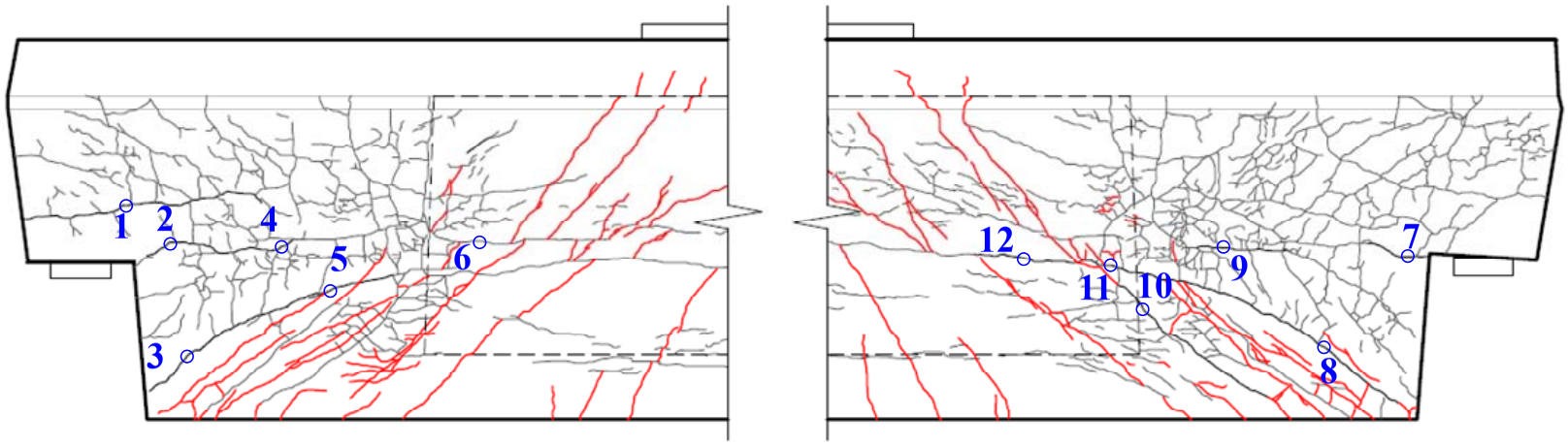

Crack	West						East					
	1	2	3	4	5	6	7	8	9	10	11	12
Initial	0.030	0.025	0.030	0.060	0.035	0.030	0.016	0.030	0.035	0.050	0.020	0.040
Final	0.030	0.025	0.050	0.060	0.060	0.035	0.020	0.080	0.035	0.040	0.125	0.050
Growth	0%	0%	67%	0%	71%	17%	25%	167%	0%	-20%	525%	25%

Figure 4-12: Measured Growth of Primary Cracks in Segment M-II

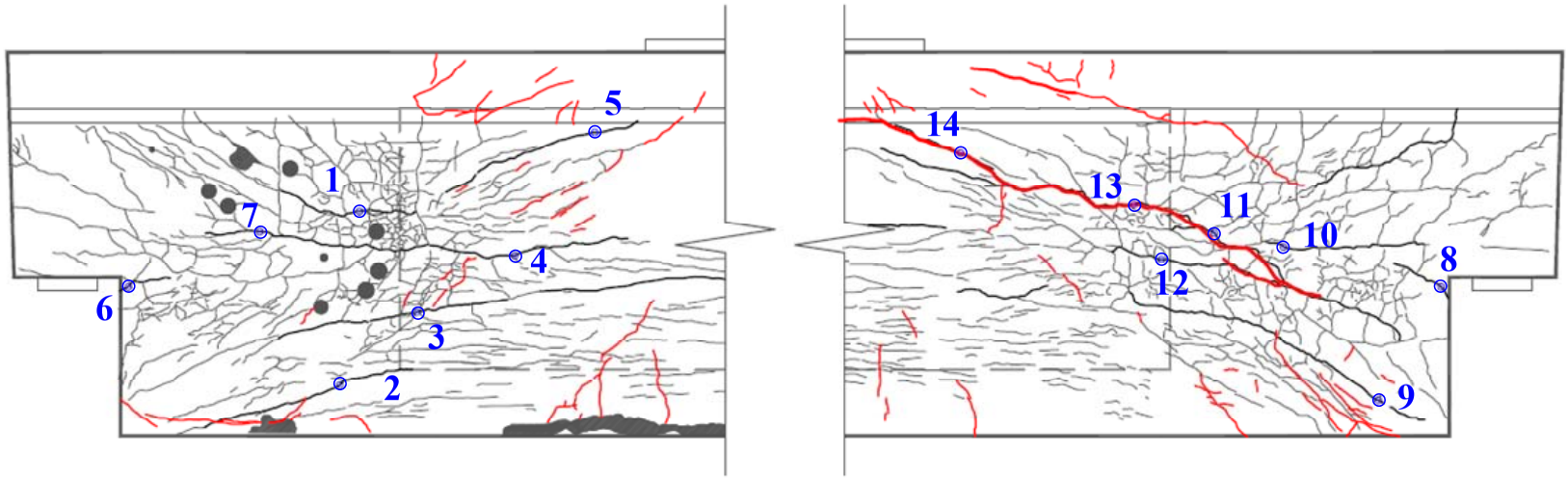

Cracks	West							East						
	1	2	3	4	5	6	7	8	9	10	11	12	13	14
Initial	0.164	0.030	0.025	0.050	0.030	0.010	0.060	0.020	0.020	0.040	0.262	0.060	0.098	0.025
Final	0.230	0.050	0.040	0.060	0.040	0.016	0.060	0.030	0.025	0.060	0.787	0.060	0.131	0.060
Growth	40%	67%	60%	20%	33%	60%	0%	50%	25%	50%	200%	0%	34%	140%

Figure 4-13: Measured Growth of Primary Cracks in Segment H-II

Loading of segments L-II, M-II, and H-II at a shear span equal to 1.85 times the effective depth resulted in similar, but more critical, shear-induced anchorage failures. In general, diagonal cracks (preexisting and load-induced) extended into and opened within the transfer length of the prestressing strands (Figure 4-14A). Subsequent extension of the diagonal cracks across the bottom side of the box beam (Figure 4-14B) was accompanied by minor spalling in several of the beams. A loud pop signified significant slip of the prestressing strands and a drastic loss of load-carrying capacity. In most cases, the shear-induced anchorage failure was followed by growth of pre-existing ASR/DEF cracks. The heavily cracked segment (H-II) produced the most sudden, pronounced failure of the damaged dapped ends (shown in Figure 4-14C). Pre-existing ASR/DEF cracks connected between the load and bottom corner of the beam, forming a large, continuous crack that widened extensively and extended into the deck under the hydraulic rams and under the beam in the strand anchorage area. The maximum applied shear resisted by H-II was 659 kips. The light (L-II) and moderately (M-II) damaged segments failed at 711 and 703 kips, respectively.

(A) Diagonal Cracking within Transfer Length

(B) Bottom-Side Anchorage Cracks

(C) Post-Failure Growth of ASR/DEF Cracks

Figure 4-14: Typical Features of Damaged Segment Failure

4.4 NOTABLE EFFECTS OF ASR/DEF ON DAPPED-END PERFORMANCE

Preliminary comparisons between the undamaged (Section 4.3.1) and damaged segment behavior (Section 4.3.2) identified a number of interesting trends related to the severity of the ASR/DEF deterioration. Those trends are reexamined here to identify the most notable serviceability and strength implications of the ASR/DEF deterioration encountered within this study. Please note that segment M-I is excluded from the majority of this discussion due to the difference in the shear span-to-depth ratio.

4.4.1 Serviceability

As traditionally defined, serviceability relates to the ability to control excessive deflections and undesirable cracking under service loads. Such considerations may not be of primary concern to the bridge owner due to the severe cracking and inherent stiffness already exhibited by the damaged dapped ends. The observations made with regards to serviceability nonetheless provide valuable evidence of the internal mechanics of an ASR/DEF-affected structure and are therefore presented here.

The serviceability characteristics of the damaged dapped ends generally support the assertion made by Deschenes et al. (2009): the expansion-induced compressive stresses within an ASR/DEF-affected member can effectively offset (and potentially supersede) the structural effects of reduced plain concrete strength and stiffness. Based on the cores tested in the current study, the heavily cracked segment (H-II) was subject to the greatest loss of concrete compressive strength and stiffness (assuming traditional relationships between strength and stiffness hold true). In spite of this deficiency, segment H-II yielded the stiffest response of the four dapped ends (shown in Figure 4-15). The stiffness of each dapped end fits well within this trend, with the lightest damage corresponding to the least stiff response and vice-versa.

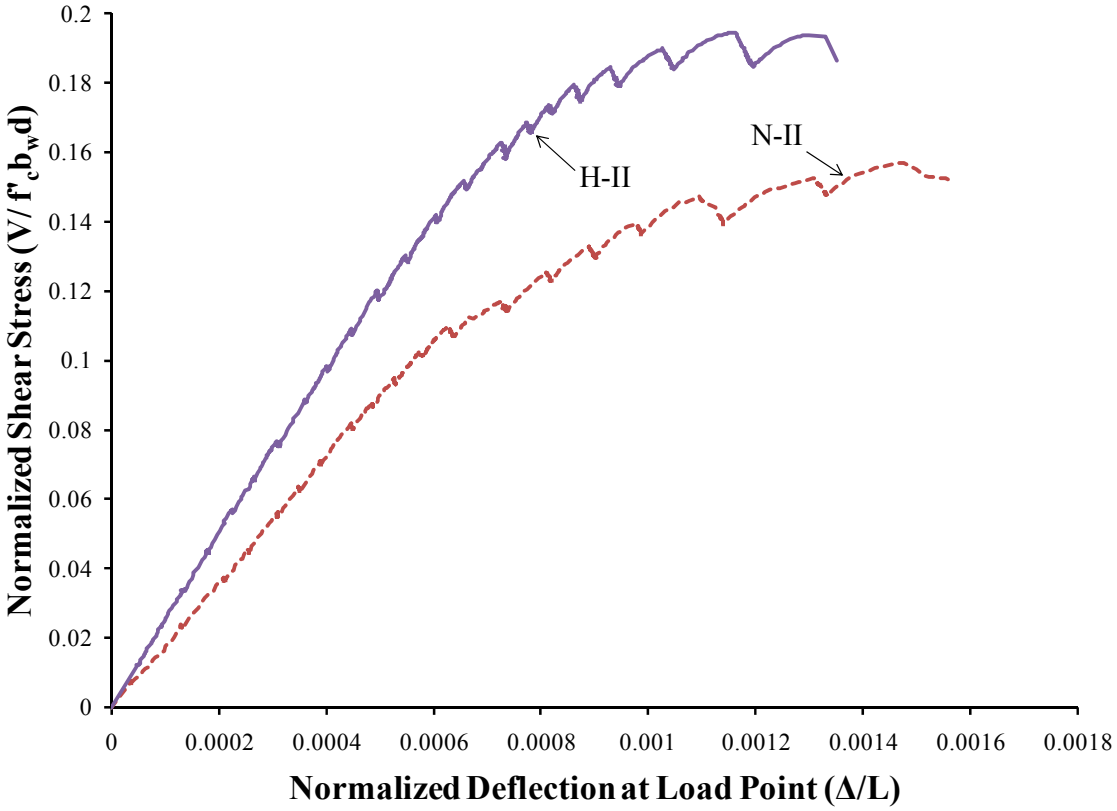

Figure 4-15: Observed ASR/DEF-Related Increase in Dapped-End Stiffness

The cracking behavior of the dapped ends further substantiated the implied effects of ASR/DEF-induced compression. The percentage of the maximum applied shear corresponding to the formation of a new crack is plotted against the severity of the deterioration in Figure 4-16. The results clearly indicate that the first cracking (newly formed diagonal crack) load increased as a function of the deterioration. More importantly, the trend suggests that the ASR/DEF-induced compression (responsible for the delay in cracking) is proportional to the severity of the deterioration. It is also interesting to note that the assigned levels of cracking correspond well with the levels of deterioration implied by the first cracking loads.

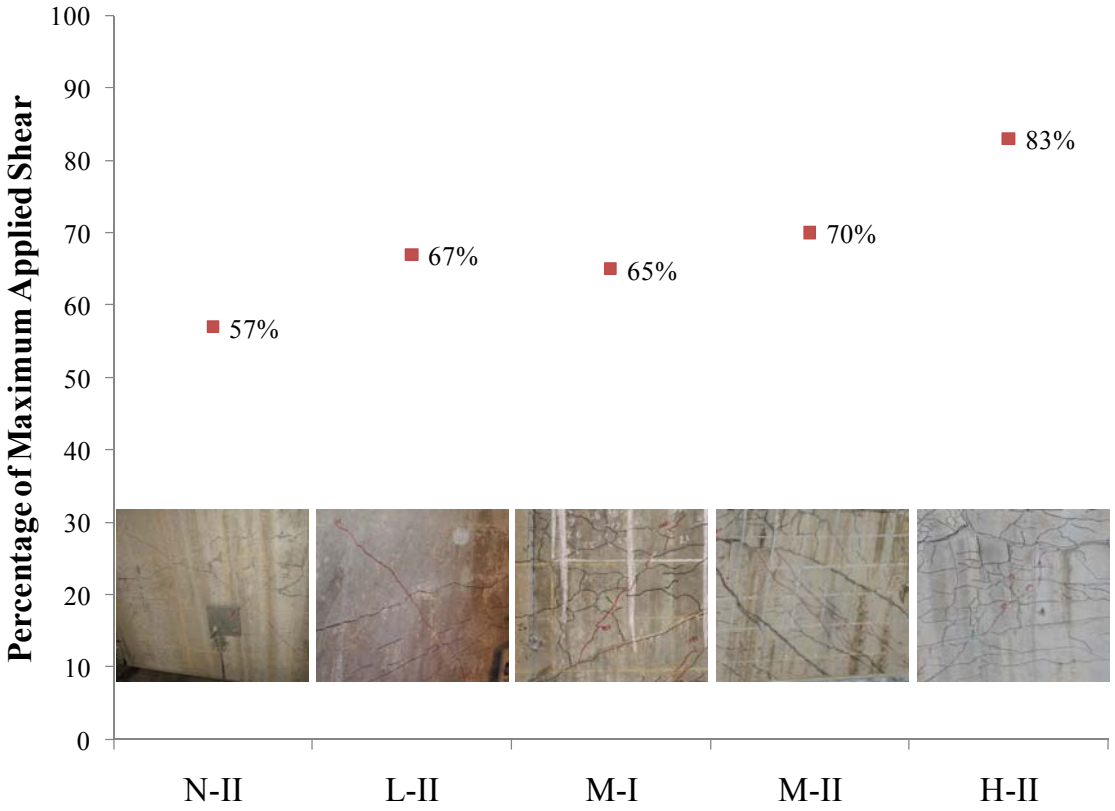

Figure 4-16: Observed ASR/DEF-Related Increase in First Cracking Load

Based on the former observations and the work of Deschenes et al. (2009), it is clear that the accumulation of ASR/DEF damage within a concrete member generates significant tensile strains and stresses in the reinforcement. That reinforcement stress is in turn equilibrated by a commensurate amount of compression in the concrete. Barring the loss of the confining reinforcement (perhaps through rebar fracture, see Chapter 2), the compression induced within the concrete will be capable of compensating for the microstructural damage done by the ASR/DEF-related expansion.

Presentation of these results is not intended to suggest that the presence of ASR/DEF is beneficial to the structural performance of a concrete member. Rather it is intended to shed light on the common misconceptions associated with the structural effects of ASR/DEF deterioration. Specifically, it is of critical importance to recognize that the outward appearance of a reinforced or prestressed concrete member affected by

ASR/DEF is not immediately indicative of a loss of structural stiffness or strength. In this unique case, surface cracking does not necessarily imply tension in the structural core (as traditionally assumed).

4.4.2 Strength

Load testing of segment M-I revealed the governing aspect of the dapped-end design used in the US 59 trapezoidal box beams: anchorage of the mild and prestressed flexural reinforcement. Following that revelation, the focus of the project shifted from evaluating the shear strength of the dap to evaluating the dapped-end strength as a whole. The maximum shear applied to each dapped end is summarized in Table 4-1 and Figure 4-17. Please note that direct comparisons to the strength of segment M-I are invalid due to the short shear span testing arrangement.

Table 4-1: Failure Loads

Beam	Shear Span to Depth Ratio	Concrete Strength (f'_c)	Failure Shear
N-II	1.85	9.28 ksi	772 kips
L-II	1.85	9.59 ksi	703 kips
M-I	1.20	11.84 ksi	912 kips
M-II	1.85	8.63 ksi	711 kips
H-II	1.85	6.39 ksi	659 kips

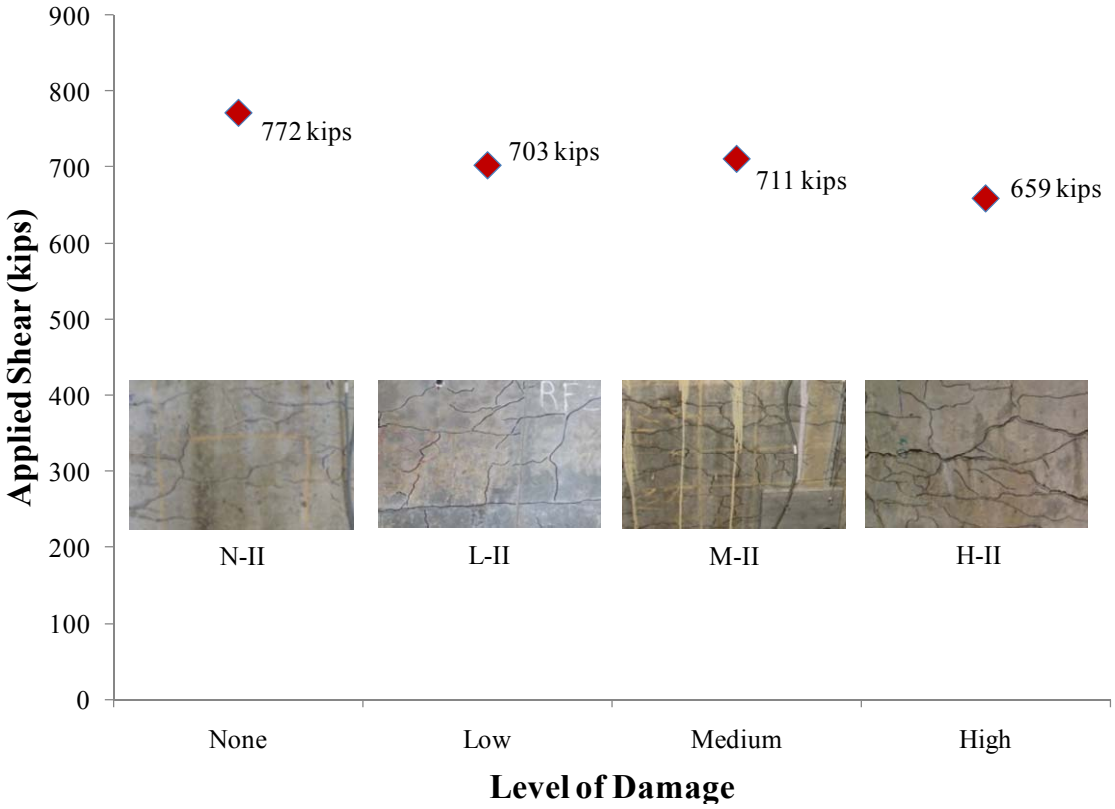

Figure 4-17: ASR/DEF-Related Capacity Trend

As shown, the results suggest a loss of dapped-end capacity with increasing deterioration. While this observation is significant, it is important to realize that the measured capacities do not give any indication of the performance of the beam in a structure. Only comparisons to valid strut-and-tie models can provide meaningful answers in that regard.

4.5 DAPPED-END CAPACITY ESTIMATED BY STRUT-AND-TIE MODELS

In this study, the capacity margin is defined as the ability of the dapped end to exceed the structural capacity estimated by applicable design provisions. It is important to consider that variation of the material properties, debonding schedules, and effective prestress forces among the trapezoidal box beam segments could have factored into the trend observed in the previous Section 4.4.2. Strut-and-tie modeling was therefore

applied to determine the nominal capacity of each dapped end and allow proper evaluation of the capacity margin. The contemporary design provisions outlined in Chapter 2 (ACI 318-08, AASHTO LRFD 2009, and TxDOT Project 0-5253 provisions) were all implemented as part of this effort. To reveal the ASR/DEF-related change in the capacity margin, the ratios of the measured-to-calculated capacities are examined within the context of the qualitative ASR/DEF damage levels.

4.5.1 Development of the Strut-and-Tie Models

Evaluation of the five dapped ends required the development of two different strut-and-tie models, one for each testing arrangement. The strut-and-tie model corresponding to shear span-to-depth ratios of 1.85 and 1.2 are shown in Figure 4-18A and Figure 4-18B, respectively. The struts are represented as dashed red lines and the ties as solid blue lines. Nodes are located at the intersections of multiple struts and ties. The general layout of each strut-and-tie model was based upon the dapped-end models presented in Chapter 2. The shear span-to-depth ratio, reinforcement layout, and bearing plate dimensions unique to each box beam segment were then used to determine the final model geometries. All of the models were in accordance with the basic theories of plasticity and requirements of the various strut-and-tie modeling procedures.

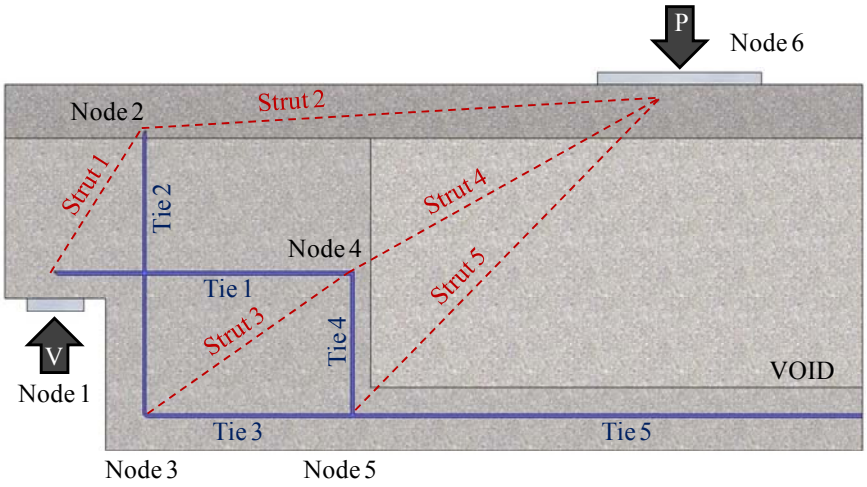

(A) STM for Segments N-II, L-II, M-II, and N-II

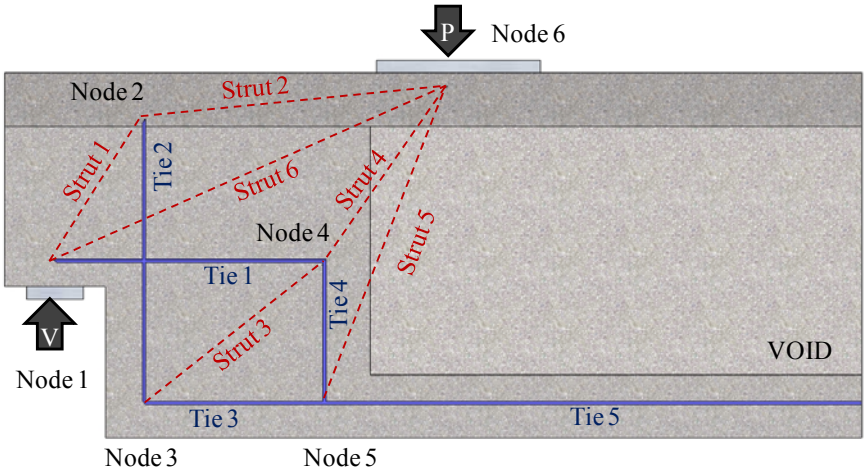

(B) STM for Segment M-I

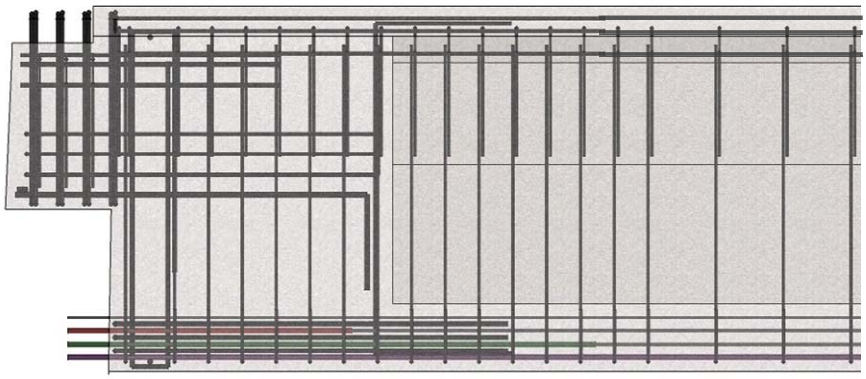

(C) Typical Dapped End Reinforcement Layout

Figure 4-18: Strut and Tie Models

The strut-and-tie models corresponding to segments N-II, L-II, M-II, and H-II were nearly identical to one another (basic layout shown in Figure 4-18A). Slight variations in the strand debonding pattern and compressive strength necessitated minor adjustments of the tie positions and node proportions. For the sake of clarity, the rationale for the placement and proportioning of each element within the first strut-and-tie model is presented below. All struts, ties and nodes are identified within Figure 4-18A.

The size and location of Node 1 was determined by the support plate geometry and the centroid of the dap flexural reinforcement (Tie 1). The horizontal centroid and vertical point of anchorage for the hanger reinforcement (Tie 2) controlled the placement of Node 2. Node 3 was positioned at the alternate end of the hanger reinforcement and aligned with the vertical centroid of the primary flexural reinforcement (mild and prestressed; Tie 3). The location of Node 4 was determined by the intersection of the flexural dap reinforcement and the vertical reinforcement at the face of the void (Tie 4). Node 5 was positioned directly below Node 4 at the vertical centroid of the primary flexural reinforcement (Ties 3 and 5). Finally, the size and location of Node 6 was determined by the load plate geometry and the depth of the compressive stress block at failure (obtained through analysis).

A separate strut-and-tie model was developed for segment M-I to account for the alternate load paths developed within the shorter shear span (shown in Figure 4-18B). The addition of Strut 6 allowed a portion of the load to flow directly from the load point to the support and limited the demand on the transverse reinforcement within the end block. As discussed in the following section, the ultimate strength of the model was thereby controlled by the anchorage of Tie 3; consistent within the test observations. Aside from the general model layout, placement and proportioning of the strut-and-tie elements for the second model was accomplished in the manner described above.

4.5.2 Capacities Estimated by the Strut-and-Tie Models

The capacity of each dapped end was calculated according to the strut-and-tie provisions of ACI 318-08, AASHTO LRFD 2009, and TxDOT Project 0-5253. To begin,

the material properties listed in Chapter 3 were used to determine the strength of each STM element (i.e. a strut, node, or tie). All of the elements were analyzed within the context of the model geometry and overall balance of forces. This included the effects of prestressing, shown in Figure 4-18 as the superposition of anchorage forces at Nodes 3 and 5. Use of a structural analysis program facilitated calculation of the maximum load corresponding to the failure of each STM element. For the sake of brevity, only the strut-and-tie capacity corresponding to the controlling STM element is presented for each box beam segment. Detailed calculations can be found in Appendix C.

Figure 4-19 includes a comparison of the strut-and-tie capacity and maximum applied loads for each of the five tests completed. The governing STM element is listed alongside the results for each dapped-end test in Table 4-2. It should be noted that load and resistance factors were not considered during the STM analyses. The computed strut-and-tie capacities are therefore compared to the measured strength of each dapped end.

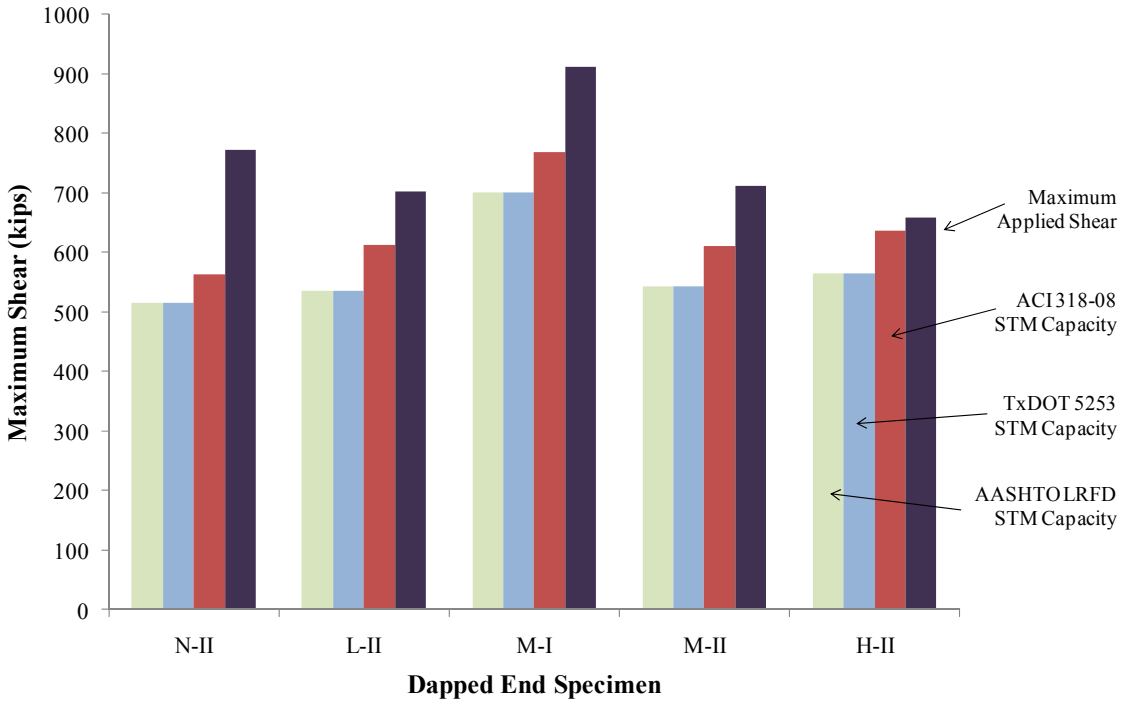

Figure 4-19: STM Capacities and Maximum Applied Loads

Table 4-2: STM Capacities and Maximum Applied Loads

			AASHTO LRFD/ TxDOT 5253			ACI 318-08		
Segment	**Total Applied Shear, V_{max}**	**Concrete Strength, f'_c**	**Capacity, V_{STM}**	**$\frac{V_{max}}{V_{STM}}$**	**Governing Element**	**Capacity, V_{STM}**	**$\frac{V_{max}}{V_{STM}}$**	**Governing Element**
N-II	772 kips	9.28 ksi	515 kips	1.5	Tie 3	563 kips	1.37	Tie 3
L-II	703 kips	9.59 ksi	536 kips	1.31	Tie 3	612 kips	1.15	Tie 3
M-I	912 kips	11.8 ksi	701 kips	1.3	Tie 3	768 kips	1.19	Tie 2
M-II	711 kips	8.63 ksi	542 kips	1.31	Tie 3	611 kips	1.16	Tie 3
H-II	659 kips	6.39 ksi	565 kips	1.17	Tie 3	637 kips	1.03	Tie 3

The analysis results were generally consistent with the failure mechanism observed in all five tests: shear-induced anchorage failure. In fact, the capacity of each strut-and-tie model was governed by failure of Tie 3 (the primary flexural reinforcement at the face of the dap) in all but one case (Tie 2 in M-I).

Application of the ACI 318 provisions to the strut-and-tie model for segment M-I suggested failure via yielding of the hanger reinforcement (Tie 2). The governing of Tie 2 was the result of alternate code approaches to the transfer of prestressing force. As currently presented in ACI 318-08, the calculated transfer length will be consistently shorter than that of AASHTO LRFD for effective prestress greater than 90 ksi (virtually all cases). In the context of the current study, the prestressing force calculated at Node 3 was therefore consistently higher when the ACI provisions were applied. This effectively reduced the demand on Tie 3 and, in the case of segment M-I, caused alternate failure modes to control. Beyond segment M-I, this detail led the ACI strut-and-tie provisions to provide higher capacity estimates for each of the five dapped ends.

It is also interesting to note that the calculated capacities provided by the AASHTO LRFD and TxDOT 5253 provisions were identical in each case. This can be attributed to the fact that the strength of each model was governed by a tension tie. The recommendations made by TxDOT Project 0-5253 were largely limited to revisions of the current AASHTO LRFD treatment of struts and nodes. Recommendations to the capacity of ties or the effects of prestressing were not made.

Irrespective of the differences between the methods, all three strut-and-tie modeling provisions provided conservative estimates of the dapped-end capacity (as summarized in Table 4-2). This result suggests that there is no immediate risk of failure in properly designed dapped ends affected by ASR/DEF deterioration of similar severity seen here. It is possible that concerns with diminishing capacity margin may become apparent in the most severe cases of ASR/DEF deterioration in the future. The ratio of the measured-to-calculated capacity for each of the dapped ends is presented in Figure 4-20 to illustrate the concern. Please recall that the dapped-end capacities provided by the AASHTO LRFD and TxDOT Project 0-5253 provisions were equivalent due to their

consistent treatment of the prestressing strand transfer length. Accordingly, the less conservative nature of the ACI transfer length provisions led to consistently higher dapped-end capacity estimates (and lower ratios of measure-to-calculated capacity).

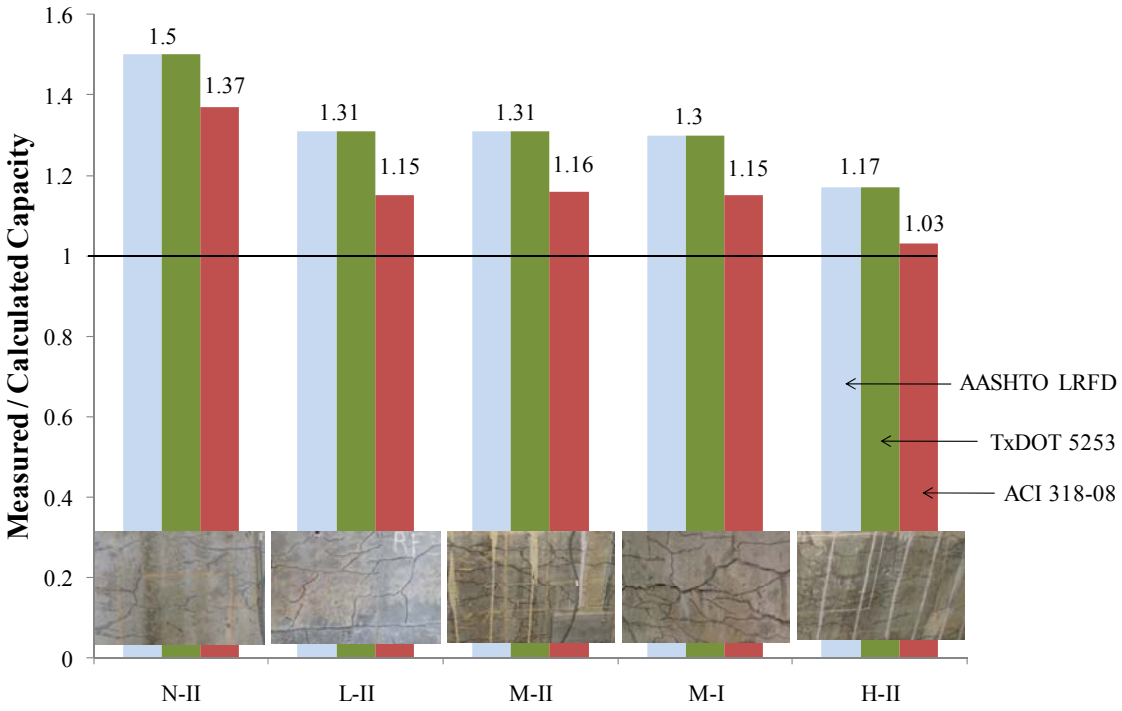

Figure 4-20: Ratio of Measured-to-Calculated Capacity

The ratios of measured-to-calculated capacity equal to, or in excess of, 1.0 are indicative of structurally safe dapped ends. As depicted in Figure 4-20, all five of the ASR/DEF-affected dapped ends were safe with respect to the ACI 318-08, AASHTO LRFD and TxDOT 5253 STM provisions. Despite this encouraging fact, it is clear that the capacity margin decreases with increasing levels of ASR/DEF-related damage.

Relative to the undamaged segment N-II, the strength for segments subject to light or moderate cracking (L-II, M-I, and M-II) was consistently lower with a capacity margin of 30 to 15 percent rather than 50 to 37 percent. Furthermore, the capacity margin of segment H-II, subject to the heaviest cracking, was only 17 to 3 percent in excess of the AASHTO/TxDOT and ACI estimate. It is likely that deterioration in excess of that

found within segment H-II would deplete the available capacity margin of similar dapped ends, rendering them unsafe with respect to current design codes.

4.6 SUMMARY

The results from the dapped-end tests and strut-and-tie analyses offered insights into the serviceability, strength, and safety of the US 59 corridor bridge structures. Crack width measurements, load-deflection plots, and concrete strain histories provided understanding into the internal mechanics of the ASR/DEF-affected beams. An ASR/DEF-related loss of dapped-end strength was initially inferred from comparisons between the severity of the premature concrete deterioration and the measured load-carrying capacity of each beam segment. Further comparisons to the load-carrying capacities estimated by contemporary strut-and-tie modeling provisions ultimately confirmed those observations: the ratio of measured to computed capacity for current dapped-end detail decreases with increasing levels of ASR/DEF-related damage.

The ASR/DEF deterioration had a noticeable effect on the service load behavior of the dapped-end detail. Increasing levels of deterioration generally led to higher dapped-end stiffness and significant delays in the formation of load-induced diagonal cracking. Briefly stated, the serviceability characteristics of the damaged dapped ends generally supported the assertion made by Deschenes et al. (2009): the expansion-induced compressive stresses within an ASR/DEF-affected member can effectively offset (and potentially negate) the structural effects of reduced plain concrete strength and stiffness. The results also highlight the critical nature of the confinement provided by well-anchored reinforcement in ASR/DEF-affected structures. Loss of the confinement (perhaps through fracture, see Chapter 2) would lead to severe implications for the integrity of damaged structures. The dapped-end test of segment M-I revealed that the governing aspect of the US 59 trapezoidal box beam design was the anchorage of the mild and prestressed flexural reinforcement. Once that was established, the remaining four beam segments were tested to examine the effects of light, moderate, and heavy ASR/DEF deterioration on the shear-induced anchorage failure of the dapped ends. Based

on a preliminary analysis of the results, it appeared that premature concrete deterioration progressively weakened the anchorage of the flexural reinforcement in the dapped-end region. The least damaged segment (N-II) supported the highest loads (772 kips of shear), while the most extensively cracked beam (H-II) could only withstand 659 kips of shear. The mildly and moderately damaged segments, L-II and M-II, failed at 703 and 711 kips, respectively.

While the observed loss of dapped-end capacity was significant, it did not give a clear indication of the capacity margin of the deteriorated dapped ends (due to variations between the structural details and material strengths). Strut-and-tie models were therefore developed to provide code-based estimates for the nominal capacities of the trapezoidal box beams with dapped ends. Application of strut-and-tie modeling provisions from AASHTO LFRD 2009, TxDOT Project 0-5253, and ACI 318-08 yielded similar predictions for the failure mode and generally conservative estimates of the dapped-end capacities. By further comparing the measured and calculated capacities, a clear trend between the level of ASR/DEF-related damage and the reserve strength of the dapped ends was made apparent: the inherent capacity margin decreased with increasing levels of ASR/DEF-related damage. In the case of the heavily deteriorated segment, the measured load-carrying capacity was only 3 and 17 percent greater than the ACI and AASHTO calculated capacities, respectively. It is likely that deterioration in excess of that found within the heavily cracked segment would deplete the available capacity margin and render the dapped-end detail unsafe with respect to current design codes. While the results suggested that there is no immediate risk of trapezoidal box beam failure, the potentially drastic implications of prolonged deterioration were emphasized.

CHAPTER 5
Forensic Investigation

5.1 OVERVIEW

Upon completion of the dapped-end testing program, three forensic techniques were applied to the trapezoidal box beam segments. The purpose of the forensic investigation was two-fold: (1) to place the box beam deterioration within the context of common ASR/DEF evaluation techniques and (2) to provide documentation of the internal ASR/DEF-related defects which contributed to the loss of structural safety. The results of the forensic investigation help to further substantiate the observations/conclusions drawn in Chapter 4.

First, the findings of a petrographic analysis are used to establish the nature of the deterioration found within three of the segments. Observations regarding the cause of deterioration, general character of the microstructural cracking, and qualitative severity of the damage are presented. Second, the results of a structural autopsy are examined to reveal notable interior cracking which contributed to the behavior and load-carrying capacity of the damaged segments. Finally, estimates of the ASR/DEF-related expansion, obtained from elastic rebound testing of the strained transverse reinforcement, are summarized and compared to the qualitative damage assessments.

5.2 PETROGRAPHIC ANALYSIS

A total of nine cores, three from the dapped ends of segments N-P (undamaged), M-P (moderately cracked) and H-P (heavily cracked), were submitted to the TxDOT Concrete Laboratory for evaluation. The petrographic analysis served three purposes: (1) to visually document and qualify the contributions of ASR and DEF deterioration, (2) to characterize the crack networks occurring within the concrete cover and structural core, and (3) to provide a qualitative comparison of the microstructural damage found within

each segment. The following discussion summarizes the results in relation to the aforementioned tasks. The detailed petrographic report can be found in Appendix D.

Visual inspection, scanning electron microscope (SEM) and spectral analyses of multiple lapped sections allowed personnel at the TxDOT Concrete Laboratory to identify microscopic features and chemical products of both ASR and DEF. It was ultimately concluded that the three segments had "suffered significant distress from alkali-silica reaction." The development of ASR deterioration was attributed to the fine aggregate fraction of the concrete mixture: "the primary ASR aggregate type is microcrystalline chert fine aggregate." Two of the images depicting a distressed fine aggregate particle are included in Figure 5-1A and Figure 5-2A. While ettringite formation was noted to fill many of the air voids and microstructural cracks, the occurrence of gapping around aggregates (see Figure 5-1B and Figure 5-2B) due to delayed ettringite formation was limited. As a result, *"it is inconclusive whether DEF has contributed to the distress based on the limited amount of true gapping due to paste expansion."*

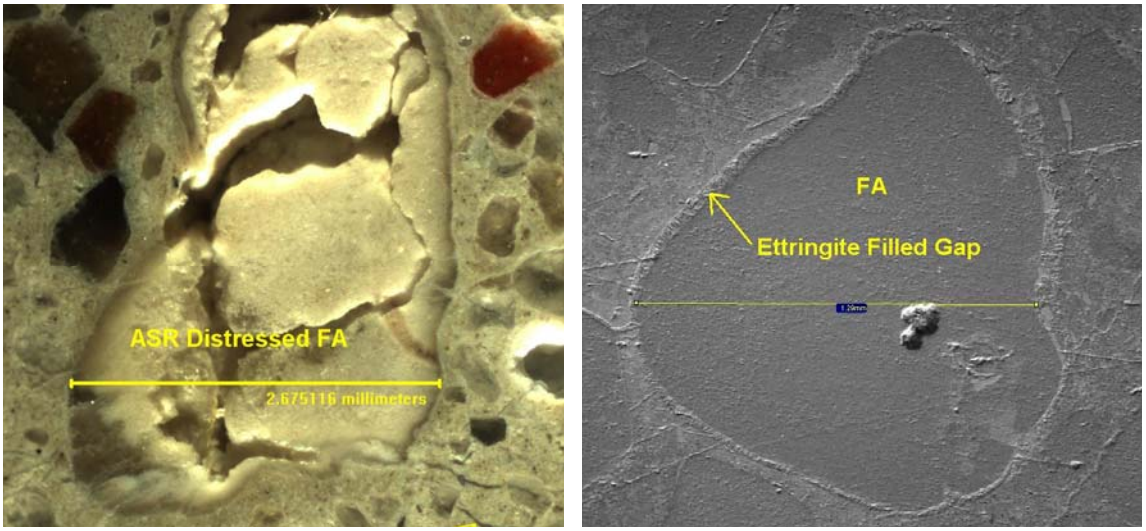

(A) Distressed Fine Aggregate (ASR) (B) Gapped Aggregate (DEF)

Figure 5-1: Examples of Microstructural Damage

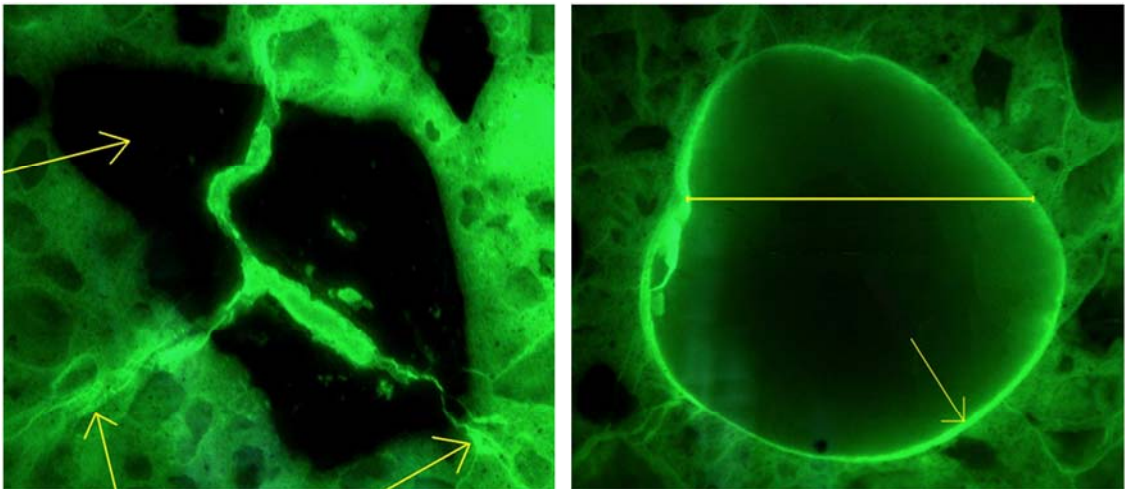

(A) Distressed Fine Aggregate (ASR) (B) Gapped Aggregate (DEF)

Figure 5-2: Fluorescence Imaging of Microstructural Damage

The diagnosis put forth by TxDOT personnel did not mirror the findings of researchers at the Concrete Durability Center (CDC) of UT Austin. Folliard and Drimalas (2008) conducted a forensic evaluation in 2004 and concluded that delayed ettringite formation was primarily responsible for the damage found in segment H-II; alkali-silica reaction only played a secondary role (see Chapter 2). It is important to note that segment H-II (evaluated by CDC) was sourced from the same trapezoidal box beam as segment H-P (evaluated by TxDOT). The concrete mixture and corresponding deterioration were therefore equivalent. The disparity between the two diagnoses highlights two critical limitations of petrographic analysis. First, the method cannot be used to distinguish the order in which the reaction products formed. Did DEF products form within pre-existing, ASR-induced cracks, or vice-versa? When products of both deleterious mechanisms are present, diagnosis of the primary mechanism is purely subjective. Second, examination of concrete samples which represent a small fraction of the total affected volume of concrete is not an effective means to precisely diagnose the cause of the damage. The consistency of the concrete mixture, curing temperatures, and exposure vary throughout the volume of an affected member. It is therefore improper to base broad diagnoses on the petrographic results from relatively few concrete samples.

In the context of the current study, the value of such diagnoses is limited. The chemical processes of ASR and DEF may differ, but the structural effects are indistinguishable to the structural engineer. Both mechanisms cause bulk volumetric expansion and microcracking of the concrete. In a reinforced structure, strains imposed on the reinforcement setup an internal force system in which reinforcement stresses are equilibrated by compression in the concrete. Where sufficient confinement is present, this compression suppresses the development of macrocracks within the structural core and generally influences the direction of macrocracks at the concrete surface. Regardless of the relative ASR and/or DEF contribution to the overall expansion, the resulting internal damage to, and outward appearance of, the deteriorated concrete member is the same. Comparison of the current petrographic results to those obtained by Deschenes et al. (2009) for an alternate set of prematurely deteriorated concrete members will further substantiate this point.

In order to investigate the distribution of ASR/DEF cracking within the cross-sections of several ASR/DEF-affected bent cap specimens, Deschenes et al. (2009) extracted a number of cores for petrographic analysis. Initial examination of the cores revealed little evidence of DEF-related damage, but a substantial number of petrographic features related to ASR deterioration. A fraction of the cores were then split lengthwise to study the distribution and orientation of the cracking along the core axis (i.e. through the width of the bent cap members). The diagram in Figure 5-3 illustrates the typical cracking pattern found within each of the extracted cores. Macrocracking perpendicular to the exterior surface generally gave way to sub-parallel cracking within the first two inches of the core length. Beyond this, cracking within the structural core did not develop in a preferential manner (e.g. it was random). Deschenes et al. (2009) suggested that the sub-parallel cracking was indicative of the high local stresses imposed by the transverse reinforcement (the direction of least restraint was perpendicular to the bar in this area). Concrete removed from the immediate influence of the reinforcement (i.e. the structural core and cover concrete) was less likely to feature such highly directional cracking.

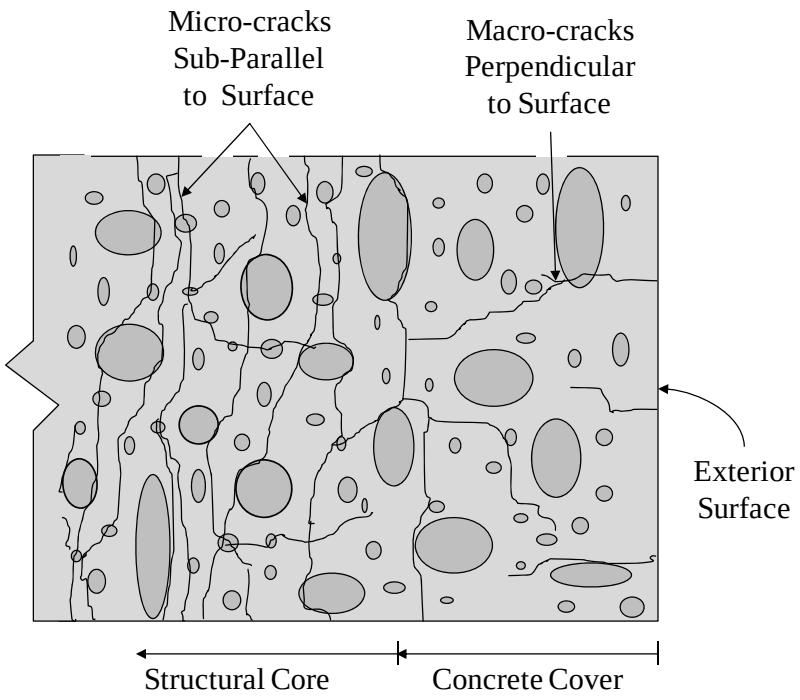

Figure 5-3: General Crack Orientation within Cores (Deschenes et al. 2009)

Examination of the cores extracted from the trapezoidal box beam segments resulted in an equivalent set of observations. In fact, the distribution of cracking through the core length is well represented by the diagram in Figure 5-3. It is important to realize that the box beams were likely affected by both ASR and DEF deterioration; based on the synthesis of petrographic results from the TxDOT Concrete Laboratory and the Concrete Durability Center. The reinforced concrete beams examined by Deschenes et al. (2009) were only affected by ASR deterioration, yet they featured the same internal damage characteristics. It is therefore difficult to claim that there are any meaningful differences between the structural effects of ASR and DEF. Collective treatment of the internally expansive mechanisms as "premature concrete deterioration" is most logical from a structural engineer's perspective.

To further evaluate petrographic analysis as a structural evaluation tool, the TxDOT Concrete Laboratory personnel were asked to qualitatively rank the severity of the deterioration found within each core. Overall assessment of the deterioration was

guided by two independent observations: (1) the number of reactive particles identified within a given length of core, and (2) the relative severity of the microstructural cracking found within the core. Interestingly, the counting of reactive particles is a major component of the damage rating index (DRI) method. As conceived, the DRI method promised to provide an accurate, quantitative assessment of ASR deterioration through careful counting of common microstructural defects (including reactive particles). Although the TxDOT personnel did not conduct a full DRI assessment, results of the counting process did not show any meaningful correlation to the qualitative damage levels (i.e. light, moderate, or heavy) or observed loss of structural safety. As depicted in Figure 5-4A, the heavily damaged segment (H-P) contained fewer reactive particles than the moderately damage segment (M-P). Final assessment of the internal damage, including observations regarding the severity of the microstructural cracking, did yield a reasonable correlation with the qualitative damage levels (see Figure 5-4B). It should be noted, however, that inspection of the internal damage did not reveal the same magnitude of disparity between the “undamaged” and “heavily damaged” segments. Cores from the heavily damaged segment were subject to a “slightly higher” level of deterioration than found within the undamaged segment.

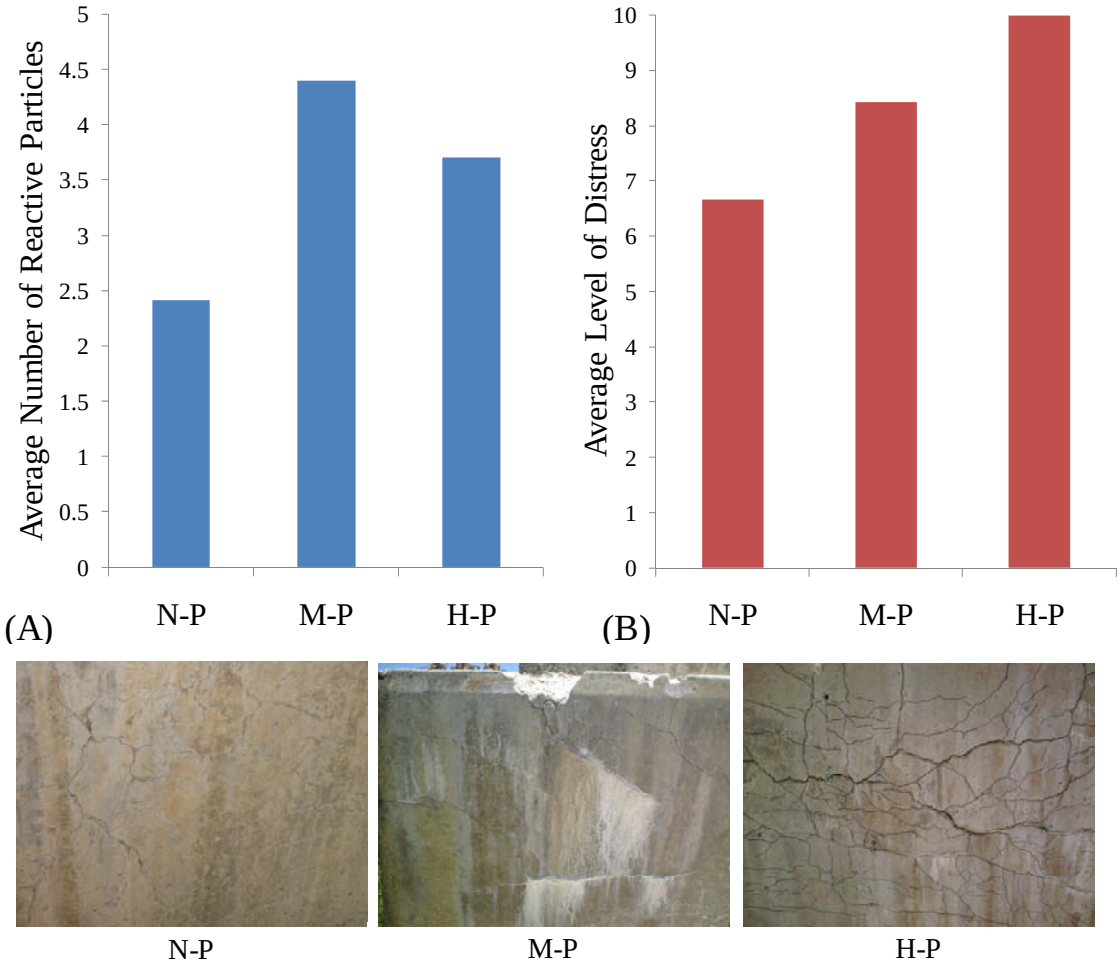

Figure 5-4: Comparison of Microstructural Damage

While the petrographic analysis did provide insights into the nature of the internal damage, the information gathered during the analysis was not of sufficient value to warrant the use of the technique during structural evaluations. Results of the petrographic analysis may be better utilized by those planning durability-related repairs, for which the microstructural nature of the deterioration is of greater concern.

5.3 BOX BEAM AUTOPSY

The value of the information gathered from load testing and forensic investigation of the five trapezoidal box beams cannot be underestimated. The box beams were fabricated using standard industry practices and allowed to deteriorate under normal

storage conditions. In a research area (namely, study of the structural effects of ASR/DEF deterioration) dominated by accelerated deterioration schemes and scaled specimens of questionable merit, the box beams promised to provide highly relevant information. Therefore, the opportunity to directly inspect the internal damage resulting from nearly 15 years of continuous deterioration had to be pursued. A segment (identified as H-A) with a standard end block exhibiting heavy deterioration equivalent to that found in H-II was therefore selected for a structural autopsy.

5.3.1 Autopsy Methods

In order to clearly identify penetration of the surface cracks into the cross-section, the standard end block was injected with epoxy prior to placing the cuts. Epoxy injection of segment H-A was a two stage process. Epoxy ports were first distributed over the cracked surface of the beam and sealed in place with a grey epoxy coating (as shown in Figure 5-5A). Once the outer epoxy seal had adequately cured, a black-colored epoxy was injected into each one of the ports shown in Figure 5-5B. Sufficient penetration into the crack network was established when a threshold injection pressure was met.

(A) Placement of Epoxy Ports (B) Epoxy Injection

Figure 5-5: Preparation of the Autopsy Segment

Segment H-A was then moved into Ferguson Structural Engineering Laboratory and carefully supported to allow incremental removal of five short end block segments. Each of the cuts was placed perpendicular to the longitudinal axis of the box beam with a

concrete wire saw. As shown in Figure 5-6, a wire embedded with diamonds was pulled around the box beam by a hydraulically powered flywheel. Continuous adjustment of the pulley assembly ensured the proper amount of contact and pressure was maintained across the entire cut.

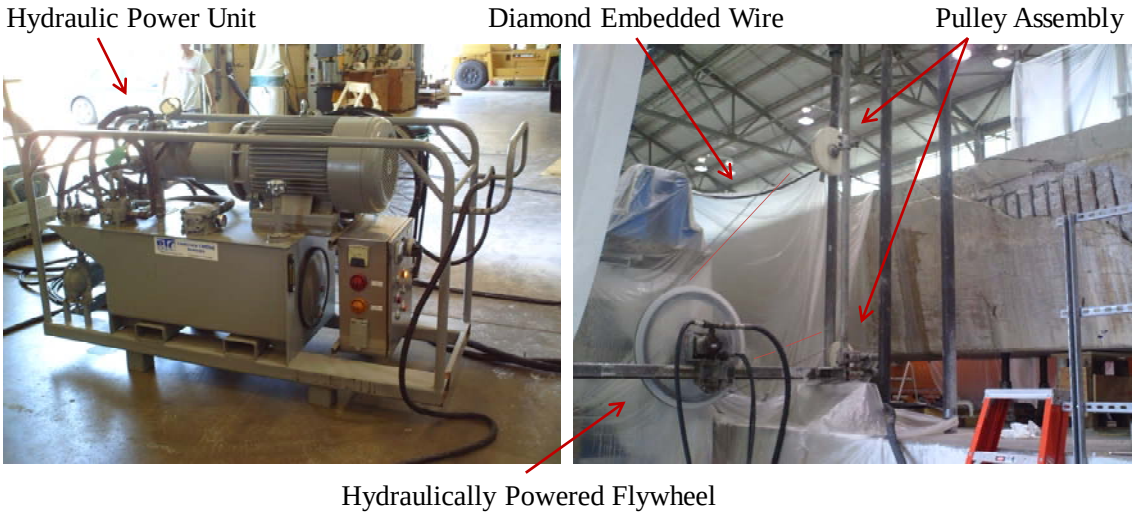

Figure 5-6: Cutting with the Concrete Wire Saw

5.3.2 Visual Inspection of Cross-Sections

A total of five cuts were made through segment H-A. The cuts were spaced at increments of 8 to 17 inches from the free end of the box beam segment as shown in Figure 5-7. The first four cuts exposed sections within the solid end block region, while the fifth passed through the void. This arrangement allowed examination of effects related to: (a) the distance from the free end of the box beam, (b) the transfer and development of the prestressing force, and (c) the transition from a solid to hollow section. Observations regarding the distribution of internal cracking and resulting cross-sectional distortion were generally used to characterize the deterioration at each section.

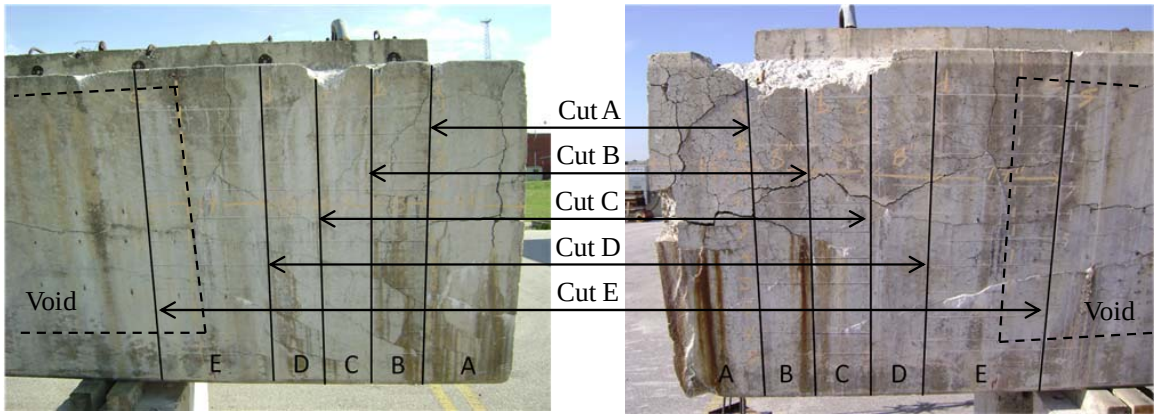

(A) East Face (B) West Face

Figure 5-7: Location of Beam Cuts

Prior to application of the epoxy, wide cracks were noted to extend from the free end onto each side face of the segment (as shown in Figure 5-7). The deterioration within the standard end block region was quite severe in comparison to most of the segments; small areas of spalling and efflorescence were indicative of mature levels of ASR and DEF. Due to the striking appearance of the box beam exterior, it was difficult to deny the potential presence of significant interior damage (even in light of the petrographic results, refer to Section 5.2).

Photographs of the four cuts placed within the solid end block are included in Figure 5-8. The orientation of each cut face is consistent with the next. Contrary to what the outward appearance suggested, the surface cracks did not penetrate deep into the structural core of the member. In fact, all of the cracks terminated within ten inches of the beam's surface. The most notable cracks ran sub-parallel to the left side of the cut faces shown in Figure 5-8. This interior cracking corresponded to the more heavily cracked, west face of the box beam segment shown in Figure 5-7B. While the wide sub-parallel cracks occasionally intersected surface cracking, they did not appear to be a direct extension of discrete surface cracks. It is more likely that the sub-parallel cracking is the result of two circumstances: (1) the presence of highly localized restraint in the vicinity of the transverse reinforcement, and (2) the lack of compatibility between the confined structural core and free concrete surface.

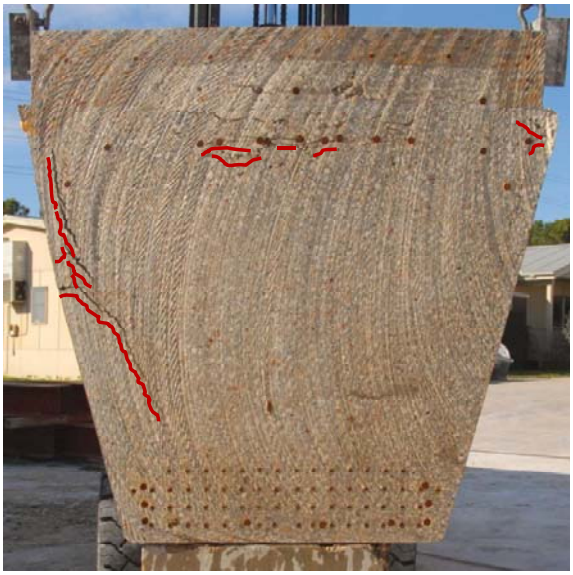

Section A – 14 inches

Section B – 22 inches

Section C – 30 inches

Section D – 38 inches

Figure 5-8: Epoxied Sections in the Solid End Block

In spite of the absence of a clearly defined structural core (as conventionally defined), sub-parallel cracking (of greatly diminished length and width) was also identified within the webs of the hollow box beam section. The photographs in Figure 5-9 illustrate the scope of the deterioration with the crack outlined with red in Figure 5-9A. Please note that penetration of the epoxy into the box beam void caused the visible

damage to the styrofoam block-out. The mechanism for the formation of such a crack within a hollow section was not immediately apparent. However, it is possible that compatibility with the solid end block forced the formation of the sub-parallel cracking. The cut through the hollow section was only located 13 inches away (or less than one quarter of the effective beam depth) from the face of the solid end block region. Furthermore, inspection of the original cuts placed within the hollow regions of the most deteriorated segments (H-II and H-A) did not reveal any sub-parallel cracking.

(A) Section E – 55 inches (B) Small Crack and Melted Styrofoam

Figure 5-9: Cut Placed in the Hollow Region of the Box Beam Segment

In general, the sub-parallel cracks diminished in width and length as the longitudinal distance from the free end of the box beam segment increased. Sub-parallel cracking within Section A (14 inches from the free end) was up to 0.40 inches in width, while the cracks found within Section E (55 inches from the free end) were a maximum of 0.08 inches in width. The maximum sub-parallel crack width is presented as a function of the distance from the free end in Table 5-1. The observed trend cannot be attributed to variation of the reinforcement details. The transverse reinforcement was consistently spaced at five inches over the length of the region under consideration.

Table 5-1: Characterization of Sub-Parallel Cracking

Section	Distance from Free End	Maximum Crack Width
A	14 inches	0.40 inches
B	22 inches	0.24 inches
C	30 inches	0.16 inches
D	38 inches	0.14 inches
E	55 inches	0.08 inches

Two equally viable explanations for the diminishing sub-parallel crack widths can be offered. First, consider that a section further from the free end will be subjected to inherently tighter boundary conditions and higher effective prestress forces. The presence of such restraint would certainly limit the development of ASR/DEF-related damage at the interior sections. Second, it is likely that the potential for severe damage was directly linked to the curing temperatures. Please recall that the most significant cracking within each of the damaged box beam segments was typically concentrated within the massive end regions. While temperature data logs are not available, the small mass of the hollow region may not have generated enough heat to trigger severe DEF deterioration mechanisms (while ASR could still occur). The gradient of temperature (and corresponding damage potential) present at the transition from the solid to hollow sections could have contributed to the diminishing severity of the sub-parallel cracking.

A number of other significant, yet visibly less apparent, internal defects were revealed during the box beam autopsy. They included: (a) debonding of transverse reinforcement, (b) cross-sectional bulging, and (c) inter-strand cracking. The formation of each defect and its significance from a structural performance standpoint is explored below. Figure 5-10 provides a complete visual description of the defects typically found within the solid cross-sections:

- *Debonding of the Transverse Reinforcement*: The cut face intersected the transverse reinforcement in two of the cross-sections (refer to Figure 5-8). In both cases it appeared as though the sub-parallel cracking led to debonding of the back-side of the transverse reinforcement. The debonded length was relatively short in both cases but could have created a splitting plane through the splice. Despite the observation, the beams subject to load testing did not suffer from stirrup anchorage failure so it can be assumed that the potential presence of a similar defect within other box beams may not impact overall structural performance.
- *Distortion of the Solid Cross-Section Geometry*: While the box beams were originally formed with straight steel forms, the side faces exhibited a slight bulge upon autopsy. Over time, the internal expansion was restrained at the corners by well anchored transverse reinforcement. The flexural stiffness of the reinforcement was not sufficient to prevent the lateral bulging of the side faces shown in Figure 5-10C. No distortion was found in the hollow cross-sections located a sufficient distance from the severe deterioration of the end region.
- *Fine Cracking Between Parallel Strands*: Due to the rapid transfer of prestressing force from the strands to the concrete, tensile (or splitting) stresses are generated in the transverse plane of the beam. While the magnitude of the tensile stress is not typically great enough to cause splitting cracks, it may be augmented by tensile stresses related to ASR/DEF actions and result in cracking in the horizontal plane of the strands. Close examination (refer to Figure 5-10D) of the exposed strand ends revealed fine cracking between a number of strands in each layer. As discussed in Chapter 4, the inter-strand cracking generated by ASR/DEF expansion is suspected to be responsible for the observed loss of anchorage and overall dapped-end capacity.

(A) Severe Sub-Parallel Cracking

(B) Debonding of Transverse Reinforcement

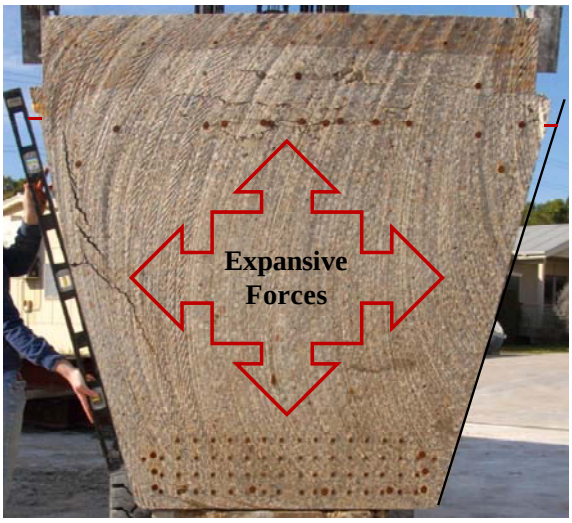

(C) Distortion of the Cross-Section Geometry

(D) Fine Inter-Strand Cracking

Figure 5-10: Typical ASR/DEF-Related Defects in Solid End Cross-Sections

5.4 ELASTIC REBOUND TESTING

Study of the structural effects of ASR/DEF deterioration has traditionally been limited to the testing of specimens constructed and conditioned in the laboratory. While

the disadvantages of such an approach were alluded to in the previous section (i.e. accelerated deterioration, use of scaled models, etc.), overwhelming preference for such testing is firmly rooted in the ability to accurately track the development of ASR/DEF deterioration through expansion measurements. Direct measurement of the expansion within the box beam segments was impossible without a suitable datum and the assessment of the deterioration was therefore left to qualitative methods.

Efforts to provide a more quantitative estimate of the deterioration were initiated after the completion of the load testing program. Borrowing on the experience of Deschenes et al. (2009), the elastic rebound or in-situ reinforcement test was selected to provide an estimate of the expansion. The fundamental basis for the test is the compatibility which exists between the reinforcement and concrete within a structural concrete member. Theoretically the strains experienced by the confining reinforcement should be equivalent to the expansion of the ASR/DEF affected concrete, excluding any external influences. Further discussion regarding the theoretical basis and practical viability of the method can be found in Deschenes et al., 2009.

Measurement of the reinforcement strains was accomplished through the destructive means shown in Figure 5-11. A hand-held jackhammer was used to expose a small length of transverse reinforcement. Removal of the concrete was carefully conducted to minimize prying or impacts that would disturb the in-situ state of stress. The bars were then cleaned and instrumented with a foil strain gage. Shortening (or elastic rebound) of the reinforcement was recorded as the cut was being placed. As long as the ASR/DEF-related expansions were less than the reinforcement yield point, the corresponding reinforcement strains would be equivalent to the concrete expansion. Expansions in excess of the reinforcement yield point would not be recovered as elastic recovery of the reinforcement does not include the effects of plastic deformations.

Figure 5-11: Exposing and Cutting the Transverse Reinforcement

Elastic rebound testing was conducted on four of the box beam segments: two heavily damaged, one moderately damaged, and one undamaged. Two of the four segments had previously been subjected to dapped-end testing. In those cases, the location of the elastic rebound testing was selected to avoid load-induced cracking. The results from all of the elastic rebound tests are summarized in Figure 5-12. Ideally, there would be correlation between the reinforcement strains and qualitative damage levels (i.e. light, moderate, heavy).

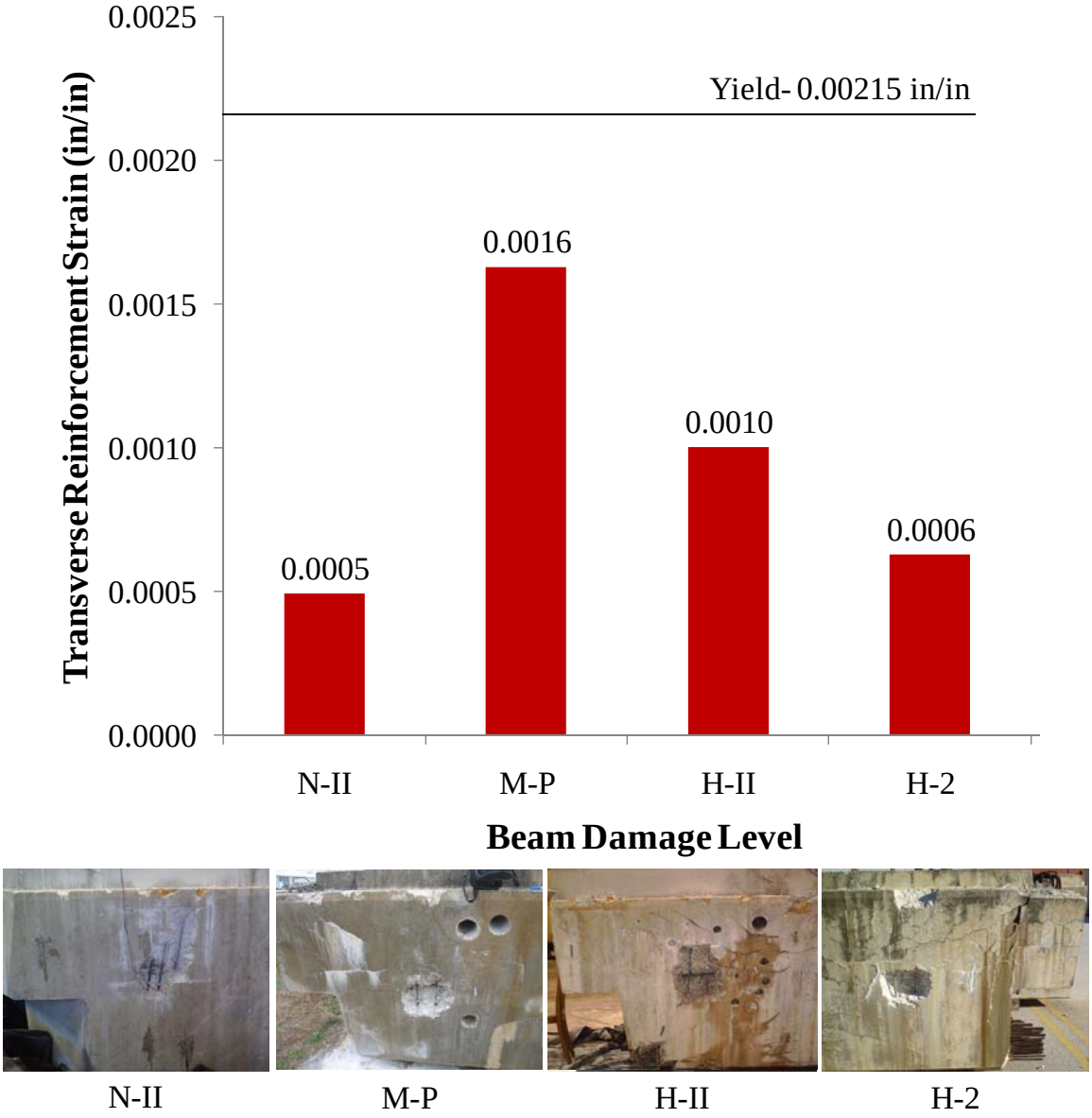

Figure 5-12: Strains from Stirrup Rebound Tests

Contrary to the expectations, the reinforcement strain measured within one of the two heavily damaged segments was of the same magnitude as that measured within the "undamaged" segment. The visual assessment of cracking did not show any relation to the transverse reinforcement strains. In the end, a number of unique aspects of the

dapped-end segments may have contributed to the poor correlation, or rather poor application, of the elastic rebound technique.

- *Irregular Crack Distribution*: In order to obtain an upper bound estimate of the ASR/DEF-related expansion (i.e. controlling case), it is advisable to conduct the elastic rebound tests in areas subject to the most severe cracking. Desirable placement of the elastic rebound tests was not generally possible in the current study due to the constraints introduced by the pre-existing core holes and load-induced cracking.
- *Unclear State of Stress*: In contrast to the work done by Deschenes et al. (2009), the state of stress within the dapped ends is not clear. This is a function of both the unique geometry and complicated reinforcement scheme. It is possible that the principal direction of expansion does not coincide with the transverse reinforcement; in which case, elastic rebound testing of the reinforcement would not provide the most applicable results.
- *Poor Reinforcement Anchorage*: The transverse reinforcement consisted of two open segments which were lapped at the box beam side faces to provide confinement. Due to the extensive nature of the sub-parallel cracking, it is conceivable that slip of the transverse reinforcement laps occurred in the most heavily damaged segments. If the slip was limited, the tensile strains would have been relieved while the structural integrity was maintained.

5.5 SUMMARY

Review of the results from a petrographic analysis, structural autopsy, and elastic rebound testing helped accomplish two goals: (1) to place the box beam deterioration within the context of common ASR/DEF evaluation techniques and (2) to provide documentation of the internal ASR/DEF-related defects which contributed to the loss of structural safety. Petrographic evidence of both ASR and DEF were found in cores taken from the lightly to heavily damaged segments. Due to conflicting interpretations of the

microstructural damage, the ultimate diagnosis of the deterioration was not conclusive. Investigation of the internal cracking pattern through the examination of both cores and full cross-sectional faces nonetheless made it clear that the large cracks found on the surface of the beams were limited to the perimeter of the box beams. With regards to the structural effects of the interior damage, fine cracking between the prestressing strands was identified as the most significant aspect of the deterioration. Lastly, elastic rebound testing revealed ASR/DEF-induced strains within the transverse reinforcement. The results did not correlate well with the qualitative damage levels for a number of reasons related to the unique geometry and complicated reinforcement schemes of the dapped ends.

CHAPTER 6
Summary and Conclusions

6.1 SUMMARY

In the decade following the completion of the US 59 corridor and Katy Central Business District (CBD) HOV lanes, many of the trapezoidal box beam bridges began to show signs of premature concrete deterioration. Cores taken from rejected, yet representative, box beams confirmed the potential for alkali-silica reaction (ASR) and delayed-ettringite formation (DEF) in beams constructed at the same precast facility. Furthermore, the rejected beams illustrated the potential severity of the ongoing ASR/DEF deterioration within the dapped-end regions of the trapezoidal box beams. Due to the complex structural details of the dapped ends and the unparalleled deterioration found within, it was impossible to find relevant test results in the literature. Load testing had never been performed to investigate the effects of premature concrete deterioration on the structural capacity of prestressed concrete beams with dapped ends.

The Texas Department of Transportation (TxDOT) has provided funding for the University of Texas at Austin (UT Austin) to conduct load tests and an autopsy on five trapezoidal box beams. The rejected dapped-end beams had been in storage at a local precast yard for nearly fifteen years and were subject to varying levels of ASR/DEF deterioration. One “undamaged” beam was accompanied by four other beams with low, moderate, and heavy levels of cracking. The most severe deterioration was characterized by minor spalling and cracks as wide as one quarter of an inch. The dapped-end beams were cut into thirds and shipped to UT Austin for load testing at Ferguson Structural Engineering Laboratory (FSEL).

With the exception of one dapped end, all of the load tests were conducted at a shear span-to-depth ratio of 1.85 to study the effects of ASR/DEF on the primary failure mechanism of the dapped end. The load carrying capacity of each dapped end was governed by shear-induced anchorage failure. Test observations of anchorage failure,

including the formation of cracks in the development region and audible pops as the prestressing strands slipped, were reinforced by the results of the strut-and-tie modeling process. Due to the limited length available for development of the prestressing strand, the computed strength of each of the strut-and-tie models was controlled by the flexural reinforcement anchorage at the bottom corner of the full depth section. The dapped-end capacities obtained from application of the most recent ACI, AASHTO, and TxDOT Project 0-5253 strut-and-tie modeling provisions were compared to the maximum applied loads from each load test. Review of the results from all five dapped ends provided insights into the relationship between the severity of the ASR/DEF deterioration and the capacity margin.

Upon completion of the dapped-end testing program, a forensic investigation was carried out to further examine the structural implications of the internal defects created by ASR/DEF deterioration. A petrographic analysis was first used to establish the nature of the microstructural damage found within three of the segments (undamaged, moderately and heavily cracked). A structural autopsy was then conducted to reveal notable interior cracking which may have contributed to the behavior and load-carrying capacity of the damaged segments. Lastly, estimates of the ASR/DEF-related expansion were obtained from elastic rebound testing of the strained transverse reinforcement and compared to the qualitative damage assessments.

6.2 CONCLUSIONS AND RECOMMENDATIONS

Motivation for the current study was rooted in the ability to obtain results which were directly applicable to the US 59 corridor and Katy/CBD HOV bridges. As detailed in the previous chapters, the observations and data gathered over the course of the study provide a clear picture of the relationship between the severity of the ASR/DEF deterioration and the structural performance of the dapped-end beams. The most important aspects of that relationship are summarized below. These conclusions and recommendations will serve as a reference for the planning of future maintenance and replacement operations on the US 59 corridor and Katy/CBD HOV lanes.

1. **The structural capacity of the dapped ends, as detailed for the US 59 corridor and Katy/CBD HOV lanes, are governed by shear-induced anchorage failure.** The initial attempt to fail the dap (partial depth portion) in shear resulted in anchorage failure of the trapezoidal box beam. Detailed review of the beam design in the context of strut-and-tie modeling revealed the critical nature of the flexural reinforcement anchorage. A significant portion of the load was being transferred through the anchorage region. Due to the relatively short length available for prestressing strand development, this detail will likely control failure of the beam end irrespective of the shear span-to-depth ratio.

2. **Moderate to heavy levels of ASR/DEF damaged the anchorage region of the primary flexural reinforcement; thereby reducing dapped-end capacities by up to 15 percent.** Two particular characteristics of the damage suggested that ongoing ASR/DEF deterioration was responsible for the loss of anchorage capacity. First, relatively large surface cracks (up to 0.03 inches wide) were identified within the prestress transfer region of all the deteriorated segments. Second, structural autopsy of one box beam segment revealed fine cracks between the prestressing strands. These defects reduced the load-carrying capacity of the heavily cracked dapped end to 659 kips; as compared to the 772 kips carried by the undamaged segment.

3. **The load-carrying capacity of comparable dapped ends may be conservatively estimated using current strut-and-tie modeling provisions in combination with core-based material strengths.** The load-carrying capacity of each dapped end, including that of the heavily damaged segment, was conservatively estimated through application of the ACI 318-08, AASHTO LRFD 2009, and TxDOT Project 0-5253 strut-and-tie provisions. With that said, the conservatism of the estimates generally decreased with increasing levels of deterioration. In the case of the heavily deteriorated

segment, the measured load-carrying capacity was only 3 and 17 percent greater than the ACI and AASHTO calculated capacities, respectively. It is likely that deterioration in excess of that found within the heavily cracked segment would deplete the capacity margin and render the dapped-end detail unconservative with respect to current design codes.

4. **The internal mechanics of an ASR/DEF-affected concrete member (as presented by Deschenes et al. 2009) were validated by both the condition and structural performance of the dapped ends.** Deschenes et al. (2009) suggested that the accumulation of ASR/DEF damage within a concrete member generates significant tensile strains and stresses in the reinforcement. That reinforcement stress is in turn equilibrated by a commensurate amount of compression in the concrete. Barring the loss of the confining reinforcement, the compression induced within the concrete impedes the development of large internal cracks and generally compensates for microstructural damage. Evidence of this phenomenon within the current study included: (1) increased dapped-end stiffness with increasing deterioration, (2) delayed formation of load-induced cracking, (3) a lack of perceptible cracking within the dapped-end cross-sections, and (4) measurable presence of significant reinforcement strains.

5. **Future infrastructure management decisions must consider the apparent loss of conservatism which occurs with increasing levels of ASR/DEF deterioration.** In contrast to the heavily cracked segment, the measured capacity of the "undamaged" segment was 37 to 50 percent greater than the capacity estimated by applicable code provisions. Ongoing ASR/DEF deterioration will continue to compromise the capacity margin available within the US 59 corridor and Katy/CBD HOV bridges. Regardless of code compliance, risks related to failure under overloads and other extreme loading scenarios will increase over the life of the bridge structures. The results of this

study will provide valuable data for making maintenance or replacement decisions where ASR/DEF related cracking is evident.

6. **Qualitative evaluation of the exterior deterioration provided a more accurate indication of the dapped-end performance than traditional (more demanding) assessment methods.** The petrographic analysis of several cores, which included traditional defect-counting exercises, failed to provide a better correlation to the load-carrying capacities of the deteriorated dapped ends. Due to the complexity of the dapped-end details, elastic rebound testing of the reinforcement also failed in this regard. From a practical standpoint, it seems that qualitative evaluation of the ASR/DEF-related cracking within affected trapezoidal box beams will provide a satisfactory indication of the capacity loss with very little effort.

6.3 FUTURE WORK

Despite the severity of surface cracking, the measured loss of dapped-end capacity related to the long-term deterioration of the beams was relatively mild. Further deterioration and the potential loss of confinement (through reinforcement fracture, refer to Chapter 2) would lead to more severe consequences. Not only would the controlling anchorage defects be exacerbated, new concerns regarding the shear strength of the dapped end would be introduced. Future work within the State of Texas should focus on the issue of ASR/DEF-induced reinforcement fracture. Definitive information regarding the potential for, and consequences of, reinforcement fracture is of paramount concern to those managing TxDOT's inventory of ASR/DEF-affected structures.

APPENDIX A
Beam Properties

Appendix A includes the concrete mixtures, beam properties, and shop drawings for the Houston prestressed concrete trapezoidal box beams with dapped ends.

Table A-1: Concrete Design Work Sheet for Design Number 392-03-95 R

Texas Highway Department — County: Harris

Construction Form 309 — Date: 7/19/95 10:41 AM

PHYSICAL PROPERTIES	Specific Gravity	% Solids	Unit Wt S S D	Sources of Materials
Fine Aggregate (FA)	2.61	0.62	101.4	Hallet
Course Aggregate (CA)	2.42	0.558	84.48	Vulcan
Water	1			Well
Cement	3.1			Capitol Type III

Design Factors			
Cement	(CF)	7.00	Sacks per cubic yard of concrete
Course Aggr.	(CAF)	74.00	Percent of maximum that is CA
Water	(WF)	4.50	Gal. per sack of cement
Air	(AF)	1.00	Percent

ADMIXTURES:

Type F = WRDA – 19

16 oz. per 100 lbs

Type D = Daratard 17

2.0 oz. per 100 lbs

BATCH DESIGN (One-Sack)	VOLUME: 1-SK Batch (CU.FT)		VOL to WT (lb) VOLx62.5xSpGr	1 sk BAT WTS	Batch Factor	Batch Wght for one CY
Yield = Cu. Ft. / Cu. Yd. / Cement Factor (CF)	27 / 7 = **3.857**					
Vol CA = Yld x CAF x Solids	3.857 x 0.74 x 0.558=	1.593	x 62.50 x 2.42 =	240.89 x	7.00 =	1686 lbs
Vol Mortar = Yld – Vol CA	3.857 - 1.593 = **2.264**					
Vol Water = Water Factor / Gal Water per cu ft	4.5 / 7.48 =	0.602	x 62.50 x 1.00 =	37.60 x	7.00 =	263 lbs
Volume One Sack Cement	1.00 x 0.485 =	0.485	x 62.50 x 3.10 =	93.97 x	7.00 =	658 lbs
Vol Air = Yld x AirFactor	3.857 x 0.010 =	0.039				
Vol Paste = Volume (Cement + Water + Air)	0.485 + 0.602 + 0.039 = **1.125**					
Vol FA = Vol Mortar – Vol Paste	2.264 - 1.125 =	1.139	x 62.50 x 2.61 =	185.84x	7.00 =	1301 lbs

Yield	3.857 cu. ft		
Total Batch Weight	3908 lbs		
Fine Aggregate Factor	Vol. of FA / FA Solids x Vol. Mortar	1.139 / 0.006 x 2.264	= 81.15

Table A-2: Concrete Design Work Sheet for Design Number 392-12-95

Tx. D.O.T. Project Date: 10/12/95 12:01 PM

PHYSICAL PROPERTIES	Specific Gravity	% Solids	Unit Wt S S D	Sources of Materials
Fine Aggregate (FA)	2.61	0.62	101.4	Hallet
Course Aggregate (CA)	2.42	0.558	84.48	Vulcan
Cement	3.1			Capitol Type III
Water	1			Well

Design Factors			
Cement	(CF)	7.00	Sacks per cubic yard of concrete
Course Aggr.	(CAF)	74.00	Percent of maximum that is CA
Water	(WF)	3.25	Gal. per sack of cement
Air	(AF)	1.00	Percent

ADMIXTURES:

Type F = WRDA – 19

17 oz. per 100 lbs

Type A = WRDA/HYCOL

3.0 oz. per 100 lbs

BATCH DESIGN (One-Sack)	VOLUME: 1-SK Batch (CU.FT)		VOL to WT (lb) VOLx62.5xSpGr	1 sk BAT WTS	Batch Factor	Batch Wght for one CY
Yield = Cu. Ft. / Cu. Yd. / Cement Factor (CF)	27 / 7 = **3.857**					
Vol CA = Yld x CAF x Solids	3.857 x 0.74 x 0.558=	1.593	x 62.50 x 2.42 =	240.89 x	7.00 =	1686 lbs
Vol Mortar = Yld – Vol CA	3.857 - 1.593 = **2.264**					
Vol Water = Water Factor / Gal Water per cu ft	3.25 / 7.48 =	0.434	x 62.50 x 1.00 =	27.16 x	7.00 =	190 lbs
Volume One Sack Cement	1.00 x 0.485 =	0.485	x 62.50 x 3.10 =	93.97 x	7.00 =	658 lbs
Vol Air = Yld x AirFactor	3.857 x 0.010 =	0.039				
Vol Paste = Volume (Cement + Water + Air)	0.485 + 0.434 + 0.039 = **0.958**					
Vol FA = Vol Mortar – Vol Paste	2.264 – 0.958 =	1.306	x 62.50 x 2.61 =	213.10x	7.00 =	1492 lbs

Yield	3.857 cu. ft
Total Batch Weight	4026 lbs
Volume of FA	1.306

Table A-3: US 59 Beam Information

GIRDER MARK NUMBER	CAST DATE	BED ID	STRAND COUNT	REASON FOR REJECTION	NOTES	BEAMS IN USE FROM SAME CASTING
RF-3R-9	7/6/95	B1	62 @ ½”	Void Floated During Concrete Placement	Girder displays severe cracking	RF-2R-8, all are exterior beams, 1st casting
RF-3R-12	7/8/95	B2	62 @ ½”	Lack of Consolidation	Girder displays severe cracking	RF-2R-8, all are exterior beams, 1st casting
RF-1R-1	7/26/95	B1	64 @ ½”	Concrete did not set in area of side & soffit	Girder displays severe cracking, Cored by UT	RF-2R-5 & RF-1R-4, all are exterior beams, 3rd casting
RF-2R-6	7/28/95	C3	56 @ ½” +2 full debond	Void Floated During Concrete Placement	Girder displays severe cracking	RF-1R-2 & RF-1R-3, all are interior beams, 4th casting
MLL-9-34	11/9/95	C3	56 @ ½” +2 full debond	Incorrect End Skew	Girder displays NO cracking. Conc strengths 5203/5512 for casting day	MLL-3-13, 58th casting

GIRDER	TRUE LENGTH	SOFFIT LENGTH	DAPPED ENDS	REBAR WEIGHT	VOID LENGTH	WEIGHT	WEIGHT PER 3 PC	CENTER PC LENGTH	END PC LENGTH	TONS
RF-3R-9	111.51	108.84	2	41.87115	101.84	139731.1	46577.03	39.70	35.90	69.87
RF-3R-12	111.22	108.55	2	41.76226	101.55	139410.3	46470.11	39.61	35.80	69.71
RF-1R-1	113.31	111.87	1	42.54703	104.87	141254.7	47084.9	40.14	36.59	70.63
RF-2R-6	111.48	108.81	2	41.85988	101.81	139693.8	46561.6	39.69	35.89	69.85
MLL-9-34	101.66	98.53	2	38.17255	89.5	131030.5	43676.82	37.23	32.21	65.52

Table A-4: Concrete Compressive Strength of US-50 Beams

GIRDER MARK	CAST DATE	MIX DESIGN #	W/C	Release Req'd	Release Actual	Design Req'd	Design Actual
RF-3R-9	7/6/95	392-3-95R	0.4	First Beam Cast and Rejected. No information available.			
RF-3R-12	7/8/95	392-3-95R	0.4	5810 psi	6340 psi @ 68.5 hrs	5810 psi	7550 psi @ 7 days
RF-1R-1	7/26/95	392-3-95R	0.4	5989 psi	6620 psi @ 51 hrs	5989 psi	8320 psi @ 8 days
RF-2R-6	7/28/95	392-3-95R	0.4	5413 psi	7050 psi @ 67 hrs	5811 psi	7080 psi @ 7 days
MLL-9-34	11/9/95	392-12-95	0.29	5012 psi	5530 psi @23 hrs	5419 psi	8630 psi @ 7 days

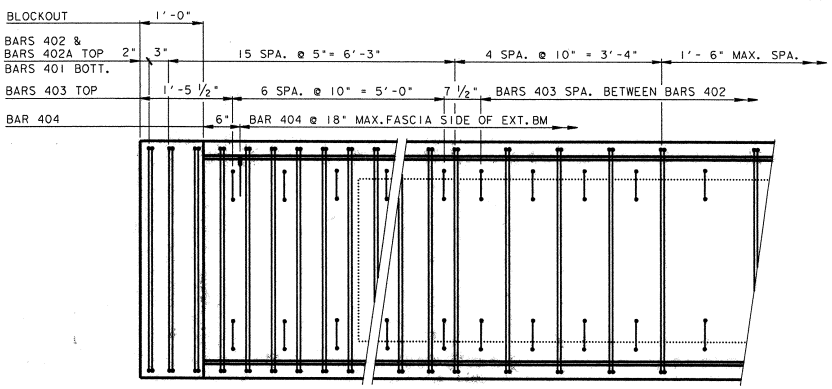

PLAN ~ NORMAL

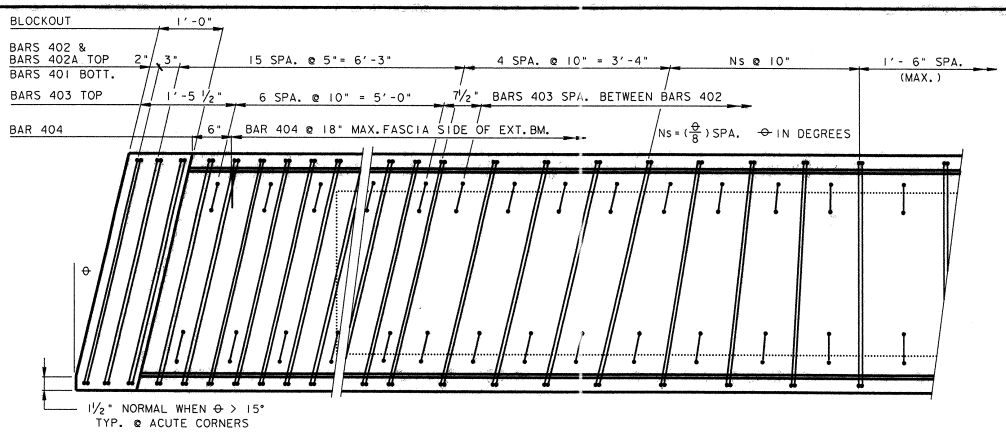

PLAN ~ SKEW

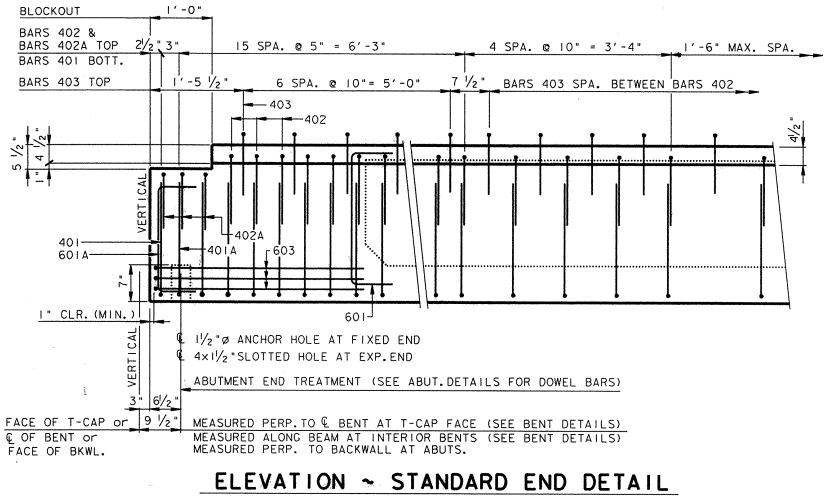

ELEVATION ~ STANDARD END DETAIL

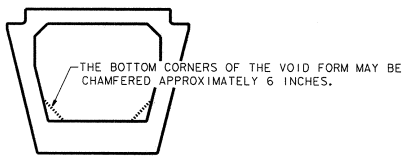

ALTERNATE VOID DETAIL

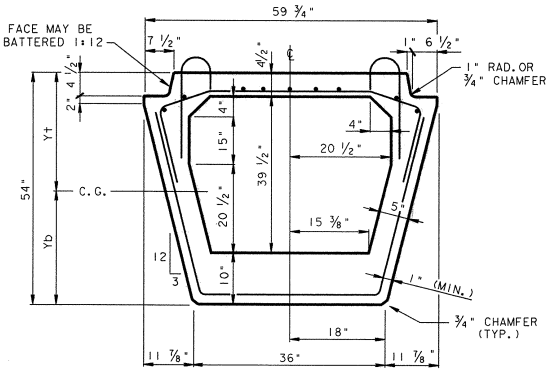

BEAM PROPERTIES	
Yb (IN.)	26.71
Yt (IN.)	27.29
WT. (LB/FT)	1154
I (IN^4)	404,968
AREA (IN^2)	1108

GENERAL NOTES:

THE PRESTRESSED BOX BEAM FABRICATOR SHALL PREPARE AND SUBMIT FOR APPROVAL SHOP DRAWINGS SUFFICIENT IN DETAIL TO ENABLE CORRECT FABRICATION AND INSPECTION WITHOUT REFERENCE TO THESE STANDARD SHEETS.

THESE BEAMS ARE DESIGNED FOR HS-20 LOADING, IN ACCORDANCE WITH AASHTO 1989 STANDARD SPECIFICATIONS.

ALL REINFORCING STEEL SHALL BE GRADE 60.

ALL CONCRETE SHALL BE CLASS H WITH STRENGTH AS SHOWN.

PRESTRESSED CONCRETE BOX BEAMS SHALL BE CAST MONOLITHICALLY IN TWO STAGES.

FABRICATOR SHALL PROVIDE POSITIVE VERIFICATION TO THE ENGINEER THAT THE WEBS, TOP FLANGE AND BOTTOM FLANGE ARE WITHIN THE DIMENSIONAL TOLERANCES SPECIFIED HEREIN.

ALL PRESTRESSING STRANDS WILL BE 1/2"DIA. 270 KSI, INITIAL PRETENSION = 31.0 KIPS. LOW RELAXATION STRANDS MUST BE USED. STRANDS WITH BOND BREAKAGE (DEBONDING) SHALL BE ENCASED IN PLASTIC TUBING ALONG THE ENTIRE DEBONDED LENGTH AND ENDS OF TUBING SEALED WITH WATERPROOF TAPE. SPLIT PLASTIC TUBING MAY BE USED PROVIDED THE SEAM OF THE TUBING IS SUFFICIENTLY SEALED WITH WATERPROOF TAPE TO PROHIBIT GROUT INFILTRATION. WRAPPING OF STRANDS WITH TAPE TO PROVIDE DEBONDING WILL NOT BE PERMITTED.

THE STRESSING PROCEDURE WILL BE SUCH THAT NO CRACKS WILL DEVELOP DURING MANUFACTURE OF THE BEAM. CRACKING IS ANTICIPATED WHEN THE CONCRETE TENSILE STRESS EXCEEDS 474 PSI. PRESTRESSED LOSSES ARE CALCULATED ON A RELATIVE HUMIDITY OF 75%.

CARDBOARD FORMS ARE NOT PERMITTED.

COST OF FURNISHING AND INSTALLING ELASTOMERIC BEARINGS AND TWO-PIECE THREADED BARS SHALL BE INCLUDED IN THE UNIT BID PRICE FOR "PRESTRESSED CONCRETE BEAMS".

MECHANICAL CONNECTOR TO DEVELOP 125% OF BAR YIELD STRENGTH.

SCREED THE TOP SURFACES OF BEAMS OR ROUGH FLOAT TO BRING MORTAR TO THE SURFACE AND COVER ALL AGGREGATE. THE SURFACE SHALL HAVE A ROUGH WOOD FLOAT OR STIFF BROOM FINISH. AGGREGATE SHALL NOT BE LOOSENED WHEN ROUGHENING THE SURFACE.

Texas Department of Transportation

PRESTRESSED CONCRETE TRAPEZOIDAL BOX BEAM
(54"-PROPERTIES)

TB-54

SHEET 1 OF 2

ORIGINAL DRAWING DATE: MAR. 1990		STATE DISTRICT	FEDERAL REGION	FEDERAL AID PROJECT NO.	SHEET
DN: C. R. B.	REVISIONS	12	6	NH 97 (62) G	911
CK: K. L. O.	1. NOTES - 4-96	COUNTY	CONTROL	SECTION	JOB	HIGHWAY
DW: EU/HB		HARRIS	0177	11	119	US59
CK: J. H. B						

ORIGINAL STANDARD

142

TB54.DGN

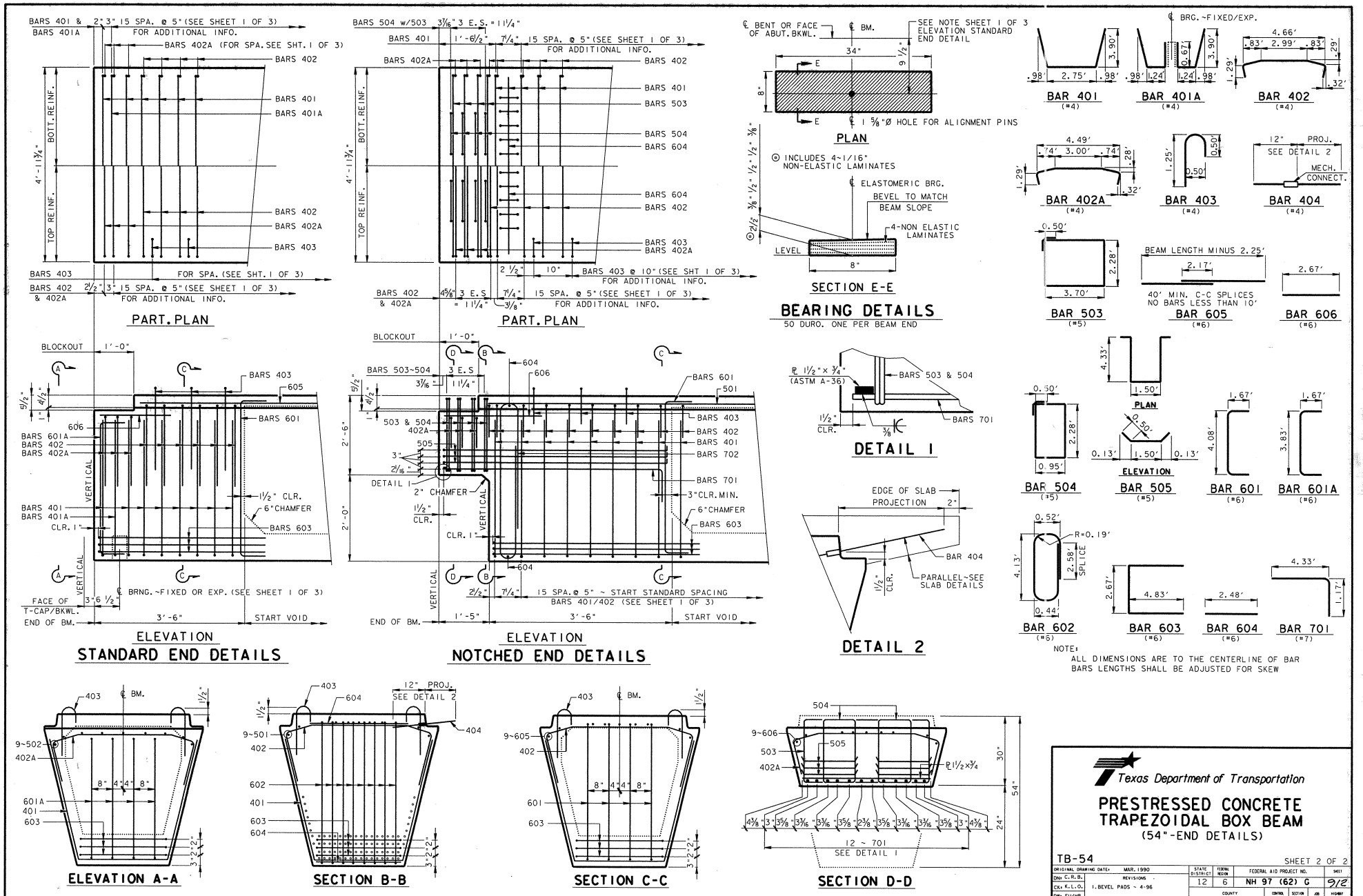

Texas Department of Transportation

PRESTRESSED CONCRETE TRAPEZOIDAL BOX BEAM
(54"-END DETAILS)

TB-54 SHEET 2 OF 2

ORIGINAL DRAWING DATE: MAR. 1990	STATE DISTRICT	FEDERAL REGION	FEDERAL AID PROJECT NO.	SHEET
DW: C.R.B. REVISIONS	12	6	NH 97 (62) C	9/2
CK: K.L.O. 1. BEVEL PADS ~ 4-96	COUNTY	CONTROL	SECTION	JOB	HIGHWAY
DW: EU/HB	HARRIS	0177	11	119	US59
CK: T.S.U					

143

ORIGINAL STANDARD

TB54.DGN

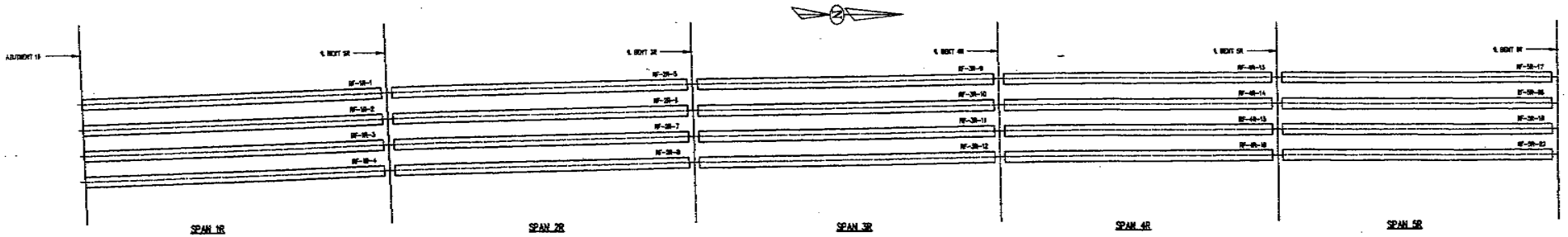

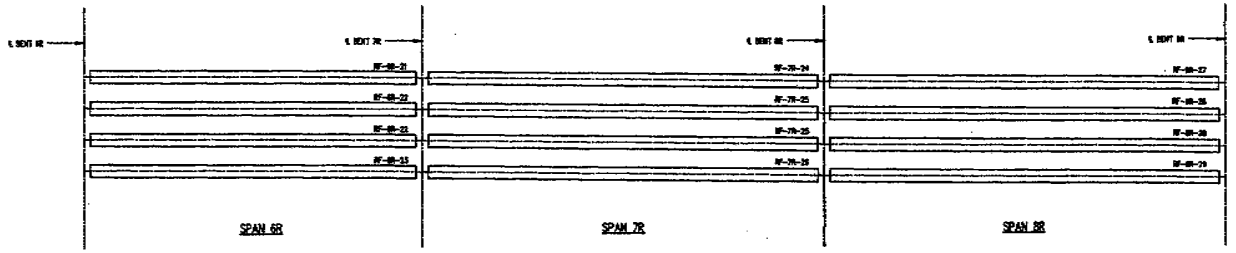

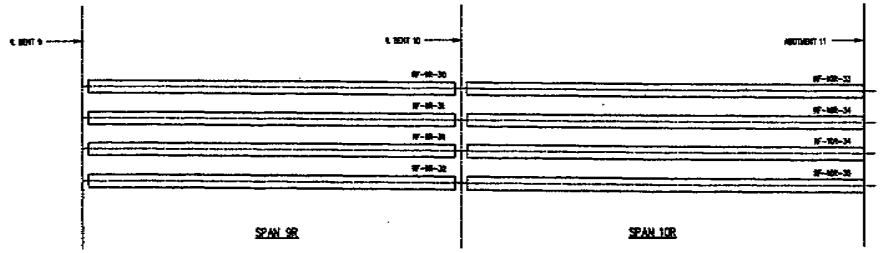

TEXAS DEPARTMENT TRANSPORTATION

☑ Approved without modification

☐ Approved with modification as shown

Date FEB 23 1995 By CKV

Approval of these drawings does not relieve the contractor of the responsibility for the correctness of detail.

BRIDGE SPAN MARK NO.

RF-4R-15

BEAM MARK LEGEND

RECEIVED
FEB 09 1995
DESIGN DIVISION

STRUCTURE: RIGHT FRONTAGE STREET OVER S.P.R.R. & LORRAINE STREET

FABRICATOR: TAYLOR BROS. PRECAST

LeBeau, Armstrong & Associates

CONTRACTOR: TAYLOR BROS., INC.

FED. ROAD DIV. NO.	STATE	PROJECT NO.	HIGHWAY NO.
6	TEXAS	0172-01-110	US 59
STATE DIST. NO.	COUNTY	CONTROL NO.	SECTION NO.	JOB NO.
12	HARRIS	6777	13	318

CONT. NO.	DWG. NO.	CHK'D BY	DATED	SHT. NO.
	SHT. TITLE: GIRDER LAYOUT			RF-1

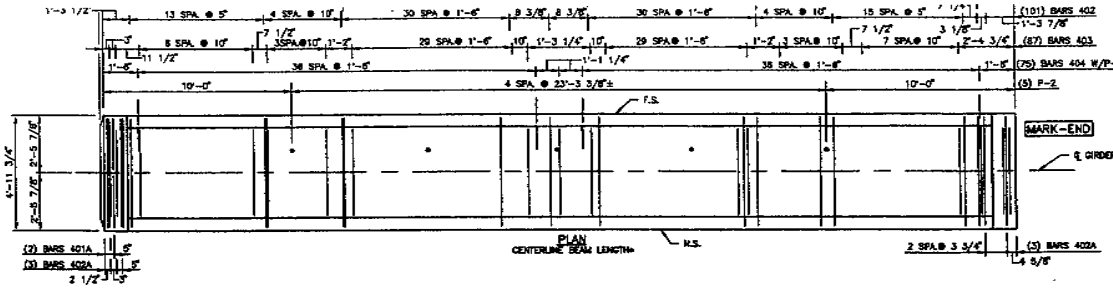

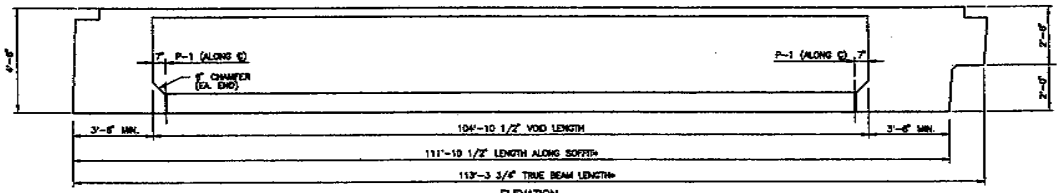

TEXAS DEPARTMENT TRANSPORTATION

☑ Approved without modification

☐ Approved with modification as shown

Date FEB 23 1995 By CKV

Approval of these drawings does not relieve the contractor of the responsibility for the correctness of detail.

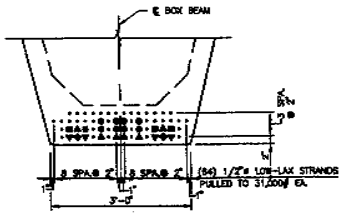

STRAND PATTERN

DEBONDING SCHEDULE
- -- NO DEBONDING
- O-- 3'-0" FROM EA. END
- □-- 6'-0" FROM EA. END
- △-- 9'-0" FROM EA. END
- ◁-- 12'-0" FROM EA. END
- ◇-- 15'-0" FROM EA. END

CONCRETE STRENGTH
RELEASE = 5,698 P.S.I.
28 DAY = 5,699 P.S.I.

REINFORCING BAR LIST

MARK	QUAN.	LENGTH	REMARKS
401	102	10'-10"	SEE TYPICAL DETAIL SHEET
401A	2	8'-0"	SEE TYPICAL DETAIL SHEET
402	101	7'-5"	SEE TYPICAL DETAIL SHEET
402A	6	7'-3"	SEE TYPICAL DETAIL SHEET
403	87	7'-3"	SEE TYPICAL DETAIL SHEET
404	75	1'-0"	STRAIGHT W/COUPLER
503	4	13'-0"	SEE TYPICAL DETAIL SHEET
504	8	7'-6"	SEE TYPICAL DETAIL SHEET
505	6	11'-2"	SEE TYPICAL DETAIL SHEET
601	5	7'-5"	SEE TYPICAL DETAIL SHEET
601A	4	7'-2"	SEE TYPICAL DETAIL SHEET
603	8	12'-4"	SEE TYPICAL DETAIL SHEET
604	2	2'-6"	STRAIGHT
605	9	110'-11"	SEE TYPICAL DETAIL SHEET
606	16	3'-2"	STRAIGHT
B-1	1	3'-8 3/8"	℄ 1 1/2x3/4" W(12) 701
702	8	12'-6"	SEE TYPICAL DETAIL SHEET
P-1	2	10"	3/4"ø SLEEVE
P-2	5	3"	2"ø SLEEVE
P-5	ONE	7"	4x1 1/2"ø SLEEVE

NOTES

1. FOR TYPICAL SECTIONS AND DETAILS SEE SHEET RF-2.
2. FOR BAR BENDING DETAILS SEE SHEET RF-2.
3. N.S. DENOTES NEAR SIDE, F.S. DENOTES FAR SIDE.
4.
5.
6.
7.
8.
9.
10.

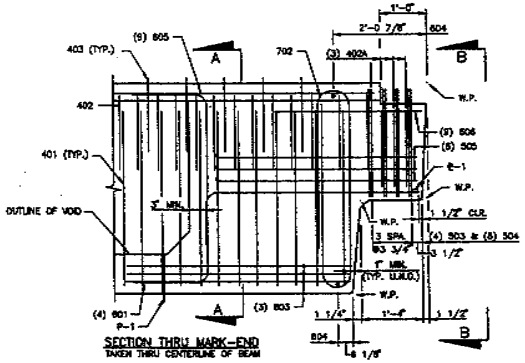

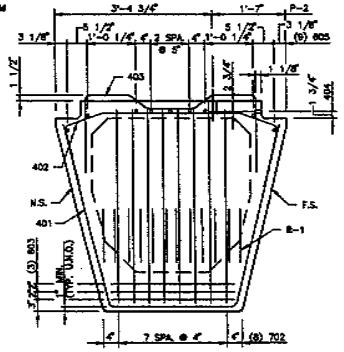

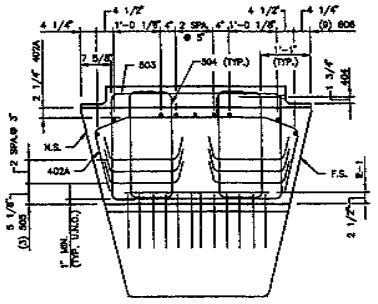

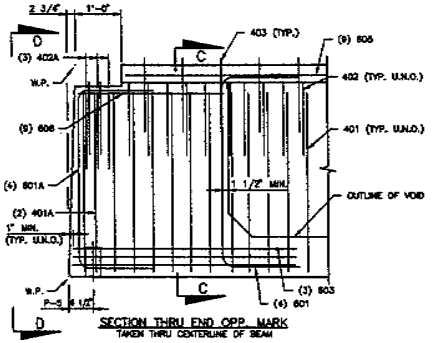

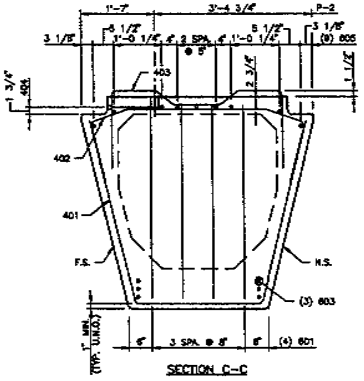

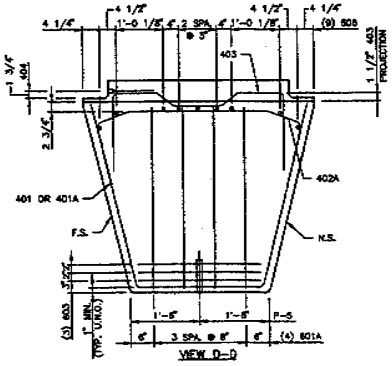

MARK	QUANTITY
RF-1R-1	ONE

STRUCTURE: RIGHT FRONTAGE STREET OVER S.P.R.R. & LORRAINE STREET

FABRICATOR: TRAYLOR BROS. PRECAST

LaBoon, Armstrong & Associates

CONTRACTOR: TRAYLOR BROS, INC.

DIST.	STATE	PROJECT NO.	HIGHWAY NO.
6	165431	CSTF-31-1(28)	IH 35
COUNTY		CONTROL NO.	SECTION NO.	JOB NO.
72	HARRIS	0177	73	718

SHEET NO. RF-3

SHT. TITLE: GIRDER PIECE DETAIL

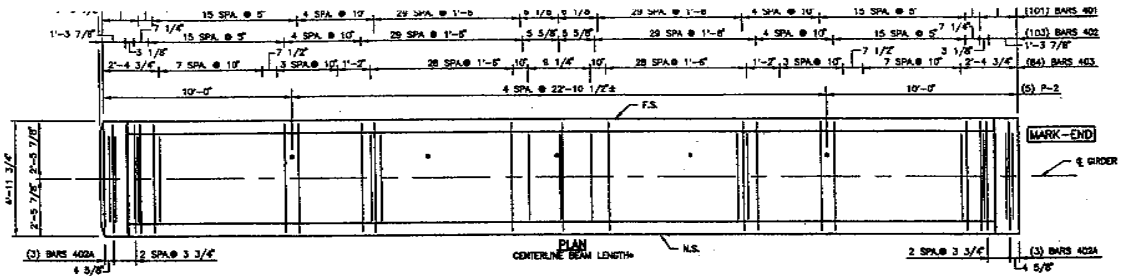

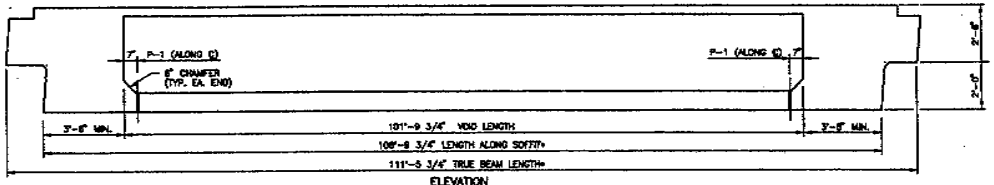

TEXAS DEPARTMENT TRANSPORTATION

☑ Approved without modification

☐ Approved with modification as shown

Date FEB 23 1995 By CKV

Approval of these drawings does not relieve the contractor of the responsibility for the correctness of detail.

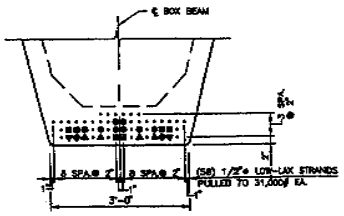

STRAND PATTERN

DEBONDING SCHEDULE

+ - NO DEBONDING
0 - 3'-0" FROM EA. END
1 - 6'-0" FROM EA. END
2 - 9'-0" FROM EA. END
3 - 12'-0" FROM EA. END
4 - 15'-0" FROM EA. END

CONCRETE STRENGTH
RELEASE = 5,234 P.S.I.
28 DAY = 5,619 P.S.I.

REINFORCING BAR LIST

MARK	QUAN.	LENGTH	REMARKS
401	101	10'-10"	SEE TYPICAL DETAIL SHEET
402	103	7'-5"	SEE TYPICAL DETAIL SHEET
402A	5	7'-3"	SEE TYPICAL DETAIL SHEET
403	84	7'-3"	SEE TYPICAL DETAIL SHEET
503	8	13'-0"	SEE TYPICAL DETAIL SHEET
504	16	7'-5"	SEE TYPICAL DETAIL SHEET
505	12	11'-2"	SEE TYPICAL DETAIL SHEET
601	8	7'-5"	SEE TYPICAL DETAIL SHEET
603	8	12'-4"	SEE TYPICAL DETAIL SHEET
604	4	2'-6"	STRAIGHT
605	8	109'-2"	SEE TYPICAL DETAIL SHEET
606	18	3'-2"	STRAIGHT
702	16	12'-9"	SEE TYPICAL DETAIL SHEET
B-1	2	3'-6 3/8"	B 1 1/2x3/4" W(12) 70#
P-1	2	10"	3/4"ø SLEEVE
P-2	5	3"	2"ø SLEEVE

NOTES

1. FOR TYPICAL SECTIONS AND DETAILS SEE SHEET RF-2.
2. FOR BAR BENDING DETAILS SEE SHEET RF-2.
3. N.S. DENOTES NEAR SIDE, F.S. DENOTES FAR SIDE.
4. P-4.
5. P-5.
6. P-6.
7. P-7.

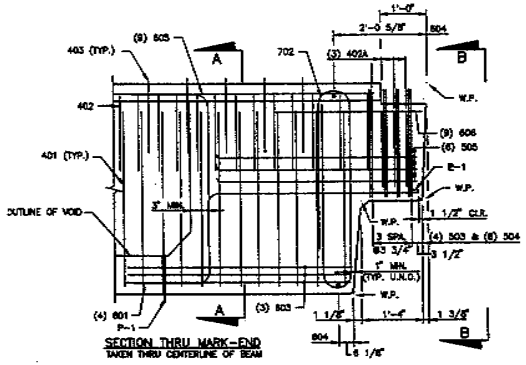

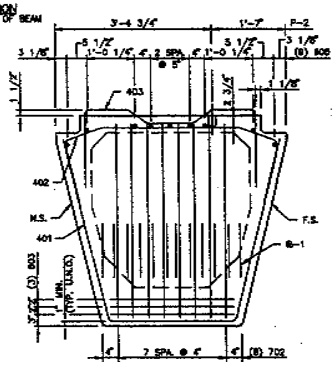

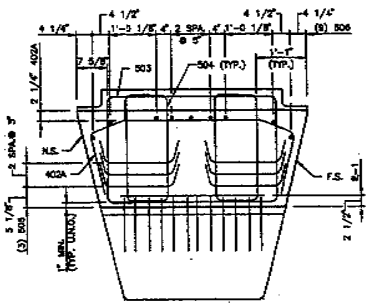

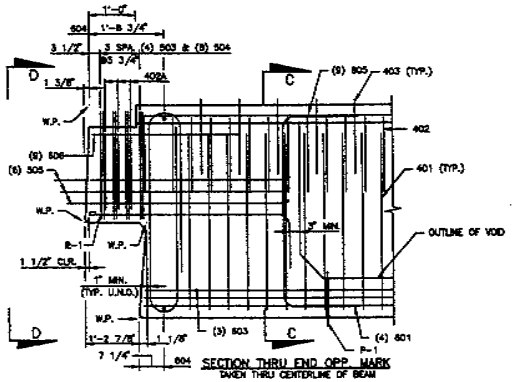

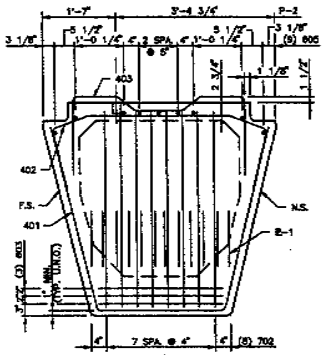

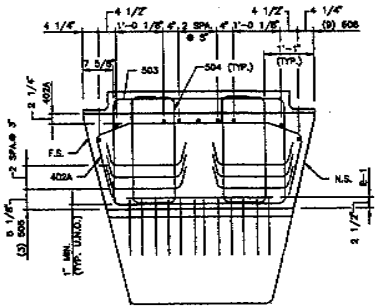

MARK #	QUANTITY
RF-2R-6	ONE

STRUCTURE: RIGHT VANTAGE STREET OVER S.P.R.R. & LORRAINE STREET

FABRICATOR: TAYLOR BROS. PRECAST

CONTRACTOR: TAYLOR BROS. INC.

DIST.	STATE	PROJECT NO.	HIGHWAY NO.
12	TEXAS	CITY-11-INT	IH 30
STATE DIST. NO.	COUNTY	CONTROL NO. SECTION NO.	JOB NO.
12	HARRIS	0177 11	115
RE JOB NO.	PROJ. ENT.	CHKD. BY	DATE: 12/94
LA JOB NO.	SHT. TITLE: GIRDER PIECE DETAIL		SHT. NO. RF-8

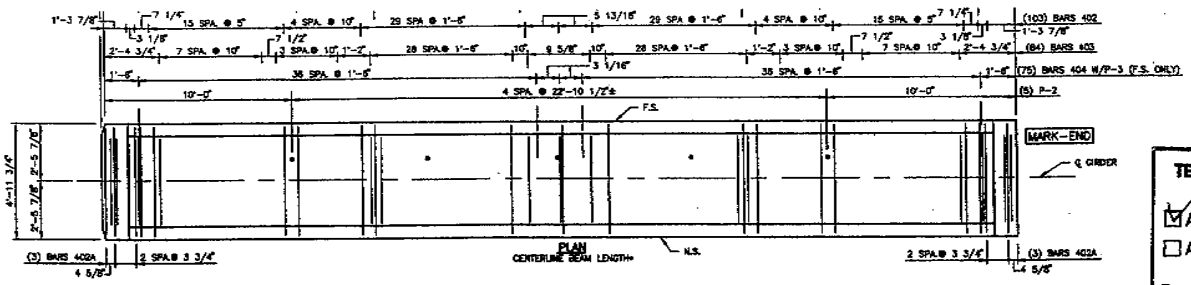

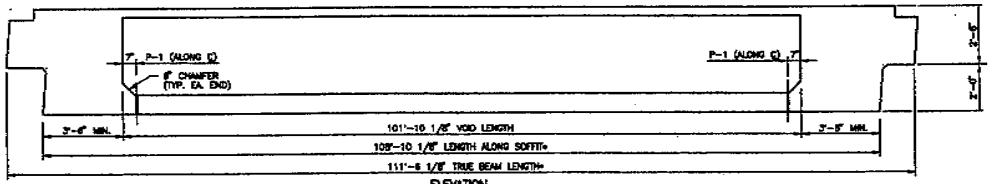

ELEVATION
ALONG CENTERLINE OF BEAM

TEXAS DEPARTMENT TRANSPORTATION

☑ Approved without modification

☐ Approved with modification as shown

Date FEB 23 1995 By CKV

Approval of these drawings does not relieve the contractor of the responsibility for the correctness of detail.

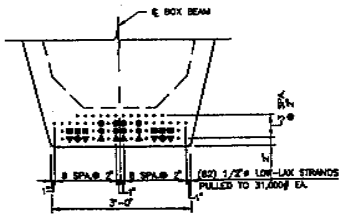

STRAND PATTERN

DEBONDING SCHEDULE
- • - NO DEBONDING
- □ - 3'-0" FROM EA. END
- ○ - 9'-0" FROM EA. END
- △ - 11'-0" FROM EA. END
- ▽ - 12'-0" FROM EA. END
- ◇ - 15'-0" FROM EA. END

CONCRETE STRENGTH
RELEASE = 4,810 P.S.I.
28 DAY = 5,810 P.S.I.

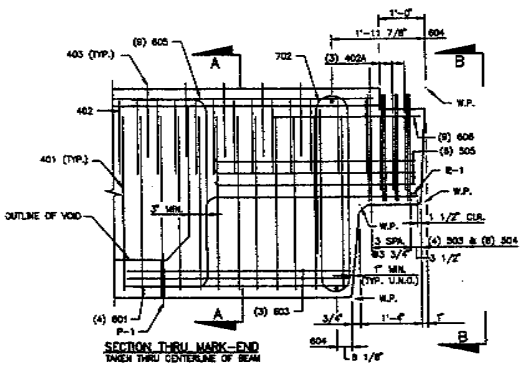

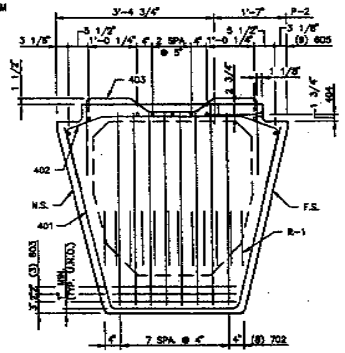

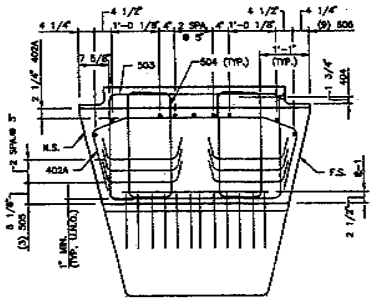

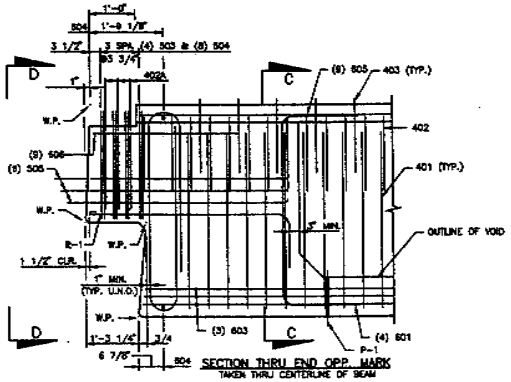

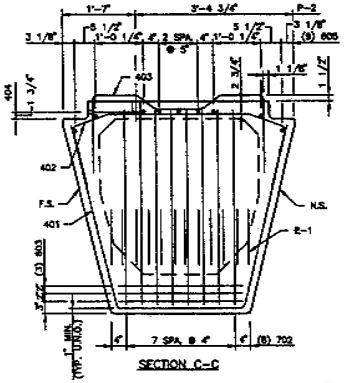

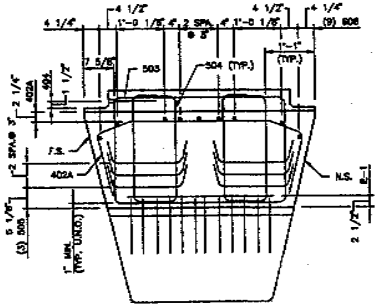

REINFORCING BAR LIST

MARK	QUAN.	LENGTH	REMARKS
401	101	10'-10"	SEE TYPICAL DETAIL SHEET
402	103	7'-5"	SEE TYPICAL DETAIL SHEET
402A	8	7'-3"	SEE TYPICAL DETAIL SHEET
403	84	7'-3"	SEE TYPICAL DETAIL SHEET
404	75	1'-0"	STRAIGHT W/COUPLER
503	8	13'-0"	SEE TYPICAL DETAIL SHEET
504	16	7'-5"	SEE TYPICAL DETAIL SHEET
505	12	11'-2"	SEE TYPICAL DETAIL SHEET
601	8	7'-5"	SEE TYPICAL DETAIL SHEET
603	6	12'-4"	SEE TYPICAL DETAIL SHEET
604	4	2'-6"	STRAIGHT
605	8	109'-2"	SEE TYPICAL DETAIL SHEET
606	18	3'-2"	STRAIGHT
702	16	12'-9"	SEE TYPICAL DETAIL SHEET
B-1	2	3'-8 3/8"	ø 1 1/2x3/4" W(12) 701
P-1	2	10"	3/4"ø SLEEVE
P-2	5	3"	2"ø SLEEVE

NOTES

1. FOR TYPICAL SECTIONS AND DETAILS SEE SHEET RF-2.
2. FOR BAR BENDING DETAILS SEE SHEET RF-2.
3. N.S. DENOTES NEAR SIDE, F.S. DENOTES FAR SIDE.
4.
5.
6.
7.
8.

MARK #	QUANTITY
RF-3R-9	ONE

STRUCTURE: RIGHT FRONTAGE STREET OVER S.P.R.R. & LORRAINE STREET

FABRICATOR: TAYLOR BROS. PRECAST

LeGrand Armstrong & Associates

CONSTRUCTION: TAYLOR BROS. INC.

STATE	PROJECT NO.	HIGHWAY NO.
DISTRICT	COUNTY	CONTROL NO.	SECTION NO.	JOB NO.
12	HARRIS	0177	71	139

DWN. BY: TB | CHK'D BY: RPGP | DATE: 12/94 | SHT. NO. RF-11

SHT. TITLE: GIRDER PIECE DETAIL

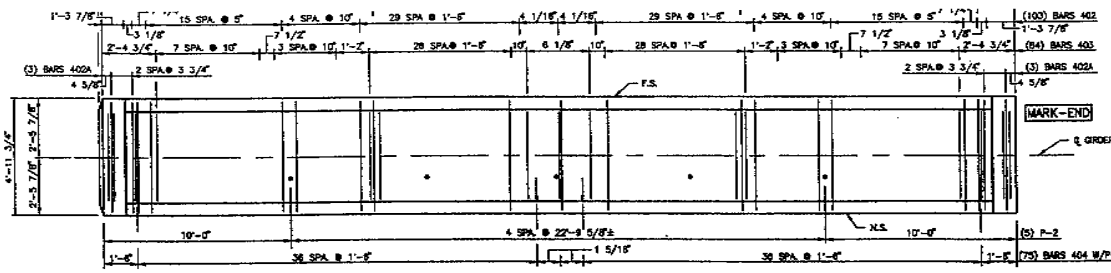

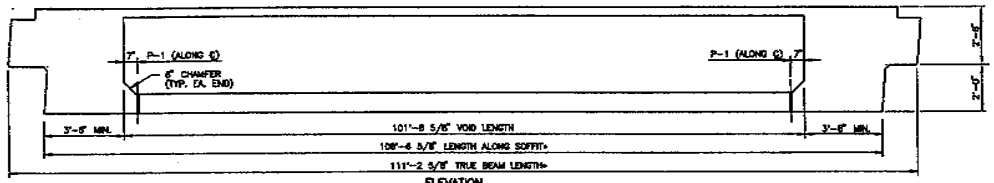

TEXAS DEPARTMENT TRANSPORTATION

☑ Approved without modification

☐ Approved with modification as shown

Date FEB 23 1995 By CKV

Approval of these drawings does not relieve the contractor of the responsibility for the correctness of detail.

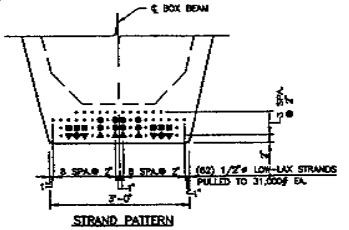

DEBONDING SCHEDULE
- - NO DEBONDING
○ - 3'-0" FROM EA. END
□ - 6'-0" FROM EA. END
◁▷ - 9'-0" FROM EA. END
▽ - 12'-0" FROM EA. END
◇ - 15'-0" FROM EA. END

CONCRETE STRENGTH
RELEASE = 5,810 P.S.I.
28 DAY = 5,810 P.S.I.

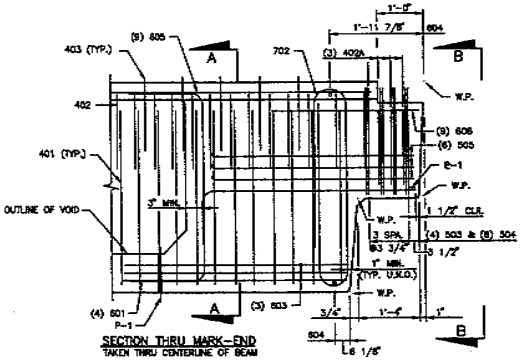

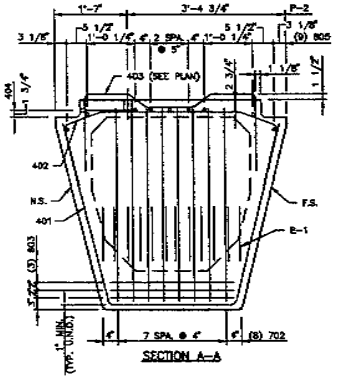

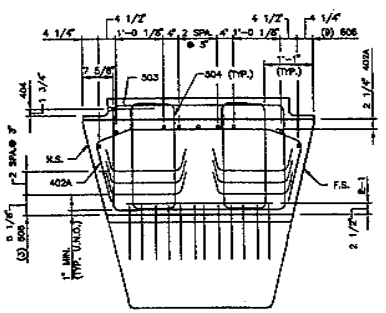

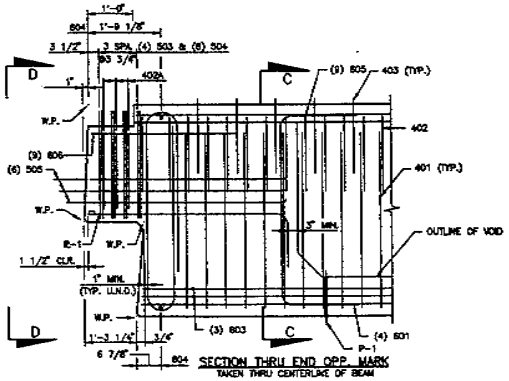

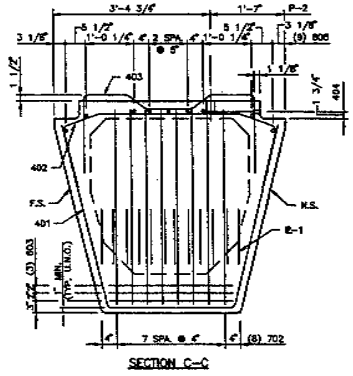

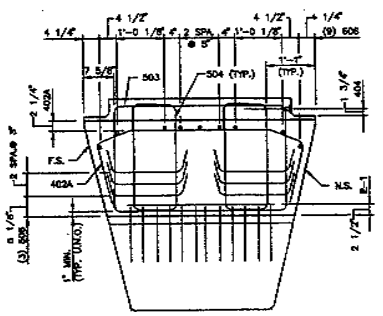

REINFORCING BAR LIST

MARK	QUAN.	LENGTH	REMARKS
401	101	10'-11"	SEE TYPICAL DETAIL SHEET
402	103	7'-5"	SEE TYPICAL DETAIL SHEET
402A	5	7'-3"	SEE TYPICAL DETAIL SHEET
403	84	7'-3"	SEE TYPICAL DETAIL SHEET
404	75	1'-0"	STRAIGHT W/COUPLER
503	8	13'-0"	SEE TYPICAL DETAIL SHEET
504	16	7'-5"	SEE TYPICAL DETAIL SHEET
505	12	11'-2"	SEE TYPICAL DETAIL SHEET
601	8	7'-5"	SEE TYPICAL DETAIL SHEET
603	6	12'-4"	SEE TYPICAL DETAIL SHEET
604	4	2'-6"	STRAIGHT
605	9	108'-11"	SEE TYPICAL DETAIL SHEET
606	18	3'-2"	STRAIGHT
702	16	12'-9"	SEE TYPICAL DETAIL SHEET
B-1	2	3'-8 3/8"	℞ 1 1/2x3/4" W(12) 701
P-1	2	10"	3/4"ø SLEEVE
P-2	5	3"	2"ø SLEEVE

NOTES
1. FOR TYPICAL SECTIONS AND DETAILS SEE SHEET RF-2.
2. FOR BAR BENDING DETAILS SEE SHEET RF-2.
3. N.S. DENOTES NEAR SIDE, F.S. DENOTES FAR SIDE.
4.
5.
6.
7.
8.
9.

STRUCTURE: RIGHT FRONTAGE STREET OVER S.P.R.R. & LORRAINE STREET

FABRICATOR: TAYLOR BROS. PRECAST

LeDoux, Armstrong & Associates, A DIVISION OF PARKHILL, SMITH & COOPER, INC., CORPUS CHRISTI, TEXAS

CONTRACTOR: TAYLOR BROS., INC.

FED. RD. DIV. NO.	STATE	PROJECT NO.			HIGHWAY NO.
6	TEXAS	0172-11-118			US 59
STATE DIST. NO.	COUNTY	CONTROL NO.	SECTION NO.		JOB NO.
12	HARRIS	0777	11		118
TR 208 NO. 8000	DWG. BY: TBI	CHK'D BY: RPCP	DATE: 12/94		SHT. NO.
LAA JOB NO. 9430040	SHT. TITLE: GIRDER PIECE DETAIL				RF-14

MARK #	QUANTITY
RF-3R-12	ONE

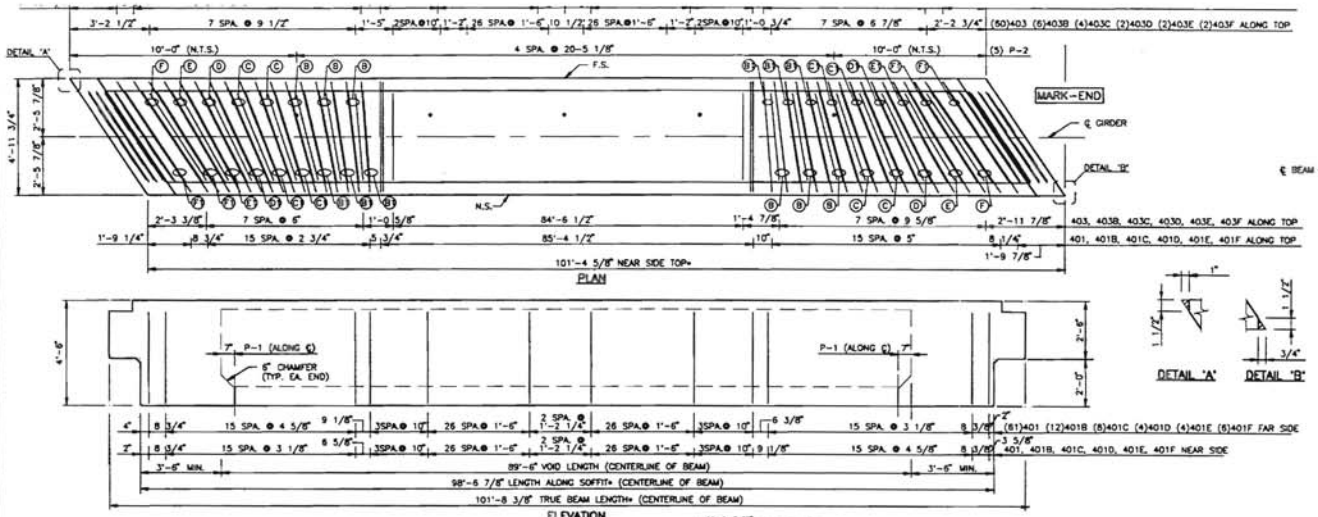

DEBONDING SCHEDULE

- = NO DEBONDING
- ○ – 3'-0" FROM EA. END
- □ – 6'-0" FROM EA. END
- △ – 9'-0" FROM EA. END
- ▽ – 12'-0" FROM EA. END
- ◇ – 15'-0" FROM EA. END
- ▲ – 18'-0" FROM EA. END
- ▼ – 21'-0" FROM EA. END
- ⊕ – 24'-0" FROM EA. END

CONCRETE STRENGTH
RELEASE = 5,012 P.S.I.
28 DAY = 5,419 P.S.I.

BAR SETS

LOCATION	BARS THIS LOCATION
B	401B, 402B & 403B
B1	401B & 402B
C	401C, 402C & 403C
C1	401C & 402C
D	401D, 402D & 403D
D1	401D & 402D
E	401E, 402E & 403E
E1	401E & 402E
F	401F, 402F & 403F
F1	401F & 402F

REINFORCING BAR LIST

MARK	QUAN.	REMARKS
401	61	SEE TYPICAL DETAIL SHEET
401B	12	SEE TYPICAL DETAIL SHEET
401C	8	SEE TYPICAL DETAIL SHEET
401D	4	SEE TYPICAL DETAIL SHEET
401E	4	SEE TYPICAL DETAIL SHEET
401F	6	SEE TYPICAL DETAIL SHEET
402	61	SEE TYPICAL DETAIL SHEET
402AF	8	SEE TYPICAL DETAIL SHEET
402B	12	SEE TYPICAL DETAIL SHEET
402C	8	SEE TYPICAL DETAIL SHEET
402D	4	SEE TYPICAL DETAIL SHEET
402E	4	SEE TYPICAL DETAIL SHEET
402F	6	SEE TYPICAL DETAIL SHEET
403	50	SEE TYPICAL DETAIL SHEET
403B	6	SEE TYPICAL DETAIL SHEET
403C	4	SEE TYPICAL DETAIL SHEET
403D	2	SEE TYPICAL DETAIL SHEET
403E	2	SEE TYPICAL DETAIL SHEET
403F	2	SEE TYPICAL DETAIL SHEET
501	9	SEE TYP. DET. SHT. (DIM 'A' = 99'-4")
502	18	STRAIGHT x 3'-7"
503A	4	SEE TYPICAL DETAIL SHEET
503B	4	SEE TYPICAL DETAIL SHEET
504A	8	SEE TYPICAL DETAIL SHEET
504B	8	SEE TYPICAL DETAIL SHEET
505C	6	SEE TYPICAL DETAIL SHEET
505D	6	SEE TYPICAL DETAIL SHEET
601	8	SEE TYPICAL DETAIL SHEET
603C	3	SEE TYPICAL DETAIL SHEET
603D	3	SEE TYPICAL DETAIL SHEET
604C	2	SEE TYPICAL DETAIL SHEET
604D	2	SEE TYPICAL DETAIL SHEET
PL-1B	ONE	R 1 1/2x3/4" W(12) 701
PL-1C	ONE	R 1 1/2x3/4" W(12) 701
702	16	SEE TYPICAL DETAIL SHEET
P-1	5	SEE TYPICAL DETAIL SHEET
P-2	5	2'ø SLEEVE

NOTES

1. FOR GENERAL NOTES SEE SHEET MLL-3 & 4.
2. FOR BAR BENDING DETAILS SEE SHEET MLL-3 & 4.
3. N.S. DENOTES NEAR SIDE, F.S. DENOTES FAR SIDE.
4. BARS 402 TO BE SPACED WITH BARS 401.
5.
6.
7.
8.

CONC. C.Y. = 35.33 | WEIGHT LBS. = 134,996

MAIN LANES OVER LYONS, (LEFT) & N.O.R.R., AND LORRAINE

FABRICATOR: TAYLOR BROS. PRECAST

CONSULTANT: LeBlanc, Armstrong & Associates, A DIVISION OF PROSOURCE ONE, INC., 4130 EAST FOWLER AVE., TAMPA, FL 33617

CONTRACTOR: TAYLOR BROS., INC.

FED. ROAD DIV. NO.	STATE	PROJECT NO.	HIGHWAY NO.
8	TEXAS	0177-11-118	US 36
STATE DIST. NO.	COUNTY	CONTROL NO. / SECTION NO.	JOB NO.
12	HARRIS	0177 / 11	118

TEXAS DEPARTMENT OF TRANSPORTATION

☒ Approved without modification

☐ Approved subject to corrections noted

Date 9-14-95 By LL

SEP 05 1995

Approval of the shop drawings does not relieve the contractor of responsibility for the correctness

TB JOB NO. 9508	DWG. BY TB	CHK'D BY MKP	DATE: 8/95	SHT. NO. MLL-37
AA JOB NO. 06320601	SHT. TITLE: GIRDER PIECE DETAIL			

MARK #	QUANTITY
MLL-9-34	ONE

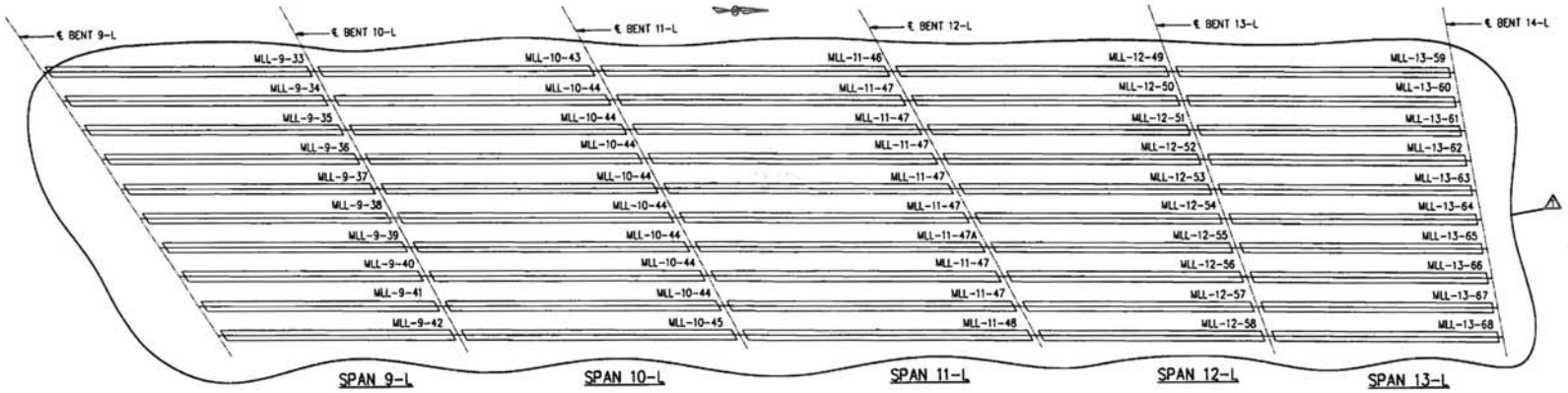

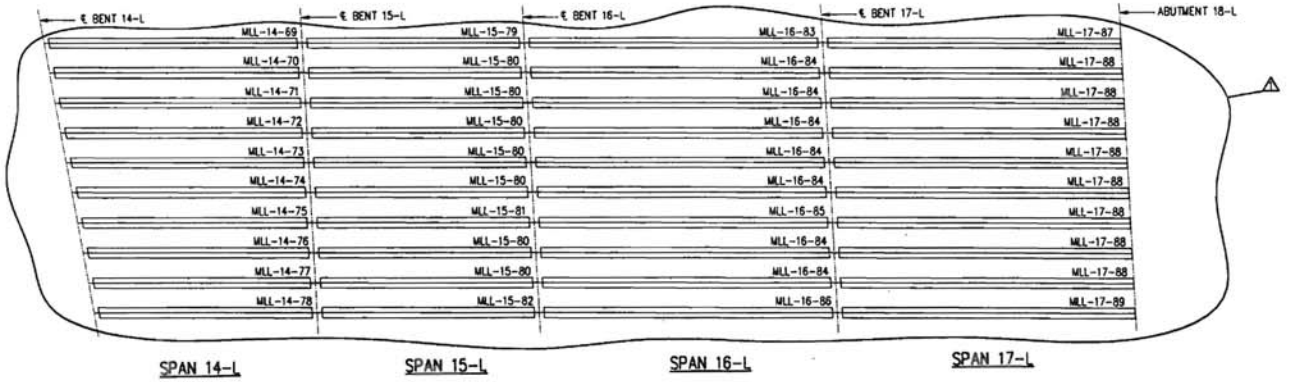

BRIDGE SPAN MARK NO.
CL-3-8

BEAM MARK LEGEND

TEXAS DEPARTMENT TRANSPORTATION

☒ Approved without modification

☐ Approved with modification as shown

Date 9.14.95 By LL

Approval of these drawings does not relieve the contractor of the responsibility for the correctness of detail.

REV.	DATE	DESCRIPTION
⚠	9/5/95	REVISED GIRDER MARK NUMBERS

STRUCTURE: MAIN LANES OVER LYONS, (LEFT) T. & N.O.R.R. AND LORRAINE

FABRICATOR: TAYLOR BROS. PRECAST

LeBlanc, Armstrong & Associates
A DIVISION OF FREDERIC R. HARRIS, INC.
4135 EAST POWLER AVE.
TYLER, TX. 75707

CONTRACTOR: TAYLOR BROS., INC.

FED. ROAD DIV. NO.	STATE	PROJECT NO.			HIGHWAY NO.
6	TEXAS	C177-11-118			US 59
STATE DIST. NO.	COUNTY	CONTROL NO.	SECTION NO.		JOB NO.
12	HARRIS	0177	11		118

TBE JOB NO. 3908 | DWG. BY: TB | CH'D BY: BRGR | DATE: 6/95 | SHT. NO.

LAA JOB NO. 06.93.00604 | SHT. TITLE: GIRDER LAYOUT | MLL-

APPENDIX B

Calculations

Appendix B includes the deboning schedule for the prestressing strands, the prestress loss calculations, and the moment capacity / compressive stress block calculations for the one of the Houston prestressed concrete trapezoidal box beams with dapped ends (MLL-9-34-A or N-II).

Prestressing Strand Debonding Schedule

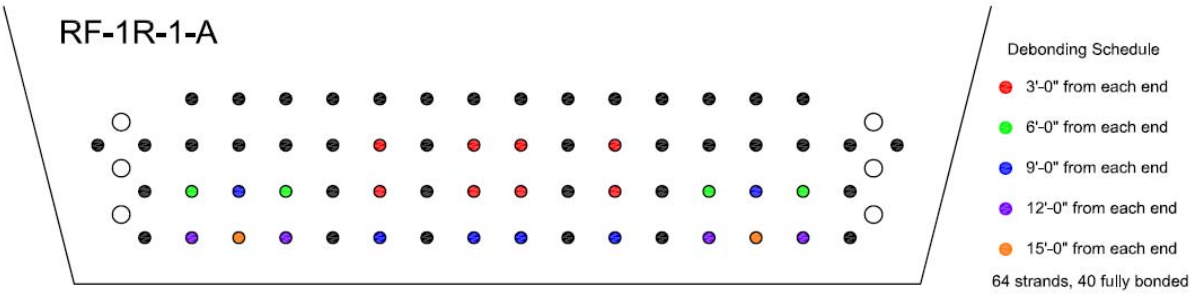

Find Center of Gravity of Steel Tie

$A_{strand} := 0.153in^2$ $n_{strand} := 40$

$A_{bar} := .44in^2$ $n_{bar} := 6$

$$cg_{strand} := \frac{6 \cdot 2in + 6 \cdot 4in + 14 \cdot 6in + 14 \cdot 8in}{n_{strand}} = 5.8 \cdot in$$

$$cg_{bar} := \frac{2 \cdot 3in + 2 \cdot 5in + 2 \cdot 7in}{n_{bar}} = 5 \cdot in$$

$$cgs := \frac{cg_{strand} \cdot n_{strand} \cdot A_{strand} + cg_{bar} \cdot n_{bar} \cdot A_{bar}}{n_{strand} \cdot A_{strand} + n_{bar} \cdot A_{bar}} = 5.559 \cdot in$$

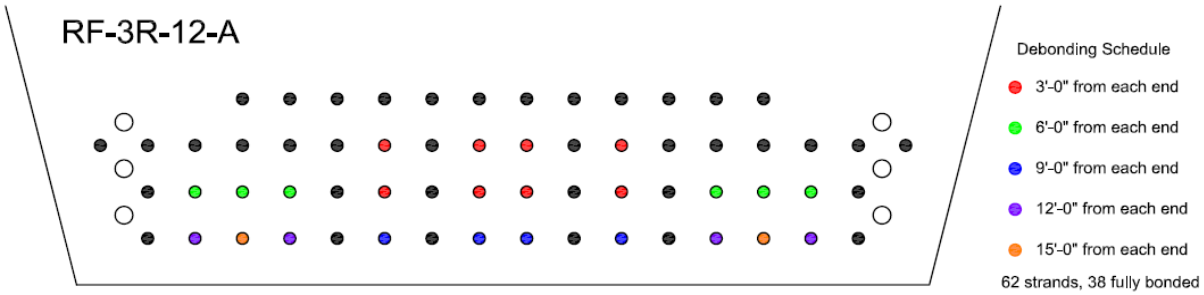

Find Center of Gravity of Steel Tie

$A_{strand} := 0.153in^2$ $n_{strand} := 38$

$A_{bar} := .44in^2$ $n_{bar} := 6$

$$cg_{strand} := \frac{6 \cdot 2in + 6 \cdot 4in + 14 \cdot 6in + 12 \cdot 8in}{n_{strand}} = 5.684 \cdot in$$

$$cg_{bar} := \frac{2 \cdot 3in + 2 \cdot 5in + 2 \cdot 7in}{n_{bar}} = 5 \cdot in$$

$$cgs := \frac{cg_{strand} \cdot n_{strand} \cdot A_{strand} + cg_{bar} \cdot n_{bar} \cdot A_{bar}}{n_{strand} \cdot A_{strand} + n_{bar} \cdot A_{bar}} = 5.471 \cdot in$$

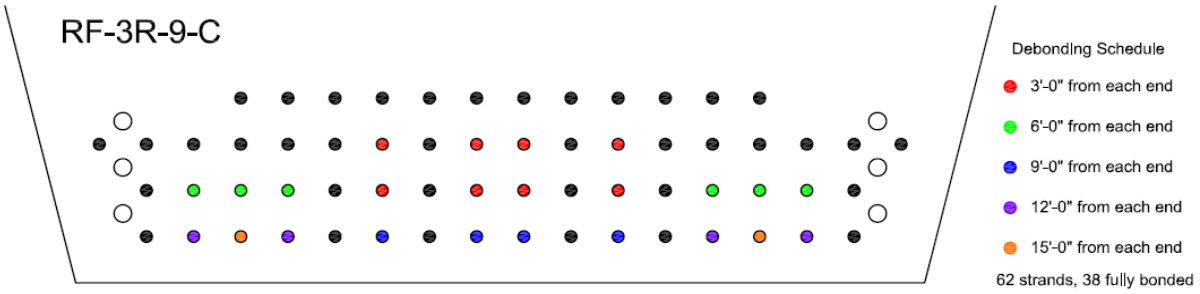

Find Center of Gravity of Steel Tie

$A_{strand} := 0.153in^2$ $n_{strand} := 38$

$A_{bar} := .44in^2$ $n_{bar} := 6$

$$cg_{strand} := \frac{6 \cdot 2in + 6 \cdot 4in + 14 \cdot 6in + 12 \cdot 8in}{n_{strand}} = 5.684 \cdot in$$

$$cg_{bar} := \frac{2 \cdot 3in + 2 \cdot 5in + 2 \cdot 7in}{n_{bar}} = 5 \cdot in$$

$$cgs := \frac{cg_{strand} \cdot n_{strand} \cdot A_{strand} + cg_{bar} \cdot n_{bar} \cdot A_{bar}}{n_{strand} \cdot A_{strand} + n_{bar} \cdot A_{bar}} = 5.471 \cdot in$$

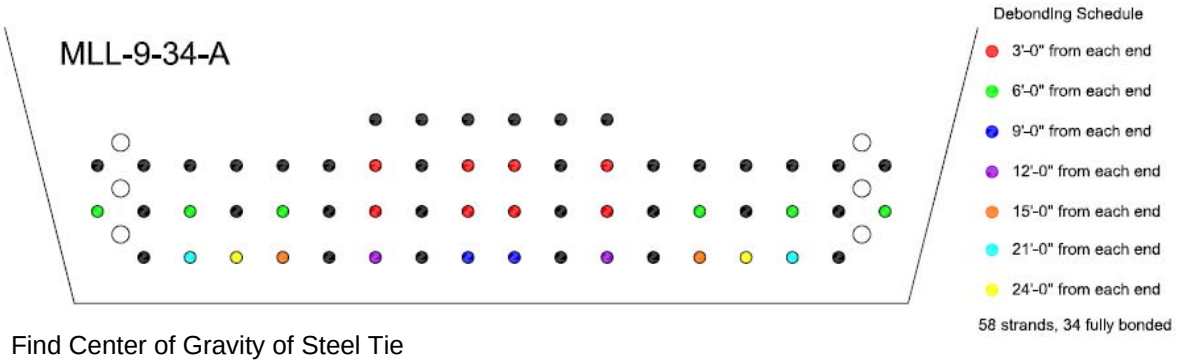

Find Center of Gravity of Steel Tie

$A_{strand} := 0.153in^2$ $n_{strand} := 34$

$A_{bar} := .44in^2$ $n_{bar} := 6$

$$cg_{strand} := \frac{6 \cdot 2in + 8 \cdot 4in + 14 \cdot 6in + 6 \cdot 8in}{n_{strand}} = 5.176 \cdot in$$

$$cg_{bar} := \frac{2 \cdot 3in + 2 \cdot 5in + 2 \cdot 7in}{n_{bar}} = 5 \cdot in$$

$$cgs := \frac{cg_{strand} \cdot n_{strand} \cdot A_{strand} + cg_{bar} \cdot n_{bar} \cdot A_{bar}}{n_{strand} \cdot A_{strand} + n_{bar} \cdot A_{bar}} = 5.117 \cdot in$$

AASHTO Estimation of Loss in Prestressing Strands

$\Delta f_{pT} := \Delta f_{pES} + \Delta f_{pLT}$ (5.9.5.1 − 1)

Prestressing Strand Properties

$f_{pu} := 270ksi$ Ultimate strength

$f_{py} := 0.9 \cdot f_{pu} = 243 \cdot ksi$ Yield Strength

$E_p := 28500ksi$ Modulus of Elasticity

$d_b := 0.5in$ Strand diameter

$A_{strand} := 0.153 \cdot in^2$ Area of strand

Concrete Section Properties

$A_g := 1131.5in^2$ Gross cross sectional area (Hollow Section)

$I_g := 404968in^4$ Gross moment of inertia

$y_b := 26.71in$ Distance from CG to bottom

$y_t := 27.29in$ Distance from CG to top

$w_{sw} := 1.154 \frac{kip}{ft}$ Self weight of beam

$A_{deck} := 296in^2$ Cross sectional area of cip deck

$y_{t\_deck} := 2.89in$ Distance from CG to top of deck

$I_{deck} := 1290in^4$ Moment of inertia of deck

RF-1R-1 (H-II)

$f'_c := 6.39ksi$ Concrete Strength at testing

$E_c := 57000 \cdot \sqrt{f'_c \cdot psi} = 4556.436 \cdot ksi$ Elastic Modulus at testing

$f'_{ci} := 6.62ksi$ Concrete Strength at release

$E_{ci} := 57000 \cdot \sqrt{f'_{ci} \cdot psi} = 4637.713 \cdot ksi$ Elastic Modulus at release

$f'_{c\_deck} := 8.02ksi$

$E_{cd} := 57000 \cdot \sqrt{f'_{c\_deck} \cdot psi} = 5104.604 \cdot ksi$

$A_c := A_g + A_{deck} \cdot \frac{f'_{c\_deck}}{f'_c} = 1503.005 \cdot in^2$

$$y_{tc} := \frac{A_g \cdot (y_t + 4in) + A_{deck} \cdot \frac{f'_{c\_deck}}{f'_c} \cdot y_{t\_deck}}{A_c} = 24.27 \cdot in$$

$y_{tb} := 58in - y_{tc} = 33.73 \cdot in$

$$I_c := I_g + A_g \cdot (y_t + 4in - y_{tc})^2 + I_{deck} + A_{deck} \cdot \frac{f'_{c\_deck}}{f'_c} \cdot (y_{t\_deck} - y_{tc})^2 = 631835.561 \cdot in^4$$

$n_{strands} := 64$ Number of strands

$A_{ps} := n_{strands} \cdot A_{strand} = 9.792 \cdot in^2$ Area of prestress steel

$P := 31kip$ Initial force in strand

$P_i := n_{strands} \cdot P = 1984 \cdot kip$ Initial prestress force

$f_{pi} := \frac{P_i}{A_{ps}} = 202.614 \cdot ksi$ Initial stress in strands

$d_p := 52in - \frac{(16 \cdot 2 + 16 \cdot 4 + 18 \cdot 6 + 14 \cdot 8)in}{64} = 47.063 \cdot in$ Depth to CG of prestress

$e_m := d_p - y_t = 19.773 \cdot in$ Prestress eccentricity

$e_{pc} := (d_p + 4in - y_{tc}) = 26.792 \cdot in$ Prestress eccentricity of composite section

$L := 113ft + 3.75in$ Length of beam

Elastic Shortening

$M_g := \frac{w_{sw} \cdot L^2}{8} = 1852.13 \cdot kip \cdot ft$ Moment due to self weight

$$\Delta f_{pES} := \frac{A_{ps} \cdot f_{pi} \cdot \left(I_g + e_m^2 \cdot A_g\right) - e_m \cdot M_g \cdot A_g}{A_{ps} \cdot \left(I_g + e_m^2 \cdot A_g\right) + \frac{A_g \cdot I_g \cdot E_{ci}}{E_p}} = 14.287 \cdot ksi \quad \text{(C5.9.5.2.3a-1)}$$

$$f_{cgp} := \frac{P_i}{A_g} + \frac{P_i \cdot e_m^2}{I_g} - \frac{M_g \cdot e_m}{I_g} = 2.584 \cdot ksi$$

$$\Delta f_{pES} := \frac{E_p}{E_{ci}} \cdot f_{cgp} = 15.877 \cdot ksi$$

Long Term Losses

Girder Shrinkage Pre-Deck

$H := 75$ Humidity (%)

$t_f := 365.24 \cdot 14 - 5.36 = 5108$ Final age (days)

$t_i := \frac{51}{24}$ Age at transfer (days)

$t_d := t_f - 12$ Age at deck placement (days)

$k_s := 1.0$

$k_{hc} := 1.56 - 0.008H$

$k_f := \frac{5}{1 + \frac{f'_{ci}}{ksi}} = 0.656$

$k_{td} := \frac{t_f}{61 - 4 \cdot \frac{f'_{ci}}{ksi} + t_f} = 0.993$

$\psi_{b\_fi} := 1.9 \cdot k_s \cdot k_{hc} \cdot k_f \cdot k_{td} \cdot t_i^{-0.118}$ eq 5.4.2.3.2-1

$k_{hs} := 2 - 0.014H = 0.95$

$\varepsilon_{bid} := k_s \cdot k_{hs} \cdot k_f \cdot k_{td} \cdot 0.48 \cdot 10^{-3}$

$K_{id} := \frac{1}{1 + \frac{E_p}{E_{ci}} \cdot \frac{A_{ps}}{A_g} \cdot \left(1 + \frac{A_g \cdot e_m^2}{I_g} \right) \cdot \left(1 + 0.7 \cdot \psi_{b\_fi} \right)} = 0.836$ eq 5.9.5.4.2.a-2

$\Delta f_{pSR} := \varepsilon_{bid} \cdot E_p \cdot K_{id} = 7.082 \cdot ksi$ Prestress loss due to shrinkage of girder concrete between time of transfer and deck placment

Girder Creep - Pre-Deck

$k_{td} := \frac{t_d}{61 - 4 \cdot \frac{f'_{ci}}{ksi} + t_d}$

$\psi_{b\_di} := 1.9 \cdot k_s \cdot k_{hc} \cdot k_f \cdot k_{td} \cdot t_i^{-0.118}$

$\Delta f_{pCR} := \frac{E_p}{E_{ci}} \cdot f_{cgp} \cdot \psi_{b\_di} \cdot K_{id} = 14.438 \cdot ksi$ Prestress loss due to creep of girder concrete between time of transfer and deck placement

Strand Relaxation - Pre-Deck

$f_{pt} := 0.75 \cdot f_{pu} = 202.5 \cdot ksi$

$K'_L := 45$

Prestress loss due to relaxation of prestressing strands between time of transfer and deck placement

$$\Delta f_{pR1} := \frac{f_{pt}}{K'_L} \cdot \frac{\log(24t_d)}{\log(24t_i)} \cdot \left(\frac{f_{pt}}{f_{py}} - 0.55 \right) \left[1 - \frac{3\left(\Delta f_{pSR} + \Delta f_{pCR}\right)}{f_{pt}} \right] \cdot K_{id} = 2.164 \cdot ksi$$

Girder Shrinkage Post-Deck

$$K_{df} := \frac{1}{1 + \frac{E_p}{E_{ci}} \cdot \frac{A_{ps}}{A_g} \cdot \left(1 + \frac{A_c \cdot e_{pc}^{\,2}}{I_c} \right) \cdot \left(1 + 0.7 \cdot \psi_{b\_fi} \right)} = 0.798$$

$$k_{td} := \frac{\left(t_f - t_d\right)}{61 - 4 \cdot \frac{f'_{ci}}{ksi} + \left(t_f - t_d\right)} = 0.258$$

$\varepsilon_{bdf} := k_s \cdot k_{hs} \cdot k_f \cdot k_{td} \cdot 0.48 \cdot 10^{-3}$

$\Delta f_{pSD} := \varepsilon_{bdf} \cdot E_p \cdot K_{df} = 1.755 \cdot ksi$

Prestress Loss due to shrinkage of girder concrete between time of deck placement and final time

Girder Creep Post-Deck

$\Delta f_{cd} := \Delta f_{pSD}$

$$k_{td} := \frac{t_f}{61 - 4 \cdot \frac{f'_{ci}}{ksi} + t_f}$$

$\psi_{b\_fd} := 1.9 \cdot k_s \cdot k_{hc} \cdot k_f \cdot k_{td} \cdot t_d^{\,-0.118}$

Prestress Loss due to creep of girder concrete between time of deck placement and final time

$$\Delta f_{pCD} := \frac{E_p}{E_{ci}} \cdot f_{cgp} \cdot \left(\psi_{b\_fi} - \psi_{b\_di} \right) K_{df} + \frac{E_p}{E_c} \cdot \Delta f_{cd} \cdot \psi_{b\_fd} \cdot K_{df} = 3.801 \cdot ksi$$

Strand Relaxation - Pre-Deck

$\Delta f_{pR2} := \Delta f_{pR1}$

Prestress loss due to relaxation of ps strands in composite section between time of deck placement and final time

$\Delta f_{pLT} := \Delta f_{pSR} + \Delta f_{pCR} + \Delta f_{pR1} + \Delta f_{pSD} + \Delta f_{pCD} + \Delta f_{pR2} = 31.404 \cdot ksi$

$f_{se\_RF1} := f_{pi} - \Delta f_{pES} - \Delta f_{pLT} = 155.334 \cdot ksi$

Stress in Prestressing Steel after all Losses

$f_{se\_RF9} := 154.6 ksi$

$f_{se\_RF12} := 152.6 ksi$

$f_{se\_MLL} := 160.6 ksi$

MLL-9-34-A (N-II) *Compression Block and Final Strand Stress Calculations*

Compression Block Calculation

$f'_c := 9.28\text{ksi}$ Compressive Strength of Concrete

$f_{se} := 160.6\text{ksi}$ Effective Stress in Strands After Losses

$f_y := 63\text{ksi}$ Yield Strength of Mild Reinforcement

$L := 32.21\text{ft}$ Beam Length

$a_{shear} := 99\text{in}$ Shear Span

$span := 369.6\text{in}$ Total Span Length

$P := 1020\cdot\text{kip}$ $V := P\cdot\dfrac{(span - a_{shear})}{span} = 746.786\cdot\text{kip}$ Ultimate Applied Load

$sw := \dfrac{46.4\text{kip}}{L} = 1.441\cdot\dfrac{\text{kip}}{\text{ft}}$ Self Weight

$M_u := V\cdot a_{shear} + sw\cdot\dfrac{a_{shear}^2}{2} = 6.21\times 10^3\cdot\text{kip}\cdot\text{ft}$ Moment due to Applied Load and Self Weight

$A_{ps} := 42\cdot 0.153\text{in}^2 = 6.426\cdot\text{in}^2$ 42 Developed Strands

$b := 58.25\text{in}$ Width of Compression Block

$d_p := 4\text{ft} + \left(4 + \dfrac{3}{16}\right)\text{in} = 52.188\cdot\text{in}$ Depth to Centroid of Prestressing Strands

$M_n := A_{ps}\cdot f_{ps}\cdot\left(d_p - \dfrac{a}{2}\right)$ Nominal Moment Capacity

$a := \dfrac{A_{ps}\cdot f_{ps}}{0.85\cdot b\cdot f'_c}$ Height of Compression Block

$$f_{ps} := \frac{A_{ps}\cdot d_p - \sqrt{\left(A_{ps}\cdot d_p\right)^2 - 4\cdot\left(\dfrac{A_{ps}^2}{2\cdot 0.85\cdot b\cdot f'_c}\right)\cdot M_u}}{2\cdot\dfrac{A_{ps}^2}{2\cdot 0.85\cdot b\cdot f'_c}} = 229.254\cdot\text{ksi}$$ Final Stress in Strands

$a := \dfrac{A_{ps}\cdot f_{ps}}{0.85\cdot b\cdot f'_c} = 3.206\cdot\text{in}$ Height of Compression Block

APPENDIX C

Strut-and-Tie Models

Appendix C includes the detailed strut-and-tie model calculations for one of the Houston prestressed concrete trapezoidal box beams with dapped ends (MLL-9-34-A or N-II) and the results from all five models.

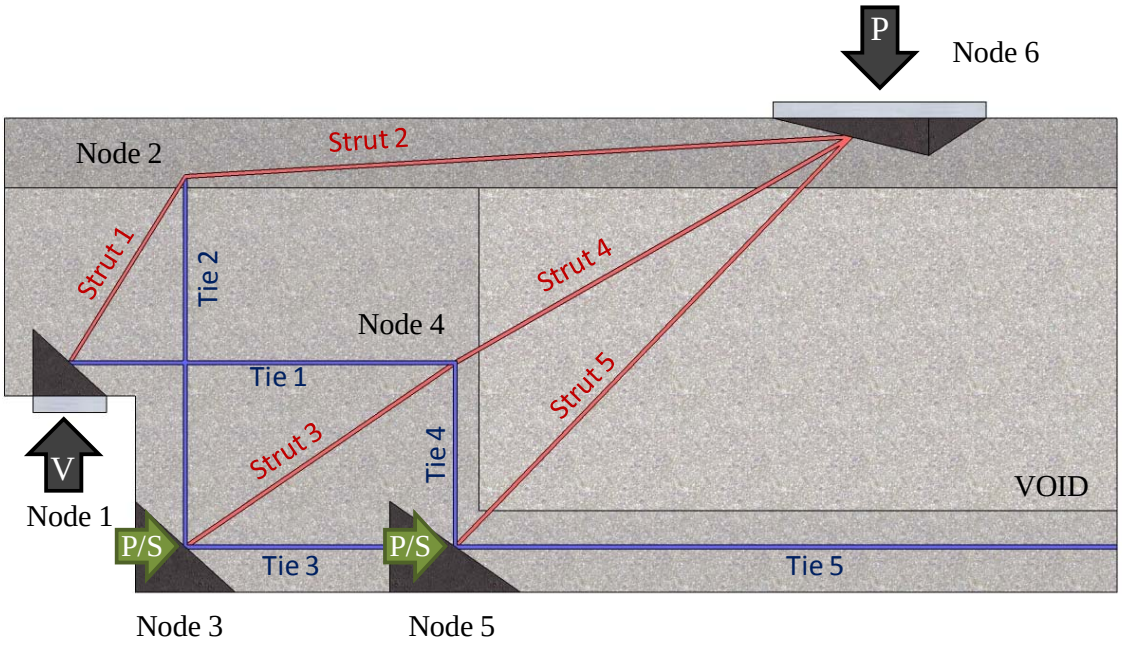

Figure C-1: Standard Dapped End Strut and Tie Model

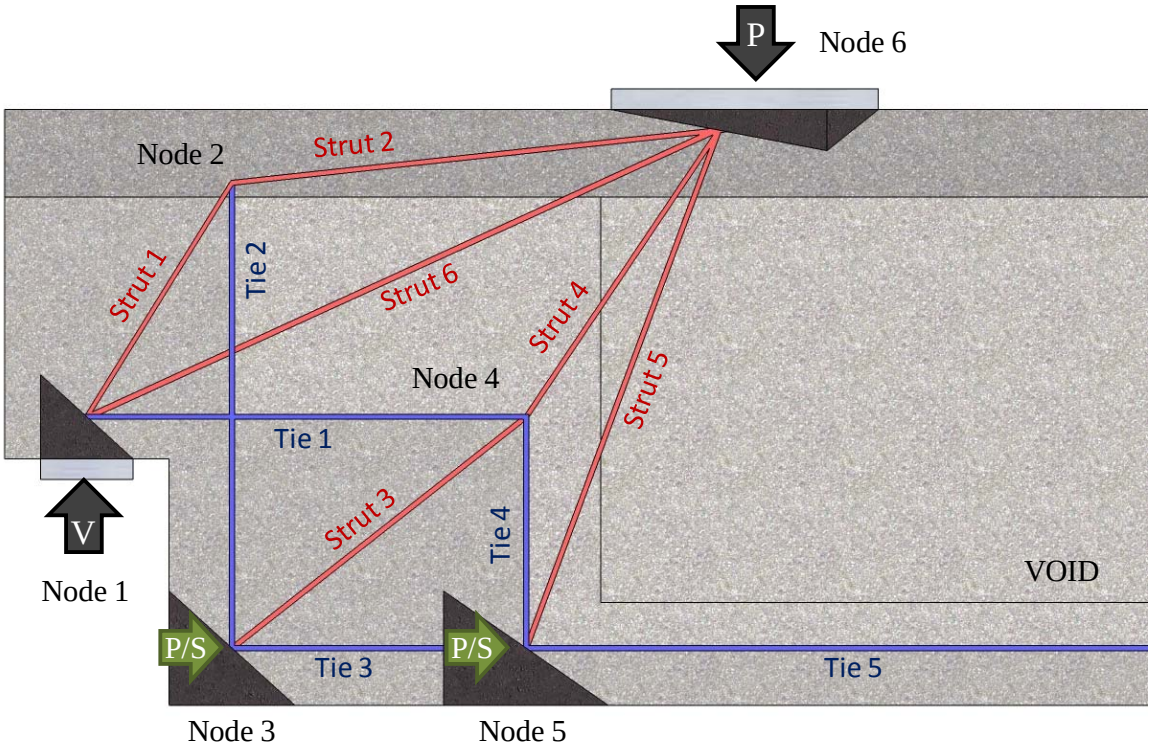

Figure C-2: Strut-and-Tie Model for RF-3R-9-A

MLL-9-34-A (N-II)

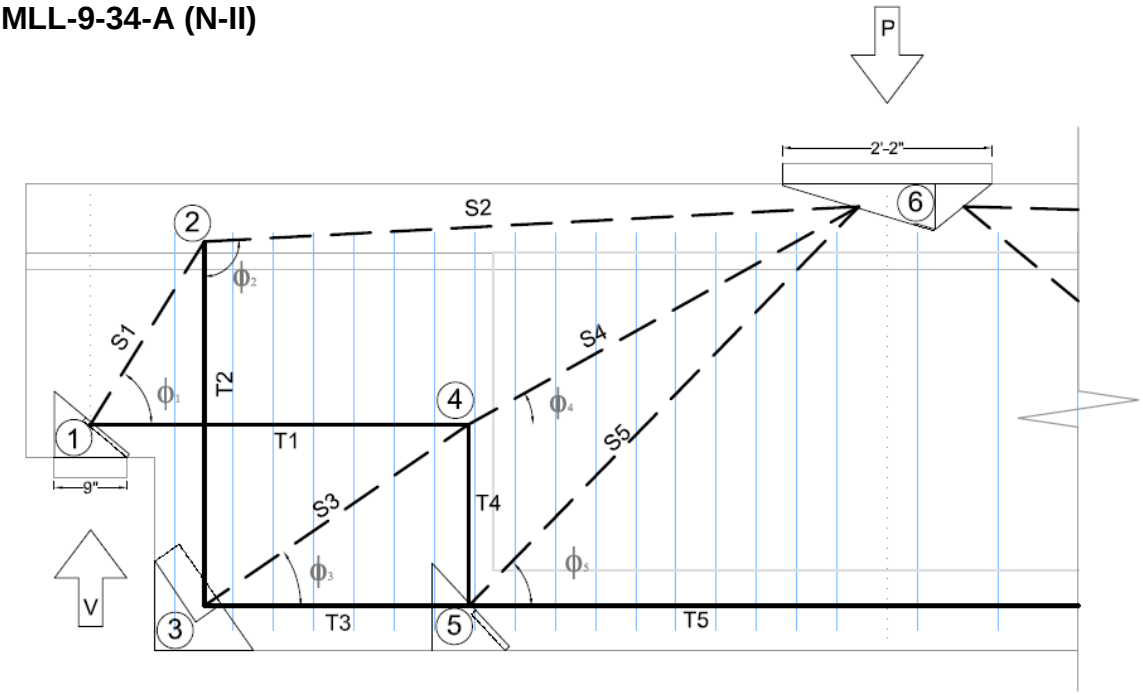

Input

$P := 1kip$ Apply a nominal 1 kip load

$span_1 := 99in$ $span_2 := 251in$

$V_1 := P \cdot \frac{span_2}{span_1 + span_2} = 0.72 \cdot kip$ $V_2 := P - V_1 = 0.28 \cdot kip$

$\varphi_1 := 58deg$ $\varphi_4 := 30deg$ $\varphi_7 := 34deg$

$\varphi_2 := 93deg$ $\varphi_5 := 46deg$ $\varphi_8 := 34deg$

$\varphi_3 := 35deg$ $\varphi_6 := 40deg$ $\varphi_9 := 40deg$

Calculations

$S_1 := \frac{V_1}{\sin(\varphi_1)} = 0.85 \cdot kip$

$T_1 := S_1 \cdot \cos(\varphi_1) = 0.45 \cdot kip$

$S_2 := \frac{S_1 \cdot \cos(\varphi_1)}{\cos(\varphi_2 - 90deg)} = 0.45 \cdot kip$

$T_2 := S_1 \cdot \sin(\varphi_1) - \left| S_2 \cdot \sin(\varphi_2 - 90deg) \right| = 0.69 \cdot kip$

$S_3 := \frac{T_2}{\sin(\varphi_3)} = 1.21 \cdot kip$

$T_3 := S_3 \cdot \cos(\varphi_3) = 0.99 \cdot kip$

$$S_4 := \frac{S_3 \cdot \cos(\varphi_3) - T_1}{\cos(\varphi_4)} = 0.63 \cdot kip$$

$$T_4 := S_3 \cdot \sin(\varphi_3) - S_4 \cdot \sin(\varphi_4) = 0.38 \cdot kip$$

$$S_5 := \frac{T_4}{\sin(\varphi_5)} = 0.53 \cdot kip$$

$$T_5 := T_3 + S_5 \cdot \cos(\varphi_5) = 1.36 \cdot kip$$

$$S_6 := \frac{P - S_2 \cdot \sin(\varphi_2 - 90deg) - S_4 \cdot \sin(\varphi_4) - S_5 \cdot \sin(\varphi_5)}{\sin(\varphi_6)} = 0.44 \cdot kip$$

$$T_6 := S_6 \cdot \sin(\varphi_6) = 0.28 \cdot kip$$

$$S_7 := S_2 \cdot \cos(\varphi_2 - 90deg) + S_4 \cdot \cos(\varphi_4) + S_5 \cdot \cos(\varphi_5) - S_6 \cdot \cos(\varphi_6) = 1.02 \cdot kip$$

$$S_8 := \frac{T_6}{\sin(\varphi_7)} = 0.51 \cdot kip$$

$$T_7 := T_5 - S_6 \cdot \cos(\varphi_6) = 1.02 \cdot kip$$

$$T_8 := S_8 \cdot \sin(\varphi_7) = 0.28 \cdot kip$$

$$T_9 := T_7 - S_8 \cdot \cos(\varphi_7) = 0.6 \cdot kip$$

$$S_{10} := \frac{T_8}{\sin(\varphi_8)} = 0.51 \cdot kip$$

$$S_9 := S_7 - S_8 \cdot \cos(\varphi_7) = 0.6 \cdot kip$$

$$T_{10} := S_{10} \cdot \sin(\varphi_8) = 0.28 \cdot kip$$

$$T_{11} := T_9 - S_{10} \cdot \cos(\varphi_8) = 0.18 \cdot kip$$

$$S_{12} := \frac{T_{11}}{\sin(\varphi_9)} = 0.28 \cdot kip$$

$$S_{11} := S_9 - S_{10} \cdot \cos(\varphi_8) = 0.18 \cdot kip$$

$$V_6 := S_2 \cdot \cos(180deg - \varphi_2) + S_4 \cdot \cos(90deg - \varphi_4) + S_5 \cdot \cos(90deg - \varphi_5) = 0.72 \cdot kip$$

$$H_6 := S_2 \cdot \sin(180deg - \varphi_2) + S_4 \cdot \sin(90deg - \varphi_4) + S_5 \cdot \sin(90deg - \varphi_5) = 1.36 \cdot kip$$

Results

$S_1 = 0.85 \cdot kip$ $T_1 = 0.45 \cdot kip$

$S_2 = 0.45 \cdot kip$ $T_2 = 0.69 \cdot kip$

$S_3 = 1.21 \cdot kip$ $T_3 = 0.99 \cdot kip$

$S_4 = 0.63 \cdot kip$ $T_4 = 0.38 \cdot kip$

$S_5 = 0.53 \cdot kip$ $T_5 = 1.36 \cdot kip$

$$N_6 := \sqrt{V_6^{\,2} + H_6^{\,2}} = 1.54 \cdot kip$$

$$\phi_{N6} := \operatorname{asin}\left(\frac{H_6}{N_6}\right) = 62.16 \cdot deg$$

MLL-9-34-A (N-II) TxDOT 5253 Provisions

$f'_c := 9.28\text{ksi}$ Compressive strength of concrete

$f_{se} := 160.6\text{ksi}$ Stress in prestress after losses

$f_y := 63\text{ksi}$ Yield stress of mild reinforcement

$f_{ys} := 70\text{ksi}$ Yield stress of stirrups

$f_{ps} := f_{se} + f_y$ Maximum stress in prestress

$d_{b6} := \frac{6}{8}\text{in}$ Diameter of #6 Bars

$d_{bs} := 0.5\text{in}$ Diameter of 1/2 in Strand

$l_{d6} := \frac{38 \cdot d_{b6} \cdot \text{ksi}}{\sqrt{f'_c \cdot \text{ksi}}} \cdot \frac{f_y}{60\text{ksi}} = 9.82 \cdot \text{in}$

AASHTO LRFD Section 5.11.2.4
Development length for bent #6 bar

$\kappa := \frac{1.6}{\text{ksi}}$

1.6 for prestensioned members with a depth greater than 24.0 inches

$l_{ds} := \kappa \cdot \left(f_{ps} - \frac{2}{3} \cdot f_{se} \right) \cdot d_{bs} = 93.23 \cdot \text{in}$

AASHTO LRFD Section 5.11.4.2
Development of prestressing strand

Node 1 - CCT Node

Bearing Face

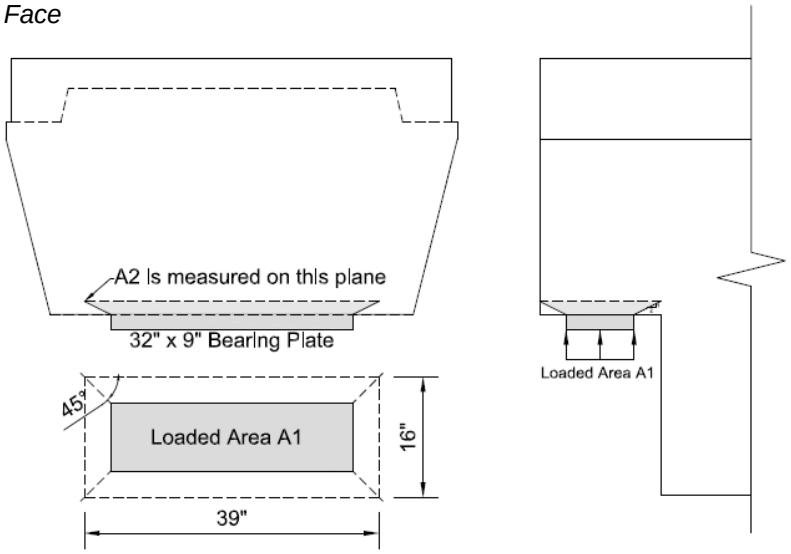

$A_1 := 32\text{in} \cdot 9\text{in} = 288 \cdot \text{in}^2$ Loaded Area

$A_2 := 39\text{in} \cdot 16\text{in} = 624 \cdot \text{in}^2$ Frustum Bottom Plane

$m := \min\left(2, \sqrt{\frac{A_2}{A_1}}\right) = 1.47$ Concrete Confinement Factor

$F_u := V_1 = 0.72 \cdot kip$ Ultimate Load

$\nu_b := 0.7$ Bearing Efficiency for a CCT node

$f_{cu} := m \cdot \nu_b \cdot f'_c = 9.56 \cdot ksi$ Concrete Ultimate Stress

$F_n := f_{cu} \cdot A_1 = 2753.81 \cdot kip$ Node Face Capacity

$SF1_{v1} := \frac{F_n}{F_u} = 3839.98$ Total Load Capacity

Strut to Node Interface-1

$F_u := S_1 = 0.85 \cdot kip$ Ultimate Load

$\nu_c := 0.45$ Efficiency for Strut-to-Node Interface without Crack Control Reinforcement

$f_{cu} := m \cdot \nu_c \cdot f'_c = 6.15 \cdot ksi$

$h_a := 8.1875in$

$\theta := \varphi_1 = 58 \cdot deg$ Dimensions of the node-to-strut interfaces calculated using the definition provided in Figure 5.6.3.2-2 in Appendix A of TXdot 5253

$l_s := 9in$

$w := h_a \cdot \cos(\theta) + l_s \cdot \sin(\theta) = 11.97 \cdot in$ Width of Strut-to-Node Interface

$b := 32 \cdot in$ Depth of Node

$F_n := f_{cu} \cdot w \cdot b = 2354.74 \cdot kip$ Node Face Capacity

$SF1_{s1} := \frac{F_n}{F_u} = 2784.56$ Total Load Capacity

Tie-1

$F_u := T_1 = 0.45 \cdot kip$

$\nu_s := 1.0$

$A_s := 12 \cdot 0.60in^2 + 12 \cdot 0.31in^2 = 10.92 \cdot in^2$ 12 #7's and 6 Double Leg #5's

$F_{tie} := \nu_s \cdot f_y \cdot A_s = 687.96 \cdot kip$ Tie Capacity

$SF1_{t1} := \frac{F_{tie}}{F_u} = 1535.21$ Total Load Capacity

$Node_1 := \min\left(SF1_{v1}, SF1_{s1}, SF1_{t1}\right) = 1535.21$ Limiting Node Capacity

Node 3 - CTT Node

STNI-3

$F_u := S_3 = 1.21 \cdot kip$

$f_{cu} := f'_c \cdot \nu_c = 4.18 \cdot ksi$

$h_a := 10.234in$

$\theta := \varphi_3 = 35 \cdot deg$

$l_s := 12.25in$

$w := h_a \cdot \cos(\theta) + l_s \cdot \sin(\theta) = 15.41 \cdot in$ Width of Strut-to-Node Interface

$F_n := f_{cu} \cdot w \cdot b = 2059.2 \cdot kip$ Node Face Capacity

$SF3_{s3} := \frac{F_n}{F_u} = 1702.73$ Total Load Capacity

Tie-2 Height determined by location of anchoring bar for vertical hangers (Bar 604) 7-3/16" from top of beam

$F_u := T_2 = 0.69 \cdot kip$

$\nu := 1.0$

$Steel_2 := 20 \cdot 0.44in^2 \cdot f_y + 8 \cdot .2in^2 \cdot f_{ys}$ 10 Double Leg #6's and 4 Double Leg #4's

$F_{tie} := \nu \cdot Steel_2 = 666.4 \cdot kip$ Tie Capacity

$SF2_{t2} := \frac{F_{tie}}{F_u} = 960.7$ Total Load Capacity

Tie-3

$F_u := T_3 = 0.99 \cdot kip$

$\nu_s := 1.0$

$A_s := 6 \cdot 0.44in^2$ 3 Double Leg #6's

$A_{ps} := 34 \cdot .153in^2 = 5.2 \cdot in^2$

$l_{avail.3} := 19.5675in$ Less than transfer length of 30in

$f_{ps.3} := \frac{f_{se} \cdot l_{avail.3}}{60 d_{bs}} = 104.75 \cdot ksi$ AASHTO LRFD EQ. 5.11.4.2-2

$F_{tie} := \nu_s \cdot \left(f_y \cdot A_s + f_{ps.3} \cdot A_{ps}\right) = 711.24 \cdot kip$ Tie Capacity

$SF3_{t3} := \frac{F_{tie}}{F_u} = 717.95$ Total Load Capacity

$Node_3 := \min\left(SF3_{s3}, SF3_{t3}, SF2_{t2}\right) = 717.95$ Limiting Node Capacity

Node 5 - CTT Node

STNI-5 $SF3_{t3} \cdot V_1 = 514.87 \cdot kip$

$F_u := S_5 = 0.53 \cdot kip$

$\nu_c = 0.45$

$f_{cu} := f'_c \cdot \nu_c = 4.18 \cdot ksi$

$h_a := 10.286in$

$\theta := \varphi_5 = 46 \cdot deg$

$l_s := 16in$

$w := h_a \cdot \cos(\theta) + l_s \cdot \sin(\theta) = 18.65 \cdot in$

$b_w := 10in$ Web width

$F_n := f_{cu} \cdot w \cdot b_w = 779.02 \cdot kip$ Node Face Capacity

$SF5_{s5} := \frac{F_n}{F_u} = 1473.02$ Total Load Capacity

Tie 4

$F_u := T_4 = 0.38 \cdot kip$

$Steel_5 := 4 \cdot .44in^2 \cdot f_y + 18 \cdot .2in^2 \cdot f_{ys} = 362.88 \cdot kip$ 4 #6's and 9 Double Leg #4's

$F_{tie} := \nu \cdot Steel_5 = 362.88 \cdot kip$ Tie Capacity

$SF4_{t4} := \frac{F_{tie}}{F_u} = 953.87$ Total Load Capacity

Tie 5

$F_u := T_5 = 1.36 \cdot kip$

$\nu_s := 1.0$

$A_{ps} := 34 \cdot .153in^2 = 5.2 \cdot in^2$

$l_{avail.5} := 48.9639in$

$f_{ps.5a} := f_{se} + \frac{l_{avail.5} - 60 \cdot d_{bs}}{l_{ds} - 60 \cdot d_{bs}} \cdot \left(f_{ps} - f_{se}\right) = 179.5 \cdot ksi$

$f_{ps.5b} := \frac{f_{se} \cdot \left(l_{avail.5} - 3ft\right)}{60 d_{bs}} = 69.4 \cdot ksi$

$F_{tie} := \nu \cdot \left(f_{ps.5a} \cdot A_{ps} + f_{ps.5b} \cdot 0.153in^2 \cdot 8\right) = 1018.68 \cdot kip$ Tie Capacity

$SF5_{t5} := \frac{F_{tie}}{F_u} = 750.12$ Total Load Capacity

$Node_5 := \min\left(SF5_{s5}, SF5_{t5}, SF4_{t4}, SF3_{t3}\right) = 717.95$ Limiting Node Capacity

Node 6 - CCC Node

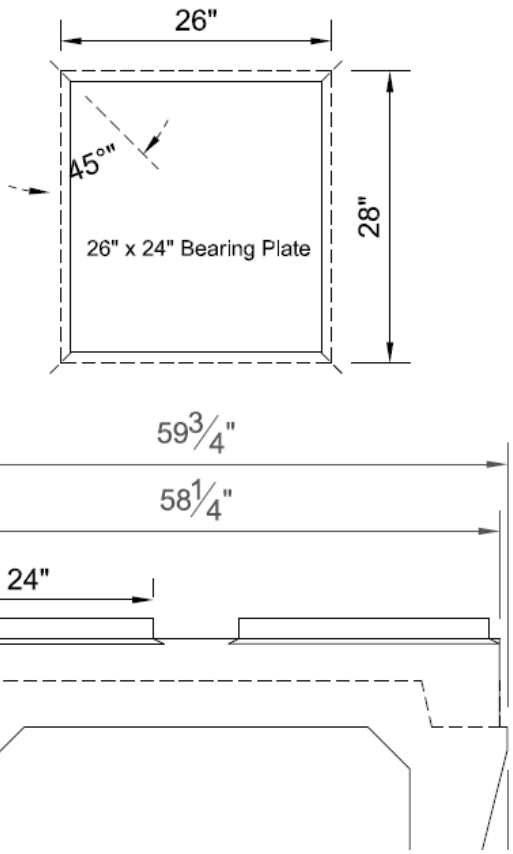

Loading Face

$A_1 := 26in \cdot 24in = 624 \cdot in^2$

$A_2 := 28in \cdot 26in = 728 \cdot in^2$

$m := \sqrt{\frac{A_2}{A_1}} = 1.08$

$F_u := P = 1 \cdot kip$

$\nu_b := 0.7$

$f_{cu} := m \cdot \nu_b \cdot f'_c = 7.02 \cdot ksi$

$F_n := f_{cu} \cdot 2 \cdot A_1 = 8756.57 \cdot kip$

$SF6_P := \frac{F_n}{F_u} = 8756.57$

STNI-2,4,5

$F_u := N_6 = 1.54 \cdot kip$

$\nu_c = 0.45$

$f_{cu} := f'_c \cdot \nu_c = 4.18 \cdot ksi$

$h_a := 5.676in$ Compression stress block "a" determined from flexural analysis

$\theta := \phi_{N6} = 62.16 \cdot deg$

$l_s := 18.98in$

$w := h_a \cdot \cos(\theta) + l_s \cdot \sin(\theta) = 19.43 \cdot in$

$b_6 := 58.25in$ Width in flange area

$F_n := f_{cu} w \cdot b_6 = 4727.37 \cdot kip$ Node Face Capacity

$SF6_{scomb} := \frac{F_n}{F_u} = 3078.22$ Total Load Capacity

$Node_6 := \min\left(SF6_P, SF6_{scomb}\right) = 3078.22$ Limiting Node Capacity

$Node := \min\left(Node_1, Node_3, Node_5, Node_6\right) = 717.95$ Smallest Node Capacity

$Capacity := P \cdot Node = 717.95 \cdot kip$ Beam Capacity

$Shear_{5253} := Capacity \cdot \frac{V_1}{P} = 514.87 \cdot kip$ Beam Shear Capacity

MLL-9-34-A

Strut and Tie Check (ACI Appendix A.3 and A.4 pg 388-392)

$A_{4b} := 0.2in^2$

$A_{5b} := 0.31in^2$

$A_{6b} := 0.44in^2$

$A_{7b} := 0.60in^2$

$A_{strand} := 0.153in^2$

Check if struts are reinforced:

$b_s := 10in$ Smallest expected strut width

$s := 5in$ Stirrup spacing

$\alpha_1 := 116deg$ Maximum strut angle

$\alpha_2 := 34deg$ Minimum strut angle

$A_{si1} := \frac{0.003 \cdot b_s \cdot s}{\sin(\alpha_1)} = 0.17 \cdot in^2$ Equation A-4

$A_{si2} := \frac{0.003 \cdot b_s \cdot s}{\sin(\alpha_2)} = 0.27 \cdot in^2$

$A_{prov} := 2 \cdot A_{4b} = 0.4 \cdot in^2$ Minimum steel provided

$\beta_s := 0.75$ Strut Efficiency Factor - All struts classified at reinforced

Strut 1

$h_a := 8.1875in$ Height of node

$\theta := \varphi_1 = 58 \cdot deg$

$l_s := 9in$ Length of node

$w_1 := h_a \cdot \cos(\theta) + l_s \cdot \sin(\theta) = 11.97 \cdot in$ Width of node

$b_1 := 32in$ Minimum strut width

$Strut_1 := 0.85 \cdot \beta_s \cdot f'_c \cdot b_1 \cdot w_1 = 2266.28 \cdot kip$ Nominal compressive strenth of strut

$V_{s1} := \frac{Strut_1}{S_1} = 2679.96$ Capacity based on strut 1

Strut 2

$w_2 := 5.326\text{in}$ Width of node

$b_2 := 54\text{in}$ Minimum strut width

$\text{Strut}_2 := 0.85 \cdot \beta_s \cdot f'_c \cdot b_2 \cdot w_2 = 1701.47 \cdot \text{kip}$ Nominal compressive strenth of strut

$V_{s2} := \frac{\text{Strut}_2}{S_2} = 3791.69$ Capacity based on strut 2

Strut 3

$h_a := 10.234\text{in}$ Height of node

$\theta := \varphi_3 = 35 \cdot \text{deg}$

$l_s := 12.25\text{in}$ Length of node

$w_3 := h_a \cdot \cos(\theta) + l_s \cdot \sin(\theta) = 15.41 \cdot \text{in}$ Width of node

$b_3 := 34\text{in}$ Minimum strut width

$\text{Strut}_3 := 0.85 \cdot \beta_s \cdot f'_c \cdot b_3 \cdot w_3 = 3099.53 \cdot \text{kip}$ Nominal compressive strenth of strut

$V_{s3} := \frac{\text{Strut}_3}{S_3} = 2562.96$ Capacity based on strut 3

Strut 4

$h_a := 5.676\text{in}$ Approximate height of smeared node

$\theta := \phi_{N6} = 62.16 \cdot \text{deg}$

$l_s := 18.98\text{in}$ Length of node

$w_4 := h_a \cdot \cos(\theta) + l_s \cdot \sin(\theta) = 19.43 \cdot \text{in}$ Width of node

$b_4 := 10\text{in}$ Minimum strut width

$\text{Strut}_4 := 0.85 \cdot \beta_s \cdot f'_c \cdot b_4 \cdot w_4 = 1149.72 \cdot \text{kip}$ Nominal compressive strenth of strut

$V_{s4} := \frac{\text{Strut}_4}{S_4} = 1835.28$ Capacity based on strut 4

Strut 5

$h_a := 10.286\text{in}$ Height of node

$\theta := \phi_{N6} = 62.16 \cdot \text{deg}$

$l_s := 16\text{in}$ Length of node

$w_5 := h_a \cdot \cos(\theta) + l_s \cdot \sin(\theta) = 18.95 \cdot \text{in}$ Width of node

$b_5 := 10\text{in}$ Minimum strut width

$\text{Strut}_5 := 0.85 \cdot \beta_s \cdot f'_c \cdot b_5 \cdot w_5 = 1121.18 \cdot \text{kip}$ Nominal compressive strenth of strut

$V_{s5} := \frac{\text{Strut}_5}{S_5} = 2119.99$ Capacity based on strut 5

Tie 1

$A_{t1} := 12 \cdot A_{7b} + 12 \cdot A_{5b} = 10.92 \cdot in^2$ 12 #7's and 6 Double Leg #5's

$Tie_1 := f_y \cdot A_{t1} = 687.96 \cdot kip$ Nominal tensile strenth of tie

$V_{t1} := \frac{Tie_1}{T_1} = 1535.21$ Capacity based on tie 1

Tie 2

$Steel_{t2} := 20 \cdot A_{6b} \cdot f_y + 8 \cdot A_{4b} \cdot f_{ys}$ 10 Double Leg #6's and 4 Double Leg #4's

$Tie_2 := Steel_{t2} = 666.4 \cdot kip$ Nominal tensile strenth of tie

$V_{t2} := \frac{Tie_2}{T_2} = 960.7$ Capacity based on tie 2

Tie 3

$A_{t3} := 6 \cdot A_{6b}$ 3 Double Leg #6's

$A_{ps} := 34 \cdot A_{strand} = 5.2 \cdot in^2$

$f_{ps.3} := \frac{3ksi \cdot l_{avail.3}}{d_{bs}} = 117.4 \cdot ksi$ ACI 318-08 EQ 12-4

$Tie_3 := f_y \cdot A_{t3} + f_{ps.3} \cdot A_{ps} = 777.06 \cdot kip$ Nominal tensile strenth of tie

$V_{t3} := \frac{Tie_3}{T_3} = 784.4$ Capacity based on tie 3

Tie 4

$Steel_{t4} := 4 \cdot A_{6b} \cdot f_y + 18 \cdot A_{4b} \cdot f_{ys}$ 4 #6's and 9 Double Leg #4's

$Tie_4 := Steel_{t4} = 362.88 \cdot kip$ Nominal tensile strenth of tie

$V_{t4} := \frac{Tie_4}{T_4} = 953.87$ Capacity based on tie 4

Tie 5

$A_{ps1} := 34 \cdot A_{strand} = 5.2 \cdot in^2$

$A_{ps2} := 8 \cdot A_{strand} = 1.22 \cdot in^2$

$f_{ps.5a} := \frac{l_{avail.5} \cdot ksi}{d_{bs}} + \frac{2 \cdot f_{se}}{3} = 204.99 \cdot ksi$ ACI 318-08 EQ 12-4

$f_{ps.5b} := \frac{3ksi \cdot \left(l_{avail.5} - 3ft\right)}{d_{bs}} = 77.78 \cdot ksi$

$Tie_5 := \left(f_{ps.5a} \cdot A_{ps} + f_{ps.5b} \cdot A_{ps2}\right) = 1161.59 \cdot kip$ Nominal tensile strenth of tie

$V_{t5} := \frac{Tie_5}{T_5} = 855.35$ Capacity based on tie 5

Nodal Check (ACI Appendix A.5 pg 392)

Node 1 - CCT Node

$\beta_{n1} := 0.8$ A.5.2.2

$f_{ce} := 0.85 \cdot \beta_{n1} \cdot f'_c = 6.31 \cdot ksi$

Tie 1 Face

$w_{t1} := 8.1875in$ Node width

$b_{t1} := 32in$ Minimum beam width

$V_{t1\_n} := \frac{f_{ce} \cdot w_{t1} \cdot b_{t1}}{T_1} = 3689.46$ Load at node failure

Strut 1 Face

$w_{s1} := w_1 = 11.97 \cdot in$ Node width

$b_{s1} := 32in$ Minimum beam width

$V_{s1\_n} := \frac{f_{ce} \cdot w_{s1} \cdot b_{s1}}{S_1} = 2858.63$ Load at node failure

Bearing Face

$w_{b1} := 9in$ Node width

$b_{b1} := 32in$ Minimum beam width

$V_{b1\_n} := \frac{f_{ce} \cdot w_{b1} \cdot b_{b1} \cdot m}{V_1} = 2737.27$ Load at node failure

$V_{n1} := \min\left(V_{t1\_n}, V_{s1\_n}, V_{b1\_n}\right) = 2737.27$

Node 3 - CTT Node

$\beta_{n2} := 0.60$ A.5.2.3

$f_{ce} := 0.85 \cdot \beta_{n2} \cdot f'_c = 4.73 \cdot ksi$

Tie 2 Face

$w_{t2} := 12.25in$ Node width

$b_{t2} := 34in$ Minimum beam width

$V_{t2\_n} := \frac{f_{ce} \cdot w_{t2} \cdot b_{t2}}{T_2} = 2841.76$ Load at node failure

Strut 3 Face

$w_{s3} := w_3 = 15.41 \cdot in$ Node width

$b_{s3} := 34in$ Minimum beam width

$V_{s3\_n} := \frac{f_{ce} \cdot w_{s3} \cdot b_{s3}}{S_1} = 2932.25$ Load at node failure

Tie 3 Face

$w_{t3} := 10.234in$ Node width

$b_{t3} := 34in$ Minimum beam width

$V_{t3\_n} := \frac{f_{ce} \cdot w_{t3} \cdot b_{t3}}{T_3} = 1662.36$ Load at node failure

$V_{n3} := \min\left(V_{t2\_n}, V_{s3\_n}, V_{t3\_n}\right) = 1662.36$

Node 5 - CTT Node

$\beta_{n2} := 0.60$ A.5.2.3

$f_{ce} := 0.85 \cdot \beta_{n2} \cdot f'_c = 4.73 \cdot ksi$

Tie 4 Face

$w_{t4} := 16in$ Node width

$b_{t4} := 34in$ Minimum beam width

$V_{t4\_n} := \frac{f_{ce} \cdot w_{t4} \cdot b_{t4}}{T_4} = 6767.71$ Load at node failure

Strut 5 Face

$w_{s5} := 19.23in$ Node width

$b_{s5} := 10in$ Beam width

$V_{s5\_n} := \frac{f_{ce} \cdot w_{s5} \cdot b_{s5}}{S_5} = 1720.9$ Load at node failure

Tie 5 Face

$w_{t5} := 10.234in$ Node width

$b_{t5} := 34in$ Minimum beam width

$V_{t5\_n} := \frac{f_{ce} \cdot w_{t5} \cdot b_{t5}}{T_5 - T_3} = 4482.6$ Load at node failure

$V_{n5} := \min\left(V_{t4\_n}, V_{s5\_n}, V_{t5\_n}\right) = 1720.9$

Node 6 - CCC Node

$\beta_{n2} := 1.0$ A.5.2.3

$f_{ce} := 0.85 \cdot \beta_{n2} \cdot f'_c = 7.89 \cdot ksi$

Strut 2, 4, 5 Face

$w_{t6} := 19.6144in$ Node width

$b_{t6} := 58.25in$ Beam width

$V_{t6\_n} := \frac{f_{ce} \cdot w_{t6} \cdot b_{t6}}{N_6} = 5868.38$ Load at node failure

Bearing

$w_{b6} := 18.98in$ Node width

$b_{b6} := 58.25in$ Minimum beam width

$V_{b6\_n} := \frac{f_{ce} \cdot w_{b6} \cdot b_{b6} \cdot 2}{N_6} = 11357.14$ Load at node failure

$V_{n6} := \min\left(V_{t6\_n}, V_{b6\_n}\right) = 5868.38$

Capacity

$Strut := P \cdot \min\left(V_{s1}, V_{s2}, V_{s3}, V_{s4}, V_{s5}\right) = 1835.28 \cdot kip$

$Tie := P \cdot \min\left(V_{t1}, V_{t2}, V_{t3}, V_{t4}, V_{t5}\right) = 784.4 \cdot kip$

$Node := P \min\left(V_{n1}, V_{n3}, V_{n5}, V_{n6}\right) = 1662.36 \cdot kip$

$Capacity := \min(Strut, Tie, Node) = 784.4 \cdot kip$

$Shear_{ACI} := Capacity \cdot \frac{V_1}{P} = 562.53 \cdot kip$

MLL-9-34-A

Strut and Tie Check (AASHTO LRFD Section 5.6.3)

$P_{ult} := 717.95$ Ultimate Load in Kips(iterative)

Tie 1

$A_{t1} := 12 \cdot A_{7b} + 12 \cdot A_{5b} = 10.92 \cdot in^2$ 12 #7's and 6 Double Leg #5's

$E := 29000ksi$

$Tie_1 := f_y \cdot A_{t1} = 687.96 \cdot kip$ Nominal tensile strenth of tie

$P_{t1} := \frac{Tie_1}{T_1} = 1535.21$ Capacity based on tie 1

$\varepsilon_{t1} := \frac{P_{ult} \cdot T_1}{A_{t1} \cdot E} = 0.00101594 \cdot \frac{in}{in}$

Tie 2

$Steel_{t2} := 20 \cdot A_{6b} \cdot f_y + 8 \cdot A_{4b} \cdot f_{ys}$ 10 Double Leg #6's and 4 Double Leg #4's

$A_{t2} := 16 \cdot A_{6b} + 8 \cdot A_{4b}$

$Tie_2 := Steel_{t2} = 666.4 \cdot kip$ Nominal tensile strenth of tie

$P_{t2} := \frac{Tie_2}{T_2} = 960.7$ Capacity based on tie 2

$\varepsilon_{t2} := \frac{P_{ult} \cdot T_2}{A_{t2} \cdot E} = 0.00198759 \cdot \frac{in}{in}$

Tie 3

$A_{t3} := 6 \cdot A_{6b}$ 3 Double Leg #6's

$A_{ps} := 34 \cdot A_{strand} = 5.2 \cdot in^2$

$f_{ps.3} := \frac{f_{se} \cdot l_{avail.3}}{60 d_{bs}} = 104.75 \cdot ksi$ AASHTO LRFD EQ. 5.11.4.2-2

$Tie_3 := f_y \cdot A_{t3} + f_{ps.3} \cdot A_{ps} = 711.24 \cdot kip$ Nominal tensile strenth of tie

$P_{t3} := \frac{Tie_3}{T_3} = 717.95$ Capacity based on tie 3

$\varepsilon_{t3} := \frac{P_{ult} \cdot T_3}{(A_{t3} + A_{ps}) \cdot E} = 0.00312743 \cdot \frac{in}{in}$

Tie 4

$Steel_{t4} := 4 \cdot A_{6b} \cdot f_y + 18 \cdot A_{4b} \cdot f_{ys}$ 4 #6's and 9 Double Leg #4's

$A_{t4} := 4 \cdot A_{6b} + 18 \cdot A_{4b}$

$Tie_4 := Steel_{t4} = 362.88 \cdot kip$ Nominal tensile strenth of tie

$P_{t4} := \frac{Tie_4}{T_4} = 953.87$ Capacity based on tie 4

$\varepsilon_{t4} := \frac{P_{ult} \cdot T_4}{E \cdot A_{t4}} = 0.00175714 \cdot \frac{in}{in}$

Tie 5

$A_{ps1} := 34 \cdot A_{strand} = 5.2 \cdot in^2$

$A_{ps2} := 8 \cdot A_{strand} = 1.22 \cdot in^2$

$f_{ps.5a} := f_{se} + \frac{l_{avail.5} - 60 \cdot d_{bs}}{l_{ds} - 60 \cdot d_{bs}} \cdot \left(f_{ps} - f_{se}\right) = 179.5 \cdot ksi$ AASHTO LRFD EQ. 5.11.4.2-2

$f_{ps.5b} := \frac{f_{se} \cdot \left(l_{avail.5} - 3ft\right)}{60 \cdot d_{bs}} = 69.4 \cdot ksi$ Nominal tensile strenth of tie

$Tie_5 := \left(f_{ps.5a} \cdot A_{ps} + f_{ps.5b} \cdot A_{ps2}\right) = 1018.68 \cdot kip$

$P_{t5} := \frac{Tie_5}{T_5} = 750.12$ Capacity based on tie 5

$\varepsilon_{t5} := \frac{P_{ult} \cdot T_5}{\left(A_{ps1} + A_{ps2}\right) \cdot E} = 0.00523194 \cdot \frac{in}{in}$

Strut 1

$\alpha_s := \varphi_1$ — Smallest angle between the compressive strut and adjorning tension ties (deg)

$\varepsilon_s := \varepsilon_{t1}$ — Tensile strain in concrete in the concrete in the direction of the tension tie (in/in)

$\varepsilon_1 := \varepsilon_s + (\varepsilon_s + 0.002)\cdot(\cot(\alpha_s))^2$ — Strain in compressive strut

$f_{cu} := \min\left(\frac{f'_c}{0.8 + 170\cdot\varepsilon_1}, 0.85\cdot f'_c\right) = 7.89\cdot ksi$ — Limiting Compressive Stress

$h_a := 8.1875in$ — Height of node

$\theta := \varphi_1 = 58\cdot deg$

$l_s := 9in$ — Length of node

$w_1 := h_a\cdot\cos(\theta) + l_s\cdot\sin(\theta) = 11.97\cdot in$ — Width of node

$b_1 := 32in$ — Minimum strut width

$Strut_1 := f_{cu}\cdot b_1\cdot w_1 = 3021.71\cdot kip$ — Nominal compressive strenth of strut

$P_{s1} := \frac{Strut_1}{S_1} = 3573.28$ — Capacity based on strut 1

Strut 2

$\alpha_s := \varphi_2$ — Smallest angle between the compressive strut and adjorning tension ties (deg)

$\varepsilon_s := \varepsilon_{t2}$ — Tensile strain in concrete in the concrete in the direction of the tension tie (in/in)

$\varepsilon_1 := \varepsilon_s + (\varepsilon_s + 0.002)\cdot(\cot(\alpha_s))^2$ — Strain in compressive strut

$f_{cu} := \min\left(\frac{f'_c}{0.8 + 170\cdot\varepsilon_1}, 0.85\cdot f'_c\right) = 7.89\cdot ksi$ — Limiting Compressive Stress

$w_2 := 5.326in$ — Width of node

$b_2 := 54in$ — Minimum strut width

$Strut_2 := f_{cu}\cdot b_2\cdot w_2 = 2268.62\cdot kip$ — Nominal compressive strenth of strut

$P_{s2} := \frac{Strut_2}{S_2} = 5055.58$ — Capacity based on strut 2

Strut 3

$\alpha_s := \varphi_3$ Smallest angle between the compressive strut and adjorning tension ties (deg)

$\varepsilon_s := \varepsilon_{t3}$ Tensile strain in concrete in the concrete in the direction of the tension tie (in/in)

$\varepsilon_1 := \varepsilon_s + (\varepsilon_s + 0.002)\cdot(\cot(\alpha_s))^2$ Strain in compressive strut

$f_{cu} := \min\left(\frac{f'_c}{0.8 + 170\cdot\varepsilon_1}, 0.85\cdot f'_c\right) = 2.98\cdot ksi$ Limiting Compressive Stress

$h_a := 10.234in$ Height of node

$\theta := \varphi_3 = 35\cdot deg$

$l_s := 12.25in$ Length of node

$w_3 := h_a\cdot\cos(\theta) + l_s\cdot\sin(\theta) = 15.41\cdot in$ Width of node

$b_3 := 34in$ Minimum strut width

$Strut_3 := f_{cu}\cdot b_3\cdot w_3 = 1563.59\cdot kip$ Nominal compressive strenth of strut

$P_{s3} := \frac{Strut_3}{S_3} = 1292.91$ Capacity based on strut 3

Strut 4

$\alpha_s := \varphi_4 + 90deg$ Smallest angle between the compressive strut and adjorning tension ties (deg)

$\varepsilon_s := \varepsilon_{t4}$ Tensile strain in concrete in the concrete in the direction of the tension tie (in/in)

$\varepsilon_1 := \varepsilon_s + (\varepsilon_s + 0.002)\cdot(\cot(\alpha_s))^2$ Strain in compressive strut

$f_{cu} := \min\left(\frac{f'_c}{0.8 + 170\cdot\varepsilon_1}, 0.85\cdot f'_c\right) = 7.08\cdot ksi$ Limiting Compressive Stress

$h_a := 5.676in$ Height of node

$\theta := \phi_{N6} = 62.16\cdot deg$

$l_s := 18.98in$ Length of node

$w_4 := h_a\cdot\cos(\theta) + l_s\cdot\sin(\theta) = 19.43\cdot in$ Width of node

$b_4 := 10in$ Minimum strut width

$Strut_4 := f_{cu}\cdot b_4\cdot w_4 = 1375\cdot kip$ Nominal compressive strenth of strut

$P_{s4} := \frac{Strut_4}{S_4} = 2194.9$ Capacity based on strut 4

Strut 5

$\alpha_s := \varphi_5$ — Smallest angle between the compressive strut and adjorning tension ties (deg)

$\varepsilon_s := \varepsilon_{t5}$ — Tensile strain in concrete in the concrete in the direction of the tension tie (in/in)

$\varepsilon_1 := \varepsilon_s + (\varepsilon_s + 0.002)\cdot(\cot(\alpha_s))^2$ — Strain in compressive strut

$f_{cu} := \min\left(\frac{f'_c}{0.8 + 170\cdot\varepsilon_1}, 0.85\cdot f'_c\right) = 3.27\cdot ksi$ — Limiting Compressive Stress

$h_a := 10.286in$ — Height of node

$\theta := \phi_{N6} = 62.16\cdot deg$

$l_s := 16in$ — Length of node

$w_5 := h_a\cdot\cos(\theta) + l_s\cdot\sin(\theta) = 18.95\cdot in$ — Width of node

$b_5 := 10in$ — Strut width

$Strut_5 := f_{cu}\cdot b_5\cdot w_5 = 620.15\cdot kip$ — Nominal compressive strenth of strut

$P_{s5} := \frac{Strut_5}{S_5} = 1172.62$ — Capacity based on strut 4

Nodal Check (AASHTO LRFD Section 5.6.3.5)

Node 1 - CCT Node

$f_{ce} := 0.75\cdot f'_c = 6.96\cdot ksi$

Tie 1 Face

$w_{t1} := 8.1875in$ — Node width

$b_{t1} := 32in$ — Minimum beam width

$P_{t1\_n} := \frac{f_{ce}\cdot w_{t1}\cdot b_{t1}}{T_1} = 4069.26$ — Shear at node failure

Strut 1 Face

$w_{s1} := w_1 = 11.97\cdot in$ — Node width

$b_{s1} := 32in$ — Minimum beam width

$P_{s1\_n} := \frac{f_{ce}\cdot w_{s1}\cdot b_{s1}}{S_1} = 3152.9$ — Load at node failure

Bearing Face

$w_{b1} := 9in$ — Node width

$b_{b1} := 32in$ — Minimum beam width

$P_{b1\_n} := \frac{f_{ce}\cdot w_{b1}\cdot b_{b1}\cdot m}{V_1} = 3019.04$ — Load at node failure

$P_{n1} := \min(P_{t1\_n}, P_{s1\_n}, P_{b1\_n}) = 3019.04$

Node 3 - CTT Node

$f_{ce} := 0.65 \cdot f'_c = 6.03 \cdot ksi$

Tie 2 Face

$w_{t2} := 12.25in$ Node width

$b_{t2} := 34in$ Minimum beam width

$P_{t2\_n} := \frac{f_{ce} \cdot w_{t2} \cdot b_{t2}}{T_2} = 3621.85$ Load at node failure

Strut 3 Face

$w_{s3} := w_3 = 15.41 \cdot in$ Node width

$b_{s3} := 34in$ Minimum beam width

$P_{s3\_n} := \frac{f_{ce} \cdot w_{s3} \cdot b_{s3}}{S_1} = 3737.18$ Load at node failure

Tie 3 Face

$w_{t3} := 10.234in$ Node width

$b_{t3} := 34in$ Minimum beam width

$P_{t3\_n} := \frac{f_{ce} \cdot w_{t3} \cdot b_{t3}}{T_3} = 2118.69$ Load at node failure

$P_{n3} := \min\left(P_{t2\_n}, P_{s3\_n}, P_{t3\_n}\right) = 2118.69$

Node 5 - CTT Node

$f_{ce} := 0.65 \cdot f'_c = 6.03 \cdot ksi$

Tie 4 Face

$w_{t4} := 16in$ Node width

$b_{t4} := 10in$ Minimum beam width

$P_{t4\_n} := \frac{f_{ce} \cdot w_{t4} \cdot b_{t4}}{T_4} = 2536.91$ Load at node failure

Strut 5 Face

$w_{s5} := 19.23in$ Node width

$b_{s5} := 10in$ Beam width

$P_{s5\_n} := \frac{f_{ce} \cdot w_{s5} \cdot b_{s5}}{S_5} = 2193.31$ Load at node failure

Tie 5 Face

$w_{t5} := 10.286in$ Node width

$b_{t5} := 34in$ Minimum beam width

$P_{t5\_n} := \frac{f_{ce} \cdot w_{t5} \cdot b_{t5}}{T_5 - T_3} = 5742.14$ Load at node failure

$P_{n5} := \min\left(P_{t4\_n}, P_{s5\_n}, P_{t5\_n}\right) = 2193.31$

Node 6 - CCC Node

$f_{ce} := 0.85 \cdot f'_c = 7.89 \cdot ksi$

Strut 2, 4, 5 Face

$w_{t6} := w_5 = 18.95 \cdot in$ Node width

$b_{t6} := 58.25 in$ Minimum beam width

$P_{t6\_n} := \frac{f_{ce} \cdot w_{t6} \cdot b_{t6}}{N_6} = 5670.08$ Load at node failure

Bearing

$w_{b6} := 18.98 in$ Node width

$b_{b6} := 58.25 in$ Minimum beam width

$P_{b6\_n} := \frac{f_{ce} \cdot w_{b6} \cdot b_{b6} \cdot 2}{N_6} = 11357.14$ Load at node failure

$P_{n6} := \min\left(P_{t6\_n}, P_{b6\_n}\right) = 5670.08$

Capacity

$Strut := P \cdot \min\left(P_{s1}, P_{s2}, P_{s3}, P_{s4}, P_{s5}\right) = 1172.62 \cdot kip$

$Tie := P \cdot \min\left(P_{t1}, P_{t2}, P_{t3}, P_{t4}, P_{t5}\right) = 717.95 \cdot kip$

$Node := P \min\left(P_{n1}, P_{n3}, P_{n6}\right) = 2118.69 \cdot kip$

$Capacity := \min(Strut, Tie, Node) = 717.95 \cdot kip$

$Shear_{AASHTO} := Capacity \cdot \frac{V_1}{P} = 514.87 \cdot kip$

Comparison

$Shear_{5253} = 514.87 \cdot kip$ Failure of Tie 3

$Shear_{ACI} = 562.53 \cdot kip$ Failure of Tie 3

$Shear_{AASHTO} = 514.87 \cdot kip$ Failure of Tie 3

	TxDOT 5253	ACI 318-08	AASHTO LRFD
Node 1			
Bearing	$SF1_{v1} \cdot V_1 = 2753.81 \cdot kip$	$V_{b1\_n} \cdot V_1 = 1963.01 \cdot kip$	$P_{b1\_n} \cdot V_1 = 2165.09 \cdot kip$
STNI 1	$SF1_{s1} \cdot V_1 = 1996.93 \cdot kip$	$V_{s1\_n} \cdot V_1 = 2050.04 \cdot kip$	$P_{s1\_n} \cdot V_1 = 2261.08 \cdot kip$
Tie 1	$SF1_{t1} \cdot V_1 = 1100.97 \cdot kip$	$V_{t1\_n} \cdot V_1 = 2645.87 \cdot kip$	$P_{t1\_n} \cdot V_1 = 2918.24 \cdot kip$
Node 3			
STNI 3	$SF3_{s3} \cdot V_1 = 1221.1 \cdot kip$	$V_{s3\_n} \cdot V_1 = 2102.84 \cdot kip$	$P_{s3\_n} \cdot V_1 = 2680.09 \cdot kip$
Tie 2	$SF2_{t2} \cdot V_1 = 688.96 \cdot kip$	$V_{t2\_n} \cdot V_1 = 2037.95 \cdot kip$	$P_{t2\_n} \cdot V_1 = 2597.39 \cdot kip$
Tie 3	$SF3_{t3} \cdot V_1 = 514.87 \cdot kip$	$V_{t3\_n} \cdot V_1 = 1192.15 \cdot kip$	$P_{t3\_n} \cdot V_1 = 1519.4 \cdot kip$
Node 5			
STNI 5	$SF5_{s5} \cdot V_1 = 1056.36 \cdot kip$	$V_{s5\_n} \cdot V_1 = 1234.13 \cdot kip$	$P_{s5\_n} \cdot V_1 = 1572.91 \cdot kip$
Tie 4	$SF4_{t4} \cdot V_1 = 684.06 \cdot kip$	$V_{t4\_n} \cdot V_1 = 4853.41 \cdot kip$	$P_{t4\_n} \cdot V_1 = 1819.33 \cdot kip$
Tie 5	$SF5_{t5} \cdot V_1 = 537.94 \cdot kip$	$V_{t5\_n} \cdot V_1 = 3214.66 \cdot kip$	$P_{t5\_n} \cdot V_1 = 4117.94 \cdot kip$
Node 6			
Load Point	$SF6_{P} \cdot V_1 = 6279.71 \cdot kip$	$V_{b6\_n} \cdot V_1 = 8144.69 \cdot kip$	$P_{b6\_n} \cdot V_1 = 8144.69 \cdot kip$
STNI Combo	$SF6_{scomb} \cdot V_1 = 2207.52 \cdot kip$	$V_{t6\_n} \cdot V_1 = 4208.46 \cdot kip$	$P_{t6\_n} \cdot V_1 = 4066.26 \cdot kip$
Tie 1	$SF1_{t1} \cdot V_1 = 1100.97 \cdot kip$	$V_{t1} \cdot V_1 = 1100.97 \cdot kip$	$P_{t1} \cdot V_1 = 1100.97 \cdot kip$
Tie 2	$SF2_{t2} \cdot V_1 = 688.96 \cdot kip$	$V_{t2} \cdot V_1 = 688.96 \cdot kip$	$P_{t2} \cdot V_1 = 688.96 \cdot kip$
Tie 3	$SF3_{t3} \cdot V_1 = 514.87 \cdot kip$	$V_{t3} \cdot V_1 = 562.53 \cdot kip$	$P_{t3} \cdot V_1 = 514.87 \cdot kip$
Tie 4	$SF4_{t4} \cdot V_1 = 684.06 \cdot kip$	$V_{t4} \cdot V_1 = 684.06 \cdot kip$	$P_{t4} \cdot V_1 = 684.06 \cdot kip$
Tie 5	$SF5_{t5} \cdot V_1 = 537.94 \cdot kip$	$V_{t5} \cdot V_1 = 613.41 \cdot kip$	$P_{t5} \cdot V_1 = 537.94 \cdot kip$
Strut 1	$SF1_{s1} \cdot V_1 = 1996.93 \cdot kip$	$V_{s1} \cdot V_1 = 1921.92 \cdot kip$	$P_{s1} \cdot V_1 = 2562.55 \cdot kip$
Strut 2		$V_{s2} \cdot V_1 = 2719.18 \cdot kip$	$P_{s2} \cdot V_1 = 3625.58 \cdot kip$
Strut 3	$SF3_{s3} \cdot V_1 = 1221.1 \cdot kip$	$V_{s3} \cdot V_1 = 1838.01 \cdot kip$	$P_{s3} \cdot V_1 = 927.2 \cdot kip$
Strut 4		$V_{s4} \cdot V_1 = 1316.16 \cdot kip$	$P_{s4} \cdot V_1 = 1574.05 \cdot kip$
Strut 5	$SF5_{s5} \cdot V_1 = 1056.36 \cdot kip$	$V_{s5} \cdot V_1 = 1520.33 \cdot kip$	$P_{s5} \cdot V_1 = 840.93 \cdot kip$

Table C-1: MLL-9-34-A STM (N-II) Shear Capacities

		AASHTO LRFD	TxDOT 5253	ACI 318-08
Node 1	Bearing	2,165 kips	2,754 kips	1,963 kips
	S-T-N-I 1	2,261 kips	1,997 kips	2,050 kips
	Tie 1	2,918 kips		2,646 kips
Node 3	S-T-N-I 3	2,680 kips	1,221 kips	2,103 kips
	Tie 2	2,597 kips		2,038 kips
	Tie 3	1,519 kips		1,192 kips
Node 5	S-T-N-I 5	1,573 kips	1,056 kips	1,234 kips
	Tie 4	1,819 kips		4,853 kips
	Tie 5	4,118 kips		3,215 kips
Node 6	Load Point	8,115 kips	6,280 kips	8,145 kips
	S-T-N-I Combined	4,066 kips	2,208 kips	4,208 kips
Ties	Tie 1	1,101 kips	1,101 kips	1,101 kips
	Tie 2	689 kips	689 kips	689 kips
	Tie 3	515 kips	515 kips	563 kips
	Tie 4	684 kips	684 kips	684 kips
	Tie 5	538 kips	538 kips	613 kips
Struts	Strut 1	2,563 kips	1,997 kips	1,922 kips
	Strut 2	3,626 kips		2,719 kips
	Strut 3	927 kips	1,221 kips	1,838 kips
	Strut 4	1,574 kips		1,316 kips
	Strut 5	841 kips	1,056 kips	1,520 kips

Table C-2: RF-3R-12-A (L-II) STM Shear Capacities

		AASHTO LRFD	TxDOT 5253	ACI 318-08
Node 1	Bearing	2,237 kips	2,846 kips	2,029 kips
	S-T-N-I 1	2,337 kips	2,064 kips	2,119 kips
	Tie 1	3,016 kips		2,734 kips
Node 3	S-T-N-I 3	2,942 kips	1,307 kips	2,308 kips
	Tie 2	2,684 kips		2,106 kips
	Tie 3	1,697 kips		1,331 kips
Node 5	S-T-N-I 5	1,662 kips	1,151 kips	1,304 kips
	Tie 4	1,923 kips		5,129 kips
	Tie 5	4,709 kips		3,695 kips
Node 6	Load Point	8,275 kips	6,628 kips	8,275 kips
	S-T-N-I Combined	4,213 kips	2,228 kips	4,244 kips
Ties	Tie 1	1,101 kips	1,101 kips	1,101 kips
	Tie 2	689 kips	689 kips	689 kips
	Tie 3	536 kips	536 kips	612 kips
	Tie 4	700 kips	700 kips	700 kips
	Tie 5	564 kips	564 kips	656 kips
Struts	Strut 1	2,627 kips	2,063 kips	1,986 kips
	Strut 2	3,747 kips		2,810 kips
	Strut 3	943 kips	1,307 kips	1,967 kips
	Strut 4	1,544 kips		1,286 kips
	Strut 5	915 kips	1,151 kips	1,638 kips

Table C-3: RF-3R-9-A (M-I) STM Shear Capacities

		AASHTO LRFD	TxDOT 5253	ACI 318-08
Node 1	Bearing	2,762 kips	3,513 kips	2,505 kips
	S-T-N-I 1	3,118kips	2,754 kips	2,827 kips
	S-T-N-I 6	16,265 kips	14,364 kips	14,747 kips
	Tie 1	3,077 kips		2,789 kips
Node 3	S-T-N-I 3	4,022 kips	2,277 kips	3,156 kips
	Tie 2	3,694 kips		2,898 kips
	Tie 3	2,754 kips		2,161 kips
Node 5	S-T-N-I 5	3,142 kips	2,189 kips	2,465 kips
	Tie 4	2,759 kips		7,360 kips
	Tie 5	15,661 kips		12,288 kips
Node 6	Load Point	15,275 kips	9,012 kips	15,275 kips
	S-T-N-I Combined	7,834 kips	3,725 kips	7,893 kips
Ties	Tie 1	910 kips	910 kips	910 kips
	Tie 2	768 kips	768 kips	768 kips
	Tie 3	701 kips	701 kips	791 kips
	Tie 4	813 kips	813 kips	813 kips
	Tie 5	832 kips	832 kips	952 kips
Struts	Strut 1	3,158 kips	2,754 kips	2,650 kips
	Strut 2	4,861 kips		3,726 kips
	Strut 3	2,410 kips	2,277 kips	3,427 kips
	Strut 4	1,902 kips		2,450 kips
	Strut 5	2,790 kips	2,189 kips	3,119 kips
	Strut 6	16,473 kips	14,364 kips	14,856 kips

Table C-4: RF-3R-9-C (M-II) STM Shear Capacities

		AASHTO LRFD	TxDOT 5253	ACI 318-08
Node 1	Bearing	2,013 kips	2,561 kips	1,826 kips
	S-T-N-I 1	2,103 kips	1,857 kips	1,906 kips
	Tie 1	2,714 kips		2,451 kips
Node 3	S-T-N-I 3	2,648 kips	1176 kips	2,077 kips
	Tie 2	2,415 kips		1,895 kips
	Tie 3	1,527 kips		1,198 kips
Node 5	S-T-N-I 5	1,496 kips	1036 kips	1,174 kips
	Tie 4	1,730 kips		4,616 kips
	Tie 5	4,238 kips		3,325 kips
Node 6	Load Point	7,447 kips	5,964 kips	7,445 kips
	S-T-N-I Combined	3,791 kips	2,005 kips	3,820 kips
Ties	Tie 1	1,101 kips	1,101 kips	1,101 kips
	Tie 2	689 kips	689 kips	689 kips
	Tie 3	542 kips	542 kips	611 kips
	Tie 4	700 kips	700 kips	700 kips
	Tie 5	570 kips	570 kips	660 kips
Struts	Strut 1	2,364 kips	1,857 kips	1,787 kips
	Strut 2	3,372 kips		2,529 kips
	Strut 3	848 kips	1,176 kips	1,770 kips
	Strut 4	1,389 kips		1,158 kips
	Strut 5	824 kips	1,036 kips	1,474 kips

Table C-5: RF-1R-1-A (H-II) STM Shear Capacities

		AASHTO LRFD	TxDOT 5253	ACI 318-08
Node 1	Bearing	1,491 kips	1,896 kips	1,352 kips
	S-T-N-I 1	1,557 kips	1,375 kips	1,412 kips
	Tie 1	2,009 kips		1,822 kips
Node 3	S-T-N-I 3	1,924 kips	855 kips	1,510 kips
	Tie 2	1,789 kips		1,403 kips
	Tie 3	1,095 kips		859 kips
Node 5	S-T-N-I 5	1,108 kips	773 kips	869 kips
	Tie 4	1,281 kips		3,418 kips
	Tie 5	3,195 kips		2,507 kips
Node 6	Load Point	5,514 kips	4,421 kips	5,514 kips
	S-T-N-I Combined	2,821 kips	1,497 kips	2,828 kips
Ties	Tie 1	1,101 kips	1,101 kips	1,101 kips
	Tie 2	689 kips	689 kips	689 kips
	Tie 3	565 kips	565 kips	637 kips
	Tie 4	700 kips	700 kips	700 kips
	Tie 5	594 kips	594 kips	686 kips
Struts	Strut 1	1,735 kips	1,375 kips	1,323 kips
	Strut 2	2,496 kips		1,872 kips
	Strut 3	615 kips	855 kips	1,287 kips
	Strut 4	1,016 kips		857 kips
	Strut 5	614 kips	773 kips	1,097 kips

APPENDIX D

Petrographic Analysis

Petrographic Analysis

03/30/2010

Report:	UT ASR DEF
Date Received:	03/3/2010
Structure Type:	Unknown
Sample Type:	Core
Location:	Unknown
Coarse Aggregate Producer:	NA
Coarse Aggregate Type:	Crushed Limestone
Fine Aggregate Producer:	NA
Fine Aggregate Type:	Siliceous Sand
Cement Producer:	NA
Cement Type:	NA

Comments:

This petrographic analysis was performed in response to a request from Caroline Herrera, P.E., (CST/Soils and Aggregates Branch Director) to assist the University of Texas in an ASR/DEF investigation of nine submitted cores. The following objectives were specified by UT:

- General observations on concrete quality. (Comments on placement, mixture proportions, water-cement ratio).
- Visual documentation of ASR and/or DEF micro structural damage. (Images depicting gel/ettringite locations, cracking and gapping of paste/aggregate interfaces).
- Qualitative study of damage severity in each sample. (Comparison of micro structural damage between all samples).
- Qualitative study of damage progression through the length of the sample. (Comparison of micro structural damage in surface and core concretes of each sample).

General observations on concrete quality (comments on placement, mixture proportions, water-cement ratio)

General Appearance: Nine cores were submitted for analysis and were designated as: P1, P2, P3, P4, P5, P6, P7, P8 and P9. The submitted cores were 3-3/4 inch in diameter and ranged from 7.5 to 13 inches in length. Cores P1, P2, P5, P7, P8 and P7 had obvious distress cracks on the surface of the core.

Water/Cement Ratio: None of the cores had abnormal or elevated w-c ratio. Cores P1, P2 and P3 had a slightly lower w-c ratio than the remaining cores. In order to estimate w-c ratio, a mix design plus a standard job site cylinder would have been required.

Proportioning and types of aggregate: Without a batch design we could not determine if excesses or deficiencies exist between the point count data and the theoretical values from the batch design. Based on point count data the paste volume indicate a high sack mix. Coarse aggregate consist of crushed limestone and a small percentage of chert. Fine aggregate consist of quartz, agate, feldspar, carbonates, sandstone and chert. The following table summarizes the point count data:

Core ID	Paste Volume	FA Volume	CA Volume	% Entrapped Air	% Entrained Air
P1	26.61	27.01	42.29	3.03	0.92
P2	28.59	27.14	40.45	2.24	1.58
P3	28.07	34.82	34.68	1.10	1.21
P4	29.42	31.71	36.3	1.21	0.81
P5	26.28	22.1	49.73	0.81	0.81
P6	30.09	31.31	34.82	2.16	1.08
P7	33.42	29.92	35.44	0.67	0.40
P8	28.3	32.27	38.28	0.38	0.51
P9	29.69	31.98	36.57	0.27	1.21

Paste content and appearance: Paste content is indicative of a high sack mix and appearance is normal except for the numerous fine micro cracking observed in the cores. No fly ash or other mineral admixtures were present in the mix.

Air Content: Non-Air Entrained.

Degree of Hydration: Normal.

Carbonation: Carbonation was noted at the exterior surface of all the cores. The following chart represents the depth of carbonation for each core:

Core ID	Carbonation Depth From Exterior Surface of Core	Carbonation Depth Observed Along Surface Crack
P1	1/16”	1/8”
P2	3/32”	NA
P3	3/32	5/8”
P4	3/16	7/16”
P5	1/32”	¾”
P6	1/8”	NA
P7	3/16”	3/8”
P8	1/8”	3/16”
P9	3/16”	NA

Deleterious Reaction Mechanism: All cores have suffered significant distress from ASR. The primary ASR aggregate type is a microcrystalline chert fine aggregate. Ettringite was observed filling most of the micro crack generated by ASR distress. Ettringite was also noted in many of the air voids and in some discrete nests within the paste. The occurrence of gapping around aggregates due to paste expansion (DEF) was limited. Complete gapping of the aggregates was only observed in a minor amount of the particles. It is inconclusive whether DEF has contributed to the distress based on the limited amount of true gapping due to paste expansion.

Microscopic documentation of ASR and/or DEF micro structural damage.
(Images depicting ASR gel/ettringite formation, cracking and gapping at paste/aggregate interfaces)

ASR Related Evidence

Image of Core P5 illustrating ASR distress cracking from reactive fine aggregate.

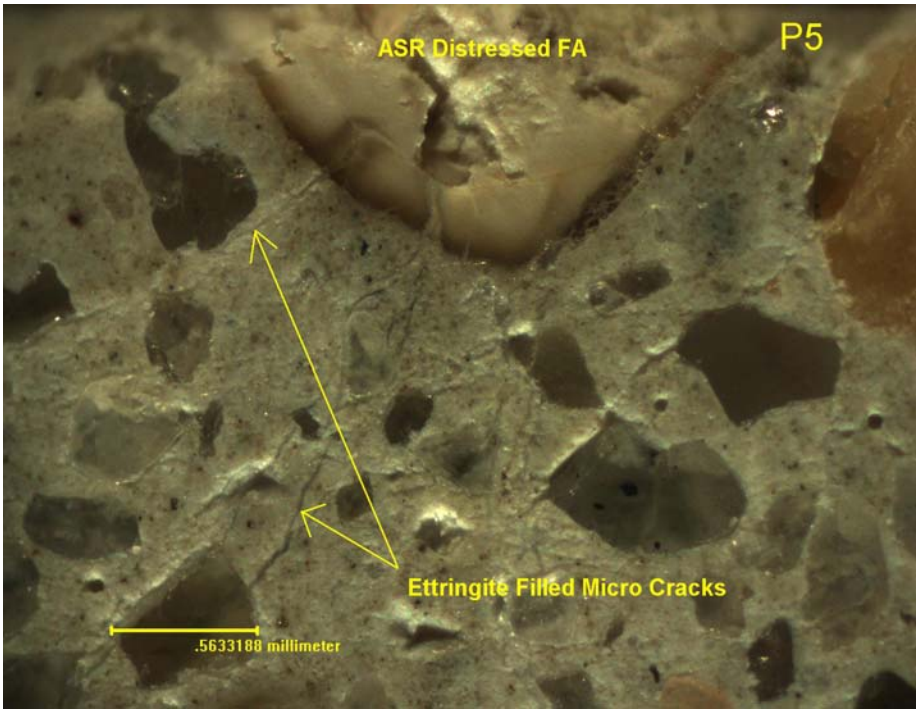

Image illustrating ettringite filled gap surrounding fine aggregate

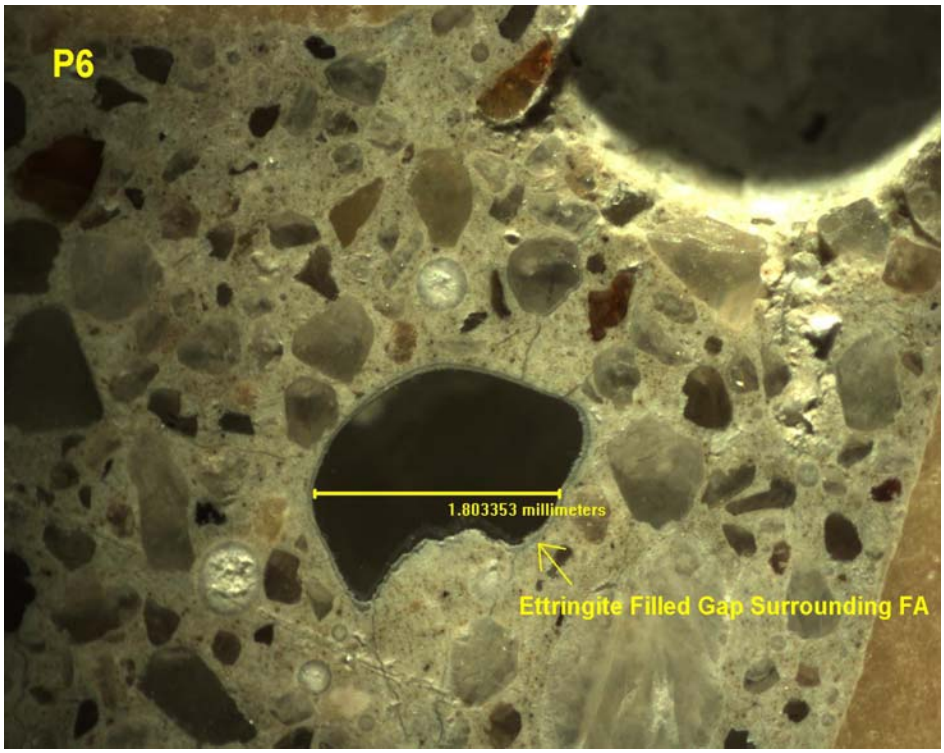

Image illustrating highly distress fine aggregate

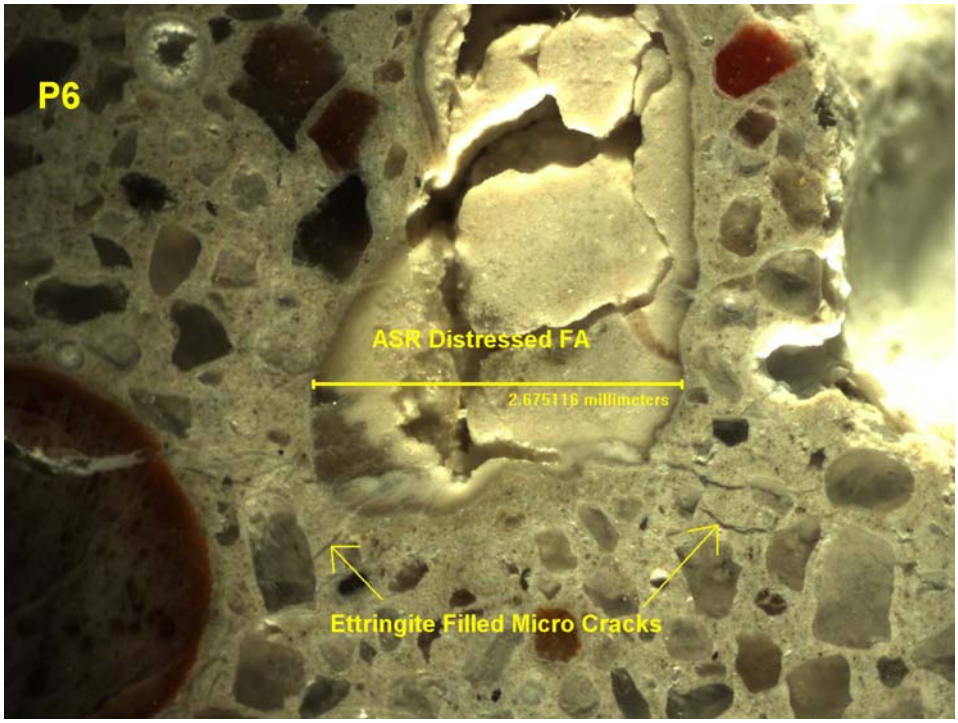

Image illustrating fine network of ettringite filled micro cracks and ASR distressed fine aggregate

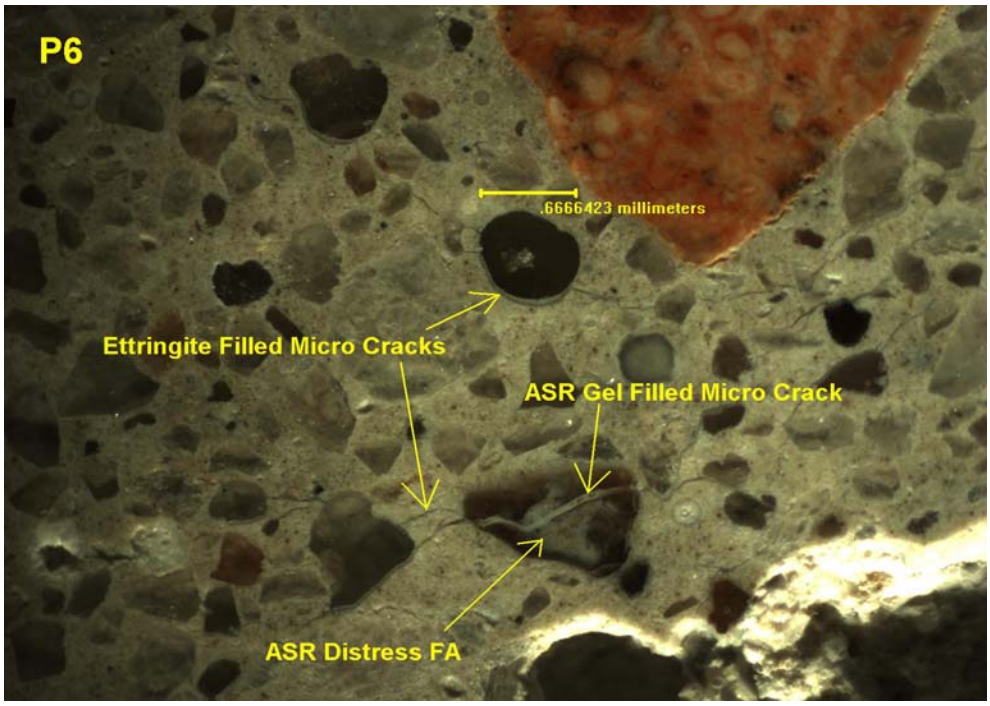

Image illustrating ettringite filled micro cracks

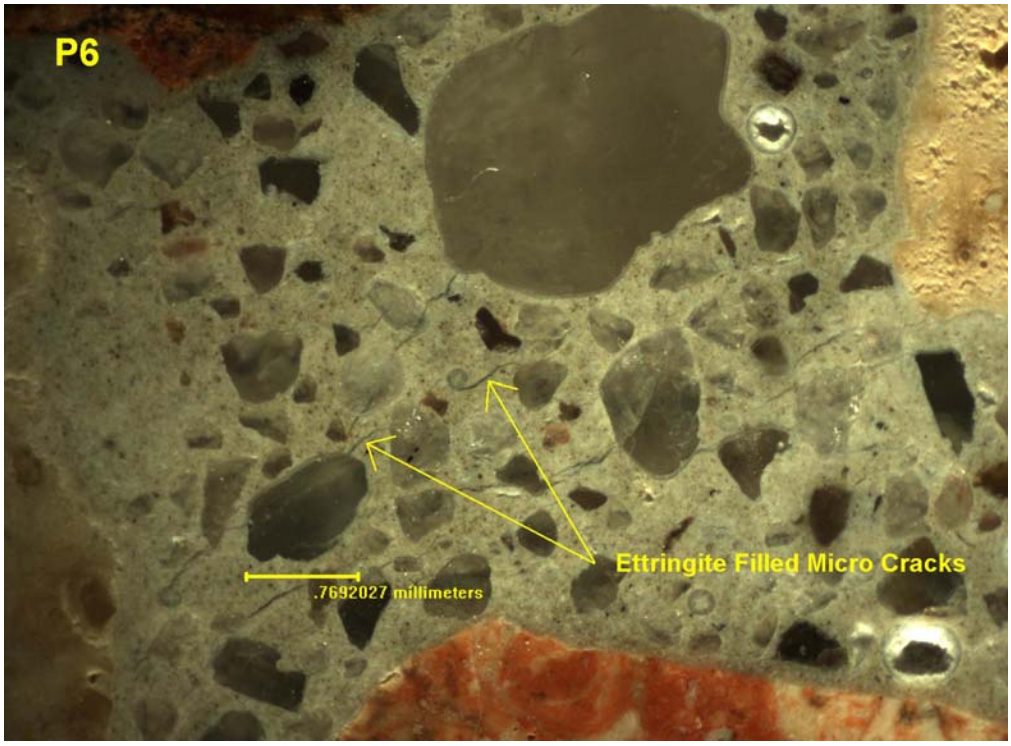

Fluorescence Microscopy Documentation

Fluorescent imaging is very useful tool in highlighting the fine micro cracking associated with PCD mechanism. The following images illustrate the level of distress associated with the reaction:

Fluorescent image illustrating ASR distressed fine aggregate and associated distress cracking

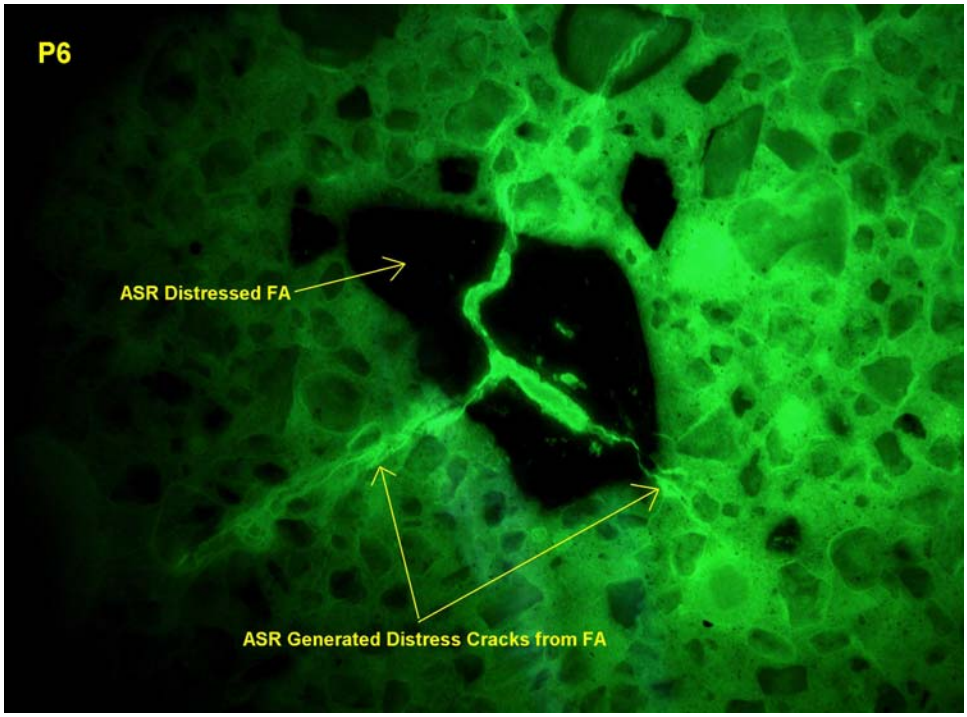

ASR distress fine aggregate

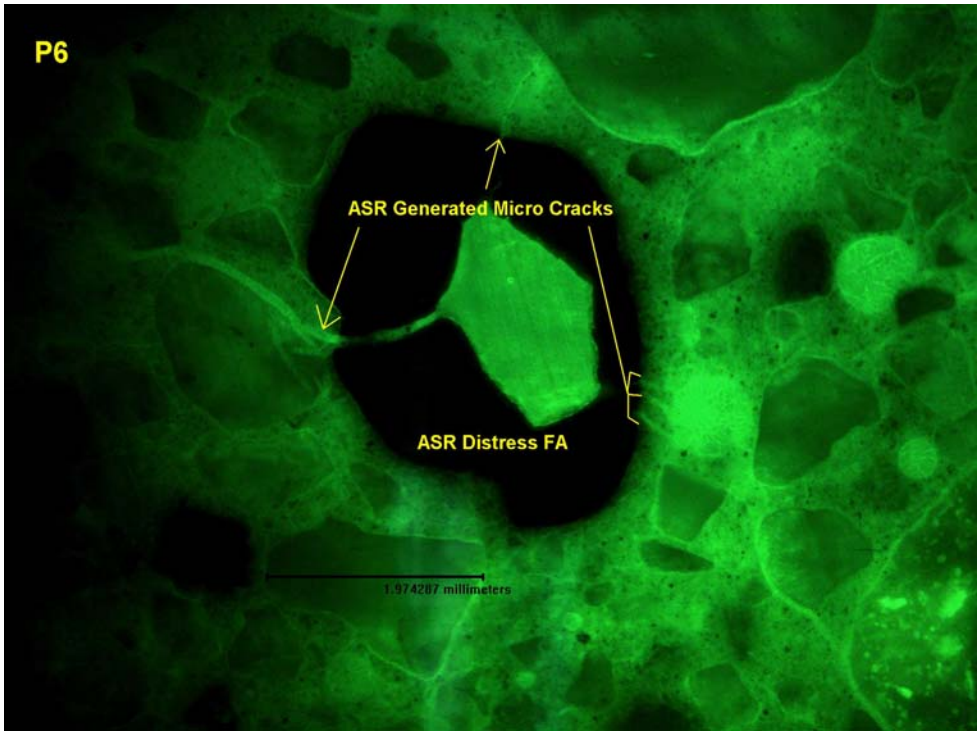

Highly distressed fine aggregate illustrating radial distress cracking

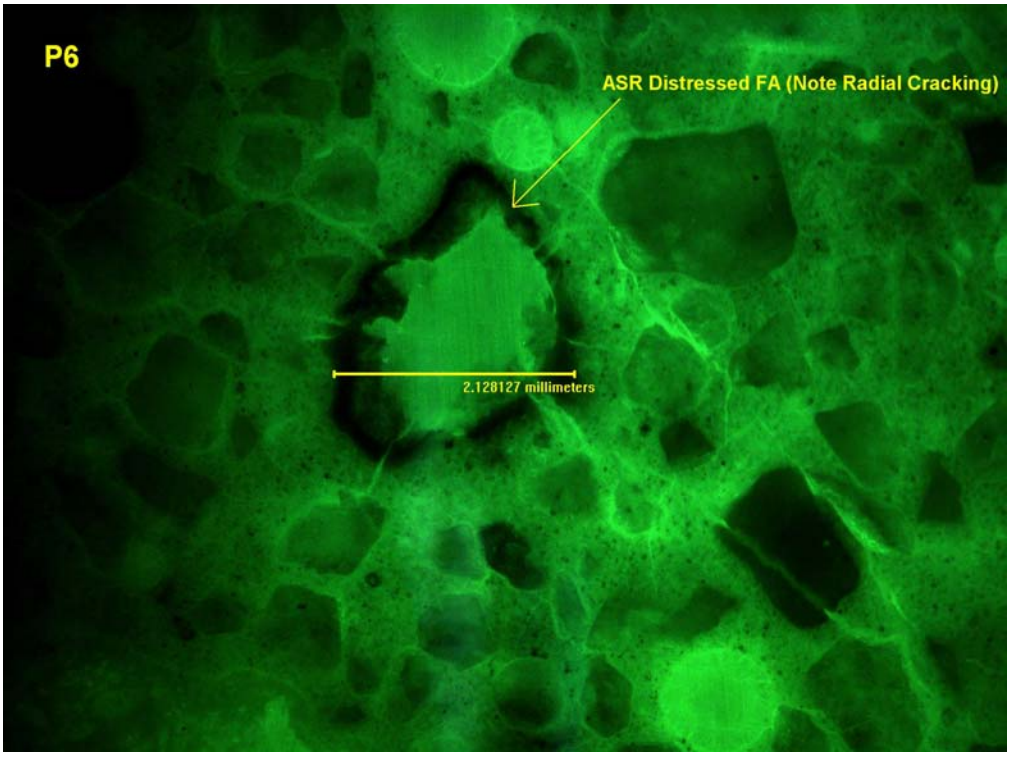

Image illustrating ettringite filled gap surrounding aggregate

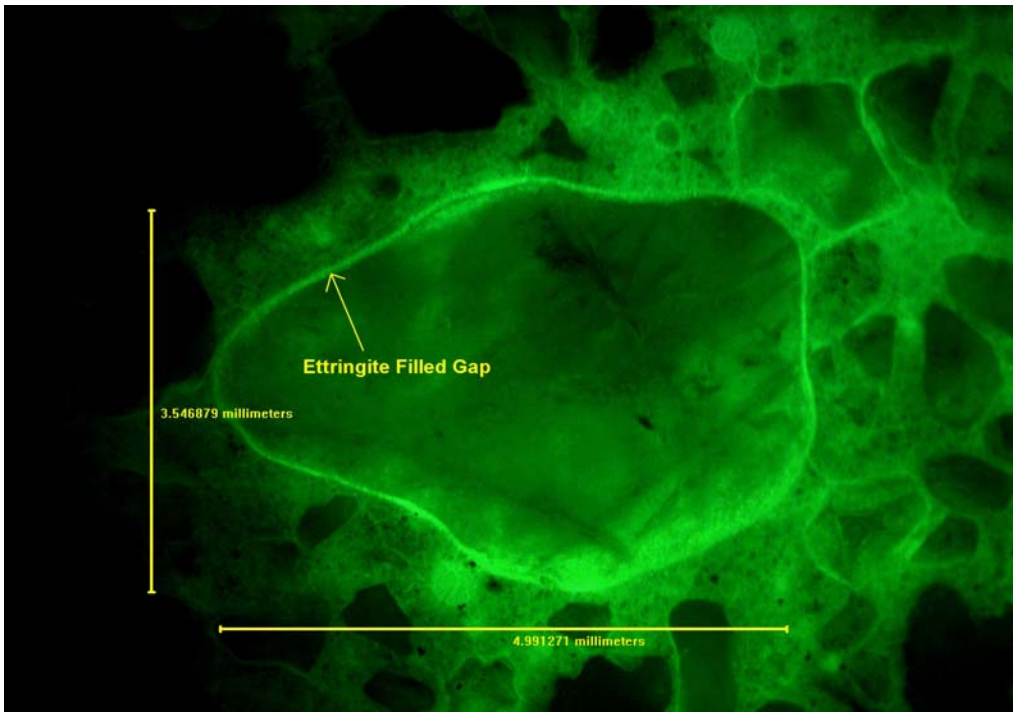

Image illustrating ettringite filled gap around FA

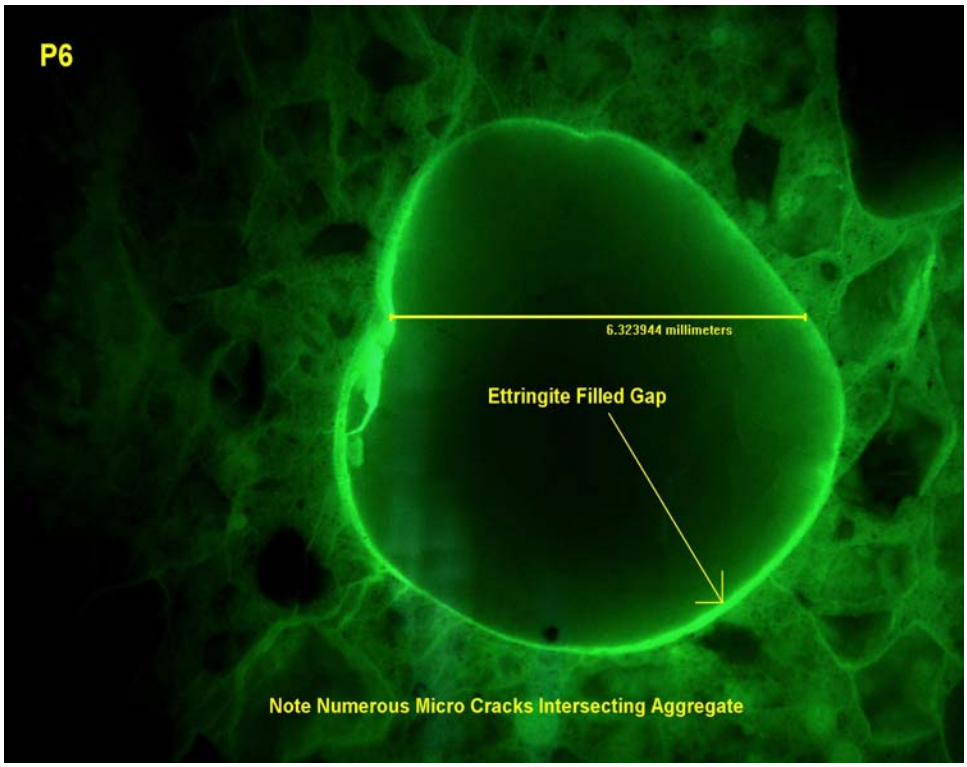

Image illustrating intersection of ettringite filled micro cracks

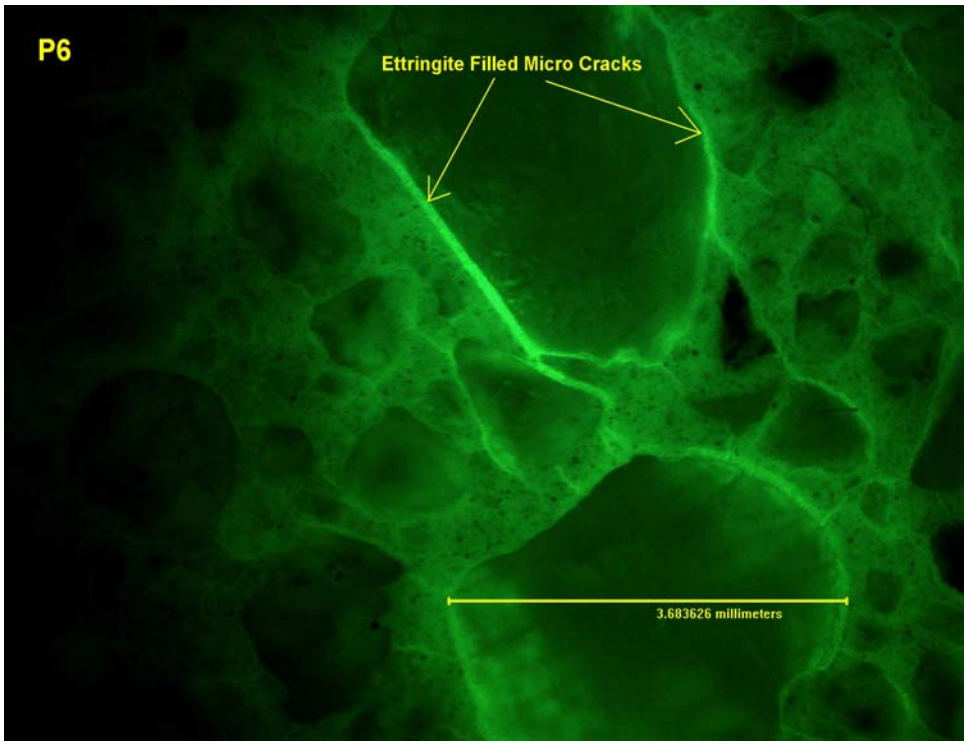

ASR distress fine aggregate

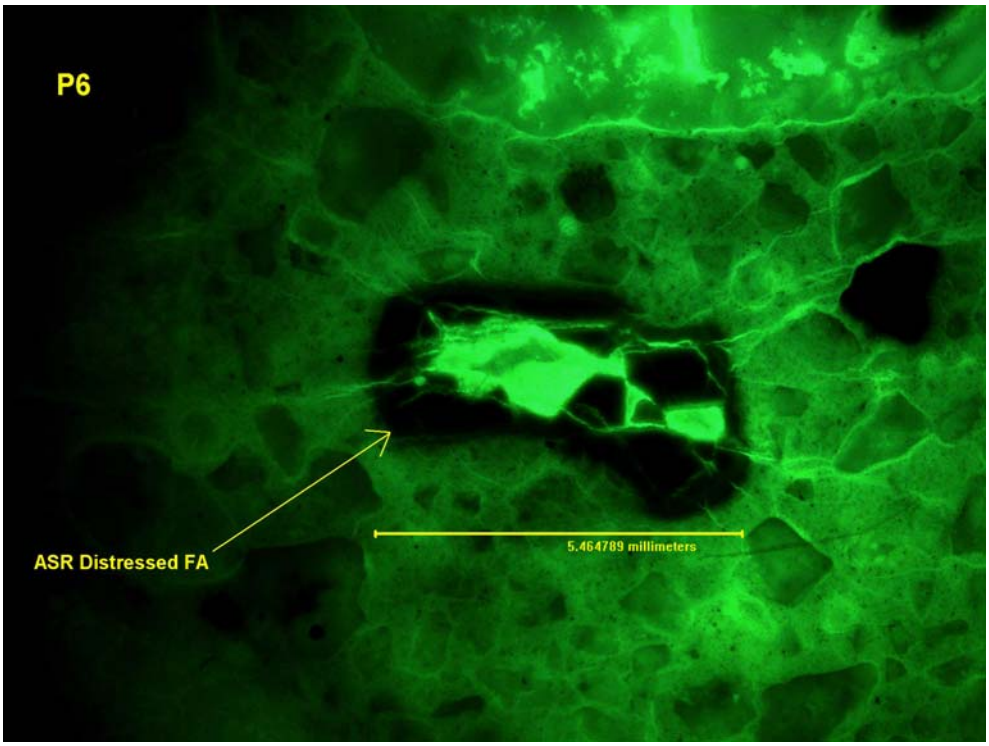

Scanning Electron Microscope (SEM) Documentation

The SEM analysis was performed on a Hitachi brand 3200N variable pressure microscope with a Oxford EDS system. This tool was used to document and confirm the type of PCD responsible for the distressed concrete. EDS spectral analysis was used to verify reaction site chemistry and relationship to other phases in the mix (paste, aggregate). EDS elemental dot mapping was performed to document the location of reaction product within the mix. The following images document numerous ASR distressed aggregates and ettringite formation sites:

ASR distress aggregate with gel filled air void

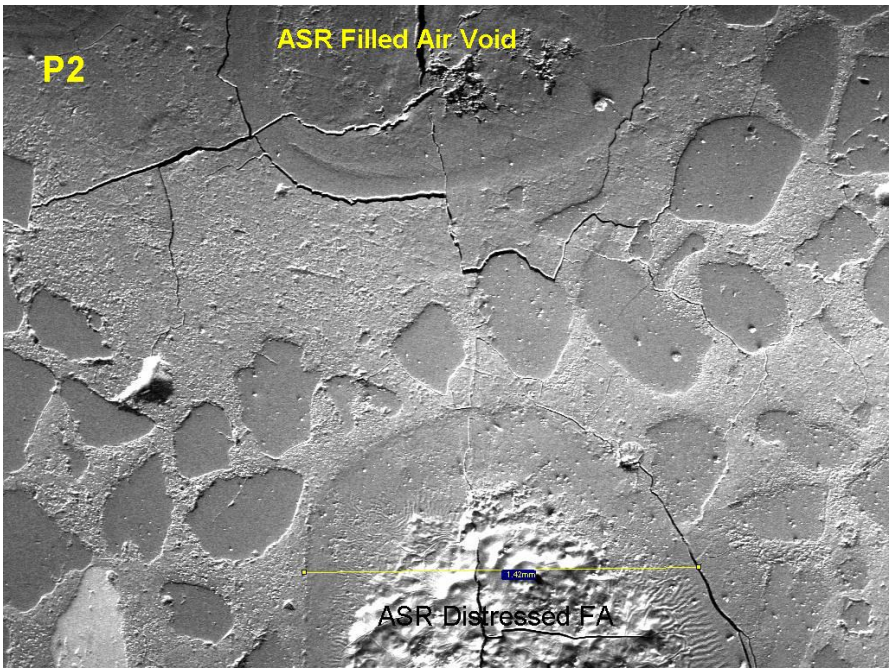

SEM/EDS spectra taken in gel filled air void

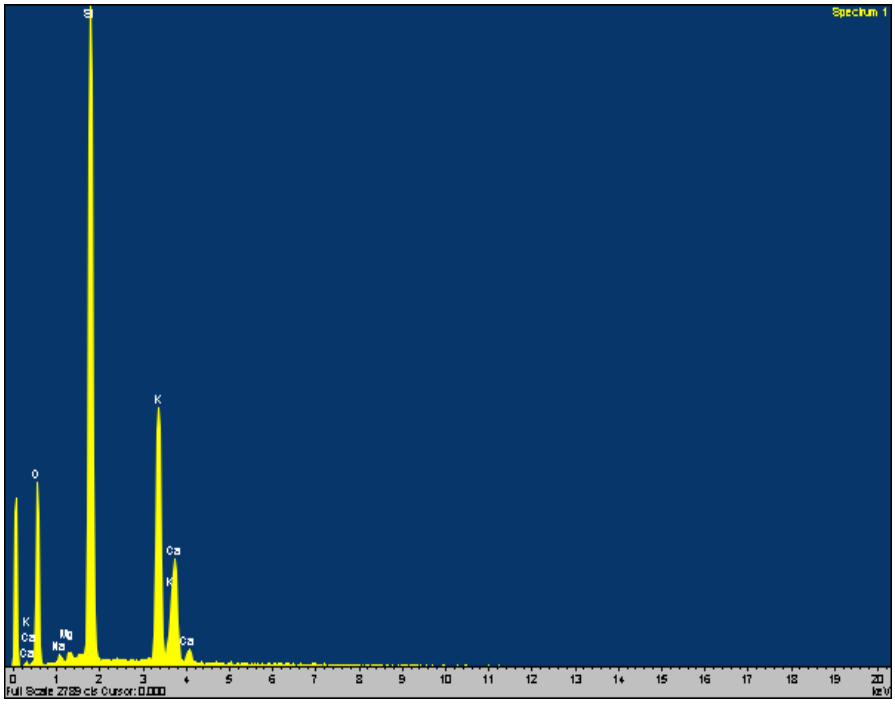

SEM image and EDS spectra illustrating ASR distress with associated reaction products

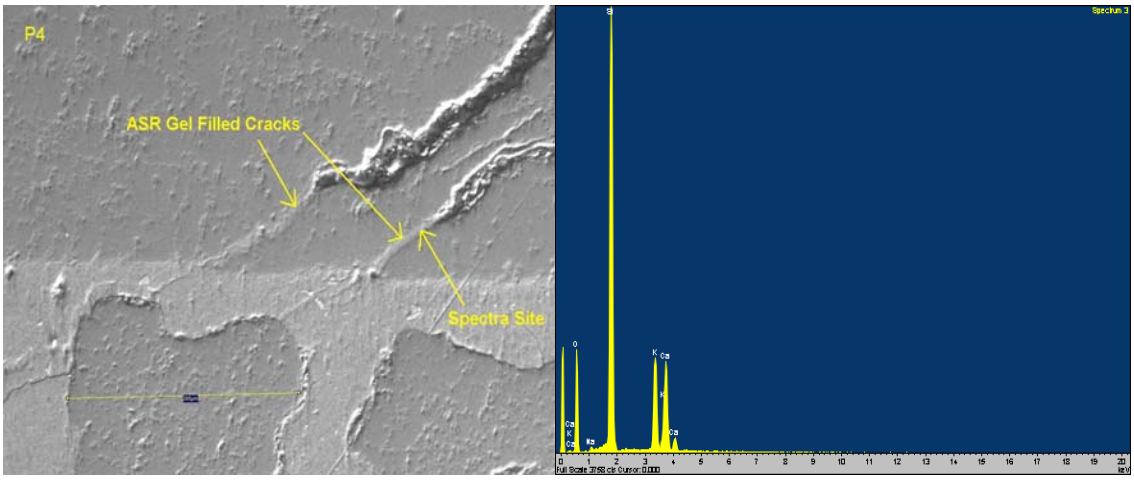

ASR distress aggregate

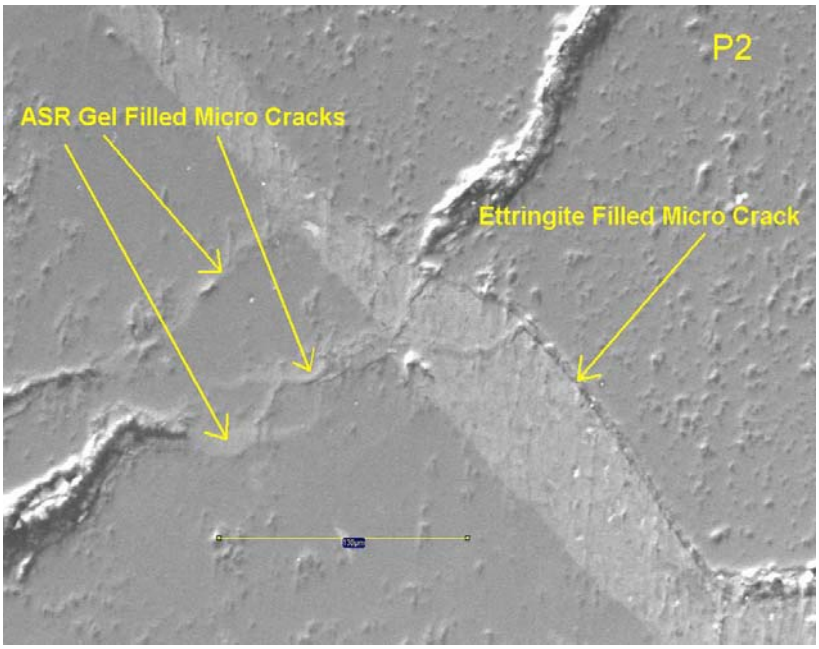

Image illustrating numerous fine ettringite filled micro cracks

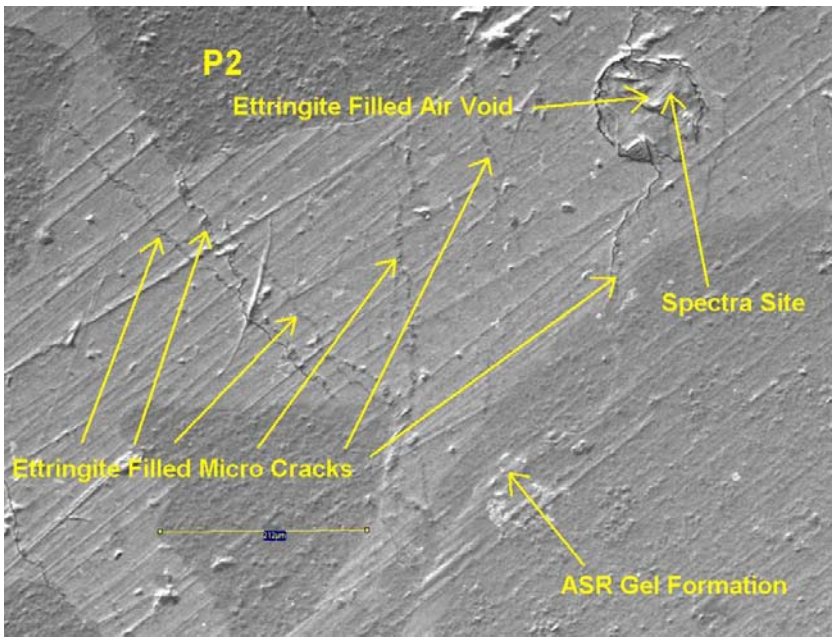

SEM/EDS spectra illustrating elemental chemistry of ettringite

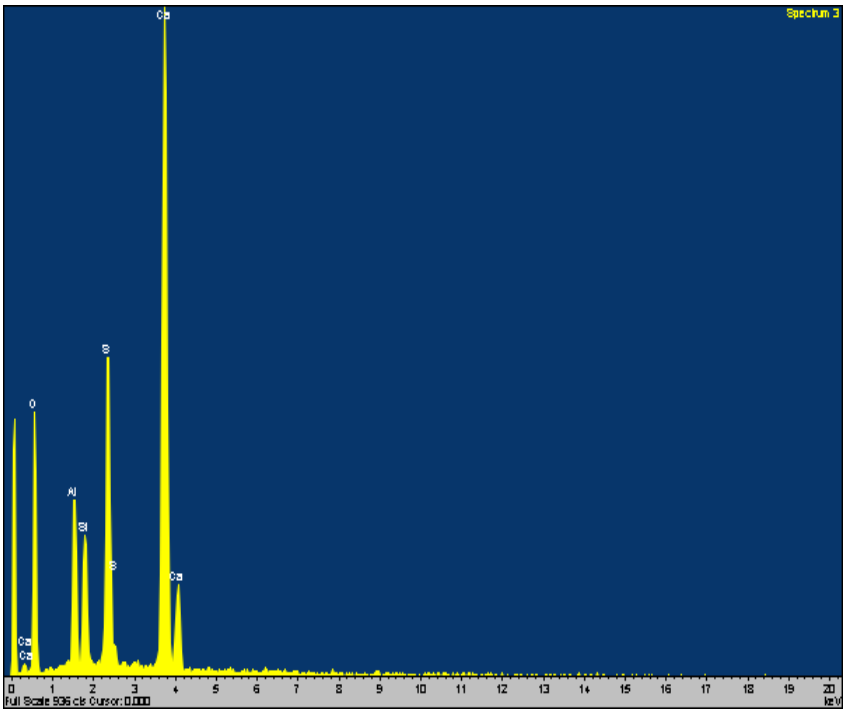

ASR distressed FA and associated gel formation

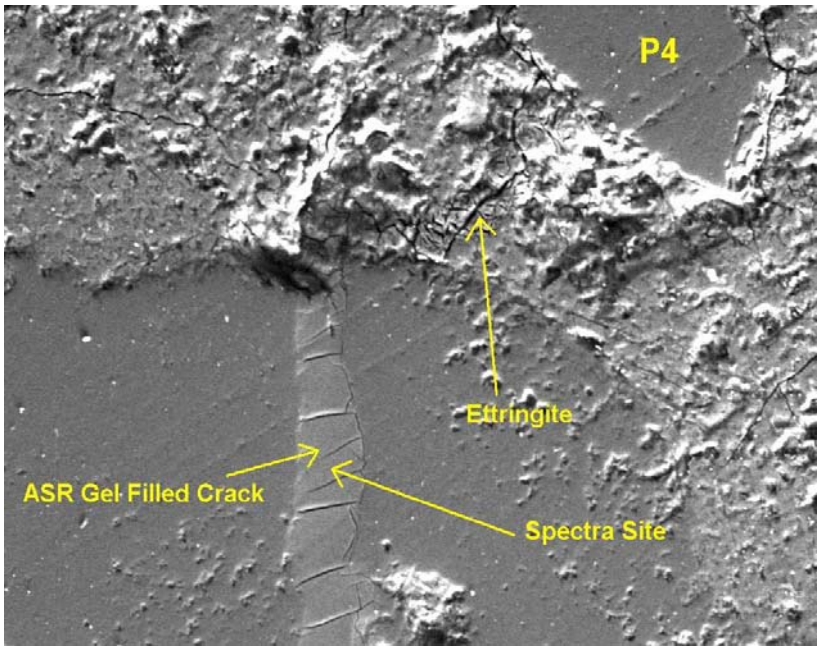

SEM/EDS spectra confirming ASR gel chemistry

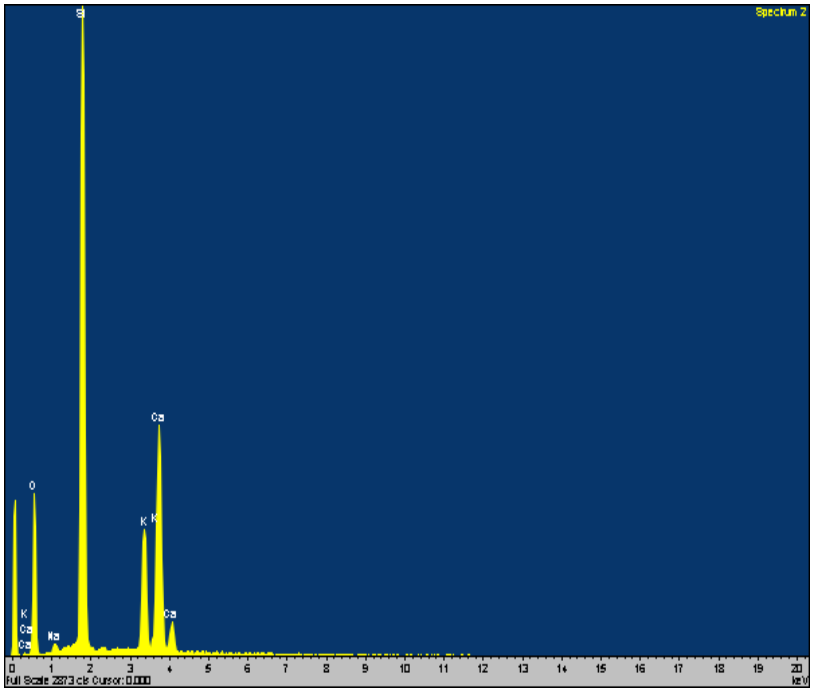

ASR distress FA

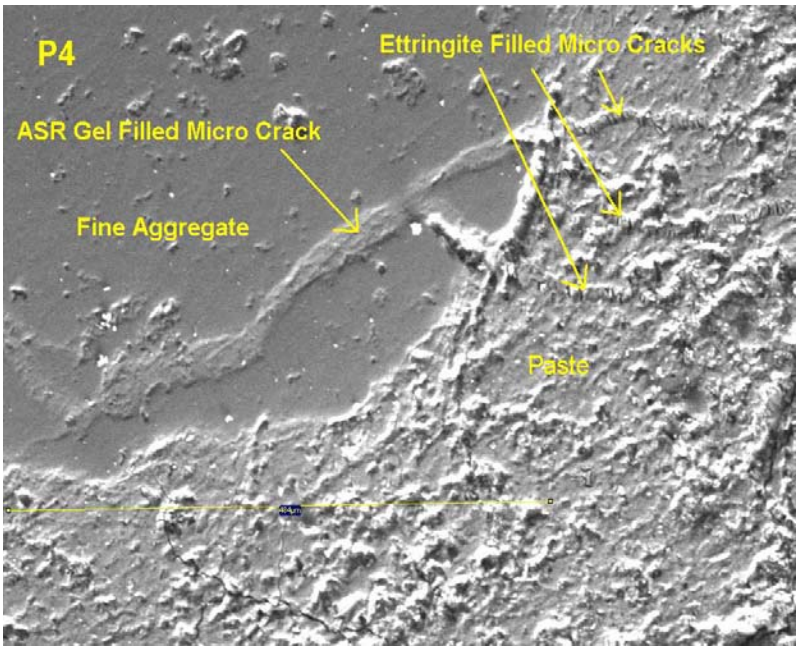

ASR distress FA illustrating gel formation and significant dissolution of the reactive aggregate.

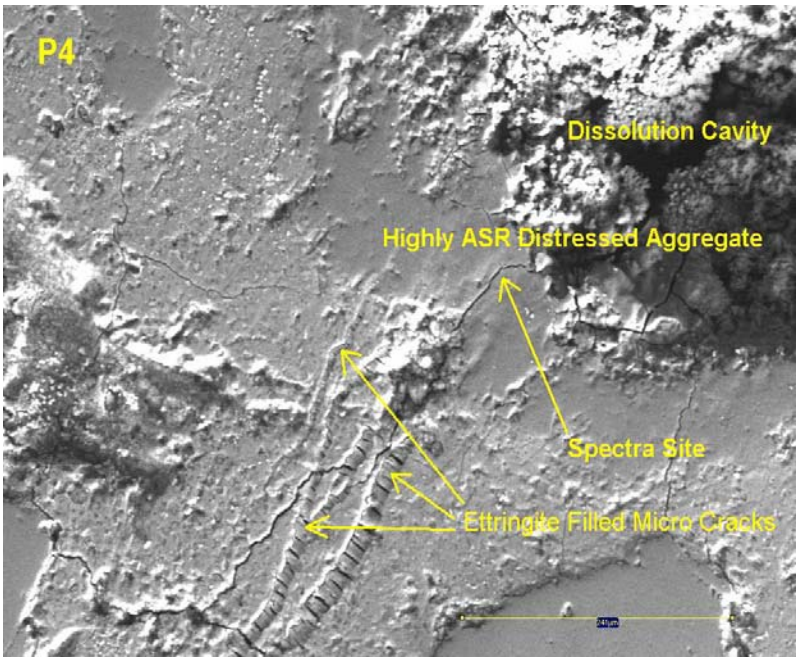

SEM/EDS spectra confirming gel chemistry

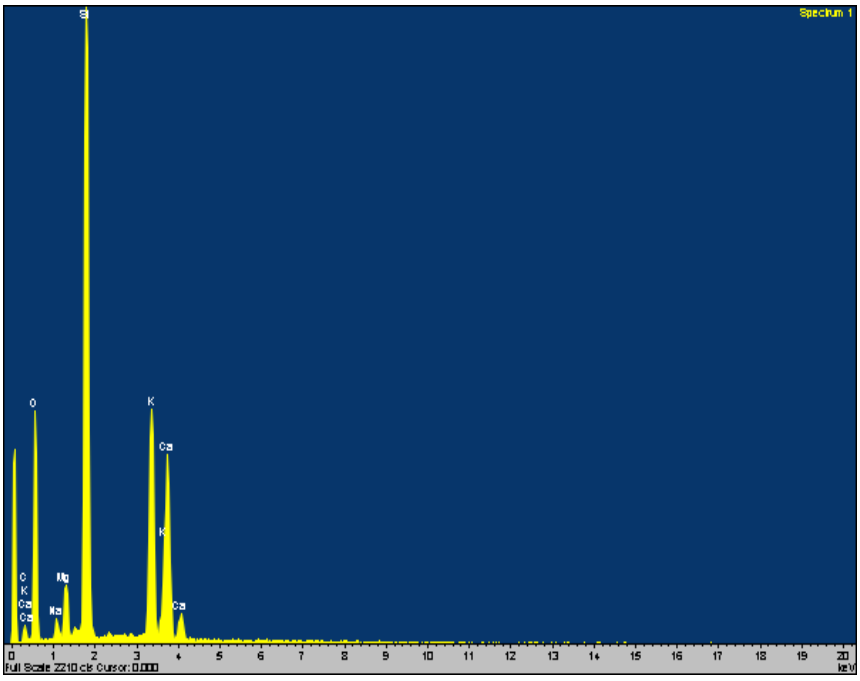

Highly ASR distressed aggregate

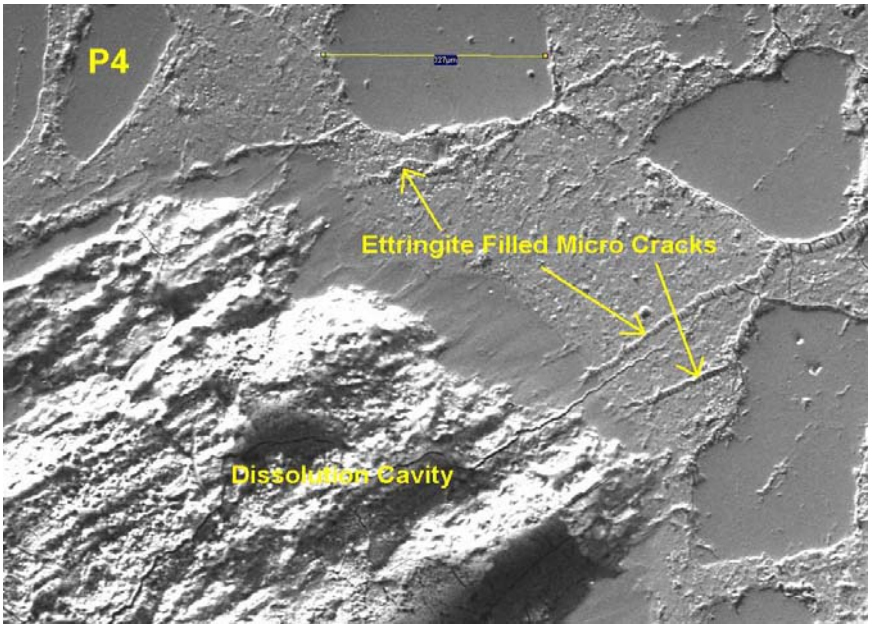

SEM/EDS spectra confirming ASR gel chemistry

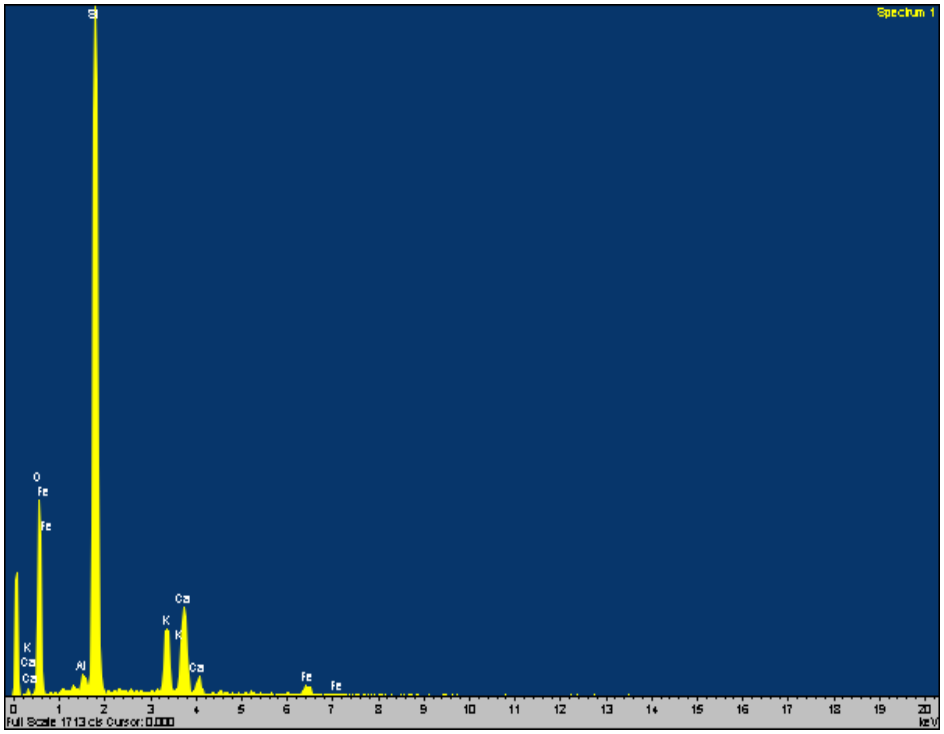

Image illustrating ettringite filled gap around FA

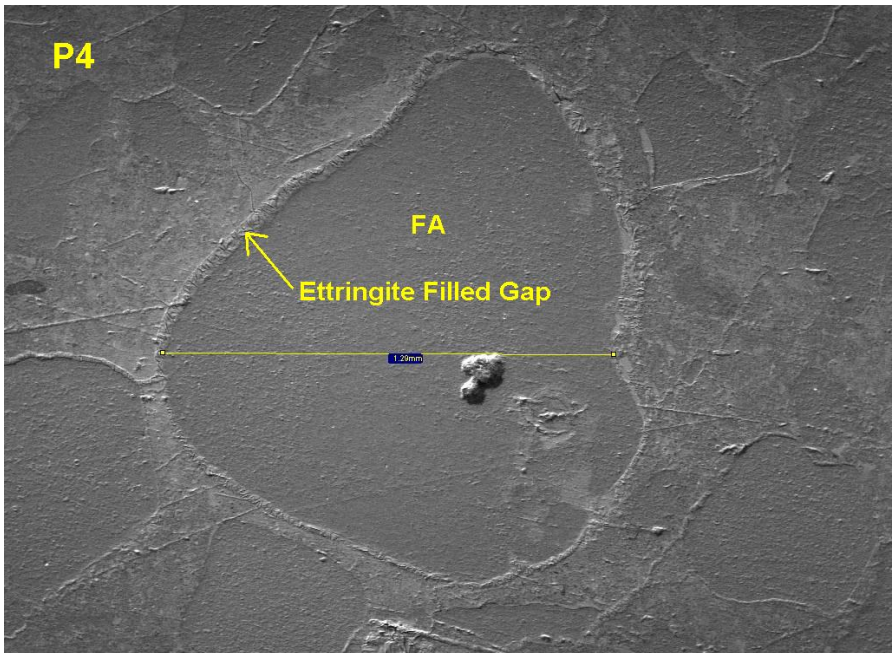

SEM/EDS Dot map illustrating sulfur rich ettringite filled gap and silica rich FA

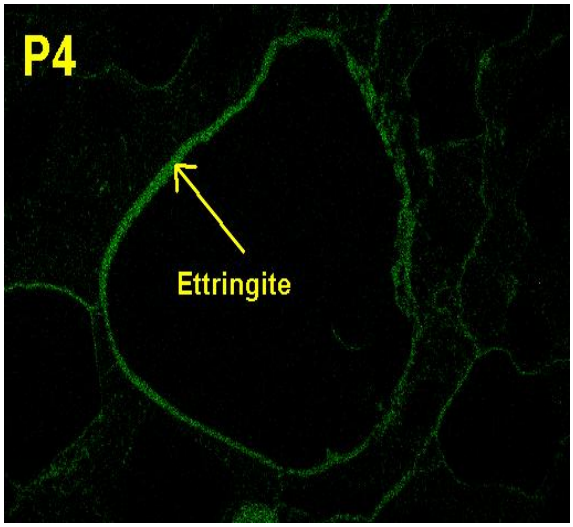

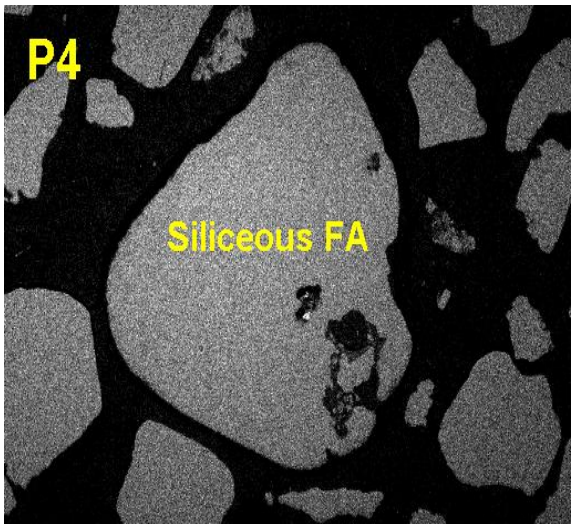

Image illustrating numerous ettringite filled micro cracks

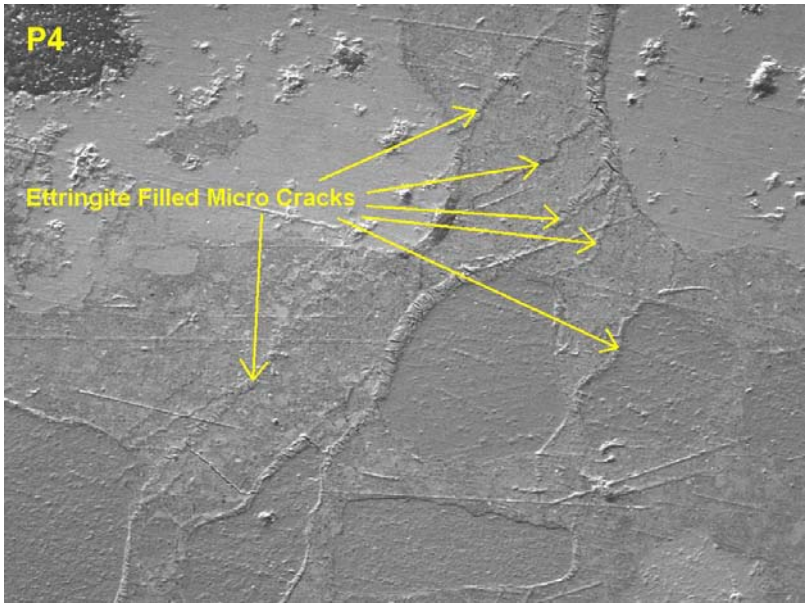

Sulfur Dot map illustrating ettringite filled micro cracks

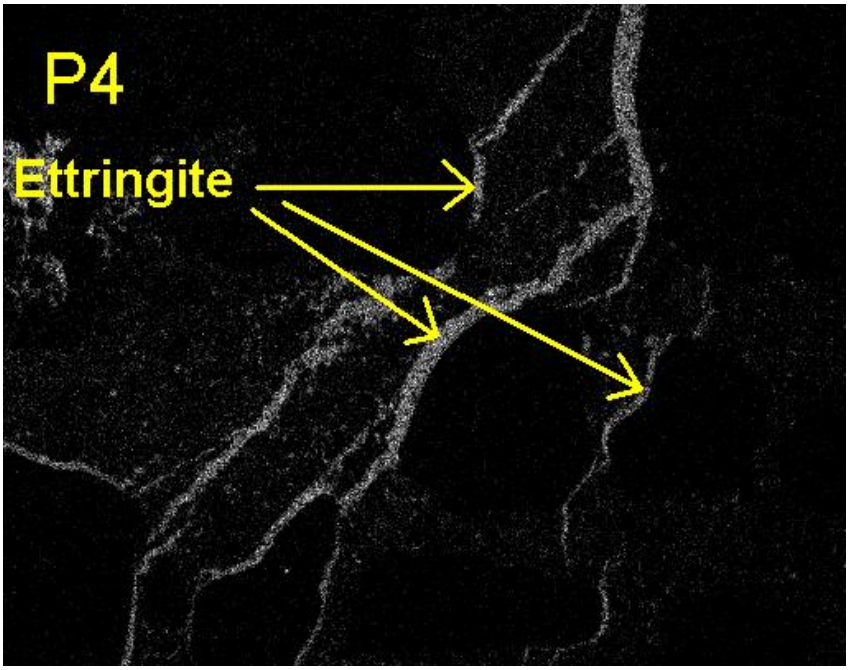

Image illustrating ettringite filled micro cracks

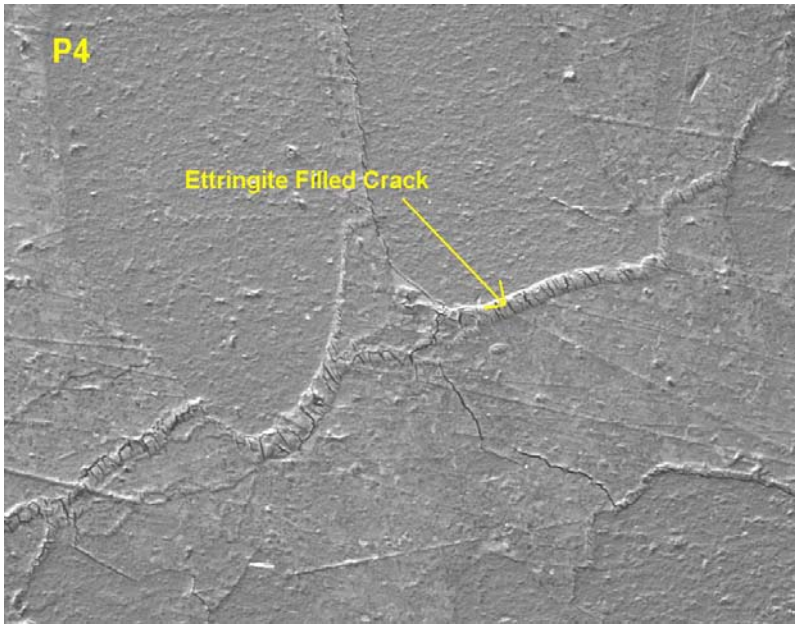

Image illustrating ASR distress aggregate and ettringite formation

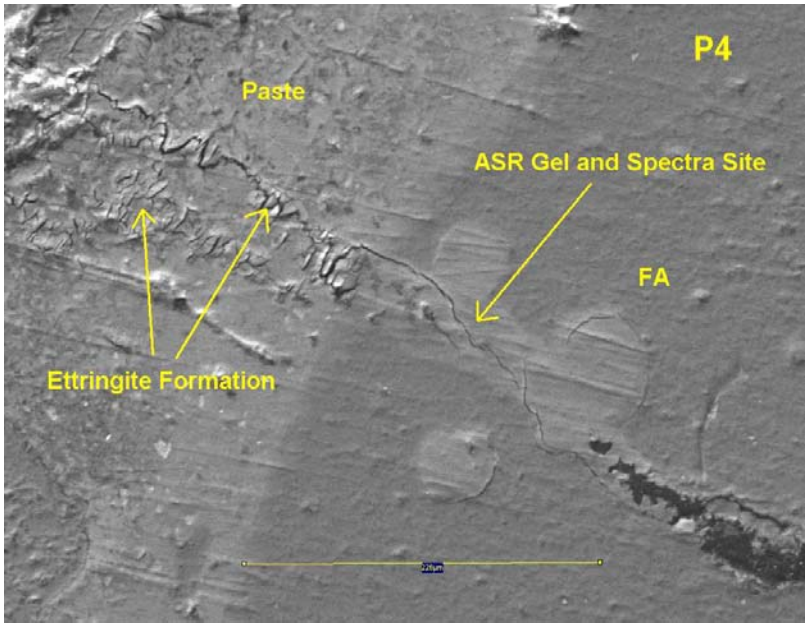

SEM/EDS spectra confirming ASR gel chemistry

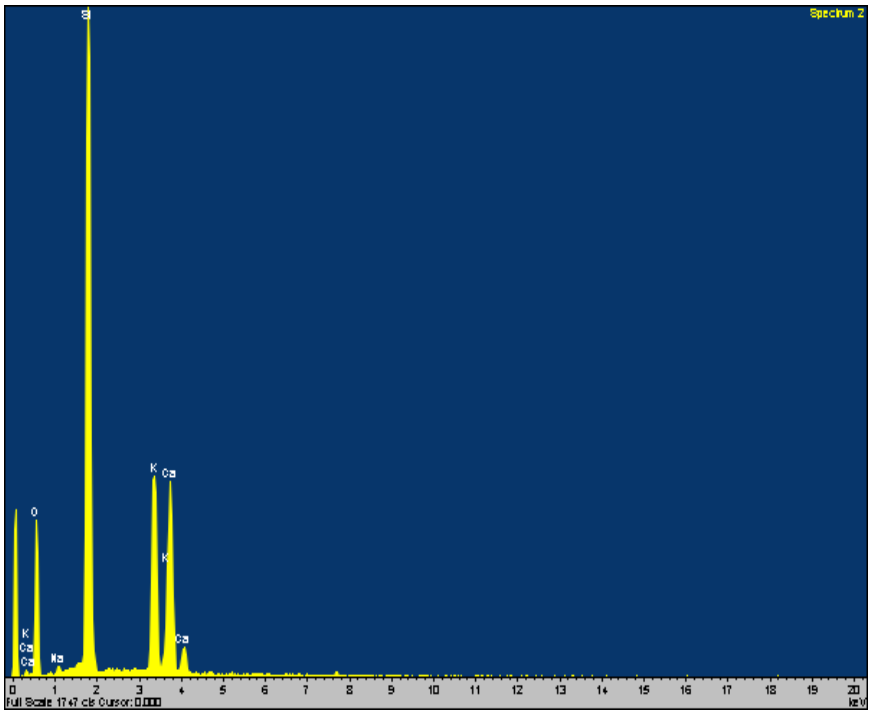

Image illustrating ASR site and ettringite filled crack

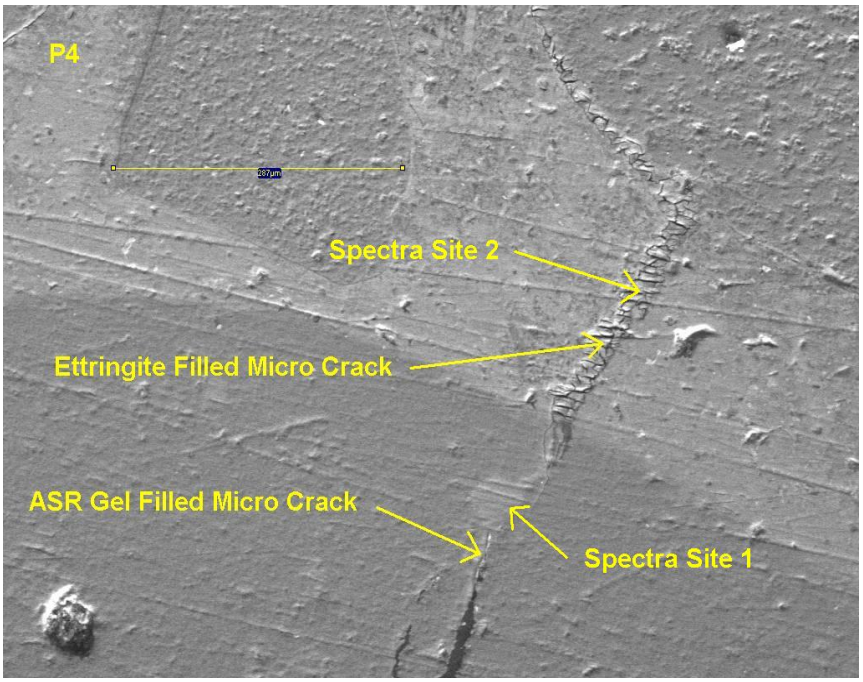

SEM/EDS spectra sites confirming ASR gel and ettringite chemistry

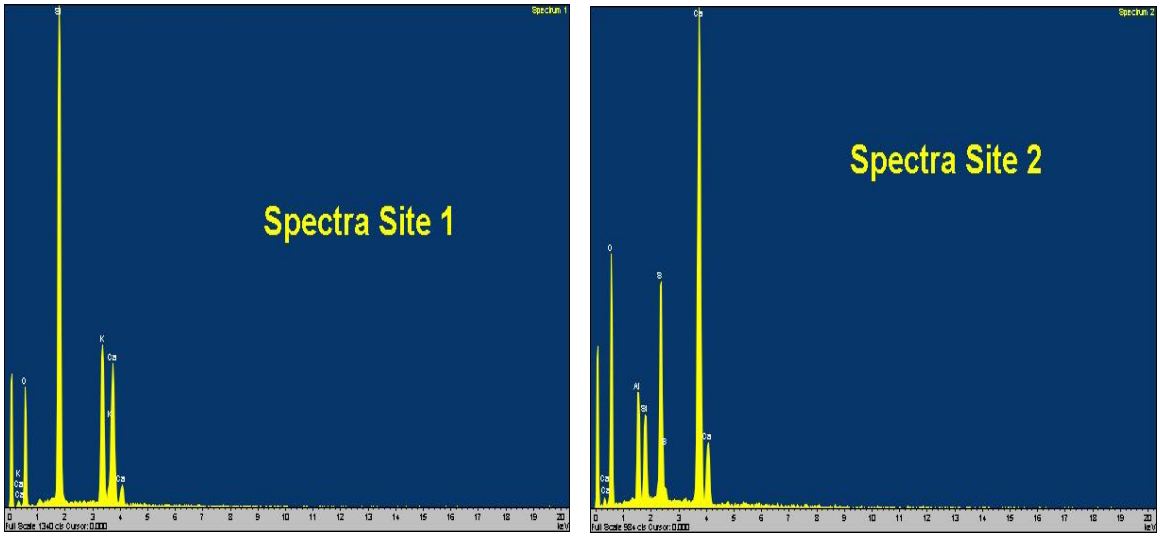

Image illustrating ASR distress intermediate size aggregate

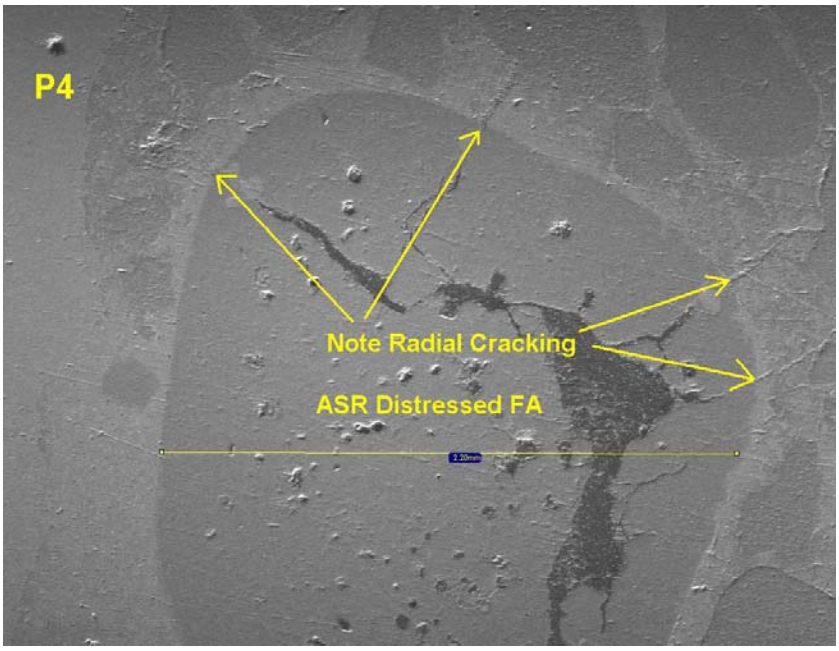

Qualitative study of damage severity in each sample and damage progression through the length of the sample. (Comparison of micro structural damage between all samples).

Core #	Total Length	Micro Structural Damage and # Reactive Particles Counted on Cross-Sectional Polished Slab			
		Top 4 Inches	4-8 Inches	4-12 Inches or Remainder	Remainder
P1	10 “	3 reactive particles. Primary Macro vertical crack propagated full length of section and pierced numerous CA. Fine ettringite filled cracks associated with FA reactivity oriented more vertical become sub-parallel to surface with depth. Overall level of distress is low to moderate.	6 reactive particles. Primary crack continues another 1-1/2 in this section. Ettringite filled fine micro cracks associated with FA ASR. Distress level is moderate.	9 reactive particles in remaining 2”. Fine ettringite filled cracks associated with ASR. Similar distress level as 4-8 section.	
P2	8-3/4 “	7 reactive particles. Two surface cracks one ¾ “deep and the other 3/8 inch deep. Fine ettringite filled crack oriented more vertical becoming sub-parallel to surface with depth.	12 Reactive particles. Ettringite filled fine micro cracks associated with FA ASR. Distress level slightly higher than P1.	15 reactive particles in remaining 2-3/4”. Ettringite filled fine micro cracks associated with FA ASR. Distress level slightly higher than P1.	

		Level of distress slightly higher than P1.			
P3	10-1/2”	4 reactive particles. Three shallow surface cracks ranging from 7/8 to 2/8 in depth. Some fine ettringite filled cracks. Level of distress is less than P1 and P2.	16 reactive particles. Fine ettringite filled cracking and level of distress is similar to P1.	4 reactive particles in remaining 2-1/2”. Level of distress is less than P1 and P2.	
P4	8-1/2”	13 reactive particles. Several shallow ¼ to 1/8 “surface cracks. Distress level similar to P2.	16 reactive particles. Numerous fine ettringite filled micro cracks oriented sub-parallel to surface. Slightly higher level of distress than P2.	3 reactive particles in remaining 2-1/2 “. Lower # ASR particles than P1, P2 and P3. Abundant ettringite filled cracks. Level of distress similar to P2.	
P5	11”	9 reactive particle. Surface cracks to 1-1/2 inch deep. Fine etringite filled micro cracks increase in lower section. Level of distress is higher than P2.	23 reactive particles. Abundant fine ettringite filled cracks and larger crack in lower section pierced limestone CA. Level of distress is higher than P2.	12 reactive particles in remaining 3 inches. Abundant fine ettringite filled micro cracks. Larger cracks piercing limestone CA oriented sub-parallel to the surface. Level of distress	

				similar to 4-8 section.	
P6	13-1/2”	12 reactive particles. Fine ettringite filled micro crack increasing with deep to abundant level. Level of distress is similar to P5.	23 reactive particles. Abundant ettringite filled micro cracks oriented both vertical and sub-parallel to surface. Level of distress is higher than P5.	18 reactive particles. Abundant etringite filled micro cracks. Larger cracks oriented sub-parallel to surface piercing numerous limestone CA. Level of distress is higher than P5.	3 reactive particles in remaining 1-1/2 “. Ettringite filled micro cracks abundant. Larger cracks oriented parallel to surface were observed. Level of distress is higher than P5.
P7	10-3/4”	14 reactive particles. Surface crack to ½ inch and larger cracks oriented near vertical to sub-parallel to the surface. Abundant fine ettringite filled micro cracks increase with deep of section. Level of distress is similar to P6.	19 reactive particles. Abundant ettringite filled micro cracks. Some larger cracks in top section running sub-parallel to surface. Level of distress is similar to P6.	18 Reactive particles in remaining 2-3/4 “. Abundant ettringite filled micro cracks. Level of distress is similar to P6.	
P8	12-3/4”	13 reactive particles. Surface crack to 3/8 inch deep. Fine ettringite filled micro cracks oriented more vertical in top section	22 reactive particle. Abundant ettringite filled micro cracks. Level of distress is similar to P6 and P7.	24 reactive particles. Micro cracking similar to 4-8 section. Level of distress is similar to P6 and P7.	3 reactive particles in remaining 3/4 “section. Level of distress similar to 8-12 section.

		and sub parallel with depth. Larger cracks oriented sub-parallel to surface in lower section. Level of distress is similar to P6 and P7.			
P9	7-1/2”	9 reactive particles. Surface crack to 3/8 deep. Level of distress is similar to P3.	18 reactive particles in remaining 3-1/2”. Level of distress is similar to 4-8 section in P3.		

The following schematic is a representation of the cracking and orientation observed in these specimens.

Representation of Micro Structural Damage

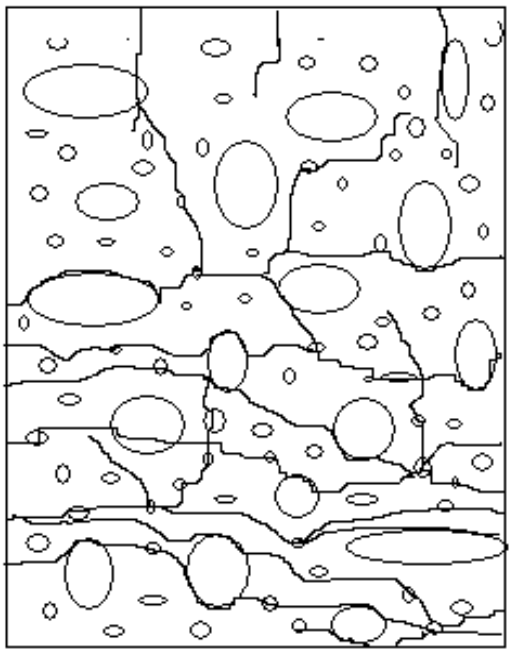

Conclusion: Based on this analysis ASR is the primary PCD mechanism responsible for the distressed concrete in all 9 cores. A microcrystalline chert fine aggregates is the principle lithologic mineral associated with the reaction. Micro structural damage from the ASR resulted in an extensive network of fine micro cracks (see above images) observed throughout these cores. The expansive reactions resulting in development of larger vertical surface crack seen in most of the cores.

It is inconclusive whether DEF has played a role in the distressed concrete. Due to the limited occurrence of true gapping (resulting from bulk expansion of the paste) DEF does not appear to have played a significant role in the distress. Most of the site that appear to be gapping were created as a result of ASR generated micro cracks intersecting the aggregate and then partially wrapping around them (fluorescent and SEM demonstrates this occurrence). Bifurcation of the intersecting cracks can sometime make it look like gapping has occurred. It is unclear whether the ettringite precipitation and potential imbibing of moisture could generate enough stress to potentially widen these cracks at the paste aggregate interfaces. Ettringite was noted as small discrete nests within the paste and in air voids. A coating of ettringite was also noted where the rebar had dislodged (on imprint of rebar) during the polishing process in Core P4. This indicates that either a separation occurred (debonding) between the rebar and paste forming a gap large enough for ettringite precipitation or possibly settlement gaps or thermal cracks had occurred.

.

References

"AASHTO LRFD Bridge Besign Specifications." Washington, D.C.: American Association of State Highway and Transportation Officials, 2009.

ACI Committee 318. "Building Code Requirements for Structural Concrete (ACI 318-08)." Farmington Hills: American Concrete Institute, 2008.

Ahmed, Tarig, Eldon Burley and Stephen Rigden. "Effect of Alkali-Silica Reaction on Tensile Bond Strength of Reinforcement in Concrete Tested under Static and Fatigue Loading." ACI Materials Journal 96-M42. July/August 1999. 419-428.

Bach, Finn, Torsten S. Thorsen and M. P. Nielsen. "Load-Carrying Capacity of Structural Members Subjected to Alkali-Silica Reactions." Construction and Building Materials. Vol. 7. 2. Butterworth-Heinemann Ltd, 6 January 1993. 109-115.

Bae, Sungjin, et al. "Anchor Bolt Behavior in ASR/DEF-Damaged Drilled Shafts." Technical Report: IAC 88-5DDIA004. Austin: The University of Texas at Austin, February 2007.

Bauer, Stacy, et al. "Alkali-Silica Reaction and Delayed Ettringite Formation in Concrete: A Literature Review." CTR Technical Report 0-4085-1. Austin: The University of Texas at Austin: Center for Transportation Research, February 2006.

Bindrich, Bryan V., James O. Jirsa and Oguzhan Bayrak. "The Effects of Alkali-Silica Reaction and Delayed-Ettringite Formation on the Structural Performance f the Dapped End Region of Prestressed Concrete Trapezoidal Box Beams." Austin: The University of Texas at Austin, May 2009.

Birrcher, David, et al. "Strength and Serviceability Design of Reinforced Concrete Deep Beams." CTR Technical Report 0-5253-1. Vol. Texas Department of Transportation. Center for Transportation Reasearch at The University of Texas at Austin, April 2009.

Boenig, A., et al. "Bridges with Premature Concrete Deterioration: Field Observations and Large-Scale Testing." Research Report 1857-1. Austin: Center for Transportation Research, The University of Texas at Austin, October 2001.

Brown, Michael D., et al. "Design for Shear in Reinforced Concrete Using Strut-and-Tie Models." CTR Research Report 0-4371-2. Austin: The University of Texas at Austin, April 2006.

Chana, P. S. and D. M. Thompson. "Laboratory Testing and Assessment of Structural Members Affected by Alkali Silica Reaction." Aggregate Reaction in Concrete. The 9th International Conference on Alkali, 1992. 156-166.

Clayton, N., R. J. Currie and R. M. Moss. "Effects of Alkali-Silica Reaction on the Strength of Prestressed Concrete Beams." The Structural Engineer. Vol. 68. 15. 1990. 287-292.

Deschenes, Dean J., Oguzhan Bayrak and Kevin J. Folliard. "ASR/DEF- Damaged Bent Caps: Shear Tests and Field Implications." Technical Report No. 12-8XXIA006. Austin: The University of Texas at Austin, August 2009.

Deschenes, Dean Joseph. ASR/DEF- Damaged Bent Caps: Shear Tests and Field Implications. Austin: The University of Texas at Austin, 2009.

Farney, J. A. and B. Kerkhoff. "Diagnosis and Control of Alkali-Aggregate Reactions in Concrete." Concrete Technology (2007): 1-11.

Folliard, Kevin J. and Thano Drimalas. "Brief Summary of Evaluation of Houston Box Beams." Unpublished Raw Data. The Univsersity of Texas at Austin, 18 March 2008.
Hobbs, Don W. "Countering Alkali-Silica Reaction in Concrete." Concrete Construction. November 1989. 948-950.

Kubo, Y., et al. "Experimental Study of Fracture of Reinforced Steel Bar in Concrete Structures Due to Alkali-Silica Expansion." Durability of Concrete. Vols. SP-212. Ed. V. M. Malhotra. Sixth CANMET/ACI, 1 June 2003. 637-652.

Lawrence, B. L., et al. "Evaluation and Mitigating Measures for Premature Concrete Distress in Texas Department of Transportation Concrete Elements." Cement, Concrete, and Aggregates 1999: 73-81.

Miyagawa, Toyoaki, et al. "Fracture of Reinforcing Steels in Concrete Structures Damaged by Alkali-Silica Reaction - Field Survey, Mechanism and Maintenance." Journal of Advanced Concrete Technology. Vol. 4. No. 3. Japan Concrete Institute, October 2006. 339-355.

Mohammed, Tarek Uddin, Hidenori Hamada and Toru Yamaji. "Alkali-Silica Reaction-Induced Strains over Concrete Surface and Steel Bars in Concrete." ACI Materials Journal. ACI, March-April 2003. 133-142.

Morgan, Edward. "UT ASR DEF." Petrographic Analysis. Austin: Texas Department of Transportation. Unpublished Report, 30 March 2010.

Roche, J. M., R. E. Klingner and T. J. Fowler. "Bridges with Premature Concrete Deterioration: Fatigue Testing of Full-Scale, Prestressed Concrete Box Girders Failing in Shear." Research Report 1857-3. Austin: Center for Transportation Research, The Universtiy of Texas at Austin, October 2001.

Vogel, J. "ASR Affected Trapezoidal Box Beams." TrapBeamIACDescription. 2008.

Vita

Nancy Anne Larson was born in Annapolis, Maryland on November 18, 1986 to Michael and Janet Larson. She is the first of three children with younger sister, Abby, and brother, Curtis. Nancy graduated from Gunston Day School in Centreville, Maryland in June of 2004. She received a Bachelor of Science in Civil Engineering degree with Highest Honors from Lehigh University in Bethlehem, Pennsylvania in May of 2008.

In August of 2008, she enrolled in the civil engineering graduate program at The University of Texas at Austin where she worked as a research assistant at the Phil M. Ferguson Structural Engineering Laboratory. Nancy graduated with a Master of Science in Engineering in August of 2010 and will continue to work towards a Doctor of Philosophy at The University of Texas at Austin.

Permanent address and email: 2640 Bennett Point Road
Queenstown, MD 21658
NancyAnneLarson@gmail.com

This thesis was typed by the author.